



Universidade do Minho

Escola de Engenharia

Sapienza Università di Roma

Dipartimento di Ingegneria Strutturale e Geotecnica

Angelo Gaetani

**Seismic Performance of Masonry Cross Vaults:
Learning from Historical Developments
and Experimental Testing**

Tese de Doutoramento (Co-tutela)

Engenharia Civil / Estruturas

Ingegneria Strutturale e Geotecnica

Trabalho efectuado sob a orientação do

Professor Doutor Paulo B. Lourenço (UMinho)

Professor Doutor Giorgio Monti (Sapienza)

DECLARAÇÃO

Nome: Angelo Gaetani

Endereço electrónico: angelo.gaetani@uniroma1.it

Telefone: +39 06 4458 5399

Número do Bilhete de Identidade: Passaporte YA 2182456

Título tese (co-tutela com Sapienza Università di Roma - Italy):

Seismic performance of masonry cross vaults: learning from historical developments and experimental testing

Orientadores:

Professor Doutor Paulo José Brandão Barbosa Lourenço (UMinho)

Professor Doutor Giorgio Monti (Sapienza)

Ano de conclusão: 2016

Designação do Doutoramento:

Engenharia Civil

Escola de Engenharia

Departamento de Engenharia Civil

Nos exemplares das teses de doutoramento ou de mestrado ou de outros trabalhos entregues para prestação de provas públicas nas universidades ou outros estabelecimentos de ensino, e dos quais é obrigatoriamente enviado um exemplar para depósito legal na Biblioteca Nacional e, pelo menos outro para a biblioteca da universidade respectiva, deve constar uma das seguintes declarações:

1. É AUTORIZADA A REPRODUÇÃO INTEGRAL DESTA TESE/TRABALHO APENAS PARA EFEITOS DE INVESTIGAÇÃO, MEDIANTE DECLARAÇÃO ESCRITA DO INTERESSADO, QUE A TAL SE COMPROMETE;
2. É AUTORIZADA A REPRODUÇÃO PARCIAL DESTA TESE/TRABALHO (indicar, caso tal seja necessário, nº máximo de páginas, ilustrações, gráficos, etc.), APENAS PARA EFEITOS DE INVESTIGAÇÃO, , MEDIANTE DECLARAÇÃO ESCRITA DO INTERESSADO, QUE A TAL SE COMPROMETE;
3. DE ACORDO COM A LEGISLAÇÃO EM VIGOR, NÃO É PERMITIDA A REPRODUÇÃO DE QUALQUER PARTE DESTA TESE/TRABALHO

Universidade do Minho, ____ / ____ / ____

Assinatura: _____

Acknowledgements

First of all, I want to thank my supervisors for guiding my research. I would like to express my deepest gratitude to Professor Giorgio Monti for his care since the first time we met, and for making the initial contacts leading to the joint program with UMinho. I am indebted to Professor Paulo Lourenço for his full support, encouragement and interesting discussions. I will always value his endless assistance and the time I spent within his research group. A special thanks goes to Professor Achille Paolone, mentor and unofficial advisor, for his invaluable friendship and for his incitement along all the research.

The experimental tests performed at Sapienza University of Rome would not have been successful without the assistance of the laboratory technicians of Structures and Materials Laboratory and Hydraulics Laboratory, to whom I am grateful. I express my thanks to Nuno Mendes (UMinho) for his constant and kind availability, for the endless discussions on the numerical modelling and his precious advices. Professor Gabriele Milani (Polytechnic of Milan) is also gratefully acknowledged for sharing his expertise and the software about limit analysis.

I am extremely grateful to all my friends and colleagues of both universities (Sapienza and UMinho) for their comments and interest in my work, as well as the enduring encouragement and the great time we had together. In particular, I spent almost eighteen months in Portugal and I have such a wonderful memories I cannot thank them enough. A huge thank you to my closest friends who supported and helped me during the tremendous work of the last weeks. This thesis would not be completed without them.

Finally, I would like to express my unending gratitude to my family for their love and unconditional support. To my brother Massimo and his family for their loving care, and to my little nephew Alessandro for his enthusiasm and cheerfulness. I wish him the brightest future.

Abstract

Considering the seismic behaviour of cultural heritage buildings, an influential role is played by masonry vaults, often representing the most vulnerable part of the construction. Despite their long-lasting history and the damage observation following the Italian earthquakes of the recent past, research in this area is still limited. In this regard, the present thesis is devoted to the study of the seismic behaviour of masonry groin vaults, considered as one of the most diffused vault type in European seismic prone areas in cloisters, palaces and churches. Groin vaults are resulting from the intersection at a right angle of two semi-cylindrical shells on a square bay, and can be addressed as the simplest form of cross vaults, defined as a combination (compound) of curved shells whose thrust converges along the diagonals to isolated abutments. The goal of this work is met via an integration of laboratory tests and numerical analyses.

The first part of the thesis reviews the historical developments of the cross vault, the structural methods adopted by the scientific community and the damage evidences after laboratory experiments and post-seismic observation. The subsequent part deals with shaking table tests on a scaled arch built with dry-joint 3D printed voussoirs. The experimental campaign had a twofold purpose. On the one hand it gave insight into the seismic behaviour of masonry arches and, on the other hand, thanks to the tracking motion system employed to record the tests, it provided valuable information to calibrate a three-dimensional numerical model.

The physical model was studied using a commercially available FEM software, namely DIANA (from TNO Delft), assuming rigid-infinitely resistant blocks and Coulomb friction interfaces. The nonlinear analyses regarded both the static and dynamic behaviour, shading light on the influence of interface stiffness and damping. The numerical model was subsequently extended to the study of the three-dimensional behaviour of groin vaults. In particular, the analyses focused on the results available in literature following a recent experimental campaign on a 1:5 scaled vault. The model was able to properly catch the maximum strength and the failure mechanism recorded in

the quasi-static tests. Analogies between the nonlinear behaviour of the vault and the free-standing rigid block undergoing incremental horizontal force are also discussed.

The last part of the thesis is dedicated to a sensitivity analysis aimed at evaluating the influence of the main geometrical and mechanical parameters on the seismic capacity and failure mechanisms of groin vaults. A non-commercial code implemented in Matlab, based on the upper bound approach of standard limit analysis, was used. The results were finally processed through a multiple linear regression analysis in order to get simplified analytical equations for expedite seismic evaluation of existing groin vaults.

Keywords: cross vault, groin vault, dry-joint arch, shaking table, seismic capacity, time history analysis, limit analysis

Resumo

Considerando o comportamento sísmico do património cultural edificado, as abóbadas de alvenaria desempenham um papel fulcral, sendo comumente a parte mais vulnerável da estrutura. Apesar da sua importância histórica e dos danos observados após os sismos recentes ocorridos em Itália, o trabalho de investigação realizado nesta área é limitado. Neste sentido, a presente tese é focada no estudo do comportamento sísmico de abóbadas de aresta de alvenaria, considerado um dos tipos de abóbada mais difundidos em claustros, palácios e igrejas, em áreas de grande vulnerabilidade sísmica na Europa. As abóbadas de aresta resultam da intersecção em ângulo reto de duas abóbadas de berço com a mesma flecha, resultando numa forma quadrangular em planta. Esta configuração pode ser entendida como a forma mais simples de abóbadas de cruzaria, definida como uma combinação de elementos de casca curvos, cujo impulso converge ao longo das diagonais para suportes isolados. O objetivo deste trabalho é cumprido através da realização de ensaios de laboratório e análises numéricas.

A primeira parte da tese compreende a revisão bibliográfica da evolução histórica da abóbada de cruzaria, dos métodos de análise estrutural adotados pela comunidade científica e dos danos observados em provetes ensaiados em laboratório e em inspeções efetuadas pós-sismo. A parte subsequente descreve os ensaios realizados em mesa sísmica, de um modelo à escala de um arco de alvenaria de junta seca, constituído por aduelas imprimidas em 3D. A campanha experimental teve um duplo propósito. Por um lado, proporcionou um aprofundamento no estudo do comportamento sísmico de arcos de alvenaria, e por outro lado, graças ao sistema de rastreamento de movimento utilizado para monitorizar os testes, forneceu informações essenciais para a calibração do modelo numérico tridimensional.

O modelo físico foi estudado usando um programa de elementos finitos comercial, DIANA (de TNO Delft), assumindo um conjunto de blocos resistentes infinitamente rígidos e o modelo constitutivo de Coulomb para a fricção nas interfaces. As análises não lineares realizadas, estáticas e dinâmicas, revelaram a influência da rigidez e do amortecimento das interfaces no

comportamento global. O modelo numérico foi de seguida alargado ao estudo do comportamento tridimensional de abóbadas de aresta. Em particular, a análise numérica focou-se nos resultados publicados de uma campanha experimental realizada recentemente, focada num modelo à escala 1:5 de uma abóbada. O modelo conseguiu reproduzir a força máxima e o mecanismo de colapso observados nos ensaios quasi-estáticos. Comparações entre o comportamento não linear da abóbada e a análise de blocos rígidos submetidos a um aumento incremental da força horizontal também são discutidas.

A última parte da tese é dedicada a uma análise de sensibilidade dos principais parâmetros geométricos e mecânicos, que influenciam a capacidade sísmica resistente e a formação de mecanismos de colapso de abóbadas de aresta. Para tal, foi implementada uma rotina não comercial no programa Matlab, baseada no teorema cinemático da análise limite. Os resultados foram analisados através de regressões lineares múltiplas, de forma a obter equações analíticas simplificadas, para avaliação sísmica expedita das abóbadas de aresta existentes.

Palavras-chave: abóbada de cruzaria, abóbada de aresta, arcos de junta seca, mesa sísmica, capacidade sísmica, análise dinâmica não linear, análise limite

Sommario

La conoscenza del comportamento strutturale delle volte in muratura rappresenta un aspetto essenziale per la conservazione e la salvaguardia del patrimonio storico-architettonico nei confronti dell'azione sismica. Tuttavia, nonostante i rilievi di agibilità post sismici condotti in Italia negli ultimi quarant'anni abbiano evidenziato la forte vulnerabilità di tali elementi costruttivi, la ricerca in questo campo è ancora limitata.

A tal riguardo, il presente lavoro di tesi ha come obiettivo lo studio del comportamento sismico della volta a crociera, considerata una tra le più diffuse tipologie di strutture voltate nei Paesi europei ad alto rischio sismico. In particolare, lo studio ha interessato la più semplice forma di volta a crociera, ottenuta come intersezione perpendicolare di due gusci semicilindrici (senza costoloni) su campata quadrata (*groin vault*). La metodologia adottata si basa su analisi numeriche agli elementi finiti in accordo con evidenze sperimentali.

Lo stato dell'arte della tesi è dedicato agli sviluppi storici della volta a crociera dal punto di vista tecnico e formale, alla descrizione dei modelli strutturali adottati dalla comunità scientifica per la relativa analisi, e ai più frequenti danneggiamenti rilevati in seguito a terremoti o durante esperimenti di laboratorio. Nella fase successiva, invece, si analizza il comportamento su tavola vibrante di un arco costruito a secco con conci realizzati con stampante 3d. La campagna sperimentale ha avuto un duplice obiettivo: se da un lato ha dato modo di approfondire la conoscenza del comportamento dinamico di questo elemento strutturale, dall'altro, grazie alla tecnica di *tracking motion* adottata per l'acquisizione degli spostamenti dei conci, ha permesso la messa a punto di un modello numerico tridimensionale.

Questo è stato realizzato con un programma commerciale agli elementi finiti (DIANA della TNO di Delft) assumendo i conci rigidi e infinitamente resistenti con interfaccia attritiva alla Coulomb. Le analisi non lineari hanno riguardato sia il comportamento statico che dinamico, evidenziando l'influenza della rigidità degli elementi di interfaccia e del coefficiente di smorzamento. Dopo aver validato il modello numerico, questo è stato esteso allo studio della volta a crociera. In

particolare, le analisi hanno interessato i risultati (disponibili in letteratura) di una recente campagna sperimentale su una volta a crociera in scala 1:5. Il modello numerico è riuscito a cogliere in maniera apprezzabile la massima capacità e i meccanismi di rottura rilevati durante gli esperimenti (condotti in maniera quasi statica), evidenziando varie analogie con il comportamento non lineare del blocco rigido soggetto a forze orizzontali incrementali.

Infine, l'ultima parte della tesi è dedicata all'analisi di sensibilità per la valutazione dell'influenza dei principali parametri geometrici e meccanici sulla capacità della volta a crociera e sui conseguenti meccanismi di rottura. A tal proposito è stato utilizzato un software non commerciale implementato in Matlab sulla base del teorema cinematico dell'analisi limite standard. I risultati di queste analisi sono stati quindi processati attraverso delle regressioni lineari multiple al fine di ottenere equazioni analitiche semplificate per la valutazione speditiva di volte a crociera esistenti.

Parole chiave: volta a crociera, arco con giunti a secco, tavola vibrante, capacità sismica, analisi dinamica non lineare, analisi limite

Table of contents

List of figures	xv
List of tables.....	xxi
Chapter 1. Introduction.....	1
1.1 General context of the work.....	1
1.2 Outline of the thesis.....	3
References	6
Chapter 2. Literary review.....	7
2.1 Abstract.....	7
2.2 Form evolution.....	8
2.3 Rules of thumb.....	12
2.3.1 Review of main treatises.....	12
2.3.2 Main elements dimensions.....	17
2.4 From historical methods to limit analysis.....	20
2.5 Modern structural analysis methods.....	25
2.5.1 Application to masonry cross vaults.....	26
2.6 Damages understating and experimental tests.....	35
2.6.1 Gravitational loads and settlements.....	35
2.6.2 Seismic load.....	40
2.7 Summary.....	46
References	48
Chapter 3. Dry-joint arch under base impulse signal.....	55
3.1 Abstract.....	55
3.2 Literature overview.....	56
3.3 Experimental setup.....	58

3.3.1 Overall description	58
3.3.2 Data acquisition.....	59
3.4 Experimental tests	60
3.4.1 Tilting tests.....	60
3.4.2 Signal processing	61
3.4.3 Experimental results.....	62
3.5 Numerical analyses.....	66
3.5.1 Overall description	66
3.5.2 Static nonlinear analysis.....	67
3.5.3 Time history analysis	71
3.6 Scale effect	75
3.7 Summary	77
References	78
Chapter 4. Seismic analysis of masonry groin vaults	81
4.1 Abstract	81
4.2 General aspects on block interlocking.....	81
4.3 Brief description of experimental tests and results.....	85
4.3.1 Layout	85
4.3.2 Main results.....	87
4.4 Numerical modelling	89
4.5 In-plane shear mechanism	91
4.5.1 Interface stiffness	92
4.5.2 Influence of geometrical nonlinearities	96
4.6 Tilting test.....	99
4.6.1 Interface stiffness	99
4.6.2 Influence of geometrical nonlinearities.....	101
4.6.3 Seismic direction.....	104
4.7 Summary	106
References	108
Chapter 5. Sensitivity analysis on groin vaults	111
5.1 Abstract	111
5.2 Adopted structural analysis code.....	112
5.3 Analysis overview	115
5.3.1 Boundary conditions	115

5.3.2 Geometry: diameter, thickness, angle of embrace	116
5.3.3 Infill as assigned load and mass.....	117
5.3.4 Description of the model.....	117
5.4 Simply supported vault.....	120
5.4.1 Failure mechanisms	120
5.4.2 Range of input parameters	121
5.4.3 Multiple linear regression analysis (MLR)	124
5.4.4 Characteristic value and uncertainties.....	128
5.5 In-plane shear	129
5.5.1 Failure mechanisms	130
5.5.2 Range of input parameters for each mechanism	130
5.5.3 Multiple linear regression analysis	135
5.5.4 Characteristic value and uncertainties.....	136
5.6 Summary	137
References	138
 Chapter 6. Conclusions.....	 139
6.1 Summary of results	139
6.2 Future works.....	143
References	145

List of figures

Figure 2-1. Baths of Diocletian - Rome, 298 - 305/6 AD: a) particular from the inner perspective by E. Paulin [1890]; b) nowadays, Basilica of St. Mary of the Angels and the Martyrs, Rome, Italy	8
Figure 2-2. Cross vaults forms: a) diagrammatic plan of Central European and English Gothic vaults after [Wilson, 1990] and b) the so-called <i>crazy vaults</i> in the St. Hugh's Choir of the Lincoln Cathedral, UK ©John Reynolds.....	10
Figure 2-3. Cross vaults geometry: a) classification after Barthel [1993] and b) different shapes using the same diagonal arches after Strommer [Strommer, 2008]	11
Figure 2-4. Description of a quadripartite vault after [Ching, 1995]	11
Figure 2-5. Fr. Derand's rule: a) application to different type of arches [Derand, 1643, p. 2, plate 1], b) to the Cathedral of Girona, Spain, and c) to the Sainte Chapelle, Paris, France [Huerta, 2004]	12
Figure 2-6. Abutment width calculation: a) Hernán Ruiz el Joven's rule considering the arch thickness (after Navascués Palacio, 1974); b) German gothic proportions, where l represents the chorus span (Koeopf, 1969 after Huerta, 2004).....	13
Figure 2-7. Latin cross plan church according to Cataneo [1567]: a) general plan scheme and b) longitudinal cross-section; the main dimensions are reported in c) and d). The side of the pier is the module (6feet) and all relative proportions are shown in bold.....	14
Figure 2-8. Graphical construction for the abutment width of an arch according to a) de La Hire [1712] and b)Valadier [1832].....	16
Figure 2-9. Valadier's geometrical construction (Chart 256) for calculating the abutment's dimensions for a cross vault.....	16
Figure 2-10. Palladio's rule of thumb: a) abutment width over span and b) plan and section of Palace of the Loggia, Brescia, Italy (Rondelet, 1802 after Huerta, 2004)	17
Figure 2-11. Comparison between traditional rules of thumb	18
Figure 2-12. Rodrigo Gil's rules of thumb: abutment width and inner pier diameter (w_b , h_p , s are, respectively, the bay width, the pier height and the span of the vault)	19
Figure 2-13. Mascheroni's analysis of cross vault (Chart XII).....	21
Figure 2-14. Cross vault analysis through inverted catenaries after [Beranek, 1988]	22
Figure 2-15. Graphical statics applied to cross vaults according to a) Wittmann [1879], b) Planat [1887], c) Körner [1901] and d) Wolfe [1921]	23

Figure 2-16. Example according to the approximated method by Ungewitter- Mohrmann for a cross vault, in case of a 200 mm thick sandstone vault and a ratio $f/s = 1:2$ [Heyman, 1995], where f is the height and s is the span 24

Figure 2-17. Slicing technique: a) patterns of slicing [Ungewitter and Mohrmann, 1890] and b) “ball principle”[Abraham, 1934]..... 24

Figure 2-18. Different force distributions for a groin vault according to O’Dwyer [1999]: a) forces towards the corners, b) parallel lateral arches, c) finer pattern. d) Cross vault analysis by Block [2009] 26

Figure 2-19. Cross vault analysis from [Fraternali, 2010]: a) geometry and loading data of the unreinforced cross vault; b) thrust surface and stress function (only vertical loading); c) final meshing (left) and force network (right) 28

Figure 2-20. Rib cross vault: a) geometry and loading condition and b) relative failure mechanism [Creazza et al., 2002]; c) failure mechanism, section view, d) front view and e) normalized power dissipated patch [Milani et al., 2008] 29

Figure 2-21. Rib cross vault tested by Faccio et al. [1999]: a) damage contours at intrados of cross vault for incremental displacements and at collapse for the deformed configuration [Creazza et al., 2002]; b) deformed shapes at peak [Milani and Tralli, 2012] 31

Figure 2-22. Macro-element method [Cannizzaro, 2011]: a) four noded element with diagonal spring and interfaces links; b) interface element; c) model of a cross vault..... 32

Figure 2-23. Crack pattern in a wall in case of an inclined point load: a) horizontal and b) vertical cross section [Mastrodicasa, 1943] 36

Figure 2-24. Collapse mechanisms for a cross vault according to Giovannetti [2000]..... 36

Figure 2-25. Cathedral in Tui (Spain): a) nave and b) lateral aisle 37

Figure 2-26. Sabouret cracks according to a) Abraham [1934] and b) Heyman [1983]. c) Typical crack pattern for different types of cross vaults according to Barthel [1993] 38

Figure 2-27. Possible collapse mechanisms according to Holzer [2011]: a) barrel vaults with lunettes and b) most frequent failure mechanism for cross vault 38

Figure 2-28. Crack pattern for diagonal displacement of the abutments: a) intrados; b) and c) possible damage on the extrados [Como, 2013]..... 38

Figure 2-29. Experimental test by Faccio et al. [1999]: a) geometry, load condition and referenced points, b) experimental setup, c) central displacement transducer at the intersection of the ribs 39

Figure 2-30. Cross vault tests: a) loading arrangement and b) crack formation at the intrados around the keystone [Theodossopoulos et al., 2002]; c) test setup [Foraboschi, 2004] 39

Figure 2-31. Collapse mechanisms caused by a) diagonal and b) transverse displacement of the support..... 40

Figure 2-32. Main Italian earthquakes in the last forty years (adapted from [Brandonisio et al., 2013, p. 695]) 41

Figure 2-33. M7: longitudinal response of central nave colonnade [Regione Toscana, 2003; Dipartimento della Protezione Civile, 2013]..... 42

Figure 2-34. Mechanisms M8, M9, M12, M18, M24 (nave, lateral aisle, transept, apse/presbytery and chapels respectively)..... 43

Figure 2-35. In place shear test for 1:5 scale model groin vault: a) monotonic and b) cyclic test [Rossi et al., 2014]..... 43

Figure 2-36. Collapse mechanism of a tilted groin vault: a) parallel and b) rotate by 45° [Shapiro, 2012]	44
Figure 2-37. Cross vault tested in NTUA, Athens: a) interior view of the cross vault tested in NTUA; b-c-d) damages at the end of the test	45
Figure 2-38. Cross vault tested in ENEA Casaccia Research Center, Rome: a) vaulted structures of the Mosque; b) damage mode of the vault; c) specimen allowed displacements; d) scheme of vault geometry	45
Figure 3-1. The SDOF mechanism for an arch under base excitation: a) first half cycle, b) recovering and impact, c) second half cycle	56
Figure 3-2. Test arch geometrical dimensions	58
Figure 3-3. Experimental setup	60
Figure 3-4. Example of Bohman window in time and frequency domain	61
Figure 3-5. 1.3 g, 10 Hz pre-and post-windowed signal (dash-dot blue line and black solid line, respectively)	62
Figure 3-6. Comparison between input signal (drive) and recorded signal (dot black line and red solid line, respectively)	63
Figure 3-7. 1.3 g, 10 Hz signal: displacement time history	64
Figure 3-8. 7 Hz and 0.6 g impulse (first replicate): significant frames for hinge location	65
Figure 3-9. 7 Hz and 0.6 g impulse (first replicate): deformed shape at 0.17 s and hinge location	65
Figure 3-10. Results of the shaking table tests	67
Figure 3-11. Elements adopted for the nonlinear DIANA FEM analysis: a) T18IF triangular interface element (topology and displacements); b) TE12L tetrahedral elements, geometry and shape function	68
Figure 3-12. Arch capacity curves varying the interface stiffness	69
Figure 3-13. Hinge location for: a) $K_n = K_t = 0.1 \text{ N/mm}^3$, and b) $K_n = K_t = 10 \text{ N/mm}^3$	70
Figure 3-14. Tilting test failure mechanism: a) frame recorded during the experiment and b) deformed shape of the numerical analysis (the lowest voussoirs are additional and simulate the fixed supports)	70
Figure 3-15. Sketch of the arch voussoirs by means of marker location and position of the control points	72
Figure 3-16. Displacement of the two control points: numerical and experimental results	73
Figure 3-17. Displacement of the two control points: numerical and experimental results	74
Figure 3-18. Results of the numerical analyses with $K_n = K_t = 0.1 \text{ N/mm}^3$	75
Figure 3-19. 1.3 g - 10 Hz signal ultimate displacement: comparison between a) FEM analysis (representation scale 1:1) and b) recorded frame of the test	75
Figure 4-1. Brick arrangement: a) contemporary bricks placed at the intersection by means of timber scaffolding; b) usual intersection of webs in a rib vault [Cangi, 2012 after Rossi, 2015]	83
Figure 4-2. Different blocks disposition on a cross vault with respect the web generatrix: a) parallel; b) orthogonal; c) oblique (herringbone bond)	83

Figure 4-3. Groin vault: block arrangement parallel to the generatrix [Giovanetti (ed. by), 2000]	83
Figure 4-4. Groin vault: herringbone bond arrangement [Giovanetti (ed. by), 2000]	84
Figure 4-5. Experimental model for cross vault testing: a) [Shapiro, 2012]; b) [Van Mele et al., 2012]; c) [Rossi, 2015]	84
Figure 4-6. Overall dimension of the model: a) [Rossi et al., 2015]; b) front view (measures in mm)	85
Figure 4-7. Displacement settings considered in the experimental campaign	86
Figure 4-8. Tilting tests: a) tilting angle β and b) rotation ϕ around its orthogonal axis	86
Figure 4-9. Test setup: a) layout and b) overview for the in-plane shear mechanism	88
Figure 4-10. Mechanism A: a) typical position of the hinges; b) force - displacement curves ($F_s - d_s$), where the quantities are considered over the total weight W and the span l , respectively	88
Figure 4-11. Tilting angle of the vault β on the basis of the seismic action direction ϕ	89
Figure 4-12. Block pattern adopted in the present study: a) methodology; b) extrados and intrados view	90
Figure 4-13. Zenith view of the vault during the tilting tests with $\phi = 9^\circ$: a) sliding of the upper part of the vault, b) crack interruption	91
Figure 4-14. Typical deformed shape of the vault after in-plane shear action without lateral constrains (graphic scale 10:1): a) zenith view and b) detail of the corner	92
Figure 4-15. Layout of the numerical model for in-plane shear mechanism	93
Figure 4-16. In-plane shear mechanism: comparison between the experimental (grey) and the numerical results with $K_n = 1$ and $K_t = 0.1, 0.4, 1$ MPa/mm (neglecting UL)	93
Figure 4-17. In-plane shear mechanism: deformed shape with $K_n = 1$, $K_t = 0.1, 0.4, 1$ MPa/mm (neglecting UL) and d_s/l around 3% (graphic scale 4:1 with colours according to total x-y-z displacement). Picture of the test. Circles indicate local failure of perimetral blocks	94
Figure 4-18. In-plane shear mechanism: numerical results considering $K_n = K_t = 0.5, 1, 10$ MPa/mm	95
Figure 4-19. In-plane shear mechanism: capacity curve considering a 10% reduction of the thickness and $K_n = K_t = 0.5$ MPa/mm	96
Figure 4-20. In-plane shear mechanism: comparison between the experimental (grey) and the numerical results with $K_n = 1$ and $K_t = 0.1, 0.4, 1$ MPa/mm (considering UL)	97
Figure 4-21. In-plane shear mechanism: deformed shape with $K_n = 1$, $K_t = 0.1, 0.4, 1$ MPa/mm (considering UL) - graphic scale 3:1 with colours according to total x-y-z displacement. Pictures of the test	97
Figure 4-22. In-plane shear mechanism: numerical results considering $K_n = K_t = 0.5, 1, 10$ MPa/mm	98
Figure 4-23. Schematization of the nonlinear behaviour of a rigid block undergoing horizontal action: a) limit condition and b) supposed real behaviour	99
Figure 4-24. Layout of the numerical model for tilting test	100
Figure 4-25. Lateral view of tilting test for increasing load: nonlinear analyses ($K_n = K_t = 1$ MPa/mm), a) with and b) without considering lateral steel plates (graphic scale 1:1); c) experimental result	100

Figure 4-26. Azimuth view of tilting test: nonlinear analyses ($K_n = K_t = 1$ MPa/mm), a) with and b) without considering lateral steel plates (graphic scale 2:1); c) experimental result	100
Figure 4-27. Tilting test: numerical results with $K_n = 1$ and $K_t = 0.1, 0.4, 1$ MPa/mm (neglecting UL)	101
Figure 4-28. Tilting test: deformed shape with $K_n = 1, K_t = 0.1, 0.4, 1$ MPa/mm (neglecting UL), graphic scale 1:1 and colours according to total x-y-z displacement (see also Figure 4-25)....	102
Figure 4-29. Tilting test: numerical results with $K_n = 1$ and $K_t = 0.1, 0.4, 1$ MPa/mm (considering UL)	102
Figure 4-30. Tilting test: deformed shape (seismic direction = 0°) with $K_n = 1, K_t = 0.1, 0.4, 1$ MPa/mm (considering UL)	103
Figure 4-31. Tilting test: numerical results considering $K_n = K_t = 0.5, 1, 10$ MPa/mm.....	104
Figure 4-32. Horizontal load multiplier of the vault according to the seismic direction ϕ : experimental and numerical results ($K_n = K_t = 1$ MPa/mm)	104
Figure 4-33. Comparison between the experimental and numerical failure mechanism according to different seismic directions ($9^\circ, 18^\circ, 27^\circ, 36^\circ, 45^\circ$) with $K_n = K_t = 1$ MPa/mm (azimuth view)	105
Figure 5-1. Masonry six-noded wedge: a) single element and four-noded interface; b) contiguous masonry elements (global and local frame of reference) [Milani et al., 2009b]	113
Figure 5-2. Plan view and boundary conditions for groin vaults: a) simply supported; b) in-plane shear (strut/tie between rollers).....	116
Figure 5-3. Groin vault description for three different angles of embrace ($120^\circ, 130^\circ$ and 140°), which control other geometrical parameters: a) constraint location; b) span, rise and infill calculation	116
Figure 5-4. Schematization of the infill load/mass according to Clemente [1997].....	118
Figure 5-5. Infill schematization according to the central angle.....	118
Figure 5-6. Mesh pattern adopted (e.g. $Th = 1/50$)	119
Figure 5-7. Most frequent mechanisms for simply supported groin vaults.....	121
Figure 5-8. Ranges of the input parameters according to the most frequent mechanisms.....	122
Figure 5-9. Frequency of the most frequent mechanisms according to the input parameters... ..	124
Figure 5-10. Variation of the load multiplier according to the failure mechanisms and the input parameters	125
Figure 5-11. Scatter plots of the prediction models according to MLR.....	127
Figure 5-12. Most frequent mechanisms for groin vaults subjected to in-plane shear.....	131
Figure 5-13. Ranges of the input parameters for each failure mechanism (in-plane shear).....	132
Figure 5-14. Frequency of the most frequent mechanisms according to the input parameters for groin vaults subjected to in-plane shear	134
Figure 5-15. Variation of the load multiplier according to the most frequent mechanisms and the input parameters for groin vaults subjected to in-plane shear.....	134
Figure 5-16. Scatter plots of the prediction models according to MLR (in-plane shear).....	136

List of tables

Table 2-1. Rodrigo Gil de Hontañón’s rules for dimensions of piers, abutments and keystones, where one Castellano foot is approximately equal to 0.28 m and one quintal is about 0.46 kN (100 old Spanish pounds)	15
Table 2-2. Overall description of rules applicable to cross vaults. In particular, w_a is the abutment width, d_p is the pier diameter and s is the span of the vault (for Rodrigo Gil’s see Table 2-1)...	18
Table 2-3. Rules of thumb for the main elements of the church related to the cross vault: s_n and s_c are the span of the central nave and of chorus respectively, whereas s is the span of the element considered	20
Table 2-4. Comparison of the available structural analysis methods for vaulted masonry structures	34
Table 3-1. Slip table system specifications	58
Table 3-2. Mesh sensitivity analysis ($\lambda = 0.29$ from tilting test).....	69
Table 3-3. Tilting test: comparison between experimental, literature [Clemente, 1998], and FE results	70
Table 3-4. Scale factors for similitude law (linearly elastic behaviour), where L, t and M stand for length, time and mass, respectively.....	76
Table 4-1. In-plane shear mechanism: parameters adopted for the nonlinear static analyses.....	91
Table 5-1. Geometrical parameters considered in the sensitivity analysis.....	116
Table 5-2. Mechanical parameters adopted and piecewise linear approximation of the failure criterion [Lourenço and Rots, 1997]	119
Table 5-3. Mechanism occurrence frequency for simply supported groin vault.....	120
Table 5-4. Variation of the input parameters according to the most frequent mechanisms	123
Table 5-5. Standardized regression coefficients	127
Table 5-6. Calculation for the 5% fractile of the predicted values.....	129
Table 5-7. Mechanism occurrence frequency for groin vaults subjected to in-plane shear	130
Table 5-8. Variation of the input parameters according to the most frequent mechanisms of groin vaults subjected to in-plane shear	133
Table 5-9. Standardized coefficients for groin vaults subjected to in-plane shear.....	135
Table 5-10. Calculation for the 5% fractile of the predicted values.....	137

Chapter 1.

Introduction

1.1 General context of the work

Clay brick, stone and masonry vaults are diffused all over the world with almost seven thousand years of history [Choisy, 1873]. Representing probably the first form of permanent dwellings in the prehistory (e.g. the beehive houses in the Middle East), the vaults assumed a religious and political symbolism that have likewise developed over time. The Arch of Constantine, Baths of Caracalla and Pantheon are a few examples of impressive vaults built by Romans [Adam, 1988; Marta, 1990]. During the Middle Ages, the construction of vaults was strongly influenced by economic and technological aspects (e.g. as enduring substitutes to the easy inflammable timber beams and floors) reaching a level of beauty and technological perfection that still impresses the modern observer.

However, despite the relevance and the long-lasting history of vaults, which clearly indicates some sort of consolidated design process, in ancient times, the workmanship followed what would be presently defined as “a rudimentary scientific approach”, i.e. trial-and-error and experience. In fact, each building could be considered a scaled specimen of a new one to be built, if not by effectively using a scaled model, as for the case of Brunelleschi’s dome [Heyman, 1966]. Based on successful achievements, ancient builders gathered competence under so-called *rules of thumb*. According to the classical idea of beauty founded on numerical proportions, until the end of the 18th century, these rules were made up by simple geometrical definitions with notable results. In fact, as long as strength is not involved, the theory of proportions provides correct outcomes [Di Pasquale, 1996]. It is still unclear if these rules were based on formal or structural aspects, but,

undoubtedly, ancient techniques slowly reached high levels of complexity long before theory caught up with them.

Nevertheless, the rules of thumb addressed only dead loads. The first reference to seismic behaviour of vaults is found in the *Naturalis Historia* (around 79 AD) by Pliny the Elder, who described small pozzolana concrete vaults as the safest place in case of earthquake. Unfortunately, the high seismic vulnerability of the masonry vaults soon revealed itself. For instance, in 1909, following the catastrophic earthquake of Messina in 1908, an Italian Royal Decree, although in a limited territory, forbade their construction.

Due to a growing interest in conservation of cultural heritage buildings, it is only in recent times that new attention is being paid to the seismic vulnerability of masonry constructions. In particular, the systematic collection of damage that occurred during strong Italian earthquakes in the last 40 years have emphasised the high vulnerability of vaulted structures, sometimes with incalculable loss in terms of cultural heritage. The collapse of the vaults frescoed by Giotto and Cimabue in the Basilica of St. Francis of Assisi in 1997 is an appalling example. More recently, Podestà et al. [2010] showed that L'Aquila earthquake in 2009 damaged more than 70% of vaults of the inspected churches.

This proves how the seismic vulnerability of masonry vaulted structures is still an open and delicate issue in the conservation of historical buildings. In this regard, considering the cross vault as one of the most diffused and fascinating structural typologies of the European cultural built heritage, the present thesis deals with the seismic behaviour of the groin vault, which is the simplest kind of cross vaults, obtained by the intersection at a right angle of two semi-circular barrel vaults. This choice is imposed by the complexity of this structural element and of the phenomena that affect its response.

The goal of the thesis is accomplished through a phased study based on numerical analyses and experimental activities. In order to tune the numerical model for nonlinear static and time history analyses, the dynamic behaviour of a simple vaulted structure was addressed first. For this purpose, a scaled arch was assembled using dry-joint 3D printed voussoirs undergoing base impulse motion. The experimental activity gave insight into the structural behaviour of this element and the motion tracking system provided kinematic data to properly calibrate the numerical model.

Assuming perfectly rigid voussoirs, attention was paid basically only to the interface constitutive law. In this regard, considering a unilateral (no tension) Coulomb (with friction) interface, a sensitivity analysis on the normal and tangential stiffness is presented. On the other hand, the

implementation of a time history analysis requested the calibration of the overall damping. In particular, the effects of viscous and hysteretic damping are also evaluated.

Consequently, the model of the arch was extended to the study of the groin vault recently tested by Rossi and Co-workers [2014, 2015; 2015]. The experiments discussed in the present work regarded: a) in-plane horizontal shear distortion and b) horizontal inertial forces proportional to the mass (tilting test), both performed quasi-statically. Again the influence of the interface stiffness was evaluated, showing appreciable results in terms of ultimate strength and deformation.

Finally, with the aim of an expedite assessment of the seismic capacity and the failure mechanism for groin vaults, a standard limit analysis code was implemented. Along with the low computational efforts, limit analysis is suggested by some Codes of Practice as the most appropriate approach in the professional field. The outcome of this phase was then processed using Multiple Regression Analysis, providing straightforward expressions for a preliminary safety assessment of existing groin vaults.

1.2 Outline of the thesis

Without claiming to fully treat this topic, for which specialized literature in the field of architectural history is suggested, the **second chapter** is devoted to the evolution of cross vaults from the geometrical and constructive standpoint, two essential features in structural modelling. In this regard, historical written sources, as manuals and treatises, represent an essential support. Since these sources of information were often conceived with no structural purposes, only a critical analysis of the sources gave the possibility to clarify implicit information, e.g. on dimensions of the main elements and constructive phases. This almost forgotten knowledge, validated by the very existence of those buildings today, represents valuable information about the structural decisions made by ancient builders. Moreover, being an essential aspect for an efficient and respectful conservation of historical monuments, accurate structural analysis should be integrated with detailed historical investigation. As an example, the proper geometrical representation of the vault may highlight the original double-curvature webs, which generally lead to a larger capacity for gravitational loads, i.e. resistant-by-shape structures.

As far as the structural analysis methods are concerned, considering the typical difficulties posed by historical masonry buildings (e.g. material, morphology and geometry), the study of vaulted structures often requests complex and sophisticated nonlinear strategies. On the other hand, conversely to the research field, simplified but still accurate approaches are available for practitioners and engineers. In this scenario, with the aim of clarifying the current state of the

knowledge for the analysis of masonry vaults, the second part of the second chapter briefly discusses available software applications. For the sake of completeness, the historical structural methods are also described, highlighting the similarities with recent techniques. Many examples are reported and particular emphasis is devoted to the case of cross vaults.

Finally, in order to conclude the literary review, the most relevant damages and the experimental activities on cross vaults are briefly reviewed. This represents an essential support for the physical interpretation of the problem, and is a valuable reference to validate the mechanical parameters of structural analysis. In this regard, the available experiments according to gravitational loads, settlements and seismic load are reported. The review is extended also to the discussion of the post-seismic damage collected in the survey form for seismic damage evaluation of churches (outcome of a collaboration between the Italian Department of Civil Protection and the Italian Ministry of Cultural Heritage).

The **third chapter** is mainly devoted to the analysis of a scaled arch assembled by dry-joint 3D printed voussoirs undergoing horizontal action. Firstly, neglecting the dynamic behaviour of the specimen, tilting tests were performed to evaluate the maximum static capacity of the arch. In order to compare the results with numerical analysis, a FE (finite element) model was implemented in a commercially available software named DIANA (TNO – Delft). Assuming perfectly rigid voussoirs, the nonlinear characteristics of the interface elements were assessed by way of a sensitivity analysis.

Providing the necessity of considering the geometrical nonlinearities (by means of Updated Lagrange formulation), the study showed how the analysis can underestimate the seismic capacity of masonry arches if low stiffness values are adopted. However, the envelope of the capacity curves relative to a wide range of stiffness values well represented the nonlinear behaviour of the arch (similar to the one of a free-standing rigid block undergoing horizontal action). On the other hand, the failure mechanism is only marginally affected by the interface properties.

Moreover, given the susceptibility of rigid blocks to the base impulse excitation [Zhang and Makris, 2001; DeJong et al., 2008; DeJong and Dimitrakopoulos, 2014], the experimental activities focused on the capacity of the arch undergoing windowed sine impulses with different frequency and amplitude. In order to avoid misleading results related to the manual assemblage of the specimen, each test was repeated three times (runs). The almost 70 runs provided significant results allowing assessing an exponential failure curve in the frequency-amplitude domain. The outcome of impulse base motion tests available in literature were also examined, highlighting the differences in terms of failure mechanisms and seismic capacity.

During the tests, the in-plane motion of the arch was recorded by a high-speed camera (400 Hz). Thanks to four markers located on the corners of each voussoir and a tracking motion system, the displacement history of all the elements was also recorded. The collected data represented a valuable support for the final calibration of the mechanical parameters of the numerical model.

Once validated, the model was extended to the three-dimensional analysis of groin vaults, whose outcomes are reported in the **fourth chapter**. In particular, the analyses focused on the experimental tests performed by Rossi and Co-workers [2014, 2015; 2015] on 1:5 scaled vault. The vault was built by dry-joint 3D printed blocks and the quasi-static tests regarded imposed displacements of the abutments and tilting analysis (according to different seismic directions). After a brief description of both the physical and numerical model with few comments on the block pattern and consequent interlocking, the results were compared in terms of both ultimate strength capacity and failure mechanisms.

Regarding the tests on the in-plane shear distortion, the comparison concerned also the experimental capacity curve, displaying a good analogy with the nonlinear behaviour of a free-standing block undergoing incremental horizontal force. In this regard, following the results of the numerical analyses, a possible strategy for evaluating the seismic behaviour of the vault is proposed.

Finally, the **fifth chapter** presents the results of a sensitivity analysis aimed at evaluating the influence of the geometrical parameters (namely, thickness, span, rise, height of the infill) on the seismic capacity of groin vaults. The author marginally developed the adopted code, originally from Milani et al. [2009a, 2009b], which is written in Matlab according to the upper bound (kinematic theorem) of standard limit analysis (associated flow rule). As far as the mechanical parameters are concerned, they are based on the Italian Code and only the influence of the tensile strength is evaluated. Furthermore, following the damage discussion presented in the literature review and in Chapter 4, the influence of boundary conditions was also evaluated.

With the aim of identifying the most frequent failure mechanisms, the results of the analysis have been visually inspected and ordered according to the input parameters. This also gave the possibility to heuristically deduce the range of parameters associated to a particular mechanism. Relating this catalogue to a multiple linear regression analysis, allowed creating a valuable tool for quick seismic evaluation of groin vaults, which may represent the first step for filling the lack of recommendations in the current Codes of Practice.

References

- Adam, J.-P. (1988). *L'arte di costruire presso i romani: materiali e tecniche*. (Longanesi, Ed.). Milano.
- Choisy, A. (1873). *L'art de bâtir chez les Romains*. (Ducher et C.ie, Ed.). Paris: Librairie generale de l'architecture et des travaux publics (Anastatic reprint, Bologna: Forni, 1984).
- DeJong, M., De Lorenzis, L., Adams, S., & Ochsendorf, J. A. (2008). Rocking Stability of Masonry Arches in Seismic Regions. *Earthquake Spectra*, 24(4), 847–865.
- DeJong, M., & Dimitrakopoulos, E. G. (2014). Dynamically equivalent rocking structures. *Earthquake Engineering & Structural Dynamics*, 43(10), 1543–1563.
- Di Pasquale, S. (1996). *L'arte del costruire. Tra conoscenza e scienza*. Venezia: Marsilio.
- Heyman, J. (1966). The stone skeleton. *International Journal of Solids and Structures*, 2(2), 249–279.
- Marta, R. (1990). *Architettura romana. Tecniche costruttive e forme architettoniche del mondo romano*. (Kappa, Ed.) (2nd ed.).
- Milani, G., Milani, E., & Tralli, A. (2009a). Upper Bound limit analysis model for FRP-reinforced masonry curved structures. Part I: Unreinforced masonry failure surfaces. *Computers & Structures*, 87(23-24), 1516–1533.
- Milani, G., Milani, E., & Tralli, A. (2009b). Upper bound limit analysis model for FRP-reinforced masonry curved structures. Part II: Structural analyses. *Computers & Structures*, 87(23-24), 1534–1558.
- Podestà, S., Brignola, A., Curti, E., Parodi, S., & Lemme, A. (2010). Damage assessment and seismic vulnerability of churches: the Abruzzo earthquake. *Ingegneria Sismica*, XXVII(1), 21–35.
- Zhang, J., & Makris, N. (2001). Rocking response of free-standing blocks under cycloidal pulses. *Journal of Engineering Mechanics*, 127(5), 473–483.

Chapter 2.

Literary review

2.1 Abstract

With the aim of reviewing the knowledge on the structural behaviour of cross vaults, the present chapter introduces this element from a historical perspective, by describing the evolution of the main geometrical shapes together with ancient practical rules used to size them. For a detailed review on historical aspects of arches, vaults and domes, the reader is referred to [Huerta, 2004], whereas [Willis, 1842] still represents a valuable reference for the study of gothic vault geometry.

Regarding building materials, stereotomy and construction process, not tackled in this dissertation, the reader is also referred to [Adam, 1988; Becchi and Focè, 2002; Trevisan, 2011]. However, with the aim of considering the effect of interlocking, few considerations about the brick/block pattern of cross vaults will be reported in Chapter 4 (FEM analysis).

The second part of the chapter deals with advancements in structural analysis methods for masonry vaulted structures from the pioneer works of the 18th century until the most recent techniques. The history of continuum mechanics and of arch theory are only briefly outlined for the purpose of the subsequent developments, as they have been treated in depth in other references, such as [Heyman, 1972; Benvenuto, 1991; Di Pasquale, 1996; Kurrer, 2008].

Finally, since the fundamental role in understanding the complex three-dimensional behaviour and validating the structural analysis methods, the last part of the chapter focuses on the possible damages for cross vaults. According to structural analyses and experimental tests, the discussion focuses on the effects due to gravitational loads, settlements and seismic action. Regarding the last one, a valuable reference is represented by the model for seismic damage evaluation of

churches provided by the Italian Civil Defence Agency [Dipartimento della Protezione Civile, 2013].

2.2 Form evolution

Cross vaults appeared in Europe during the Roman Empire Age (1st century BC – 5th century AD) with the construction of thermal baths. The first form was the rounded cross vault composed by the orthogonal intersection of two semi-circular barrel vaults, i.e. two semi-cylindrical shells on a square bay with no ribs [Alberti, 1485], which is generally referred to as groin vault. The Basilica of Maxentius and the Baths of Diocletian (Figure 2-1), both spanning more than 25 m, are remarkable results of the Roman technical skills and of the unique features of *opus caementicium* (pozzolana concrete). Several authors described its efficiency as a “miracle” [Branca, 1783] while Cavalieri San-Bartolo [1826] stressed the role of its tensile strength in avoiding the thrust on the supports. However, although Romans conceived the vault as a one-piece structure, Tomasoni [2008] stressed how the possible cracks development could have led the builders to strengthen the most stressed parts of the structure by placing brickwork hidden ribs in the concrete mass. For cross vaults this meant building perimeter arches and internal diagonal ribs [Choisy, 1873].

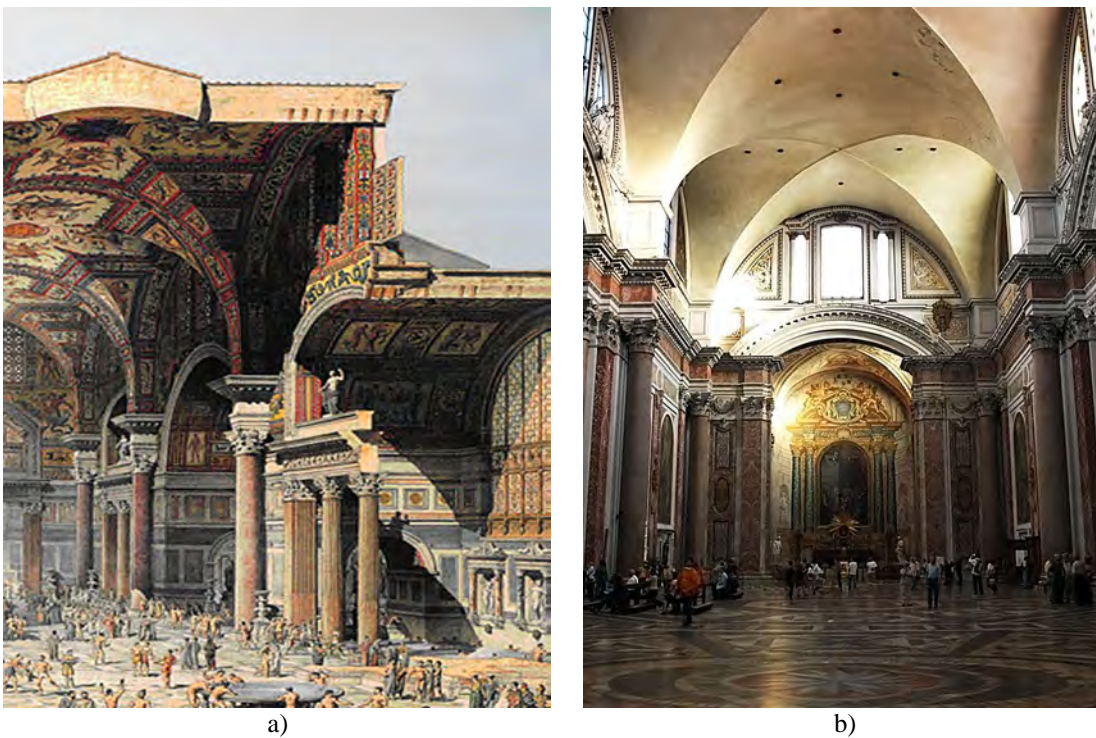


Figure 2-1. Baths of Diocletian - Rome, 298 - 305/6 AD: a) particular from the inner perspective by E. Paulin [1890]; b) nowadays, Basilica of St. Mary of the Angels and the Martyrs, Rome, Italy

At the end of the 5th century AD, the decline and subsequent fall of the Roman Empire led to the Early Middle Ages, characterized by an overall impoverishment of the building yard, both in terms of techniques and materials, and the consequent disappearance of the pozzolana concrete. It is only since the 10th century that high and wide spanned vaulted structures reappeared in Central Europe reaching the climax two centuries later when more than 350 cathedrals with the outstanding Gothic style were built in less than 30 years. This architectural style was based on a more rational and optimized building approach: each element was assigned to a precise structural role, giving to gothic churches a sense of profound elegance, along with a considerable saving of resources [Alberti, 1485; Frézier, 1737; Viollet-le-Duc, 1854; Huerta, 2004].

From the structural point of view, directing the self-weight of a vault to the four corner pillars allowed lateral walls to become non-structural elements, to be soon replaced by large stained glass windows, thus decreeing the end of the Romanesque massive style. The originally hidden ribs of the Roman vaults became now of fundamental importance: they were made visible at the intrados and, starting from the 11th century, they represented a sort of independent structural frame supporting the thinner webs - in the early stage probably disconnected each other [Willis, 1842]. Although, in the last two centuries a great debate arose regarding the structural role of the ribs during and after the construction process - see §4, but also the Suger's description of the church of St. Denis [Frankl, 1960] - studies and experiments suggest that the centring that supported the ribs remained in place until the webs were completed [Wendland, 2007]. In this so-called *rib cross vaults*, the preferential force flow path proved to be so efficient that it was possible to build them with 10-15 m span and only 0.20 m thickness, which implied less weight and, thus, less thrust [Como, 2013].

Looking at the construction process, the intersection of two semi-cylinders produces semi-elliptical diagonals, difficult to be built for the masons of that time who started to prefer segmental arcs with circular shape, that is, its centre below the springings, or semi-four-centred arc ribs [Tosca, 1707; Rondelet, 1802; Willis, 1842]. Accordingly, defining the cross arches as autonomous elements, it could be reasonable to adopt centring in-plane arches with an elementary geometry, simply and straightforwardly attainable [Wendland, 2007]. On the basis of constructive criteria of rationality and simplification, this process improved leading to design ribs with the same curvature, that is, to carve identical *vousoirs* for different parts of the vault [Willis, 1842; Palacios, 2006].

All this practical approach inevitably affected the shape, leading the crown of the vault to be higher than the lateral arches and forcing the webs to be portions of a double-curvature irregular spheroid [Frézier, 1737; Huerta, 2004], providing an higher overall stability both in the

construction process and once completed [Wendland, 2007]. Besides this first variation, although already largely adopted in Middle East countries, it was during the 12th century that the pointed arch appeared in France and England, representing a geometrical revolution allowing for an easier arrangement of the vault geometry, that is, the height of the lateral arches was no longer constrained and the bay could be rectangular. The same goal could be accomplished also rising the arch upon stilts (“stilted arch”) which are straight prolongations of the arch until meeting the springings [Willis, 1842]. The pointed arch had also structural relevance because, as stressed by Viollet-le-Duc [1854], it reveals the ability of the masons of approaching, without any scientific assumption, the closest arch shape to the thrust line (see also Section 2.4).

The geometrical palette available to the masons paved the way to a wealth of different forms that eventually culminated with the English and Spanish Gothic architecture. In order to provide a more stable support, but also for the sake of innovation or extravagance, a multiplication of ribs appeared. As an example, Figure 2-2 shows 26 different cross vault plans and the so-called *crazy vaults* of the St. Hugh’s Choir of the Lincoln Cathedral in England (1192 and 1265) that seems to challenge any structural rule. According to the shape of the vault surface, which Willis [1842] already pointed as of capital importance in examining existing vaults, a basic classification of the large variety of quadripartite cross vaults was proposed by Barthel [1993] shown in Figure 2-3a - for a more detailed investigation on the surface shape according to the traditional vault construction without formwork, the reader is referred to [Wendland, 2007]. On the other hand, Figure 2-3b shows the variation of the overall cross vault shape considering the same diagonal arches and different web profiles [Strommer, 2008].

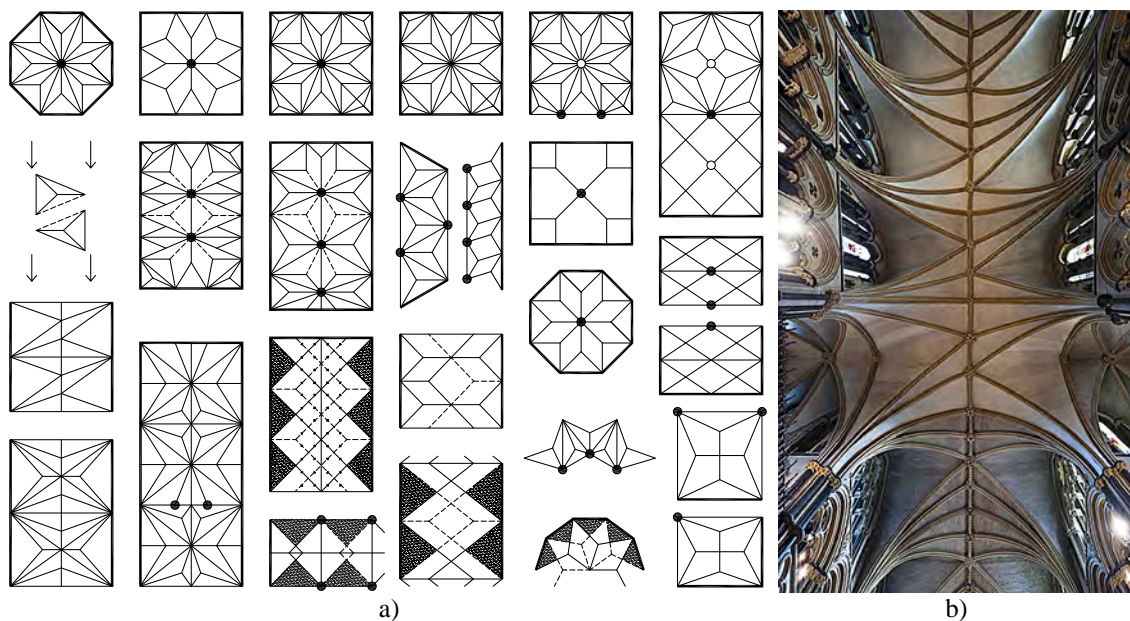


Figure 2-2. Cross vaults forms: a) diagrammatic plan of Central European and English Gothic vaults after [Wilson, 1990] and b) the so-called *crazy vaults* in the St. Hugh’s Choir of the Lincoln Cathedral, UK ©John Reynolds

Finally, for the sake of clarity and completeness, the main elements of a quadripartite cross vault are depicted in Figure 2-4 [Willis, 1842]. In particular, the lateral arches are presented, where *arc doubleau* and *arc formeret* are, respectively, transversal and parallel to the longitudinal axis. Moreover, the possible ribs marking the crown are called *longitudinal* and *transverse ridge rib*, *arc tierceron* is a rib extending between one corner and one ridge, and finally *lierne* is a rib not connected to any corner.

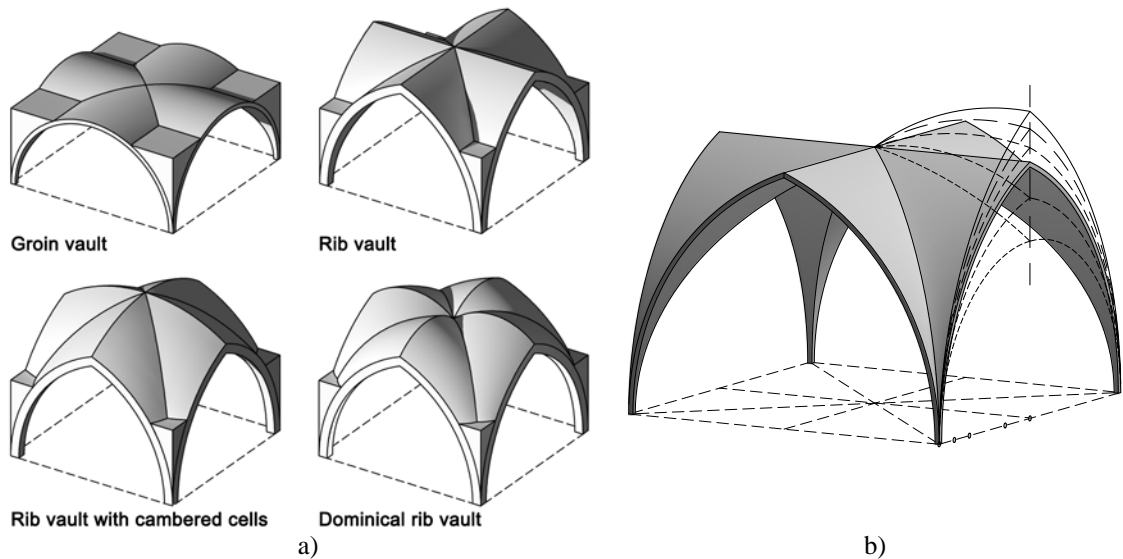


Figure 2-3. Cross vaults geometry: a) classification after Barthel [1993] and b) different shapes using the same diagonal arches after Strommer [2008]

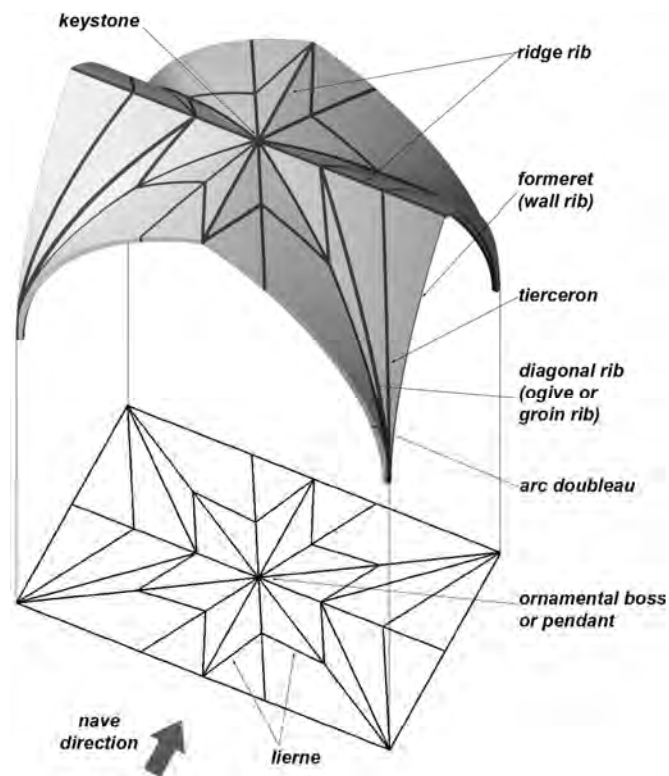


Figure 2-4. Description of a quadripartite vault after [Ching, 1995]

2.3 Rules of thumb

2.3.1 Review of main treatises

Until the 15th century, the treatises of architecture did not provide any information about the vaults design. In particular, during almost the entire Gothic period (12th – 16th century), the rules were simply handed over mostly in secrecy, appearing only in Renaissance and Baroque treatises, with a delay of almost four centuries.

The most famous rule was the so-called “Blondel’s rule”, also known as “Fr. Derand’s rule” [Derand, 1643, p. 2, plate 1; Blondel, 1675, p. 419]. It consisted in the division of the *arc doubleau* in three equal parts from which it was possible to geometrically obtain the width of the abutment as reported in Figure 2-5a [Heyman, 1982; Benvenuto, 1991; Huerta, 2004]. According to Müller [1990], the rule was already cited in Boccojani’s lost treatise of 1546, which means that it was defined at least during Late Gothic. Despite the clear relevance for Gothic structures, as showed in Figure 2-5b [Huerta, 2004], there is no evidence to consider it as a genuine gothic rule. However, the evident handiness, together with the correct ability of providing wider supports for larger thrust (from pointed to flat arches), made this rule rapidly spread, even after the Gothic period, e.g. it is still present in Vittone [1760], even in case other type of vaults are considered.

Slightly different from Fr. Derand’s rule, in 1560 Hernán Ruiz el Joven introduced the arch thickness into the geometrical construction for the abutment width design, which is possibly the first approach to take into account the weight of the vault (Figure 2-6a). Moreover, for the first time, the stabilizing importance of the infill was stressed and it was recommended to add it until half of the arch rise, while the thickness of the arch should be not less than 1/10 of the span [Navascués Palacio, 1974].

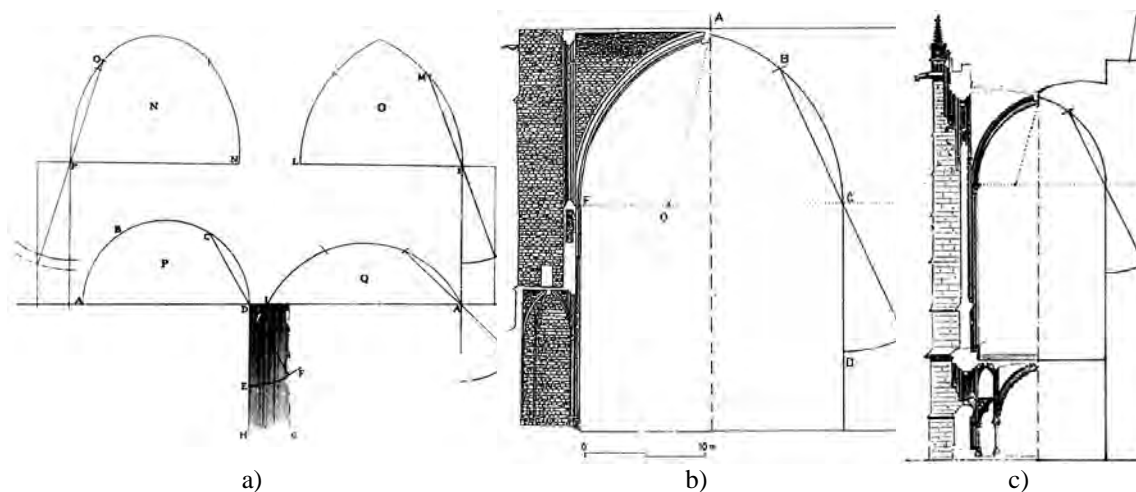


Figure 2-5. Fr. Derand’s rule: a) application to different type of arches [Derand, 1643, p. 2, plate 1], b) to the Cathedral of Girona, Spain, and c) to the Sainte Chapelle, Paris, France [Huerta, 2004]

Whereas the previous two rules concerned only the abutment width, the German gothic builders set up a list of geometrical proportions that, without any structural purpose, starting from the span of chorus, led up to the smallest details, e.g. the vault ribs cross-section (Figure 2-6b). Regarding the abutment width, it must be stressed that the resulting dimension is not referred to the vault springs (as for the other rules) but to the base of the element, allowing for slight tapering towards the top. The rules reported in Table 2-2 and Table 2-3 are provided by Coenen [1990] who collected the sources of the Late Gothic German treatises, of which only *Von des Chores Maß und Gerechtigkeit* (c. 1500) and *Wiener Werkmeisterbuch* (15th century) by unknown authors, and [Lechler, 1516] contain information to size the elements related to cross vaults [Huerta, 2004].

A similar but more pronounced approach was adopted by Cataneo [1567] who, instead of suggesting geometrical proportions, proposed the true dimensions of all the parts of five Latin cross plan churches. The Cataneo's purpose was to make the building resemble the Christ body: although rather forced with the aim of meeting tradition, this reasoning seems to disregard any structural aspect. More in detail, Figure 2-7 shows the general plan and the longitudinal cross section of a three-nave church. The abutment width is equal to one-third of the clear span of the aisle, which, together with a thick external wall, leads to an overall massive buttressing system able to balance the large thrust of the Renaissance rounded vaults. In this regard, Cataneo [1567] did not define the type of vault in the lateral aisles, even if the square bay may suggest cross or sail vaults.

During the 15th and 16th century, when the Late Gothic gives way to the Renaissance, Rodrigo Gil de Hontañón, who represents one of the most important Spanish architects of the past, wrote a booklet (c. 1544 - 1554, unfortunately lost but partially copied by Simón García before 1681) in

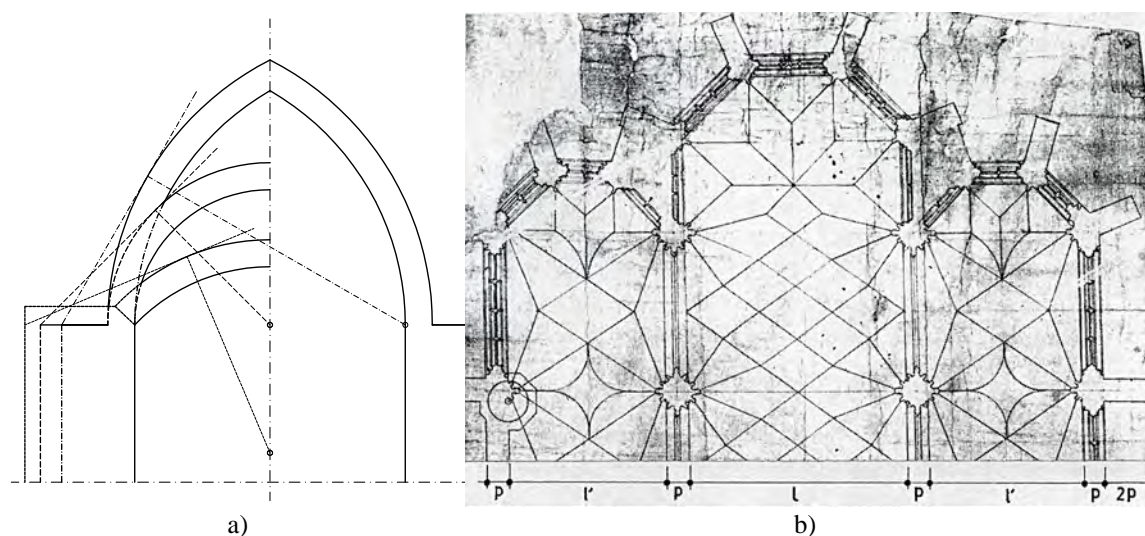


Figure 2-6. Abutment width calculation: a) Hernán Ruiz el Joven's rule considering the arch thickness (after Navascués Palacio, 1974); b) German gothic proportions, where l represents the chorus span (Koeopf, 1969 after Huerta, 2004)

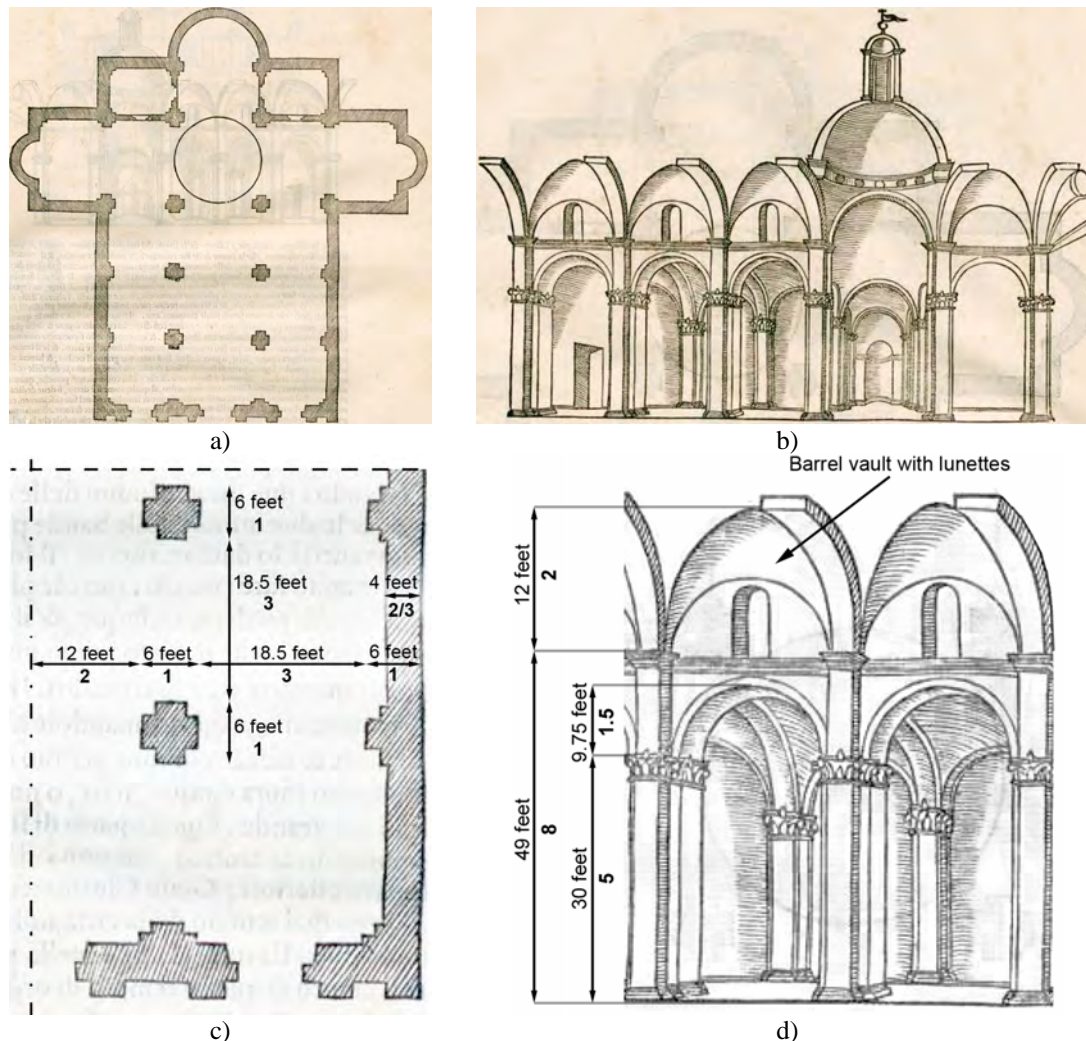


Figure 2-7. Latin cross plan church according to Cataneo [1567]: a) general plan scheme and b) longitudinal cross-section; the main dimensions are reported in c) and d). The side of the pier is the module (6feet) and all relative proportions are shown in bold

which Gothic tradition is merged with new mathematical tools and humanist ideas [Sanabria, 1982; Huerta, 2004]. Focusing only on cross vaults, he respectively: a) proposed an unexplained geometrical proportion for the abutment width equal to one fourth of the span; b) approached analytical formulations for the sizing of the pier diameter, the abutment width and the weight of the keystone (Table 2-1); c) suggested to design the minor elements of the vaults according to a forced proportion with human fingers (see Table 2-3).

Regarding the use of analytical formulations, whereas on one hand is a proof of new mathematical tools available to masons, on the other hand it reveals the efforts of Rodrigo Gil de Hontañón of considering the design process according to a proper structural intuition rather than the tradition made by simple spatial proportions [Sanabria, 1982]. Although clearly incorrect, the formula for sizing the pier diameter regards the height of the pier and the plan dimensions of the nave bay, meaning that he correctly understood the direct proportion with these geometrical quantities.

Pier diameter (at the base) [feet]	$d_p = \frac{1}{2} \sqrt{h_p + w_b + s}$	h_p	height of the pier at the springing of the vault [feet]
		w_b	central nave bay width [feet]
		s	central nave span [feet]
Abutment width (at the springing level, wall included) [feet]	$w_a = \frac{2}{3} \sqrt{h_a + \frac{2}{3} \sum r_i}$	h_a	height of the abutment at the springing of the vault [feet]
		r_i	semi-length of all the ribs connected to the abutment (except for the <i>arc formeret</i>) [feet]
		<i>The author suggested the abutment breadth equal to half of w_a</i>	
Keystone weight [quintal]	$Q = p_r \sqrt{\sum l_s - \sum l_{ns}}$	p_r	weight of ribs per unit length [quintals per feet]
		l_s	length of the structural elements [feet]
		l_{ns}	length of the non-structural elements [feet]

Table 2-1. Rodrigo Gil de Hontañón's rules for dimensions of piers, abutments and keystones, where one Castellano foot is approximately equal to 0.28 m and one quintal is about 0.46 kN (100 old Spanish pounds)

Almost one hundred years later, Friar Lorenzo de San Nicolás wrote one of the last works on architecture before the Age of Enlightenment (between 1639 and 1664) and addressed general aspects about cross vaults construction without giving practical rules about their dimensions. Nevertheless, in case of rounded cross vaults, the author erroneously pointed out that the structural stability was guaranteed only thanks to the infill weight (until one-third of the rise) with no need of abutments [Huerta, 2004].

The subsequent 18th century brought a new interest for vaulted structures, which were a key topic of modern mechanics. However, the new scientific approach was not close to the autonomy and maturity of the following centuries and, in this context, the rules of thumb still played a fundamental role. Validated by centuries-old history, the traditional rules represented the only support to validate the new theories [Benvenuto, 1991; Kurrer, 2008].

In the early 1700s, de La Hire and Belidor were the most representative figures of this *science after tradition* trend. They tried to rigorously study the arch stability (according to the wedge theory) but they just ended up with another geometrical construction (Figure 2-8a). Nevertheless, although scientifically incorrect, since it perfectly matched the tradition, this geometrical rule swiftly spread over the Europe, together with the common Fr. Derand's rule.

This trend was still present in the following century when, almost at the beginning of the wrought-iron era, despite the important developments of mechanics, Cavalieri San-Bertolo [1826] and Valadier [1832] still focused their attention on the handiness and supposedly safer tradition. In particular, since Fr. Derand's rule did not consider the thickness of the arch and the height of the abutment, Valadier proposed another graphical method. In this regard, he referenced the essays of *Accademia Reale delle Scienze* of 1712, which is the same year of de La Hire's *Memoir* (Paris),

but the comparison between the two methods reveals the apparent difference (Figure 2-8). Regarding the cross vaults abutment, Valadier applied this method on the two elemental barrel vaults obtaining the perpendicular side lengths (Figure 2-9).

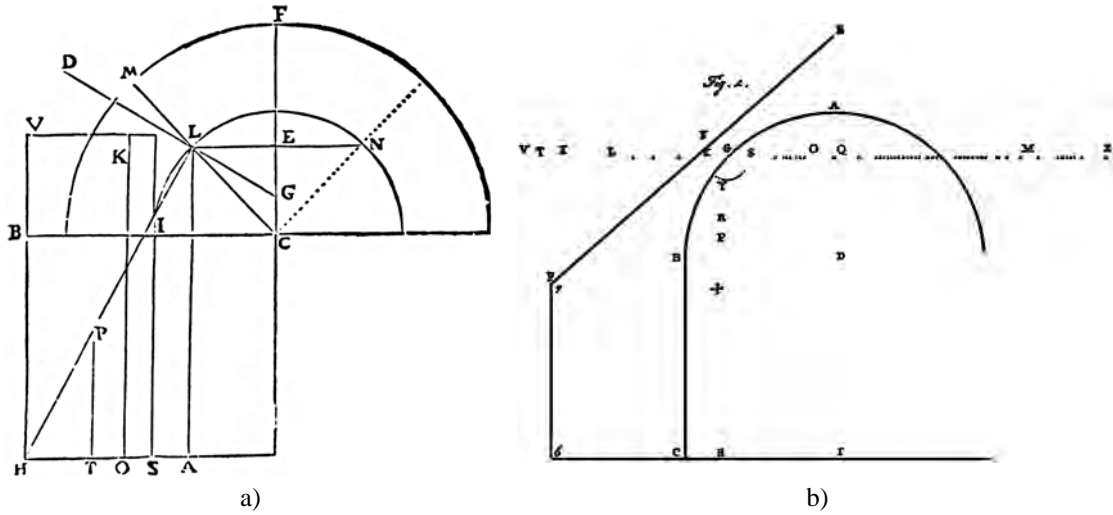


Figure 2-8. Graphical construction for the abutment width of an arch according to a) de La Hire [1712] and b) Valadier [1832]

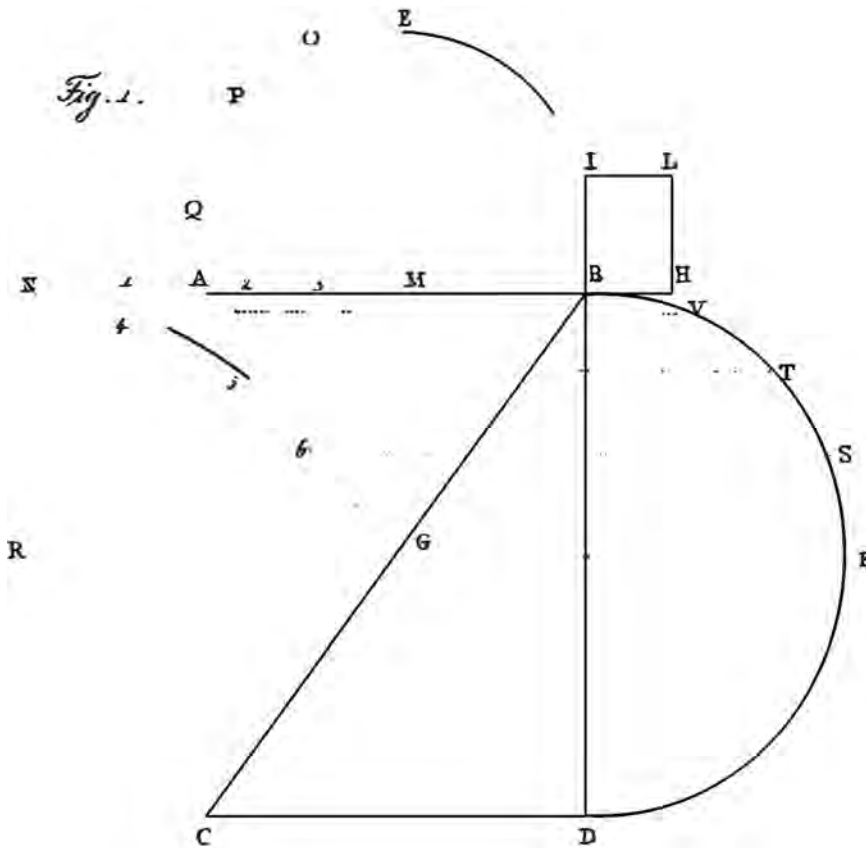


Figure 2-9. Valadier's geometrical construction (Chart 256) for calculating the abutment's dimensions for a cross vault

Finally, differently from the objective of the previous rules referring to churches, the first rules for porticos are also reported. The only available reference has been found in Palladio [1570] who, according to the weight they were supposed to bear, provided ranges of dimensions for the piers width in both public and private buildings (Figure 2-10). Considering the weight as an additional parameter made the design process nonlinear, in line with the German Late Gothic builders and Friar Lorenzo de San Nicolás who proposed slight adjustments according to the material type. However, no considerations on the piers height, i.e. slenderness, are given.



Figure 2-10. Palladio's rule of thumb: a) abutment width over span and b) plan and section of Palace of the Loggia, Brescia, Italy (Rondelet, 1802 after Huerta, 2004)

2.3.2 Main elements dimensions

In order to create a more synthetic and comparative view, the rules discussed before are now collected in graphs and tables, giving insight on the possible range of sizes of the main elements related to cross vaults of churches. Due to its importance in the overall stability of the construction, particular attention is paid to the buttressing system: abutment width and pier size. Table 2-2 reports this information together with a general description and an indication whether the thickness of the *arc doubleau* and the height of the abutment (slenderness) affected the design. In this regard, since the strict approach of German Late Gothic builders and Cataneo, all the parts of the church resulted in a fixed proportion with the module.

The relations between abutment width and span are reported in Figure 2-11 where the abscissa represents the ratio between the rise of the *arc doubleau* and the span. This is the parameter that better describes the overall shape of the vault, as 0.50 represents a semi-circular arch, while smaller or larger values represent flat or pointed arches, respectively. Fr. Derand's and Hernán Ruiz's rules shows a slight decrease of the abutments width from flat to pointed arch. The former (dash-dot line) seems to be less conservative than the latter (dotted line) with values approximately equal to 0.25 and 0.30 respectively. However, it must be stressed that the Hernán Ruiz's rule refers to the base of the abutment and, through a possible tapering towards the vault springing, it can meet the Fr. Derand's rule.

References	Description		Abutment height	Arc doubleau thickness
Fr. Derand's rule (before 1546)	Graphical method	See Fig. 6	✗	✗
Hernán Ruiz el Joven (1560)	Graphical method	See Fig. 7	✗	✓
German Late Gothic	Direct proportion (chorus w_a^c and nave w_a^n)	$w_a^c > \frac{s}{3.33}$ $w_a^n > \frac{s}{4.14}$	Fixed	Fixed
Cataneo (three nave church) (1567)	Real dimensions	$w_a = \frac{s}{3}$	Fixed	✗
Rodrigo Gil de Hontañón (1550)	Analytical formulation	$d_p = \frac{1}{2} \sqrt{h_p + w_b + s}$ $w_a = \frac{2}{3} \sqrt{h_a + \frac{2}{3} \sum r_i}$	✓	✗
De La Hire (1712) Belidor (1729)	Graphical method	Wedge theory (see Figure 2-8a)	✓	✓
Valadier (1832)	Graphical method	See Figure 2-8b and Figure 2-9	✓	✓

Table 2-2. Overall description of rules applicable to cross vaults. In particular, w_a is the abutment width, d_p is the pier diameter and s is the span of the vault (for Rodrigo Gil's see Table 2-1)

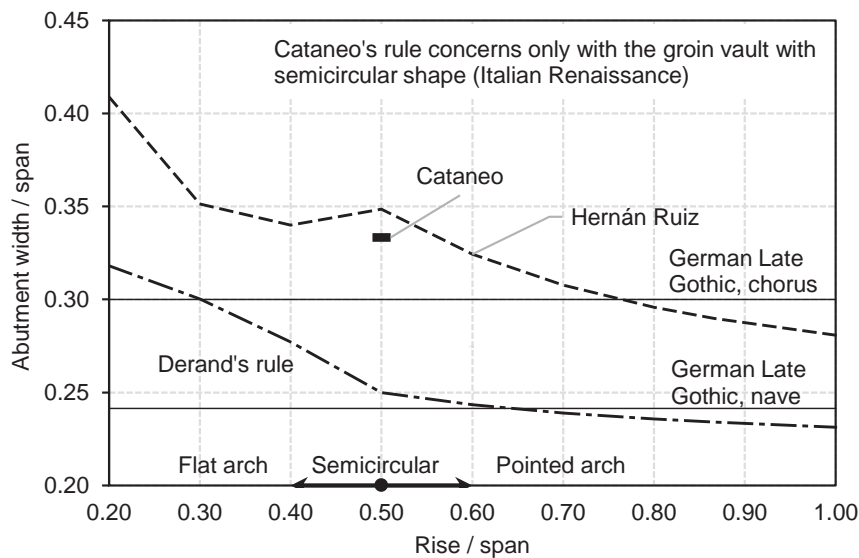


Figure 2-11. Comparison between traditional rules of thumb

The German Late Gothic rules (solid lines) provide values at the base of the elements and they are in good agreement with the previous ones. In particular, the chorus and nave abutment widths are a sort of average of the values provided by Hernán Ruiz and Derand's rule. Also the Italian Renaissance Cataneo's rule refers to a particular type of cross vault, i.e. groin vault (rise/span

ratio = 0.5). The rule provides an abutment width equal to one-third of the span, in line with Hernán Ruiz's despite their clearly different origin.

Figure 2-12 shows the relations between the abutment width and the pier diameter versus the span of the vault for Rodrigo Gil's formulation. Since the length of the ribs converging on the abutment are requested (from the springing to their respective keystone), they have been calculated on the base of the same rib scheme of the vaults in the Cathedral of Salamanca [Palacios, 2006]. Considering all the ribs with the same curvature, that is, the radius equal to half of the diagonal, and starting from the same proportions of the Cathedral (the nave bay has a span of 13m and a width of almost 10 m, thus $w_b = 0.77 s$, whereas h_p is almost two times the span), the bay width and pier height have been moderately changed.

As it is possible to see, the diameter of the pier is a little more than one half of the abutment width. Comparing the latter with the Fr. Derand's rule (leading approximately to a value equal to $s/4$), Rodrigo Gil's considerably diverges, providing similar results only for a span range between 9 and 11 m, being more conservative for smaller values of the span. Additionally, more noticeable than the previous rules, it is shown that the structural elements become slender as the span increases. Huerta [2006] attributed this trend to the stabilizing effect of the increasing weight with larger dimensions but it is also possible that the rules were used only in a limited range of spans. Finally, Table 2-3 reports the range of the dimensions provided by the rules of thumb for the other elements composing the cross vault. Even though not exhaustive, it is a general overview of the presented values whose validation is certainly desirable, both in terms of geometrical survey and

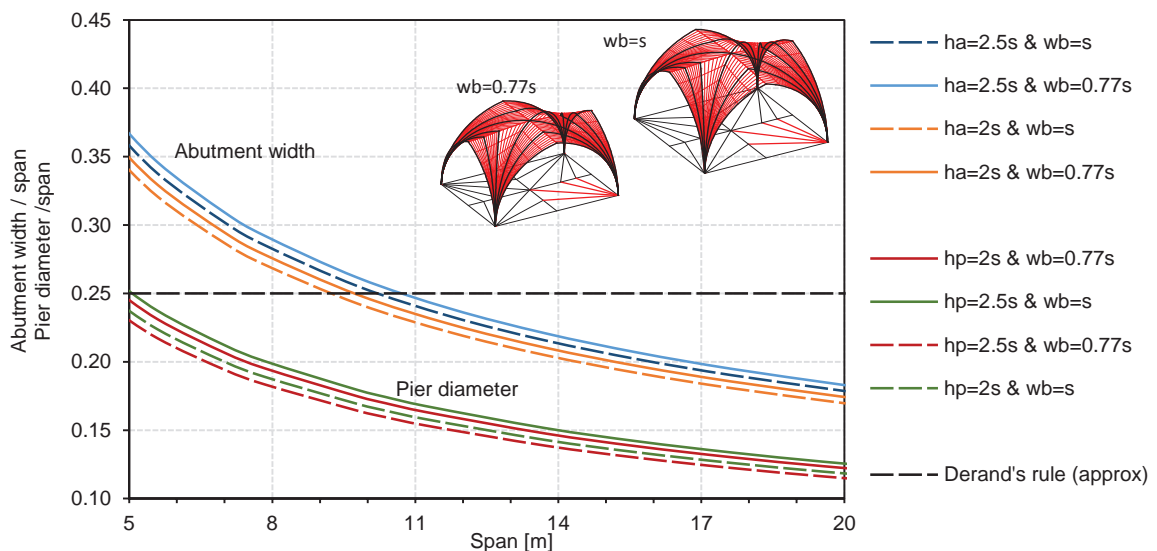


Figure 2-12. Rodrigo Gil's rules of thumb: abutment width and inner pier diameter (w_b , h_p , s are, respectively, the bay width, the pier height and the span of the vault)

Elements	References	Dimensions
<i>Arc doubleau</i>	German Late Gothic Rodrigo Gil de Hontañón (1550) Hernán Ruiz el Joven (1560)	$s_n/22.5$ (central nave) $s_n/30$ (aisle) $s/20$ Min $s/10$
Diagonal rib (Central nave)	German Late Gothic Rodrigo Gil de Hontañón (1550)	Height: $s_n/30$ Thickness: $s_n/60$ Height: $s/24$
<i>Arc tierceron</i>	Rodrigo Gil de Hontañón (1550)	Height: $s/28$
<i>Arc formeret</i>	Rodrigo Gil de Hontañón (1550)	Height: $s/30$
Web thickness	Como (2013)	$s/50 \div s/75$ (Gothic vaults)
Infill	Friar Lorenzo de San Nicolás (1639-64) Hernán Ruiz el Joven (1560)	Up to one third of the vault height (rounded cross vault) Up to half of the height of <i>arc doubleau</i>
Wall thickness (Chorus)	German Late Gothic	$s_c/10$
Wall and pier thickness (Central nave)	German Late Gothic Cataneo (1567) (three nave church)	$s_c/10$ or $0.125 \div 0.141 s_c$ Pier: $1/4$ clear nave span Wall: $\approx 1/6$ clear nave span
Wall thickness (Aisle)	German Late Gothic Cataneo (1567) (three nave church)	$s_c/10$ or $0.133 s_c$ $\approx 2/9$ clear aisle span

Table 2-3. Rules of thumb for the main elements of the church related to the cross vault: s_n and s_c are the span of the central nave and of chorus respectively, whereas s is the span of the element considered

structural performance. The complexity of the validation increases with the singularity of historical construction, where the economic possibilities of the cities, and technical skills and expertise of the local masons, could have played a decisive role in the design process [Tomasoni, 2008]. However, the survival of the rules over the centuries is an implicit and intuitive validation [Benvenuto, 1991] that can be confirmed by a statistical survey, which at the moment is missing.

2.4 From historical methods to limit analysis

During the 18th century, the study of masonry vaulted structures led modern mechanics to make great progress, providing outcomes still at the basis of current structural approaches in the framework of limit analysis. Moving from the arch-catenary analogy stated by Robert Hooke's Latin anagram in 1675, then independently extended by Gregory as a stability condition (static theorem), around 1730 Couplet described the assumptions that form the basis of limit analysis [Heyman, 1972; Benvenuto, 1991; Kurrer, 2008]. High coefficient of friction (to prevent against sliding failure), infinite compressive strength and null tensile strength still represent the usual hypotheses for analytical and simplified tools for the assessment of masonry structures.

In a scenario in which the masonry arch was the protagonist of the scientific debate, with the capital contribution of Coulomb in 1776 [Heyman, 1972], the only scholar who focused on masonry cross vaults was Mascheroni [1785]. Starting from Bouguer's lesson about the domes of

finite thickness, he criticized the *slicing technique* performed until then, and pioneered by [Frézier, 1737], which allowed to disassemble a compound vault in its elementary arches, i.e. a reduction from a three-dimensional problem into a well-known in-plane one. This was the case of the famous Poleni's report on Rome's St. Peter's Basilica in 1748. Although this approach is the easiest way to study compound vaults, it inevitably neglects the interaction between two adjacent slices, e.g. the compressive circumferential stresses of the dome [Benvenuto, 1991].

Mascheroni [1785] dedicated one chapter of his treatise to the study of compound arches and vaults. In spite of his idea about the three-dimensional behaviour of vaults, he approached the study of cross vaults by the usual slicing technique, which includes independent web strips whose resultant action is applied to the diagonal arch. However, regarding the diagonal arches and the webs as the main elements (Figure 2-13), he proposed a dual problem: given the shape of one arch, calculate the balanced profile of the other arch. He also provided hints in case the generatrix of the webs, i.e. line ML and MT in Figure 2-13, were not horizontal but inclined or curved. With this aim, he extensively used the concept of catenary, easily visualized through the cross vault analysis of Beranek [1988] in the form of inverted hanging cables (Figure 2-14) and later at the basis of the 3d catenary net proposed by Andreu et al. [2007].

After the contributions of Mascheroni and Coulomb, the interest on rigid and infinitely resistant *voussoirs* theory slowly waned, giving way to new theories, namely beams with curvilinear axis, membranes and shells, gathered all together in the framework of the elastic theory. As a consequence, for masonry arches the goal shifted from stability assessment (or limit analysis) to the solution of the linear elasticity problem, which is a statically indeterminate problem. Whereas the former was partially achieved by the ancient scholars thanks to the intuitive idea of *cracking* the structure to obtain a collapse mechanism (i.e., the kinematic theorem of limit analysis), the latter revealed itself as unsuitable for masonry structures analysis [Kurrer, 2008].

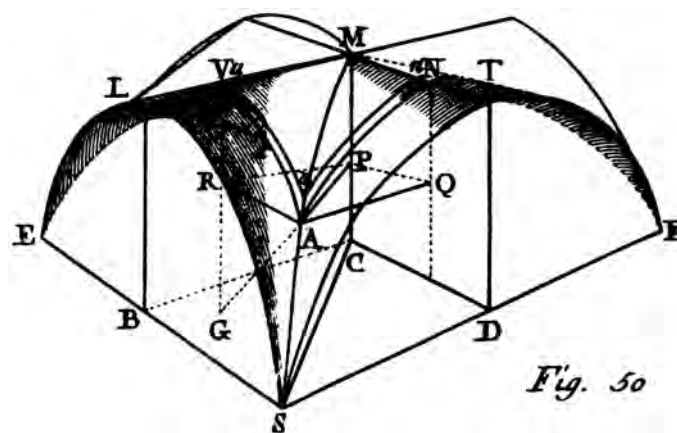


Figure 2-13. Mascheroni's analysis of cross vault (Chart XII)

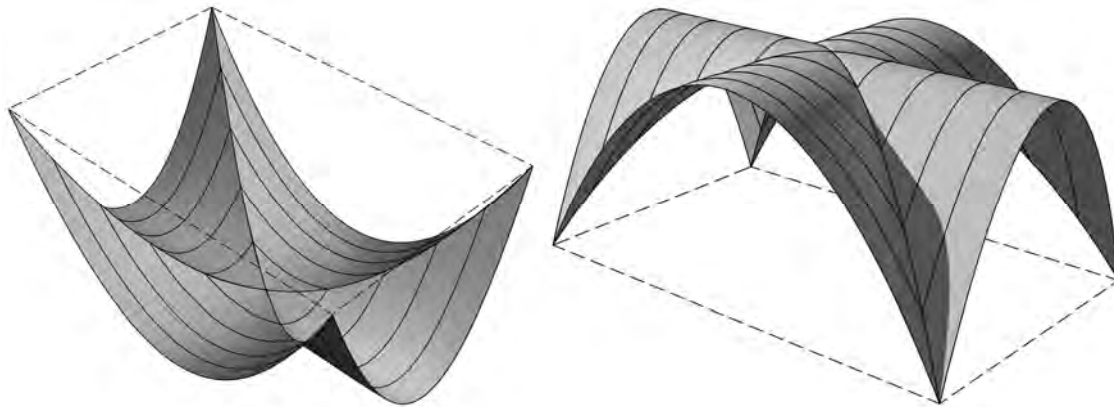


Figure 2-14. Cross vault analysis through inverted catenaries after [Beranek, 1988]

The elastic theory began in the 1820s with the Navier's *Leçons*, introducing stress analysis, comparing the resulting stress values with the material strength. Although in his work Navier considered the arch and the cross vault, there is no evidence whether he used the elastic theory to analyse either of them. According to Huerta [2010], the first elastic analysis of an *encastré* (or fully clamped, built-in) arch was anonymously published by Young in 1817, being the work revealed only in 2005. Unfortunately, another Young's work regarding the first complete theory on the *thrust line*, i.e. the line connecting the resultant forces in each cross section, remained unnoticed. It is only in 1831 when F.J. Gerstner established the theory: as the problem is statically indeterminate, he intuitively realised that the capacity increases with the number of indeterminacies [Kurrer, 2008].

Conversely, other scholars were interested in finding the "true" thrust line, sometimes adding *principles* to the equilibrium equations. Moseley, for example, formulated in 1843 the *principle of minimal resistance*, assuming that the true solution is the one with the minimal capacity [Kurrer, 2008]. Culmann [1864], instead, adopted the *principle of minimum loading*, i.e. the true thrust line is the one with the smallest deviation from the centre line, which is one of the assumptions adopted by D'Ayala and Casapulla [2001] in their analysis of hemispherical domes with finite friction.

Culmann [1864] gave also insight into graphical statics. After the pioneering *Mathematicorum Hypomnemata de Statica* by S. Stevinus in 1608 [Lourenço, 2002], at the end of the 19th century this approach gained new vigour paving the way for vaulted structures analysis (Figure 2-15). Just to mention a few, Wittmann [1879] was the first to study compound vaults, then Planat [1887] and Mohrmann with the third edition of the Gothic construction manual of Ungewitter [1890]. Some years later Körner [1901] and Wolfe [1921] used the same approach, which basically consists in the slicing technique, the only feasible for hand calculation. Recently, thanks to auto-

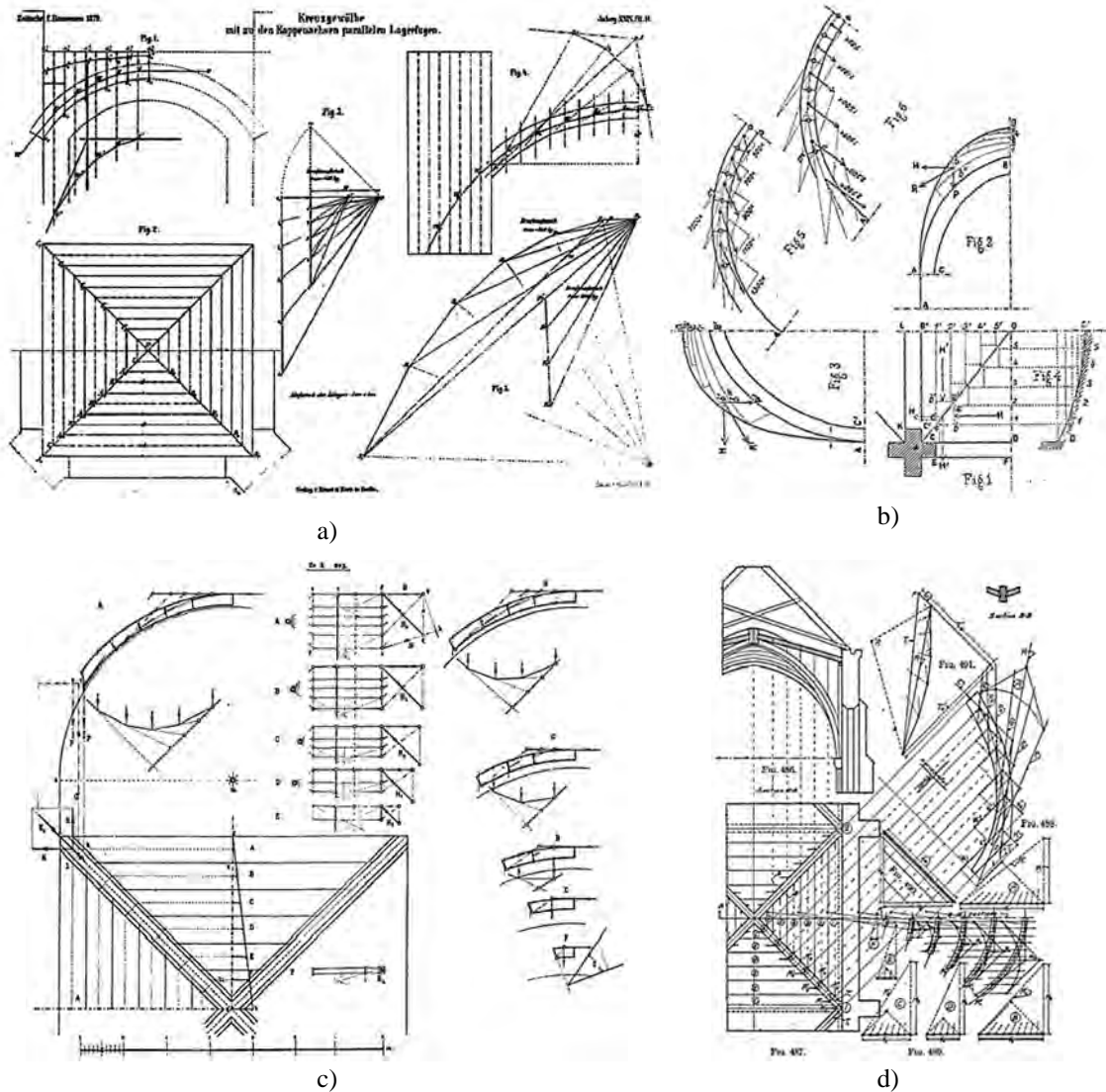


Figure 2-15. Graphical statics applied to cross vaults according to a) Wittmann [1879], b) Planat [1887], c) Körner [1901] and d) Wolfe [1921]

matic procedures, the concept has been extended to catch the three-dimensional behaviour of vaults [O’Dwyer, 1999; D’Ayala and Casapulla, 2001; Andreu et al., 2007; Block, 2009].

Ungewitter-Mohrmann [1890] presented also an easy method to obtain a good estimate of the thrust resultant and its position with respect to the springings of a cross vault. Figure 2-16 reports an example and a table for a quick calculation. The method was based on the vault thickness, the rise/span ratio and the crack observation at the crown and springings [Heyman, 1995]. Moreover, in case of slicing technique on double-curvature portions of vaults, Ungewitter-Mohrmann suggested to divide the webs in elementary arches following the idea of a ball rolling down the extrados. The same idea was followed by Sabouret [1928] and Abraham [1934] but, since only the latter provided explicative drawings (Figure 2-17), the entire credit was given to Abraham [Huerta, 2009].

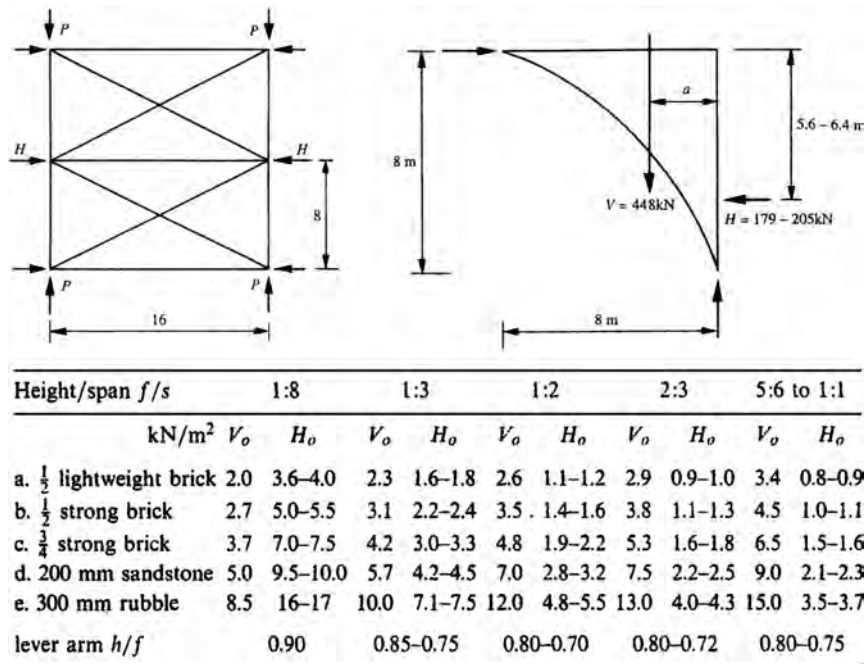


Figure 2-16. Example according to the approximated method by Ungewitter- Mohrmann for a cross vault, in case of a 200 mm thick sandstone vault and a ratio $f/s = 1:2$ [Heyman, 1995], where f is the height and s is the span

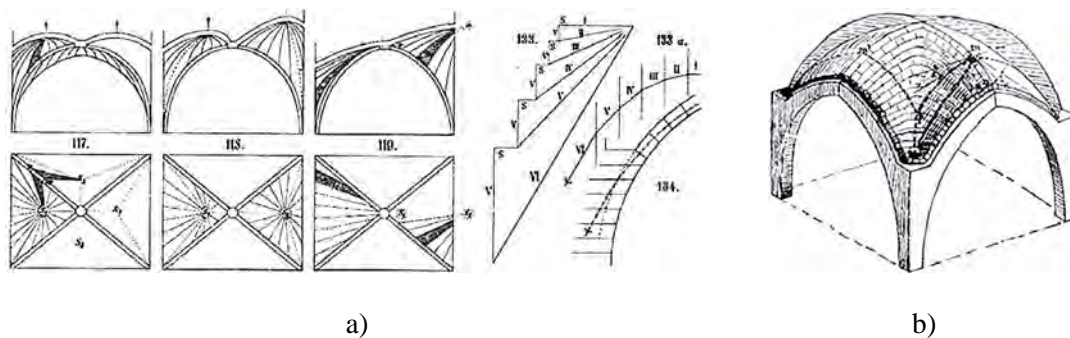


Figure 2-17. Slicing technique: a) patterns of slicing [Ungewitter and Mohrmann, 1890] and b) “ball principle”[Abraham, 1934]

In spite of these last developments in graphical methods and thrust line analysis, with the popularity of wrought-iron structures, starting from 1860s the supremacy of elastic theory was inevitable. Although clearly misleading in case of masonry structures, as stressed by Castigliano’s statement “*masonry arches as an imperfectly elastic systems*” in 1879 and the Bavarian Railways engineer Haase in 1885 [Kurrer, 2008], it is only at half of the 20th century that elastic theory definitely lost ground to plastic theory. Thanks to the studies of Drucker, Kooharian and Prager (between 1949 and 1953), later rearranged in the well-known work by Heyman [1966], ultimate load analysis re-emerged together with Couplet’s assumptions providing the ground for the three fundamental theorems of plasticity, namely uniqueness, lower bound (or static/safe) and upper bound (or kinematic).

The safe theorem of plasticity scientifically proves what was stated by Hooke and extended by Gregory almost three hundred years before. This theorem also confirms the applicability of the graphical method with the slicing technique: a masonry arch/vault is stable if at least one of the infinite admissible equilibrated thrust lines/surfaces falls entirely into the thickness of the element. Still, it is not easy to discuss the safety of the structure despite the attempts to introduce the so-called *geometrical safety factor* [Heyman, 1982].

Moreover, without entering into the merits of the debate which involved several scholars [Willis, 1835; Viollet-le-Duc, 1854; Sabouret, 1928; Abraham, 1934; Heyman, 1968; Mark, 1982; Huerta, 2009; Tarrío, 2010], the in-service structural role of cross vault ribs can be addressed in the framework of the safe theorem. The hypothesis of ribs as the main structural elements (slicing technique and graphical method) is the simplest of the infinite possible solutions and, although a stress concentration is expected in the junction between two shells surfaces, the ribs are not strictly necessary for the global equilibrium [Heyman, 1977].

Regardless of this idea, which adopted a bi-dimensional response of the vault, it is only in the last two decades that researchers have proposed alternative computational methods to meet this goal, also thanks to more appropriate constitutive laws, failure criteria and plastic flow laws [D'Ayala and Casapulla, 2001; Andreu et al., 2007; Block, 2009; Milani et al., 2014].

2.5 Modern structural analysis methods

The structural analysis of vaulted masonry structures represents a challenging issue basically due to the material nonlinearities (e.g. no tensile strength). In this regard, in the last two decades, many authors have developed suitable approaches, from simplified methodologies for practitioners up to refined and sophisticated numerical models. For an overview of the most updated existing strategies, the reader is referred to [Roca et al., 2010; Smoljanović et al., 2013; Tralli et al., 2014].

In the present section, instead, the main applications to masonry cross vaults present in literature are briefly reviewed. Eventually, all the structural methods are collected in form of table. In particular, along with the reference publications, the type of requested input (in terms of equilibrium, kinematic compatibility and constitutive law equations) as well as the strain and stress output are reported per each of them. The ability of evaluating the failure mechanism and the ultimate strength, taking into account the three-dimensional behaviour, are also stressed. Whether the method has been previously used for seismic capacity evaluation and further comments complete the discussion. The table includes also the historical methods described in the previous section.

2.5.1 Application to masonry cross vaults

According to limit analysis approach, following the contribution of O'Dwyer [1999], Block and co-worker [2009; 2014] developed a software in the framework of Thrust Network Methods. This represents a fully three-dimensional analysis that, thanks to a computational methodology based on Maxwell reciprocal force diagrams, can calculate a range of safe funicular solutions (compression-only surfaces) within whatever geometry of the structure representable as a graph of function (*a la Monge*) and vertical force distributions (thus no seismic action). Figure 2-18 shows three possible layouts of the force distribution for a groin vault and the solution (minimum/maximum thrust network) for a case study.

Another funicular three-dimensional network approach was presented by Andreu et al. [2007]. Inspired on Gaudi's hanging models, masonry structures are modelled as 3D catenary nets¹. This method, as well as the previous one, is based on the static approach of the limit analysis, i.e. safe theorem, together with convenient optimization techniques. The authors implemented the method on a bay of a Gothic church, namely Girona Cathedral in Spain, with a nave span of 22.88 m, the widest among all Gothic cathedrals.

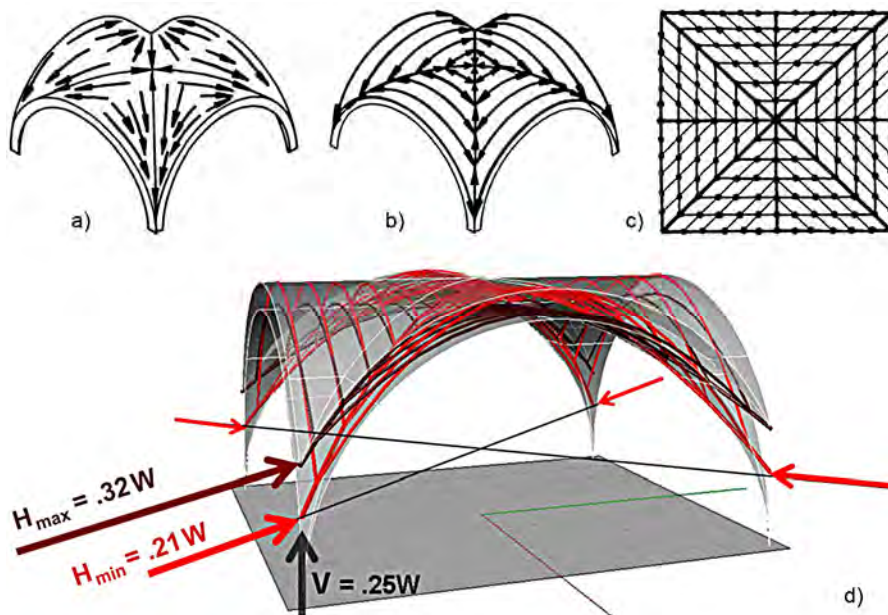


Figure 2-18. Different force distributions for a groin vault according to O'Dwyer [1999]: a) forces towards the corners, b) parallel lateral arches, c) finer pattern. d) Cross vault analysis by Block [2009]

¹ Regarding catenary networks, Kilian and Ochsendorf [2005] proposed a three-dimensional form-finding tool for the design and the analysis of compression-only structures. The applet developed (CADenary tool v.2) allows the user to experiment in real time a virtual hanging chain model.

<http://designexplorer.net/newsscreens/cadenarytool/cadenarytool.html>

Another strategy for the analysis of the stress distribution and the crack pattern in vaulted structures is presented by Fraternali [2010]. The methodology provides a statically admissible, purely compressive thrust network and it is valid in case of vaults surface representable as graph of function (*a la Monge*) and only vertical loads (thus no seismic action). The problem is reduced to the satisfaction of the vertical equilibrium seeking iteratively the thrust surface and a statical admissible stress function, that is, stress resultant internal to the vault thickness. Although the equilibrium conditions and global framework is entirely equivalent to Thrust Network Methods, in contrast, this approach, based on discretized Airy stress functions, does not consider singularities in the boundary conditions and loading, or discontinuities, such as cracks or openings, in the discretized equilibrium surfaces.

The author analysed a cross vault with square base 7.5 m long, parabolic web webs 200 mm thick, diagonal ribs 400 mm thick, and maximum rise equal to 3.2 m (Figure 2-19a). The vault has self-weight of 20 kN/m^3 , and bears a material with weight of 6 kN/m^3 filling the space in between the extrados and the horizontal plane through the vertex. Figure 2-19b shows the initial guess thrust surface and stress function whereas the Figure 2-19c the final mesh and the force network. In particular it is possible to observe that the cracks may run parallel to the wall ribs at the extrados (Sabouret cracks), along the ribs, and near the crown at the intrados, in good agreement with the cracking damage frequently observed.

Moreover, regarding the stress function, moving from the same hypotheses, a continuum approach was proposed by Baratta and Corbi [2010], where the search of the solution is set up by an energy approach. The authors provided the solution for two cases of the barrel vaults, namely with indefinite length and with constraints at its extremities. A similar approach was presented also by Angelillo et al. [2013], providing several applications to vaulted structures. In particular, the cross vaults in Palazzo Gravina in Naples were analysed. It is important to stress the fact that in both cases it is not possible to deal with the seismic action since the methodologies accommodate only vertical loads.

Following the dual approach of limit analysis, that is, the kinematic (upper bound) theorem, Milani et al. [2008] proposed a rigid-infinitely resistant six-noded triangular curved element. The plastic dissipation is thus concentrated only along the edges of adjoining elements where, according to the thick plate theory (Reissner-Mindlin), it may occur for in-plane actions, bending moment, torsion and out-of-plane shear. Considering the problem in the framework of the linear programming, the upper bound of the collapse load can be evaluated thanks to its dual formulation. This leads to the imposition of the stress state admissibility according to the actual strength domain which follows from a suitable upper bound FE homogenization procedure on a

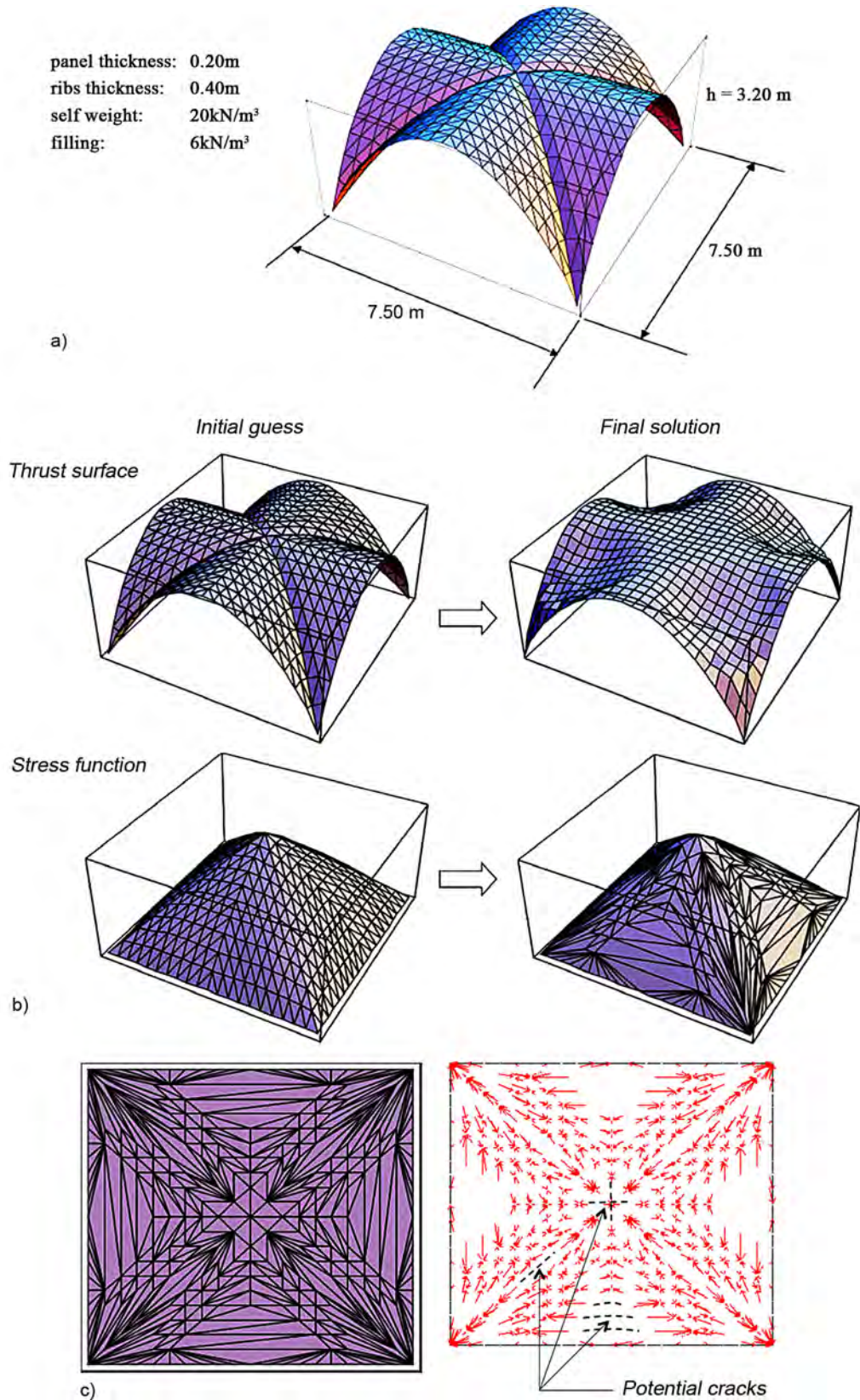


Figure 2-19. Cross vault analysis from [Fraternali, 2010]: a) geometry and loading data of the unreinforced cross vault; b) thrust surface and stress function (only vertical loading); c) final meshing (left) and force network (right)

Representative Element of Volume (REV, see ahead). Figure 2-20 shows the results of this approach on the rib cross vault tested by Faccio et al. [1999].

The same research group extended the model substituting the triangular curved element with a rigid infinitely resistant six-noded wedge [Milani et al., 2009a, 2009b]. The main difference relies essentially in the evaluation of the internal dissipation at the interfaces where the flexural behaviour is now derived from integration of membrane actions along the thickness. The proposed model was assessed again through the rib cross vault tested by Faccio et al. [1999] with appreciable results.

It must be stressed that all the methods presented above have been developed in the framework of standard limit analysis, which is based on a rigid-perfectly plastic material with associated flow law, i.e. the dilatancy angle is assumed equal to the friction angle, whereas experimental evidences indicate that dilatancy angle tends to zero². This assumption is thus not correct unless the failure mechanisms are mainly due to joints tensile cracking or the volume generated by sliding is not relevant for the response. In the other cases, in order to avoid severe underestima-

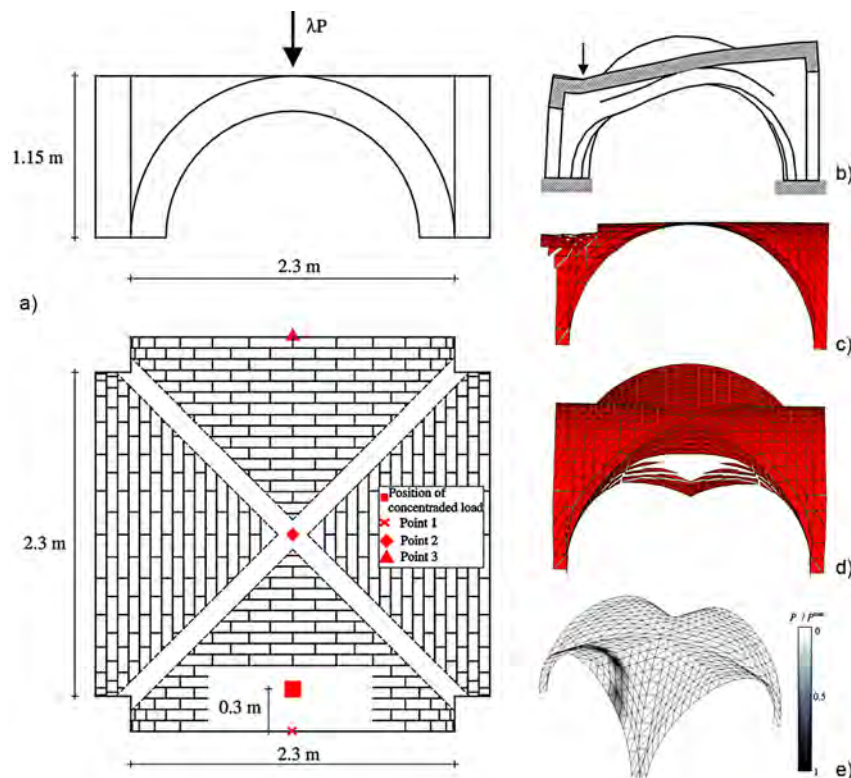


Figure 2-20. Rib cross vault: a) geometry and loading condition and b) relative failure mechanism [Creazza et al., 2002]; c) failure mechanism, section view, d) front view and e) normalized power dissipated patch [Milani et al., 2008]

²The tangent of the dilatancy angle is the ratio between normal and tangent displacements in the joint.

tions of the collapse load and incorrect failure mechanisms, the analysis should be performed with non-associative plastic flow rule, i.e. non-standard limit analysis. In this case the limit theorems are not strictly valid, the uniqueness of the ultimate load may be lost and a multiplicity of solutions may exist [Milani et al., 2008]. In this regard, in case of masonry vaulted structures, the only applications address the in-plane analysis of masonry arches: Orduña and Lourenço [2005a, 2005b] suggested a load-path following procedure whereas Gilbert et al. [2006] adopted a non-associative frictional joint model.

On the other hand, nowadays FEM represents the most used and adaptable method regarding the structural analysis of any kind of building. Complex constitutive laws capable of describing the relation between stress and strain in every point of the structure and in every step of the load history allows a complete monitoring of the structure. For further details about the structural analysis of masonry constructions, the reader is referred to [Lourenço, 1996, 1998; Calderini, 2004; Roca et al., 2010; Smoljanović et al., 2013].

Regarding the application of FEM to masonry cross vaults, according to the macro-modelling approach, Creazza et al. [2002] analysed the response of the rib cross vault under monotonic loading tested by Faccio et al. [1999] by means of two-parameters, scalar, isotropic, damage model (Figure 2-21). The model of the vault is vertically constrained, while along the horizontal directions springs are introduced in order to simulate the bound given by the framework (with a posteriori chosen stiffness). The mechanical properties of the cross vault materials, instead, are calibrated on a different experimental test [Creazza et al., 2000]. The model predicted well the peak load and the failure mode, but not the maximum displacement that resulted smaller than the experimental one.

Conversely, according to Roca et al. [2010], numerous studies are currently dedicated to the homogenization technique in order to derive the global behaviour of masonry from the behaviour of the constitutive materials [Lourenço et al., 2007]. The basic idea is to consider masonry elements as a structure themselves composed by a periodic sub-structure called *representative element of volume* (REV) [Milani and Tralli, 2012]. Accordingly, it is possible to isolate and study only this sub-element and obtain the average orthotropic equivalent mechanical properties. As pointed out by Milani and Tralli [2012], this procedure cannot be strictly applied if nonlinear material properties with softening are assumed. Moving to the cross vaults, considering the simple intersection of two barrel vaults, the zero curvature allows to identify a REV. However, the possible double curvature surfaces of the webs (see §2.2) may complicate the task since the REV cannot be strictly recognized, unless in a more general heuristic but still technically suitable approach [Milani and Tralli, 2012].

By way of the homogenization procedure, Milani and Tralli [2012] proposed a two-step model. In the first one, the simplified micro-modelling procedure was applied on the REV composed of a central brick interconnected with its six neighbours. Each brick was meshed by six noded wedge elements, assumed rigid-infinitely resistant, with nonlinear elasto-plastic and softening zero thickness interfaces. The three kinds of interfaces, brick-brick (since each brick is split in few wedge elements), head and bed joints, exhibited a frictional behaviour with limited tensile and compressive strength. The data collected in this step were then used in the following one where a macro-level analysis was performed in the framework of FE nonlinear analysis. The authors consider the case of the rib cross vault experimentally tested by Faccio et al. [1999], comparing the results also with alternative methods, among which Creazza et al. [2002] (Figure 2-21).

Another family of structural analysis methods is represented by the macro-element. These allow to model a structure by way of large blocks which identify entire portions of the structure, with a significant reduction in terms of number of degrees of freedom and computational effort. This leads also to a simplification for the constitutive laws and more understandable results. Regarding vaulted structures, Cannizzaro [2011] proposed a nonlinear macro-element for curved geometry masonry construction. Since the model is based on four- or three-node plane elements, its accuracy is strongly influenced by the mesh discretization.

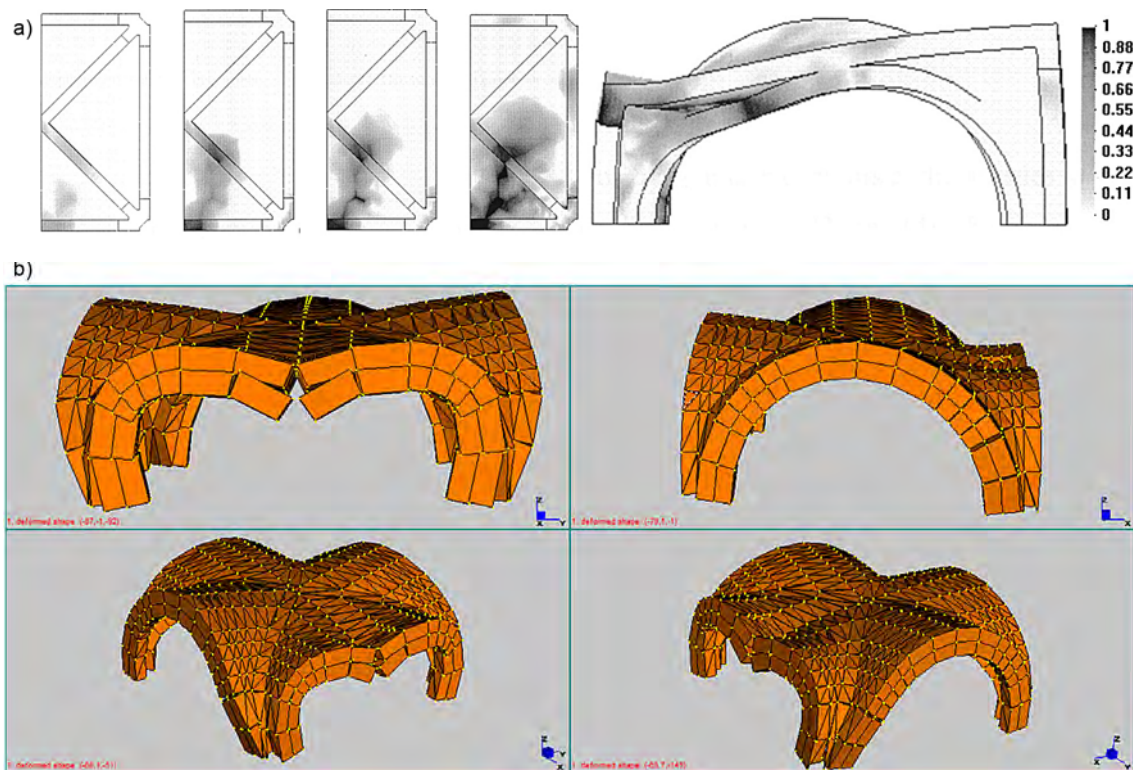


Figure 2-21. Rib cross vault tested by Faccio et al. [1999]: a) damage contours at intrados of cross vault for incremental displacements and at collapse for the deformed configuration [Creazza et al., 2002]; b) deformed shapes at peak [Milani and Tralli, 2012]

The elements are considered with rigid sides provided of a diagonal spring for taking into account the in plane deformation (Figure 2-22a). The interaction with adjoin elements, instead, is regulated by nonlinear links placed orthogonally (a sort of nonlinear fibres model) or in the plane of the interfaces (Figure 2-22b). The aim of this arrangement is to decouple the failure mechanisms, namely in plane, flexural, torsional and sliding, both in and out of plane. The amount of links is arbitrary and whereas on one hand it increments the computational effort, on the other hand it does not affect the number of degrees of freedom. As far as cross vaults are concerned, the experimental test performed by Faccio et al. [1999] was analysed where the link stiffness was calibrated through homogenized mechanical properties. Like the approach by Creazza et al. [2002], the proposed model (Figure 2-22c) well matched the ultimate load but showed displacement larger than the experiment results.

Finally, regarding the Discrete Element Method (DEM), it refers to a family of numerical methods that accounts for discontinuous systems of interacting, independent and deformable (or not) bodies. This method takes into consideration finite displacements and rotations of the bodies, including their complete separation and detecting automatically new contacts. These features make DEM able to simulate the progressive failure associated with crack propagation and significant deformation (relative motion between blocks). Although this method was born for modelling fractured rocks, historical masonry structures under seismic actions represent a natural application of this approach. However, to the author's knowledge, only Van Mele et al. [2012] adopted a DEM code (3DEC) for the analysis of a cross vault, and the reader is referred to §2.6.1 further details.

In order to propose a critical and synthetic review, Table 2-4 collects the structural analysis methods available in literature used in the analysis of masonry vaulted structures (included the ones discussed in the previous subsection). The comparison focuses on the input relations and the results (stress, strain, failure mechanism and strength). The ability of evaluating the three-dimensional behaviour of the structure is also stressed. Finally, whether the method has been previously used for seismic capacity assessments and further comments complete the discussion.

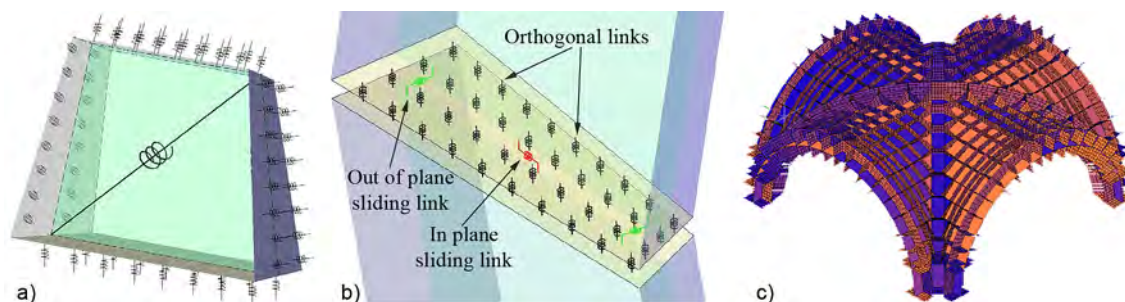


Figure 2-22. Macro-element method [Cannizzaro, 2011]: a) four noded element with diagonal spring and interfaces links; b) interface element; c) model of a cross vault

Category	Name	References	Main subject	Type of analysis	Requested equations	Strain and stress output	Failure mechanism	Ultimate strength	3D behaviour	Horizontal loads	Further comments
Historical methods	From catenary to limit analysis	From [Hooke, 1675] to [Couplet, 1729, 1730]	Arches and barrel vaults	Lower bound approach	Only equilibrium	*	*	*	*	*	In-plane analysis Thrust line within the middle third of the section [Méry, 1840]
	Slicing technique & Graphical statistics	From [Frézier, 1737] to [Abraham, 1934]	Compound vaults	Lower bound approach	Only equilibrium	*	*	*	*	*	Reduction from three-dimensional into in-plane analysis
	Standard formulation	From [Koocharian, 1953] to [Heyman, 1966]	Any kind of masonry structure	Lower or upper bound approach	Equilibrium or Compatibility	*	✓ Dual problems (limit analysis theorems)	✓	-	-	3D behaviour and horizontal loads handled only with FEM
Limit analysis	Thrust network methods	Thrust network Block and co-workers [2007; 2009; 2014]	Structures as graph of function	Lower bound approach	Only equilibrium	*	*	✓	3D compression -only net	*	Minimum and maximum thrust state solutions (within the thickness) Only gravitational loads Output: geometric safety factor Incremental load strategy until geometry safety factor equal to 1.
		Funicular network [Andreu et al., 2007]	Structures as graph of function	Lower bound approach	Only equilibrium	*	*	*	3D compression -only net	*	Iterative procedure with minimum eccentricity constrain Output: geometric safety factor
	In conjunction with FEM	Finite friction D'Ayala and co-workers [2001; 2011]	Any kind of vault	Lower bound approach	Equilibrium and Coulomb's law of friction	*	*	*	3D compression -only surface	*	Iterative procedure with minimum eccentricity and tangential stress admissibility constrain Output: geometric safety factor
		[Milani et al., 2008, 2009a, 2009b]	Any kind of masonry structure	Upper bound approach	Compatibility and yield function	*	✓	✓	✓	*	Rigid-infinitely resistant elements allowing plastic dissipation at the interfaces Homogenization technique
Non-standard limit analysis	-	-	Any kind of masonry structure	-	Equilibrium Compatibility Yield function Flow rule	*	✓	✓	✓	*	Non-associative plastic flow law Limit theorems not strictly valid Among the others: [Orduña and Lourenço, 2005a, 2005b] and [Gilbert et al., 2006]

SEISMIC PERFORMANCE OF MASONRY CROSS VAULTS

Category	Name	References	Main subject	Type of analysis	Requested equations	Strain and stress output	Failure mechanism	Ultimate strength	3D behaviour	Horizontal loads	Further comments
Membrane theory	Pure membrane theory	[Tomasoni, 2008; Como, 2013]	Thin vaults	Elastic analysis	Only equilibrium	✓	✗	✗	✓	✗	Closed form solution (the equilibrium is locally statically determined) No out-of-plane stresses Tensile stress within the structure
	Stress function	[Fraternali, 2010]	Structures as graph of function	Airy stress function	Only equilibrium	Only membrane stresses	✗	✗	3D compression-only surface	✗	Constrains: no tension and membrane forces within the thickness
FEM	Incremental nonlinear analysis	-	Any kind of structure	Any kind of analysis	Equilibrium Compatibility Constitutive	✓ In every point in every step of the load history	✓	✓	✓	✓ (Any kind of analysis)	From micro to macro-modelling Partly irreversible deformations Stiffness variability with respect of the load history Post-peak resistance degradation Stiffness and strength progressive degradation after cyclic loads
Macro-element	Macro-element	[Cannizzaro, 2011; Calì et al., 2012]	Any kind of masonry structure	Any kind except for cyclic analyses	Equilibrium Compatibility Constitutive	Stresses and strain at the interface	✓	✓	✓	✓ (No time history analysis)	Rigid side element In-plane element deformation Nonlinear springs to decouple the failure mechanisms (flexural, torsional and sliding, both in- and out-of-plane)
DEM	Universal Distinct Element Code (UDEEC)										Discontinuous systems of interacting, independent and deformable (or not) elements Finite displacements and rotations of the elements
	Non-Smooth Contact Dynamics (NSCD) Discontinuous Deformation Analysis (DDA)		Any kind of structure	Only nonlinear analyses	Equilibrium Compatibility Constitutive	✓ In every point in every step of the load history	✓	✓	✓	✓ (No simplified static and modal analysis)	Complete separation of the elements (crack propagation), detecting automatically new contacts Possible internal finite element mesh that may split and separate

Table 2-4. Comparison of the available structural analysis methods for vaulted masonry structures

2.6 Damages understating and experimental tests

The comprehension of the damage causes is of fundamental importance in understanding the force distribution and the structural behaviour of historical constructions. In this regard, the present section deals with the experimental tests and the damage observation of cross vaults considering dead loads, settlements and seismic action. For a more general discussion about gravitational loads, the reader is referred to [Mastrodicasa, 1943; Giovanetti (ed. by), 2000], whereas to [Doglioni et al., 1994; Regione Toscana, 2003; Dipartimento della Protezione Civile, 2013] in case seismic load is concerned. In addition, after Piccirilli [1989], de Vent [2011] recently proposed a supporting tool for structural damage diagnosis in masonry constructions. The forms provide several sections with possible damage patterns (#15 and #16 are dedicated to cross vaults), failure hypotheses, additional symptoms, context conditions as well as relevant references.

2.6.1 Gravitational loads and settlements

Mastrodicasa [1943] was probably the first who wrote a scientific contribution for damage understanding in masonry constructions. Although he recognized the complexity of masonry as a random material, he considered a limit theoretical model according to which masonry is assumed as absolutely brittle, homogeneous, isotropic and linearly elastic until the sudden failure occurs without exhibiting any plastic deformation.

Regarding vault damages, e.g. crushing or cracking, the author identified the possible causes in, among the others, excessive loading, chemical attack, age, inadequate bricks firing, frost and lime mortar. From the structural point of view, the abutments are affected by the vault's thrust, axial compression and flexural bending combination, as well as foundation settlement. Their possible failure can be attributed, instead, to the inadequacy of the cross-section due to material heterogeneity or building defects. In case of good quality masonry, the thrust can produce rigid movements of the buttressing elements and the vault is inevitably dragged down. However, thanks to the crack opening (due to the rather small tensile strength), the entire structure is able to find a new equilibrium state. Viollet le Duc improperly labelled this feature as "elasticity" [Di Pasquale, 1996], meaning the masonry capacity of varying the bearing system when severely damaged. Conversely, in case the buttressing system does not behave as rigid block, vault thrust can lead to local damages, as depicted in Figure 2-23 (a wall loaded by an inclined point load).

On the other hand, Figure 2-24 shows the two collapse mechanisms for cross vaults indicated in the Recovery manual for the historical centre of Città di Castello [Giovanetti (ed. by), 2000].

The first mechanism, in good agreement with Mastrodicasa [1943], regards the outward movement of the abutment with the consequent detachment of one of the webs and hinges formation at the springings and at the crown. The second mechanism is mostly a shear failure due to the differential movements of the two opposite sides of the bay, identified by the typical diagonal crack occurrence.

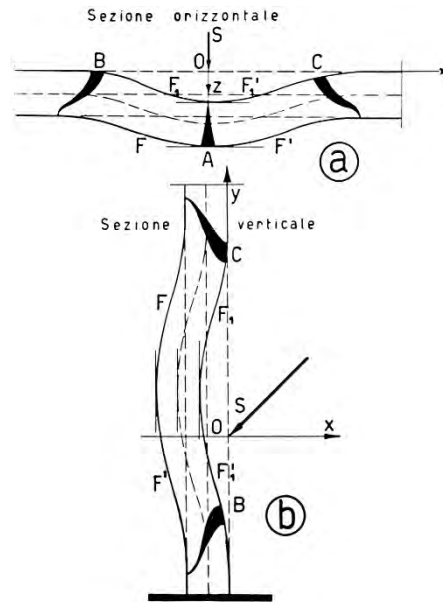


Figure 2-23. Crack pattern in a wall in case of an inclined point load: a) horizontal and b) vertical cross section [Mastrodicasa, 1943]

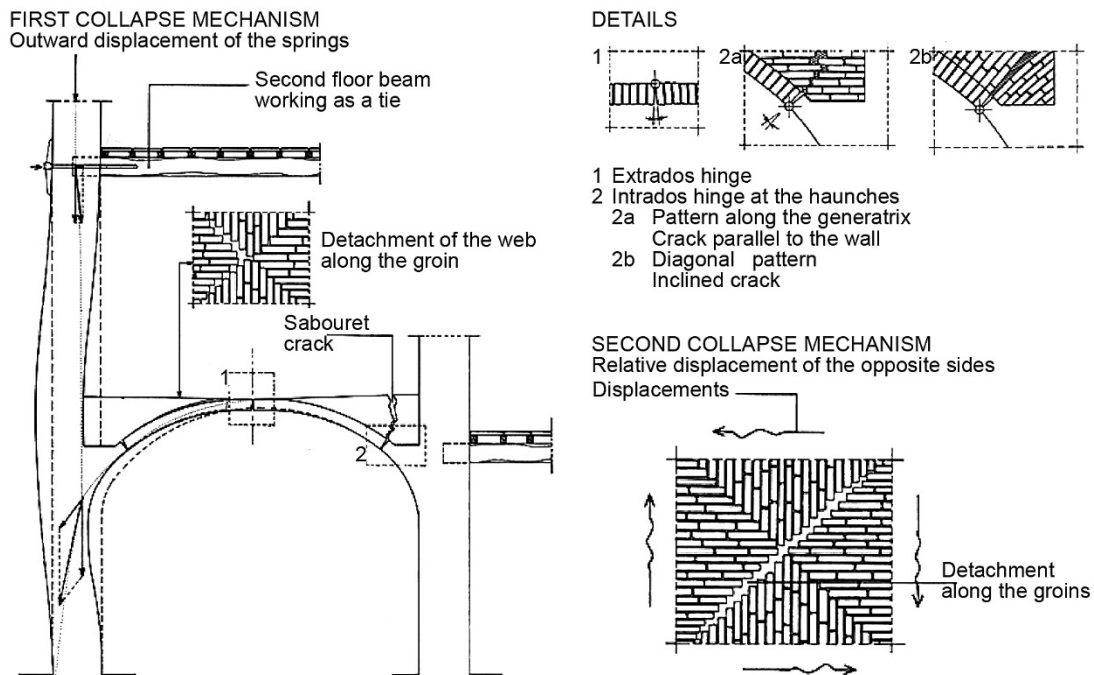


Figure 2-24. Collapse mechanisms for a cross vault according to Giovannetti [2000]

The effect of the thrust is clearly visible in the two photos of the Cathedral in Tui (Spain) reported in Figure 2-25. The first image shows the central nave where, in order to avoid excessive displacement due to the thrust of the vaults on the lateral naves, shallow arches have been placed (in fashion of flying buttresses). On the other hand, the overturning movement of the central columns have activated the mechanism in the the cross vaults of the aisle, with consequent formation of a plastic cylindrical hinge close to the crown (Figure 2-25b). With the aim of containing this mechanism, arch shaped struts have been built.

The outward movement of the supports is also responsible of the well-known *Sabouret cracks* (Figure 2-26), which are the cracks running parallel to the side walls [Heyman, 1983]. Accordingly, Barthel [1993] extended this approach to the most common type of cross vaults (Figure 2-26c) whereas Holzer [2011] proposed a graphical explanation starting from the analysis of barrel vaults with lunettes. Considering the collapse mechanism of a simple barrel vault on spreading supports (with the formation of three cylindrical hinges), the lunettes can behave as follows: depending on masonry bond, they may or not move together with the main vault. Considering the groin vault as a generalization of the vault with lunettes, the same approach can be followed but in this case the Sabouret cracks represent the most frequent mechanism (Figure 2-27).

Moreover, Como [2013] analysed a semi-circular shaped cross vault on a square plan undergoing uniform diagonal widening. The possible crack pattern at the intrados and extrados is reported in Figure 2-28.



Figure 2-25. Cathedral in Tui (Spain): a) nave and b) lateral aisle

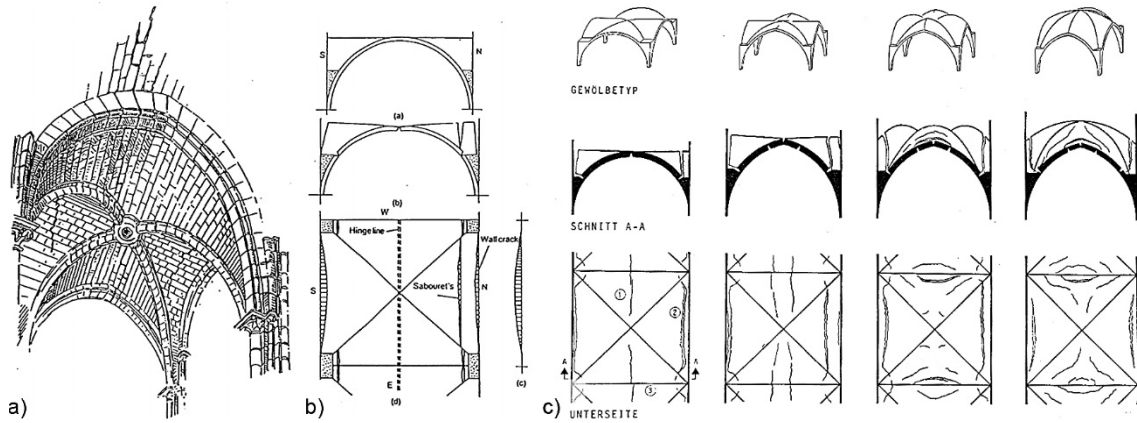


Figure 2-26. Sabouret cracks according to a) Abraham [1934] and b) Heyman [1983]. c) Typical crack pattern for different types of cross vaults according to Barthel [1993]

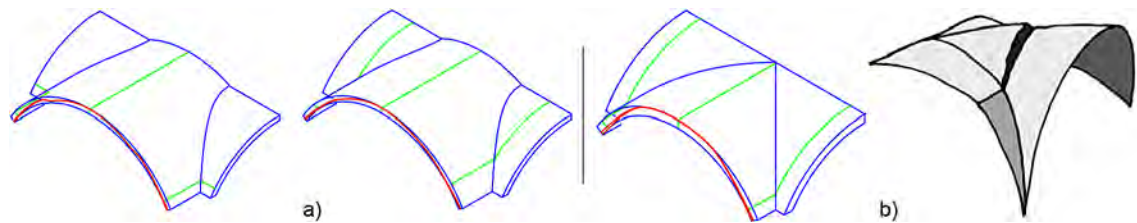


Figure 2-27. Possible collapse mechanisms according to Holzer [2011]: a) barrel vaults with lunettes and b) most frequent failure mechanism for cross vault

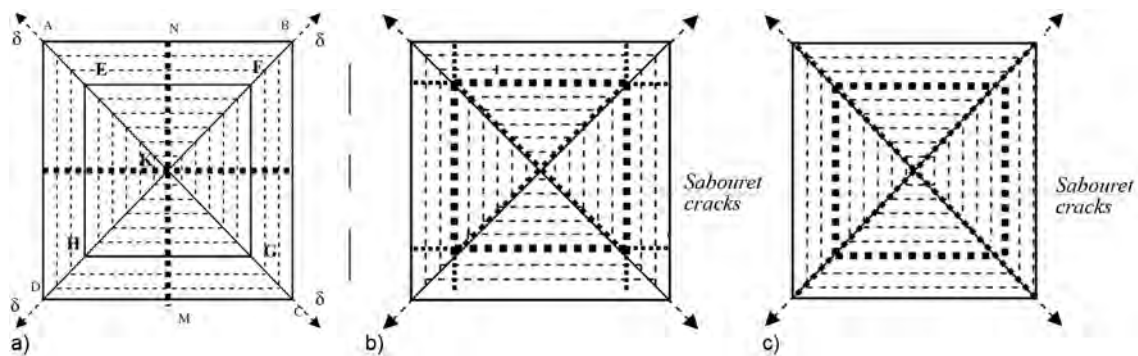


Figure 2-28. Crack pattern for diagonal displacement of the abutments: a) intrados; b) and c) possible damage on the extrados [Como, 2013]

Moving to the laboratory activities, one of the first experiments on cross vaults was performed by Mark et al. [1973] applying the photo-elastic technique to experimentally determine the stresses in two bays of the 13th century choir vaults of Cologne Cathedral. A few years later the first author performed the in-plane analysis of Mallorca Cathedral cross-section in comparison with the FEM elastic analysis [Mark, 1982].

More recently, beside [Giuffrè and Marconi, 1988; Ortolani, 1988], Ceradini [1996] studied the effect of imposed deformations in a full-scale brickwork cross vault 7.36 m span without ribs. The fracture pattern occurred with a 180 mm (1/40 of span) outward movement of all the supports.

Moreover, Faccio et al. [1999] performed a test on rib cross vault under monotonic point load. In Figure 2-29 the dimensions, the experimental setup and the position of the central displacement transducer are reported.

On the other hand, Theodossopoulos et al. [2002] took into account a wooden 1:4 scale model, representing an aisle vault of the partially collapsed Abbey Church of Holyrood in Edinburgh undergoing dead loads and horizontal displacement of the abutments (Figure 2-30a). The results of FE analysis confirmed the experimental crack pattern (Figure 2-30b) underlining the capital importance of abutments stability for the structural capacity of cross vaults. Furthermore, Foraboschi et al [2004] considered an isolated brickwork cross rib vault on four pillars under an incremental load applied to the centre of a web (Figure 2-30c). In this case, failure was dictated by the insufficient buttressing action of the webs adjacent to the loaded web.

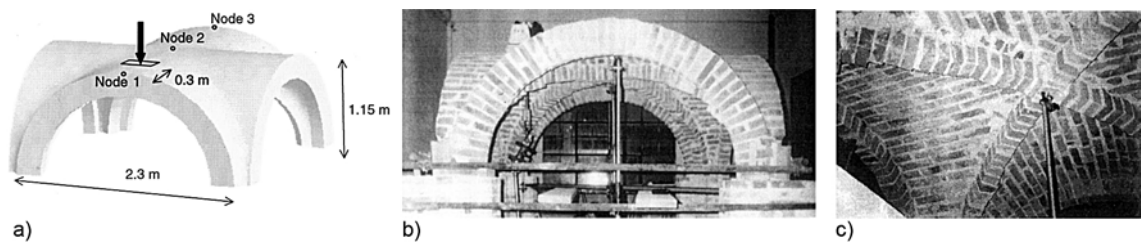


Figure 2-29. Experimental test by Faccio et al. [1999]: a) geometry, load condition and referenced points, b) experimental setup, c) central displacement transducer at the intersection of the ribs

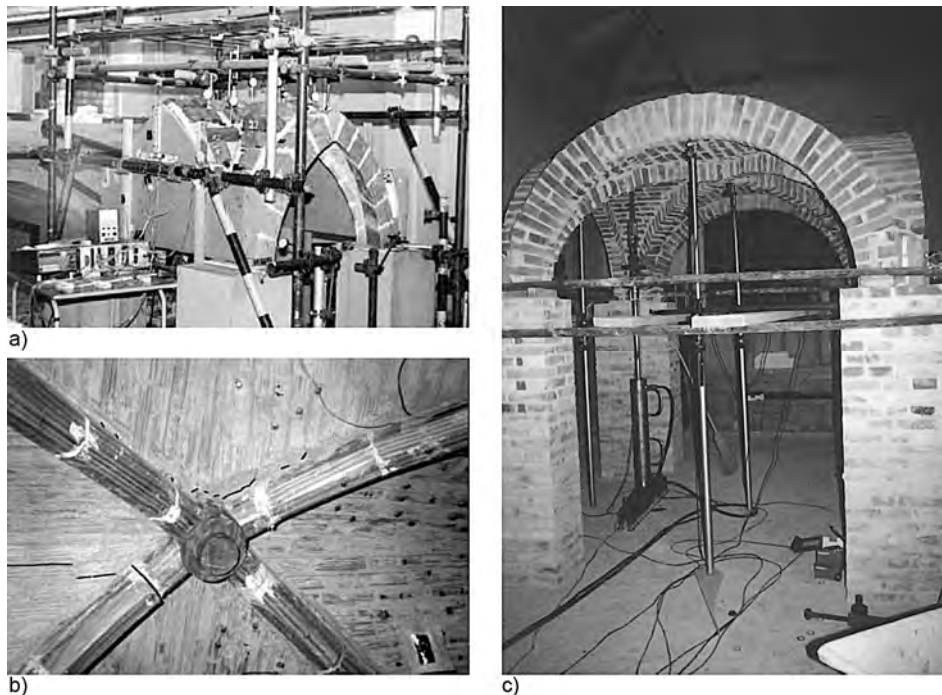


Figure 2-30. Cross vault tests: a) loading arrangement and b) crack formation at the intrados around the keystone [Theodossopoulos et al., 2002]; c) test setup [Foraboschi, 2004]

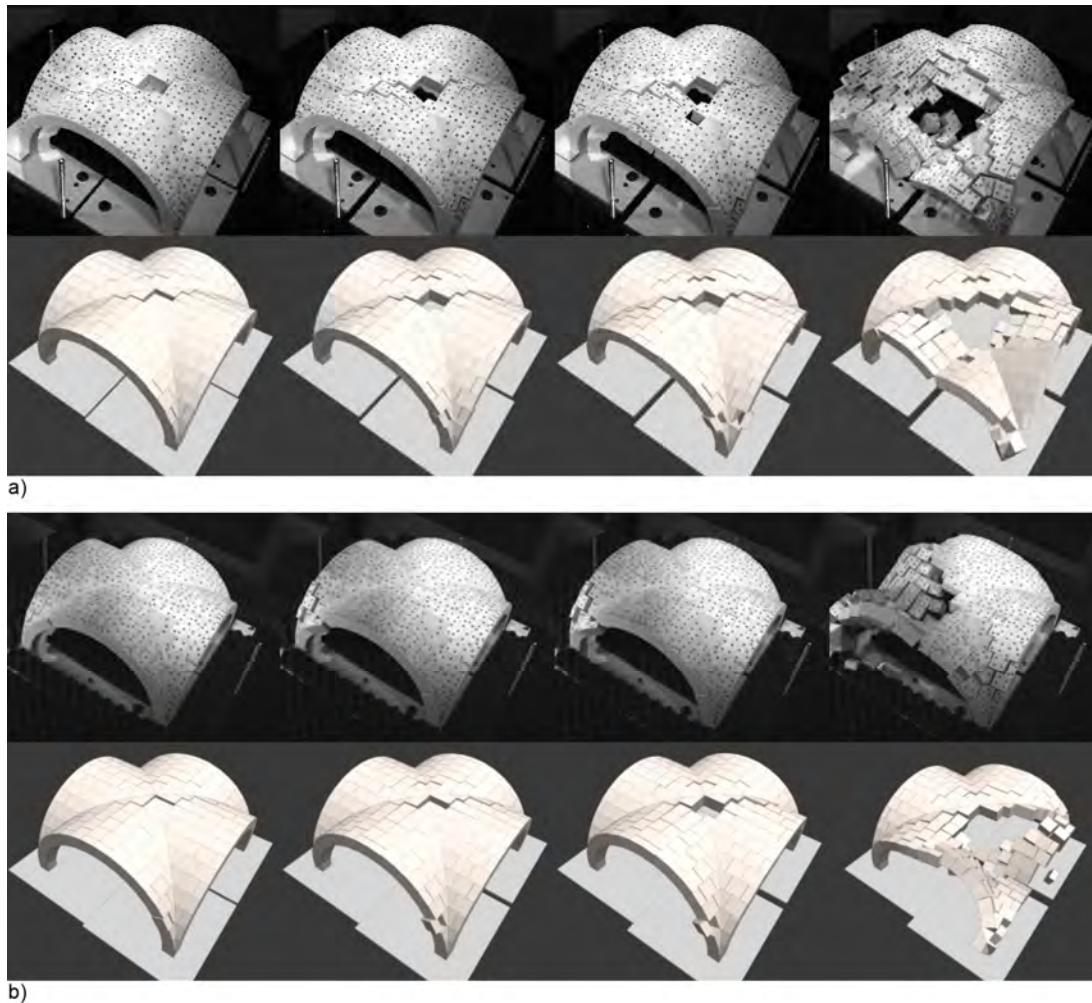


Figure 2-31. Collapse mechanisms caused by a) diagonal and b) transverse displacement of the support

Finally, Van Mele et al. [2012] studied the collapse of a 3D-printed groin vault scale model under large support displacement. Thanks to an optical measuring system, the authors compared the results with DEM analysis (3DEC). The vault had a span of 150 mm and a thickness of about 24.4 mm. Only one support was subjected to three different displacements, namely transverse, diagonal and vertical (all applied quasi-statically). Repeating the experiments three times per each direction, the results showed that the possible imperfection of the manually assembled configuration inevitably affected the displacement capacity and the overall failure mode. Conversely to the diagonal displacement (Figure 2-31a), in fact, a great discrepancy is evident comparing the experiment with transverse displacement and DEM output (Figure 2-31b), probably due to premature sliding and twisting movements at the joints of the physical model.

2.6.2 Seismic load

As exposed in the previous sections, the historical masonry constructions have been basically built to withstand only gravitational loads, showing a high vulnerability against the seismic action.

However, since the typical uncertainties of the masonry construction (namely boundary conditions, material properties, infill, load history, construction process, presence of previous damages, state of maintenance, etc.), in the last decades the scientific community has adopted a different approach based on the observation of the performance of similar structures. Starting from Friuli earthquake in 1976 (Figure 2-32), thanks to a systematic collection and understanding of the damages occurred in churches or historical centres, researchers have identified independent and considerably autonomous sub-structures called *macro-elements*³.

Since they are independent from age, technology, dimensions and overall shape of the building, the relative mechanism is considered fundamental [Dipartimento della Protezione Civile, 2013] allowing to predict the seismic behaviour simply by analogy [Regione Toscana, 2003]. This approach was presented for the first time by Doglioni et al. [1994] who, starting from the analysis of Friuli earthquake, identified the main macro-elements of churches, namely façade, aisles, apse, bell tower, dome, triumphal arches, etc. Logically, these mechanisms can be activated only in presence of a good quality masonry, otherwise the structure just disintegrates.

Starting with the analysis of the post-seismic damages after the Emilia earthquakes of 1987 [Doglioni et al., 1994], the research have gradually led to the last version of the damage survey form for churches of 2006 called A-DC Model, which describes 28 fundamental mechanisms [Dipartimento della Protezione Civile, 2013]. For further details on this research, the reader is re-

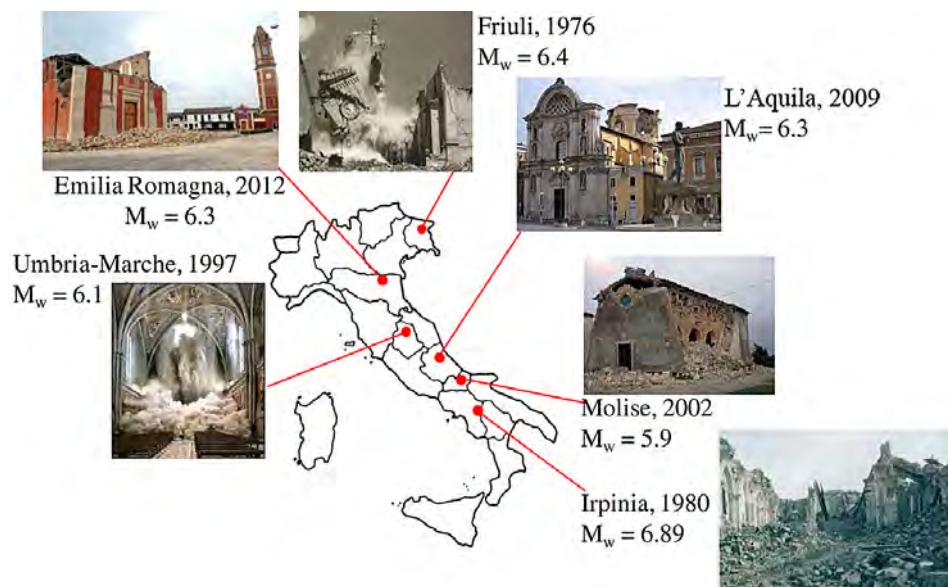


Figure 2-32. Main Italian earthquakes in the last forty years (adapted from [Brandonisio et al., 2013, p. 695])

³Although the same name, these macro-elements must not be confused with the ones described in §2.5.1.

ferred to [Giuffré, 1988; Doglioni et al., 1994; Lagomarsino, 1998; Lagomarsino et al., 2004; Sorrentino et al., 2014]. Regarding the cross vaults, the most frequent cause of failure is represented by the movements of supports, i.e. abutments or walls either in translation or overturning displacement. Sometimes, instead, the damage is localized only at the vault, above all if it is very thin or in case of concentrated loads like pillars or large infill loads [Crocì, 2000].

As reported in Figure 2-33, the mechanism labelled as M7 in the A-DC model regards the longitudinal response of the central nave colonnade due to the in-plane shear action. Its remarkable lower stiffness with respect to the external wall produces a differential translation of the two opposite sides of the vaults. This basically means shear action in the plane of the vault with the consequent presence of diagonal cracks. This mechanism is strongly influenced by the presence of heavy vaults (large thickness or stone) or previous and invasive strengthening measures as a reinforced concrete layer on top of the vault.

On the other hand, mechanisms M8, M9, M12, M18, M24 regard, respectively, the nave, lateral aisle, transept, apse (and presbytery) and chapels vaults (Figure 2-34). Also in this case, the shear action represents the main cause of the damage revealed by the severe crack pattern close to stiffer elements (triumphal arch or façade) or the detachment of the ribs. The presence of very flat or thin vaults, longer spans and concentrated loads sensibly increase the vulnerability of the vault.

Regarding the mechanism M7, Rossi et al. [2014] performed three monotonic and one cyclic tests on a 1:5 scale model of a groin vault made by 3D printed plastic blocks with dry joints (Figure 2-35). Applying an incremental horizontal differential displacement between two couples of opposite abutments, they reproduced the typical condition of a cross vault in a lateral aisle undergoing longitudinal seismic action. The damaged mechanism was characterized by the pres-

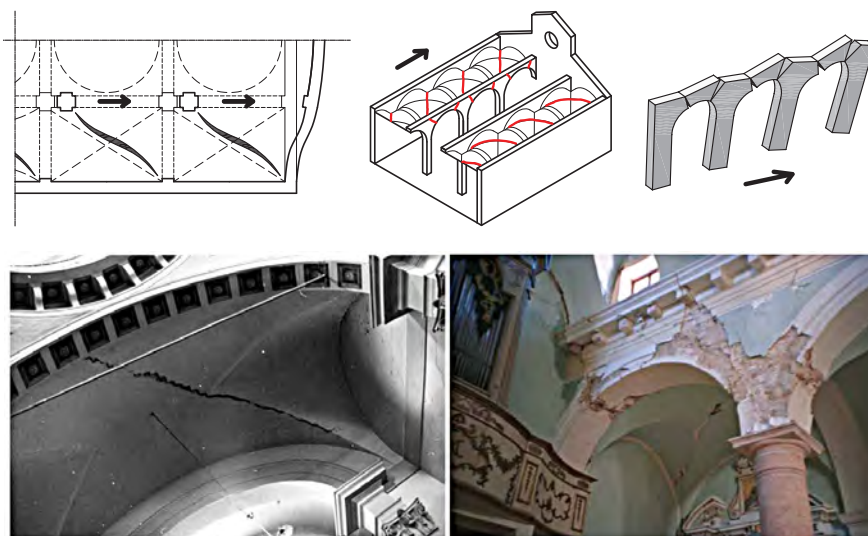


Figure 2-33. M7: longitudinal response of central nave colonnade [Regione Toscana, 2003; Dipartimento della Protezione Civile, 2013]

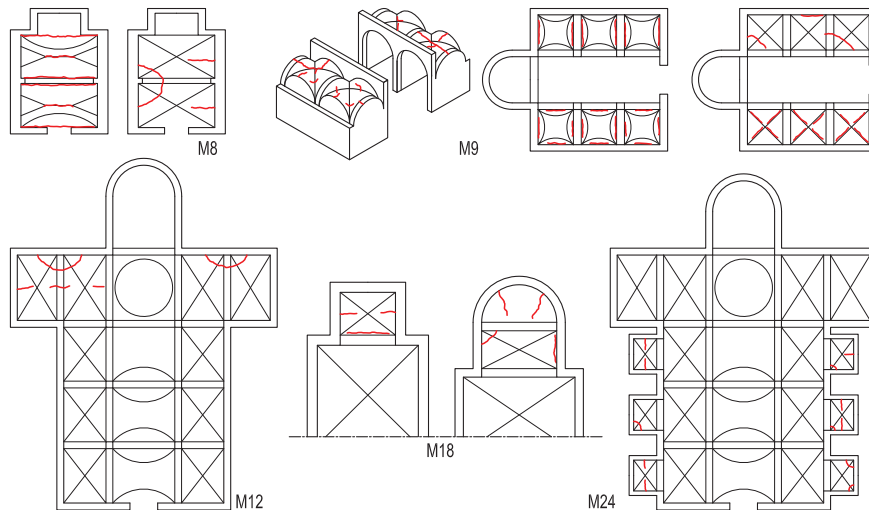


Figure 2-34. Mechanisms M8, M9, M12, M18, M24 (nave, lateral aisle, transept, apse/presbytery and chapels respectively)

ence of plastic hinges as well as the characteristic diagonal crack. However, small sliding occurrences were also observed close to the springings. On the other hand, considering the ultimate displacement capacity, the experiments provided a reference value for the ultimate drift equal approximately to 4%.

Conversely, Shapiro [2012] performed several tests on a barrel and a groin vault considering: 1) spreading supports, 2) vertical point loads applied on the extrados, 3) point loads applied to the initially deformed vault, and 4) horizontal acceleration through tilting. Although the discretization is quite coarse, the overall behaviour and the ultimate capacity of the structure are pointed out. In particular, the groin vault tested is composed by two barrel vaults 318 mm deep, 24 mm thick and an angle of embrace of 110° . Regarding the model tilting, the vault was tested according to two directions, namely parallel and rotated by 45° with respect one of the web generatrix, exhibiting a capacity of 0.67 g and 0.80 g respectively (Figure 2-36).

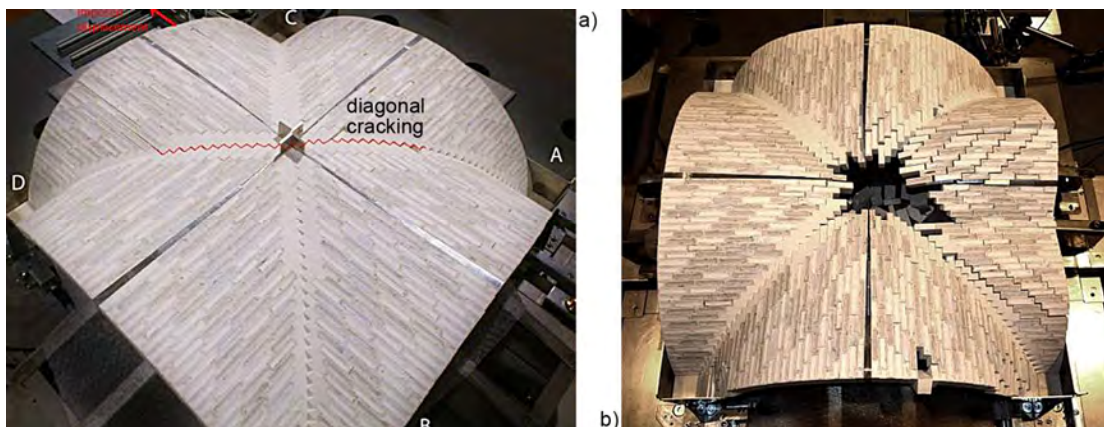


Figure 2-35. In place shear test for 1:5 scale model groin vault: a) monotonic and b) cyclic test [Rossi et al., 2014]

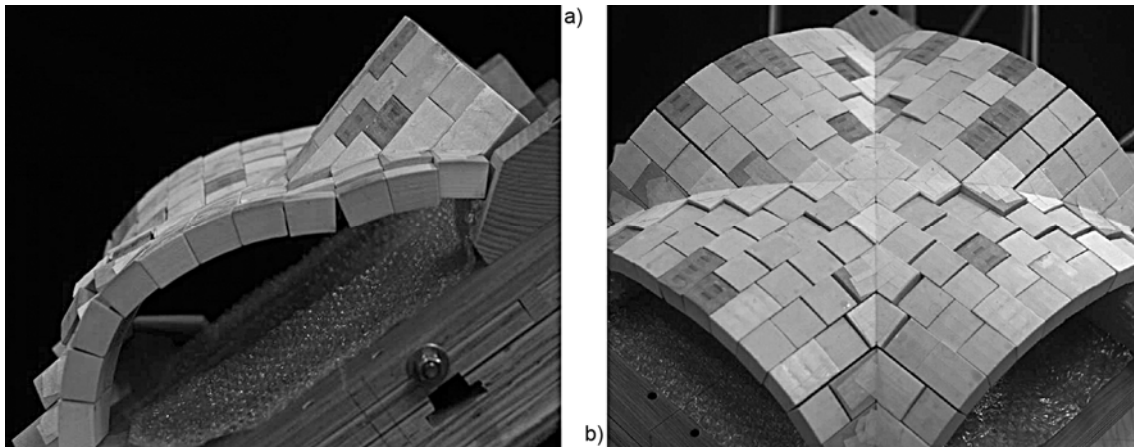


Figure 2-36. Collapse mechanism of a tilted groin vault: a) parallel and b) rotate by 45° [Shapiro, 2012]

Moving to shaking table experiments, two masonry cross vaults were tested within the European Programme NIKER (in NTUA, Athens) and PERPETUATE (in ENEA Casaccia Research Center). The first test regards a cross vault (very similar to a sail vault) of the monument of Katholikon of Dafni Monastery made of Byzantine type bricks supported by two masonry piers (Figure 2-37a-b). The dimension of the specimen in plan are $2.705 \times 2.60 \text{ m}^2$, the piers are 0.45 m thick and 2.60 m tall, whereas the total height of model is approximately equal to 2.85 m. The tests were performed using the signals recorded at Calitri during the earthquake in Irpinia (Southern Italy), considering only the first section of about 40 s. Following the first modal characterization, the model was subjected to subsequent increased scaled motions in X direction (parallel to the piers) up to the appearance of significant damage. After reaching 500% of the reference input, three biaxial tests were executed with the base acceleration increased stepwise up to 150% of original records. At the end of the test, the specimen exhibited severe damage (Figure 2-37c-d) with the cross vault detachment from the piers, cracks and sliding occurrence at the frontal arches and horizontal cracks at the piers. Moreover, a permanent deformation of 15 mm with respect to the vertical axis was registered [Mouzakis et al., 2012].

The second shaking table test concerns with the vault of the Mosque of Dey in Algiers (Figure 2-38). The full-scale masonry cross vault with asymmetric boundaries was tested with the aim of simulating the drift in its horizontal plane. In order to take into account the real boundary conditions, the wall was fully fixed whereas the columns were free to horizontally move and rotate. The studied groin vault was a perfect intersection of two brickwork barrel vaults with pointed arch, with overall dimensions of $3 \times 3 \text{ m}^2$ in plan and 2.5 m high. Figure 2-38a-c shows also the presence of a couple of wooden ties along the longitudinal direction, probably an ancient seismic strengthening technique ($80 \times 80 \text{ mm}^2$ section). The geometrical scheme reported in Figure 2-38d describes other details to better distribute the mass and to lighten the entire structure. The

signal input was the Keddara (Algeria) accelerogram (NS component) normalised and rescaled to the site of Kasbah of Algiers where the mosque is located. After a first campaign of test with tie rods, the specimen was tested without them according to four assigned nominal Peak Ground Accelerations (PGAs), namely 0.10 g, 0.15 g, 0.20 g and 0.25 g [PERPETUATE, 2012].



Figure 2-37. Cross vault tested in NTUA, Athens: a) interior view of the cross vault tested in NTUA; b-c-d) damages at the end of the test

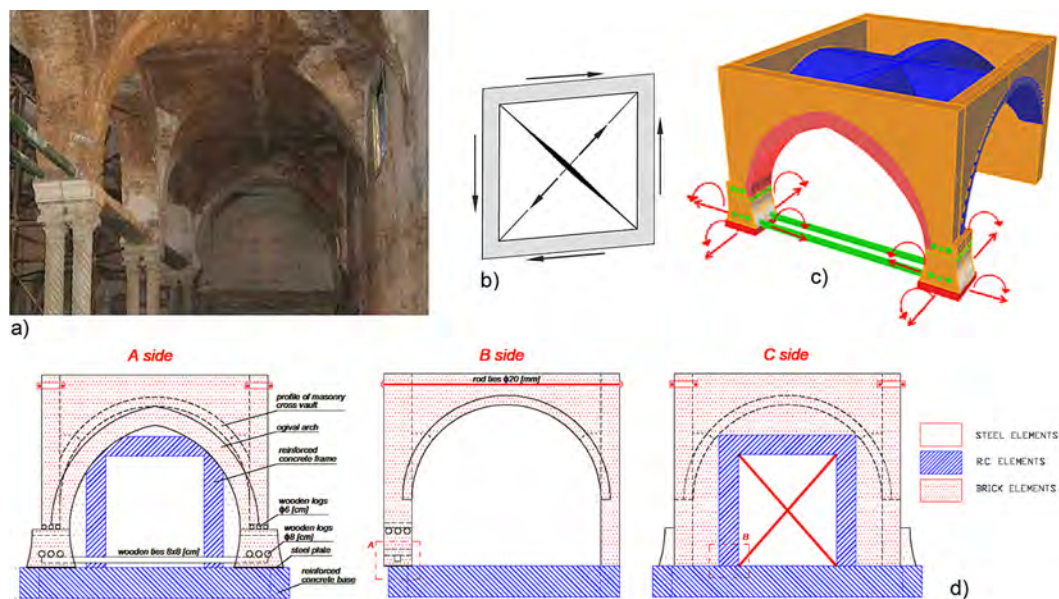


Figure 2-38. Cross vault tested in ENEA Casaccia Research Center, Rome: a) vaulted structures of the Mosque; b) damage mode of the vault; c) specimen allowed displacements; d) scheme of vault geometry

2.7 Summary

With the aim of providing grounds for further and detailed analysis, this chapter collected an exhaustive review of the available literature for masonry cross vaults. The historical developments of cross vaults reveals the uninterrupted progress of ancient builders in achieving such a high level of complexity and perfection. Without any doubt, the shape and the proper geometrical representation of the vault play a fundamental role in its overall stability [Wendland, 2007]. Double-curvature webs contribute to reach an higher capacity, i.e. resistant-by-shape structures, and *in situ* geometrical surveys could give valuable insight into the performance of these vaults, e.g. [Theodossopoulos, 2008; Rodriguez et al., 2012; Palacios and Martín Talaverano, 2013; Wendland et al., 2014; Capone et al., 2015].

On the other hand, the study of the rules of thumb provided valuable information for a database of the possible dimensions of the elements related to the cross vault. However, according to the available historical sources on this vault typology, the present study focuses more on the structural aspects related to the stability of the building, such as abutment dimensions. Nevertheless, the research has a twofold goal. It provides the basis of a parametric analysis aimed at understanding the influence of each parameter in the overall structural behaviour. At the same time, well aware of the singularities of each historical building, the collected data may represent a practical reference point for practitioners involved in monuments conservation. In this regard, further work is still requested to validate and to expand the overall database or to delimit it to a particular geographical area. In the words of Willis [1842], a catalogue of dimensions following surveys (by researchers and professionals) is rather desirable.

Regarding the structural analyses, the study of the historical methods for masonry vaulted structures, particularly cross vaults, highlighted the continuous effort of scholars and researchers in studying and explaining the statics of such a complex element. Nowadays, several works are focusing on limit analysis as a powerful tool for a quick assessment of collapse mechanism and the safety of structures composed by macro-blocks, such as vaults. As stressed in the chapter, limit analysis has an ancient origin linked to the masonry arch and, with no surprise, old outcomes are still used in modern implementations of the method, for instance the 3d compression only surface as a generalization of the thrust line.

Even though approximate, researchers of the past achieved an appreciable understanding of the stability of cross vaults under gravitational loads, but no considerations seem to have been made in case of seismic action. At the present time, whereas a certain consensus has been achieved regarding dead load and settlements, the seismic capacity of this element still represents a

challenging task in the conservation of cultural heritage buildings for both researchers and practitioners.

In this regard, in order to better understand the physical phenomenon, the study of the main damages following vertical and horizontal loads, as well as settlements, becomes essential. The main damages collected in the post-seismic survey form (provided by the Italian Department of Civil Protection) are reported together with the laboratory test results. Accordingly, of the six mechanisms individuated, only the shear failure in the horizontal plane has a clear mechanical description with a likewise well-defined crack pattern. Regarding the others, local instability and shear action are the main causes but a clear understanding of the phenomenon is still missing.

References

- Abraham, P. (1934). *Viollet-le-Duc et le rationalisme médiéval*. Paris: Vicent, Fréal et Cie.
- Adam, J.-P. (1988). *L'arte di costruire presso i romani: materiali e tecniche*. (Longanesi, Ed.). Milano.
- Alberti, L. B. (1485). *I dieci libri di architettura*. (Translated in Italian by Cosimo Bartoli, reprinted in Roma: Giovanni Zempel, 1784).
- Andreu, A., Gil, L., and Roca, P. (2007). Computational analysis of masonry structures with a funicular model. *Journal of Engineering Mechanics*, 133(4), 473–480.
- Angelillo, M., Babilio, E., and Fortunato, A. (2013). Singular stress fields for masonry-like vaults. *Continuum Mechanics and Thermodynamics*, 25(2-4), 423–441.
- Baratta, A., and Corbi, O. (2010). On the equilibrium and admissibility coupling in NT vaults of general shape. *International Journal of Solids and Structures*, 47(17), 2276–2284.
- Barthel, R. (1993). Tragverhalten gemauerter - Kreuzgewölbe. In *Aus Forschung und Lehre*, No. 26. Karlsruhe: University of Karlsruhe.
- Becchi, A., and Foce, F. (2002). *Degli archi e delle volte: arte del costruire tra meccanica e stereotomia*. (Marsilio, Ed.). Venezia.
- Benvenuto, E. (1991). *An introduction to the history of structural mechanics - Part II: vaulted structures and elastic*. Berlin: Springer.
- Beranek, W. J. (1988). Understanding of structures. In R. M. Lemaire & K. Van Balen (Eds.), *Stable-Unstable? Structural consolidation of ancient buildings* (pp. 29–44). Leuven: Leuven University Press.
- Block, P. (2009). *Thrust Network Analysis: exploring three-dimensional equilibrium*. PhD dissertation, Massachusetts Institute of Technology.
- Block, P., and Lachauer, L. (2014). Three-Dimensional (3D) Equilibrium Analysis of Gothic Masonry Vaults. *International Journal of Architectural Heritage*, 8(3), 312–335.
- Block, P., and Ochsendorf, J. (2007). Thrust network analysis: a new methodology for three-dimensional equilibrium. *Journal of the International Association for Shell and Spatial Structures (J. IASS)*, 48(3), 1–8.
- Blondel, F. (1675). *Cours d'architecture enseigné dans l'Academie royale d'architecture*. Paris: Lambert Roulland.
- Branca, G. (1783). *Manuale d'architettura*. (V. Monaldini, Ed.) (4th ed.). Roma: Con licenza dei Superiori.
- Brandonisio, G., Lucibello, G., Mele, E., and De Luca, A. (2013). Damage and performance evaluation of masonry churches in the 2009 L'Aquila earthquake. *Engineering Failure Analysis*, 34, 693–714.
- Calderini, C. (2004). *Un modello costitutivo per la muratura: formulazione ed implementazione per l'analisi di strutture complesse*. PhD dissertation, Università degli Studi di Genova.
- Caliò, I., Cannizzaro, F., and Pantò, B. (2012). A macro-element approach for modeling the nonlinear behaviour of monumental buildings under static and seismic loadings. In *World Conference in Earthquake Engineering*.
- Cannizzaro, F. (2011). *Un nuovo approccio di modellazione della risposta sismica degli edifici storici*. PhD dissertation, Università degli studi di Catania.

- Capone, M., Campi, M., and Catuogno, R. (2015). Gothic churches in Paris St Gervais et St Protais image matching 3d reconstruction to understand the vaults system geometry. In *The International Archives of the Photogrammetry, Remote Sensing and Spatial Information Sciences* (pp. 423–430). Avila (Spain).
- Cataneo, P. (1567). *L'architettura*. Venezia: In casa de' figliuoli di Aldo.
- Cavalieri San-Bertolo, N. (1826). *Istituzioni di architettura statica e idraulica*. Bologna: Tipografia Cardinali e Frulli.
- Ceradini, V. (1996). Modelli sperimentali di volte in tufo e mattoni. In *La meccanica delle murature tra teoria e progetto* (pp. 157–166). Messina.
- Ching, F. D. K. (1995). *A visual dictionary of architecture*. New York: John Wiley & Sons.
- Choisy, A. (1873). *L'art de bâtir chez les Romains*. (Ducher et C.ie, Ed.). Paris: Librairie generale de l'architecture et des travaux publics (Anastatic reprint, Bologna: Forni, 1984).
- Coenen, U. (1990). *Die spätgotischen Werkmeisterbücher in Deutschland. Untersuchung und Edition der Lehrschriften für Entwurf und Ausführung von Sakralbauten*. München: Scaneg.
- Como, M. (2013). *Statics of historic masonry constructions*. Springer-Verlag Berlin Heidelberg.
- Couplet, P. (1729). De la poussée des voûtes. *Mémoires de l'Académie Royale Des Sciences de Paris*, 79–117.
- Couplet, P. (1730). Seconde partie de l'examen de la poussée des voûtes. *Mémoires de l'Académie Royale Des Sciences Paris*, 117–141.
- Creazza, G., Matteazzi, R., Saetta, A., and Vitaliani, R. (2000). Analyses of masonry vaulted structures by using 3D damage model. In E. Oñate, K. Morgan, J. Periaux, & E. Stein (Eds.), *ECCOMAS 2000 European Congress on Computational Methods in Applied Sciences and Engineering*. Barcelona.
- Creazza, G., Matteazzi, R., Saetta, A., and Vitaliani, R. (2002). Analyses of masonry vaults: a macro approach based on three-dimensional damage model. *Journal of Structural Engineering*, 128(5), 646–654.
- Croci, G. (2000). General methodology for the structural restoration of historic buildings: the cases of the Tower of Pisa and the Basilica of Assisi. *Journal of Cultural Heritage*, 1(1), 7–18.
- Culmann, K. (1864). *Die graphische Statik (1864-1866)*. Zurich: Meyer & Zeller.
- D'Ayala, D., and Casapulla, C. (2001). Limit state analysis of hemispherical domes with finite friction. In P. B. Lourenço & P. Roca (Eds.), *Structural Analysis of Historical Constructions* (pp. 617–626). Guimarães.
- D'Ayala, D., and Tomasoni, E. (2011). Three-dimensional analysis of masonry vaults using limit state analysis with finite friction. *International Journal of Architectural Heritage*, 5(2), 140–171.
- De La Hire, P. (1712). Sur la construction des voûtes dans les édifices. In *Mémoires de l'Académie Royale des Sciences de Paris*. 70-78.
- De Vent, I. A. E. (2011). *Prototype of a diagnostic decision support tool for structural damage in masonry*. PhD dissertation, Delft University of Technology.
- Derand, F. (1643). *L'architecture des voûtes, ou l'art des traits et coupes des voûtes*. Paris: André Cailleau.
- Di Pasquale, S. (1996). *L'arte del costruire. Tra conoscenza e scienza*. Venezia: Marsilio.

- Dipartimento della Protezione Civile. (2013). *Manuale per la compilazione della scheda per il rilievo del danno ai beni culturali, chiese - MODELLO A-DC*. Ed. by Simona Papa and Giacomo Di Pasquale.
- Dogliani, F., Moretti, A., Petrini, V., and (Ed. by). (1994). *Le chiese e il terremoto. Dalla vulnerabilità constatata nel terremoto del Friuli al miglioramento antisismico nel restauro. Verso una politica di prevenzione*. Trieste: Lint Editoriale Associati.
- Faccio, P., Foraboschi, P., and Siviero, E. (1999). Volte in muratura con rinforzi in FRP (in Italian). *L'Edilizia*, 7/8, 44–50.
- Foraboschi, P. (2004). Strengthening of masonry arches with fiber-reinforced polymer strips. *Journal of Composites for Construction*, 191–202.
- Frankl, P. (1960). *The Gothic. Literary sources and interpretations through eight centuries*. (Princeton University Press, Ed.). Princeton, NJ.
- Fraternali, F. (2010). A thrust network approach to the equilibrium problem of unreinforced masonry vaults via polyhedral stress functions. *Mechanics Research Communications*, 37(2), 198–204.
- Frézier, A. F. (1737). *La théorie et la pratique de la coupe de pierres et des bois pour la construction des voûtes et autres parties des bâtiments civils et militaires, ou traité de stéréotomie à l'usage de l'architecture (1737-1739)*. Strasbourg/Paris: Charles-Antoine Jombert.
- Gilbert, M., Casapulla, C., and Ahmed, H. M. (2006). Limit analysis of masonry block structures with non-associative frictional joints using linear programming. *Computers & Structures*, 84(13-14), 873–887.
- Giovanetti (ed. by). (2000). *Manuale del recupero del Comune di Città di Castello*. Rome: DEI.
- Giuffré, A. (1988). Restoration and safety in seismic areas. The Cathedral of S. Angelo dei Lombardi (in Italian). *Palladio1*, (1), 95–120.
- Giuffré, A., and Marconi, P. (1988). Work in progress: restoration of the cathedral in S. Angelo dei Lombardi (in Italian). *Ricerche Di Storia Dell'arte*, XIII(35), 36–54.
- Heyman, J. (1966). The stone skeleton. *International Journal of Solids and Structures*, 2(2), 249–279.
- Heyman, J. (1968). On the rubber vaults of the middle ages and other matters. *Gazette Des Beaux-Arts*, 71, 177–188.
- Heyman, J. (1972). *Coulomb's memoir on statics: an essay in the history of civil engineering*. Cambridge: Cambridge University Press.
- Heyman, J. (1977). Equilibrium of shell structures. In *Oxford Engineering Science Series*. Oxford: Clarendon Press.
- Heyman, J. (1982). *The masonry arch*. Chichester: Ellis Horwood Ltd.
- Heyman, J. (1983). Chronic defects in masonry vaults: Sabouret's cracks. *Monumentum*, 26(2), 131–141.
- Heyman, J. (1995). *The stone skeleton: structural engineering of masonry architecture*. Cambridge, UK: Cambridge University Press.
- Holzer, S. (2011). Vault analysis: continuum mechanics and rigid body approaches. In *Construction History Europe- an Summer School: Two Millennia of Vaults, Domes and Shells*. Cambridge.
- Hooke, R. (1675). *A description of helioscopes, and some other instruments*. London.

- Huerta, S. (2004). *Arcos, bóvedas y cúpulas: geometría y equilibrio en el cálculo tradicional de estructuras de fábrica*. Madrid: Instituto Juan de Herrera.
- Huerta, S. (2006). Galileo was wrong: the geometrical design of masonry arches. *Nexus Network Journal*, 8(2), 25–52.
- Huerta, S. (2009). The debate about the structural behaviour of gothic vaults: from Viollet-le-Duc to Heyman. In *Construction History* (pp. 837–844). Cottbus.
- Huerta, S. (2010). Thomas Young’s theory of the arch: Thermal effects. In A. Sinopoli (Ed.), *Mechanics and Architecture: Between Epistémè and Téchne* (pp. 155–178). Roma: Edizioni di Storia e Letteratura.
- Kilian, A., and Ochsendorf, J. (2005). Particle-spring systems for structural form finding. *Journal of the International Association for Shell and Spatial Structures (J. IASS)*, 46(147), 77–84.
- Koepf, H. (1969). *Die gotischen Planrisse der Wiener Sammlungen*. Vienna: Hermann Böhlau Nachf.
- Kooharian, A. (1953). Limit analysis of voussoir (segmental) and concrete arches. *Proceedings of the American Concrete Institute*, (4), 317–328.
- Körner, C. (1901). *Gewölbte Decken. Handbuch der Architektur*. 3rd pt., vol. 2, No. 3b. Stuttgart: Arnold Bergsträsser Verlagsbuchhandlung.
- Kurrer, K.-E. (2008). *The history of the theory of structures: from arch analysis to computational mechanics*. Berlin: Ernst & Sohn.
- Lagomarsino, S. (1998). A new methodology for the post-earthquake investigation of ancient churches. In *11th European conference on earthquake engineering* (pp. 1–12). Paris.
- Lagomarsino, S., Podestà, S., Cifani, G., and Lemme, A. (2004). The 31st October 2002 earthquake in Molise (Italy): a new methodology for the damage and seismic vulnerability survey of churches. In *13th World conference on earthquake engineering* (p. 11). Vancouver, BC, Canada.
- Lechler, L. (1516). *Unterweisungen und Lehrungen für seinen Sohn Moritz*. (Original lost, copy of 1583).
- Lourenço, P. B. (1996). *Computational strategies for masonry structures*. PhD dissertation, Delft University of Technology.
- Lourenço, P. B. (1998). Experimental and numerical issues in the modelling of the mechanical behaviour of masonry. In P. Roca, J. L. González, E. Oñate, & P. B. Lourenço (Eds.), *Structural analysis of historical constructions* (pp. 57–91). Barcelona: CIMNE.
- Lourenço, P. B. (2002). Computations on historic masonry structures. *Progress in Structural Engineering and Materials*, 4(3), 301–319.
- Lourenço, P. B., Milani, G., Tralli, A., and Zucchini, A. (2007). Analysis of masonry structures: review of recent trends in homogenization techniques. *Canadian Journal of Civil Engineering*, 34(11), 1443–1457.
- Mark, R. (1982). *Experiments in gothic structure*. Cambridge: The MIT Press.
- Mark, R., Abel, J. F., and O’Neill, K. (1973). Photoelastic and finite-element analysis of a quadripartite vault. *Experimental Mechanics*, 13(8), 322–329.
- Mascheroni, L. (1785). *Nuove ricerche sull’equilibrio delle volte*. Bergamo: Francesco Locatelli.
- Mastrodicasa, S. (1943). *Dissesti statici delle strutture edilizie*. (9th ed. 1993) Milano: Hoepli.

- Méry, E. (1840). Mémoire sur l'équilibre des voûtes en berceau. *Annales Des Ponts et Chaussées*, 50–70.
- Milani, E., Milani, G., and Tralli, A. (2008). Limit analysis of masonry vaults by means of curved shell finite elements and homogenization. *International Journal of Solids and Structures*, 45(20), 5258–5288.
- Milani, G., Milani, E., and Tralli, A. (2009a). Upper Bound limit analysis model for FRP-reinforced masonry curved structures. Part I: Unreinforced masonry failure surfaces. *Computers & Structures*, 87(23-24), 1516–1533.
- Milani, G., Milani, E., and Tralli, A. (2009b). Upper bound limit analysis model for FRP-reinforced masonry curved structures. Part II: Structural analyses. *Computers & Structures*, 87(23-24), 1534–1558.
- Milani, G., Simoni, M., and Tralli, A. (2014). Advanced numerical models for the analysis of masonry cross vaults: A case-study in Italy. *Engineering Structures*, 76, 339–358.
- Milani, G., and Tralli, A. (2012). A simple meso-macro model based on SQP for the non-linear analysis of masonry double curvature structures. *International Journal of Solids and Structures*, 49(5), 808–834.
- Mouzakis, H., Adami, C. E., Karapitta, L., and Vintzileou, E. (2012). Seismic behaviour of a rehabilitated cross vault. In J. Jasieńko (Ed.), *Structural Analysis of Historical Constructions* (pp. 1665–1673). Wrocław.
- Müller, W. (1990). *Grundlagen gotischer Bautechnik*. (D. Kunstverlag, Ed.). Munchen.
- Navascués Palacio, P. (1974). *El libro de arquitectura de Hernán Ruiz, el Joven*. Madrid: Escuela Técnica Superior de Arquitectura de Madrid, ETSAM.
- O'Dwyer, D. (1999). Funicular analysis of masonry vaults. *Computers & Structures*, 73(1-5), 187–197.
- Orduña, A., and Lourenço, P. B. (2005a). Three-dimensional limit analysis of rigid blocks assemblages. Part I: Torsion failure on frictional interfaces and limit analysis formulation. *International Journal of Solids and Structures*, 42(18-19), 5140–5160.
- Orduña, A., and Lourenço, P. B. (2005b). Three-dimensional limit analysis of rigid blocks assemblages. Part II: Load-path following solution procedure and validation. *International Journal of Solids and Structures*, 42(18-19), 5161–5180.
- Ortolani, F. (1988). Seismic effect on brick vaulted structures: experiment results (in Italian). *Palladio*, I(2), 143–146.
- Palacios, J. C. (2006). The gothic ribbed vault in Rodrigo Gil de Hontañón. In *Second International Congress on Construction History* (pp. 2415–2431). Cambridge University: Queens' College.
- Palacios, J. C., and Martín Talaverano, R. (2013). Technological Development in Spanish Gothic Vaults Design. *International Journal of Architectural Heritage*, 7(2), 189–206.
- Palladio, A. (1570). *I quattro libri dell'architettura*. Venezia: Dominico de' Franceschi (Reprinted Siena: Alessandro Mucci, 1790).
- Paulin, E. J. B. (1890). *Thermes de Dioclétien*. Paris: Firmin-Didot et Cie.
- PERPETUATE. (2012). *DELIVERABLE D12 Results of experimental test on damage measures and reference values to be considered*.
- Piccirilli, C. (1989). *Consolidamento critico e sue premesse storico-strutturali*. (2nd edition, 1996); Roma: Bonsignori Editore.

- Planat, P. (1887). *Pratique de la mécanique appliquée à la résistance des matériaux*. Paris: La Construction Moderne.
- Regione Toscana. (2003). *Istruzioni tecniche per l'interpretazione ed il rilievo per macroelementi del danno e della vulnerabilità sismica delle chiese*. Venzone: ARX s.c.r.l.
- Roca, P., Cervera, M., Gariup, G., and Luca, P. (2010). Structural Analysis of Masonry Historical Constructions. Classical and Advanced Approaches. *Archives of Computational Methods in Engineering*, 17(3), 299–325.
- Rodriguez, M. A. A., López, J. C., Vivó, P. N., and Guzmán, M. T. (2012). Stonecutters' literature and construction practice in Early Modern Gothic. The tracings for a rib vault at the Cathedral of Tui. *Construction History*, 27, 1–21.
- Rondelet, J. (1802). *Traité théorique et pratique de l'art de bâtir (1802-1810)*. Paris: Chez l'auteur. (7th ed. Paris: Chez Firmin Didot, 1834–48).
- Rossi, M., Calderini, C., Lagomarsino, S., and Milani, G. (2014). Seismic response of masonry vaulted structures: experimental and numerical modelling. In P. B. Lourenço, B. A. Haseltine, & G. Vasconcelos (Eds.), *9th International Masonry Conference*. Guimarães: Universidade do Minho.
- Sabouret, V. (1928). Les voûtes d'arêtes nervurées. Rôle simplement décoratif des nervures. *Le Génie Civil* 92, 205–209.
- Sanabria, S. L. (1982). The mechanization of design in the 16th century: the structural formulae of Rodrigo Gil de Hontañón. *Journal of the Society of Architectural Historians*, 41(4), 281–293.
- Shapiro, E. E. (2012). *Collapse mechanisms of small-scale unreinforced masonry vaults*. Master thesis, Massachusetts Institute of Technology.
- Smoljanović, H., Živaljić, N., and Nikolić, Ž. (2013). Overview of the methods for the modelling of historical masonry structures. *Građevinar*, 65(7), 603–618.
- Sorrentino, L., Liberatore, L., Decanini, L. D., and Liberatore, D. (2014). The performance of churches in the 2012 Emilia earthquakes. *Bulletin of Earthquake Engineering*, 12(5), 2299–2331.
- Strommer, L. (2008). Spherical segment approximation of quadripartite vaults. *Periodica Polytechnica Architecture*, 39(1), 27–34.
- Tarrío, I. (2010). Gothic structural theories ca. 1930: the contribution of Victor Sabouret. *Advanced Materials Research*, 133-134, 137–142.
- Theodossopoulos, D. (2008). Structural design of High Gothic vaulting systems in England. *International Journal of Architectural Heritage*, 2(1), 1–24.
- Theodossopoulos, D., Sinha, B. P., Usmani, A. S., and Macdonald, A. J. (2002). Assessment of the structural response of masonry cross vaults. *Strain*, 38(3), 119–127.
- Tomasoni, E. (2008). *Le volte in muratura negli edifici storici: tecniche costruttive e comportamento strutturale*. PhD dissertation, Università degli Studi di Trento.
- Tosca, T. V. (1707). *Compendio mathemático en que se contienen todas las materias más principales de las ciencias que tratan de la cantidad (1707-15)*. Valencia: Antonio Bordazar. (2nd ed. Madrid, 1721–27. Fifth volume reprinted in *Arquitectura civil, montea y cantería*: Valencia: Librería París-Valencia, 1992; Universidad Politécnica, 2000).
- Tralli, A., Alessandri, C., and Milani, G. (2014). Computational Methods for Masonry Vaults: A Review of Recent Results. *The Open Civil Engineering Journal*, 8(1), 272–287.

- Trevisan, C. (2011). *Per la storia della stereotomia. Geometrie, metodi e costruzioni*. Roma: Aracne.
- Ungewitter, G. G., and Mohrmann, K. (1890). *Lehrbuch der gotischen Konstruktionen*. (T. O. Weigel Nachf, Ed.) (3rd ed.). Leipzig.
- Valadier, G. (1832). *L'architettura pratica dettata nella Scuola e Cattedra dell'insigne Accademia di S. Luca*. Roma: Com permesso de' Superiori.
- Van Mele, T., McInerney, J., DeJong, M., and Block, P. (2012). Physical and computational discrete modelling of masonry vault collapse. In Jerzy Jasieńko (Ed.), *Structural Analysis of Historical Constructions* (pp. 2552–2560). Wrocław.
- Viollet-le-Duc, E. E. (1854). *Dictionnaire raisonné de l'Architecture Française du XI au XVI siècle (1854-1868)*. Paris: A. Morel.
- Vittone, B. A. (1760). *Istruzioni elementari per indirizzo dei giovani allo studio dell'architettura*. Lugano: Agnelli.
- Wendland, D. (2007). Traditional Vault Construction Without Formwork: Masonry Pattern and Vault Shape in the Historical Technical Literature and in Experimental Studies. *International Journal of Architectural Heritage*, 1(4), 311–365.
- Wendland, D., Alonso, M. A., and Kobe, A. (2014). The vault with curvilinear ribs in the “Hall of Arms” in the Albrechtsburg Meissen: studies on the concept, design and construction of a complex Late Gothic rib vault. In J. Campbell et al. (Ed.), *First Conference of the Construction History Society* (pp. 459–468). Cambridge.
- Willis, R. (1835). *Remarks on the architecture of the Middle Ages, especially of Italy*. Cambridge: Pitt Press.
- Willis, R. (1842). *On the Construction of the Vaults of the Middle Ages*. London: Transactions of the Royal Institute of British Architects, Vol. 1, Part 2.
- Wilson, C. (1990). *The gothic cathedral: the architecture of the great church 1130-1530*. New York: Thames and Hudson.
- Wittmann, W. (1879). Zur Theorie der Gewölbe. *Zeitschrift Für Bauwesen*, 29, 61–74.
- Wolfe, W. S. (1921). *Graphical analysis: a handbook on graphic statics*. New York: McGraw-Hill Book Company.

Chapter 3.

Dry-joint arch under base impulse signal

3.1 Abstract

Rocking-type structures, as dry-joint masonry arches, are particularly vulnerable to impulse loading [Zhang and Makris, 2001; DeJong et al., 2008; DeJong and Dimitrakopoulos, 2014]. However, given the rocking nature of the response, it is well known that the horizontal acceleration that activates the mechanism, i.e. first oscillation with cracks occurrence, is smaller than the collapsing one. The rigid bodies, in fact, can move back to the rest position if the seismic impulse duration or the energy content are not large enough, or if no other impulses increase the oscillations [De Lorenzis et al., 2007; DeJong, 2009; Dimitri et al., 2011].

With the aim of better understanding the seismic response of vaulted masonry structures, the present chapter deals with the analysis of the seismic behaviour of a scaled arch assembled by dry-joint 3D printed voussoirs, by means of tilting and shaking table tests. The tests have been carried out in the Structures and Materials Laboratory in Sapienza University of Rome, whereas the image analysis technique was developed at the Hydraulics Laboratory of the same University.

The study had a twofold goal: on the one hand, it gave insight into the capacity of the arch undergoing base impulse excitation; on the other hand, it provided information for validating a FE numerical model based on rigid-infinitely resistant voussoirs and friction interfaces elements. Once validated, the outcomes of this phase was extended to the analysis of groin vaults, discussed in the following chapter.

Finally, since the subject of this chapter is somehow different from the general topic of the thesis, a very brief overview of the dynamic behaviour of masonry arches is also reported.

3.2 Literature overview

In the last five decades, starting with the seminal work by Housner [1963], great effort has been devoted to the study of the rigid block dynamics, either isolated or assembled. However, despite the seismic vulnerability of masonry vaulted structures, it is only in the 1990s that Oppenheim [1992] undertook the study of the rocking masonry arch. This was considered as a rigid body four-link SDOF mechanism in which the location of the four hinges was fixed and defined by a static equivalent analysis.

For the sake of clearness, the assumed movements of an arch undergoing a simple impulse excitation are depicted in Figure 3-1. Once the mechanism is formed, the arch basically moves in the opposite direction with respect to the initial acceleration (Figure 3-1a). Then, depending on the characteristics of the base acceleration, the arch may (or not) recover with an impact occurrence (Figure 3-1b) and start to move in the other direction (Figure 3-1c).

Essentially, Oppenheim [1992] did not investigate the post-impact behaviour (Figure 3-1c), that is, the failure was supposed to occur only with large rotation in the phase depicted in Figure 3-1a. In case the arch was able to recover to the rest position, it was assumed as safe (Figure 3-1b). Considering the nonlinear equation of motion for the SDOF mechanism, and implementing an idealized impulse base motion (as a sequence of constant negative and positive acceleration), the author was able to build the failure domain of the arch in the impulse magnitude-duration domain.

In the same period, Clemente [1998] performed numerical analyses on the dynamics of stone arches under three different configurations, namely free vibrations following an initial displacement, rectangular pulse and sinusoidal base acceleration. However, according to Oppenheim [1992], the author did not address the problem of the impact occurrence, focusing the attention only on the first-half cycle of rocking.

More recently, using Discrete Element Method (DEM) analyses of arches undergoing base impulse excitation, DeJong and Ochsendorf [2006] found that the approach of the cited works was not on the safe side. Only relatively large impulses cause the arch to collapse without impacts (as supposed by Oppenheim, Figure 3-1a), whereas the most critical failure mode develops for smaller impulses in the post-impact phase (Figure 3-1c). This behaviour parallels the outcomes

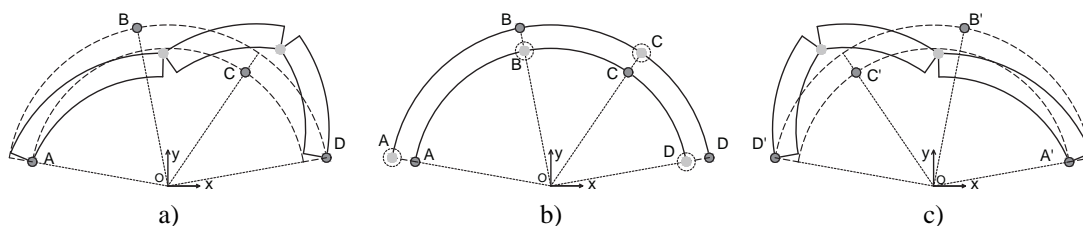


Figure 3-1. The SDOF mechanism for an arch under base excitation: a) first half cycle, b) recovering and impact, c) second half cycle

of Zhang and Makris [2001] for a free-standing rocking block. In particular, the authors defined Mode 1 and Mode 2 failure for the collapse without impact (in the fashion of Figure 3-1a) and after the impact (Figure 3-1c), respectively. The authors proved also that the rocking blocks are more susceptible to a one-sine than a one-cosine impulse.

Following Oppenheim's contribution, De Lorenzis et al. [2007] proposed an analytical model able to take into account the energy dissipation during the impact, thus to approximately catch the dynamic behaviour of the arch throughout the entire cycles of rocking. Again, the arch was modelled as a four-link SDOF mechanism where the location of the hinges was assumed coincident with the ones provided by a static analysis (Figure 3-1a). In case of impact occurrence, the hinge location simply reflected about the vertical line of symmetry of the undeformed arch (Figure 3-1b, c). The rocking behaviour was assumed to keep going back and forth producing several impacts until failure occurred or the arch returned to the rest position.

The impact problem was solved thanks to the coefficient of restitution, which relates the rotational velocity (and, analogously, the kinetic energy) pre- and post-impact. It resulted that the coefficient depends only on the geometry of the arch and the number of voussoirs, being independent of scale. Although the model provided good results compared with DEM analyses and laboratory experiments [DeJong and Ochsendorf, 2006; DeJong et al., 2008], there are clearly some limitations. The strongest one regards the assumption of fixed hinge locations, which prevent the free hinge formation before and after the impact, that is, the rotation at any non-hinged joint. Moreover, sliding between blocks is neglected.

The same research group [DeJong et al., 2008] extended the previous work by means of a shaking table tests on a scaled dry-joint arch built with autoclaved aerated concrete blocks. The tests regarded five time histories of real earthquakes, as well as harmonic signals and tilting analysis. For what concerns the capacity of the arch under one-cycle sine impulse excitation, the authors determined a simple equation fitted on the results of the analytical model, reported in Equation (3-1). The exponential curve asymptotically approaches the minimum acceleration (λ) necessary to cause the collapse of the arch (quasi-static failure), being R the centreline radius, and C_1 , C_2 , and t_{min} fitting coefficients.

$$\frac{a_p}{g} = C_1 \left(\frac{1}{f_p \sqrt{R}} - t_{min} \right)^{C_2} + \lambda \quad (3-1)$$

The equation describes the failure curve in terms of frequency f_p and impulse amplitude a_p , providing a good estimation of the stability of the arches under a one-cycle sine pulse acceleration. Theoretically, the area above the curve represents inputs which bring the arch to collapse, while the area below it provides recovery points.

3.3 Experimental setup

3.3.1 Overall description

The geometrical dimensions of the tested arch were chosen to comply with the table features, leading to a specimen of 21 voussoirs with an internal radius of 365 mm, 40 mm thick, 92 mm wide and an angle of embrace of 140° (Figure 3-2). The inclined supports of the arch (at 20°) were realized with steel angle bars bolted to the platform.

Regarding the tests, a pulley system was assembled in the laboratory for the tilting tests, while the dynamic tests were performed using the vibration system ES-6-230/GT700M produced by DONGLING Technology [2015]. This is an electrical-dynamic shaker with V-shaped guide rail with magnesium slip table $700 \times 700 \text{ mm}^2$ large and 45 mm thick. Other specifications are reported in Table 3-1. The base motion was recorded using two ceramic shear ICP[®] accelerometers produced by PCB Piezotronics: model 393A03 (1034 mV/g, 0.5 to 2000 Hz, range $\pm 5 \text{ g}$, accuracy $5 \mu\text{g}$) and model 352C33 (102.8 mV/g, 0.5 to 10000 Hz, range $\pm 50 \text{ g}$, accuracy $150 \mu\text{g}$).

The individual voussoirs have been printed with a MakerBot Replicator[™] 2X [2015]. This is a

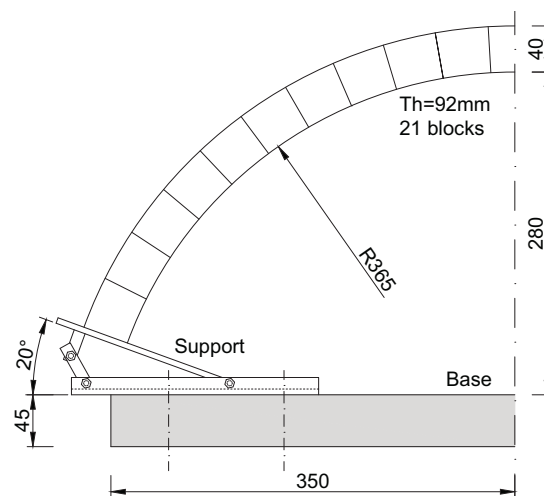


Figure 3-2. Test arch geometrical dimensions

Shock force	12kN
Usable frequency	5-2000Hz
Maximum bare table acceleration	1000m/s ²
Maximum velocity	2m/s
Maximum displacement (peak-peak)	51mm
Maximum load for vertical	300kg
Effective moving mass	58kg
Effective nominal armature mass	6kg

Table 3-1. Slip table system specifications

accuracy. The material adopted was the Acrylonitrile Butadiene Styrene (ABS) which is a widely used thermoplastic material. Once printed, in order to reach a friction coefficient comparable with masonry elements, each voussoir has been coated with a mixture of fine sand (0.2 - 1.0 mm diameter grain size) and polyester bi-component resin reaching an average friction angle equal to 34.2° . The mixture bonds well to the plastic surface without showing significant deterioration along the test campaign. The same treatment was applied also to the supports in order to maintain a consistent friction angle.

Since the material properties, namely mass density, elasticity, strength, etc., do not affect the problem [Liberatore and Spera, 2001; De Lorenzis et al., 2007; DeJong et al., 2008] (see §3.6), only the external frame of the voussoirs was printed, that is, the lateral surfaces, filling the inner part with spruce wood inserts. Considering the low density of the thermoplastic material, which could have compromised the stability of the model under accidental actions, the wooden inserts allowed reaching an overall mass density of around 450 kg/m^3 . The total mass of the specimen was thus 1.4 kg, whereas the steel supports weight 1.7 kg each.

3.3.2 Data acquisition

According to Figure 3-3, reference data were provided by an acquisition system consisting of 1) a high-speed, high-resolution camera (Mikrotron EoSens) equipped with a Nikon 50-mm focal length lens capturing gray-scale images at up to 500 fps with a resolution of 1280×1024 pixels (for the present set of measurements, images were acquired at 400 fps) and 2) a high-speed Camera Link digital video recorder operating in Full configuration (IO Industries DVR Express Core) to manage data acquisition and storage. The captured images were transferred to a personal computer under the control of the Express Core software.

The images acquired by the Mikrotron EoSens camera have been processed using a Lagrangian Particle Tracking technique named Hybrid Lagrangian Particle Tracking (HLPT) [Shindler et al., 2012]. HLPT selects image features (image portions suitable to be tracked because their luminosity remains almost unchanged for small time intervals) and tracks these from frame to frame. Though HLPT was developed to process images from fluid mechanics experiments [Moroni and Cenedese, 2015], it was successfully employed here to track the texture of objects undergoing the oscillatory motion.

The cornerstone of the image analysis algorithm is the solution of the Optical Flow (OF) equation, which defines the conservation of the pixel brightness intensity at time t . Since the OF equation is insufficient to compute the two unknown in-plane velocity components (i.e. the features) associated to a single pixel, the equation is computed in a window $W=H \times V$ (where H and V are

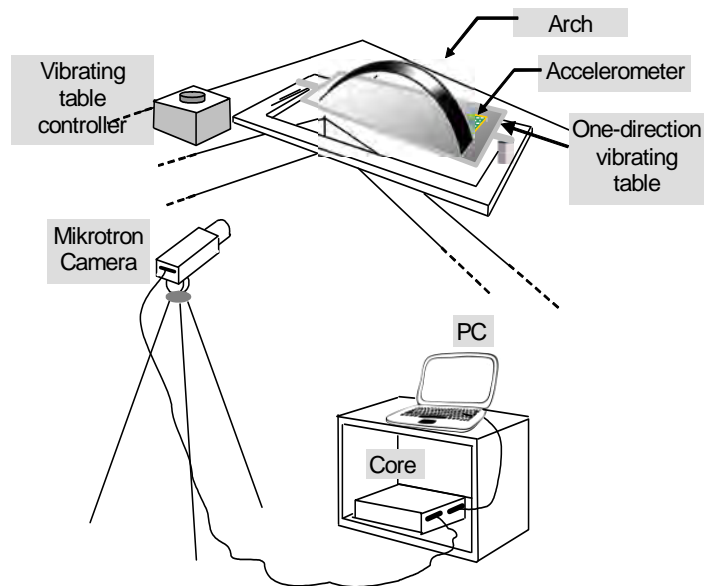


Figure 3-3. Experimental setup

the horizontal and vertical dimensions of the window respectively) centred at the pixel location. The OF equation is solved for a limited number of image pixels. The matching measure used to follow a feature (and its interrogation window) and its “most similar” region at the successive time is the “Sum of Squared Differences” (SSD) among intensity values: the displacement is defined as the one that minimizes the SSD [Moroni and Cenedese, 2005]. Once the trajectories are reconstructed, displacements, velocities, and accelerations are computed via central differences, which are second-order accurate.

3.4 Experimental tests

3.4.1 Tilting tests

The first phase of the experimental campaign focused on the tilting test, i.e. quasi-static rotation of the base platform until failure occurs. Dealing with rigid blocks, a tilting test can be regarded as a first-order seismic assessment method to evaluate the collapse mechanism and the corresponding horizontal load multiplier. This is the fraction of the gravity acceleration necessary to transform the arch in a SDOF (four-link rigid block mechanism). On the other hand, being based on a quasi-static method, it assumes an infinite duration of the loading. In reality, given the dynamic nature of the problem, the structure might experience larger peaks of acceleration for short period and recover soon after [Clemente, 1998; DeJong, 2009], being also strongly affected by the frequency contents of the input.

Finally, it must be stressed that, in the local reference, tilting the model implies that the vertical

acceleration reduces in magnitude as the horizontal acceleration increases. However, since the problem is purely based on the stability and not on the stresses within the structure, this issue is not relevant. The goal is thus only to obtain the ratio between horizontal and vertical acceleration, which is basically the tangent of the angle of tilt.

In order to account for possible imperfections due to the manual assembling, the test was performed three times providing an average horizontal load multiplier $\lambda = 0.29$.

3.4.2 Signal processing

As input for the shaking table tests, a sine shaped pulse was adopted. The signal needed to be processed in order to meet the features of the shaking table, which is based on an electrical-dynamic vibration system. The system is essentially based on a vibration control system that, through an amplifier, sends a signal to the shaking table where the armature moves back and forth in a magnetic field. Accordingly, the acceleration (thus the displacement) of the table is governed by the amount of electric current and it was not possible to have a residual current at the end of the test, i.e. no residual displacement.

In order to guarantee null displacement and velocity at the end of the test, a Bohman window was chosen to fade-in and -out the signal. The Bohman window is the convolution of two half-duration cosine lobes. In the time domain, it is the product of a triangular window and a single cycle of a cosine with a term added to set the first derivative to zero at the boundaries. As an example, considering a 1.3 g and a 10 Hz three-cycle sine signal, the calculated Bohman window is reported in Figure 3-4 in both time and frequency domain (sample rate of 400 Hz).

Moreover, since the windowing affects the initial and final part of the signal, three cycles of sine were implemented, ensuring thus a unique central impulse. Considering a 1.3 g, 10 Hz three-cycle sine signal, the effects of the windowing are reported in Figure 3-5. As it is possible to see, the

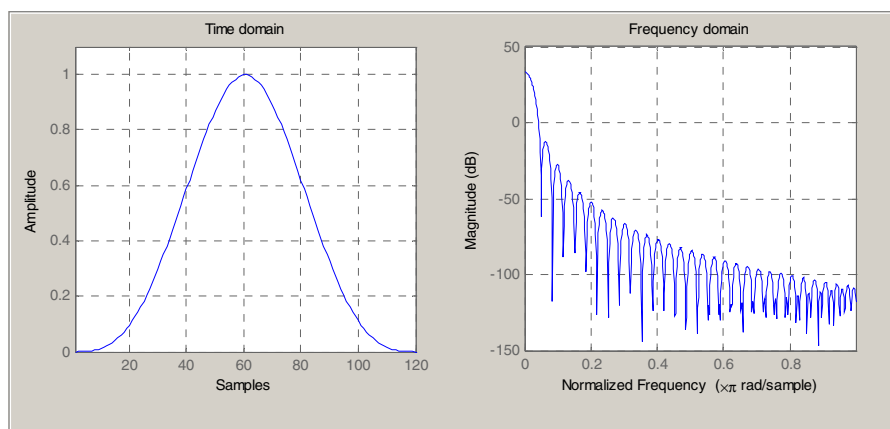


Figure 3-4. Example of Bohman window in time and frequency domain

un-windowed acceleration produces a conspicuously large residual displacement (for the sake of clarity it is stopped at the end of the first cycle). On the other hand, the two accelerations are comparable in the central part of the signal.

Considering the same signal, the comparison between the input acceleration history (i.e. drive) and the accelerogram recorder on the table is reported in Figure 3-6. The comparison is extended to velocity and displacement, as single and double integration of the acceleration. As it is possible to see, the output signal matched almost perfectly the input one for what concerns the frequency, but the peak acceleration is slightly larger for the recorded one. Moreover, this signal shows minor parts with high frequency acceleration, probably due to small impacts of the table in the change of directions. However, given their short duration, they are not expected to modify the final results. In this regard, De Lorenzis et al. [2007] state that at high frequencies an arch does not fail by hinging and rocking, but it may fail due to long-lasting vibration between the voussoirs.

3.4.3 Experimental results

The experimental campaign was aimed at determining the failure curve in the frequency-amplitude domain for the given shape of the impulse signal. The curve is an interpolation of the failure inputs, but, by extension, it may indicate the threshold for the stability condition: the area below the curve indicates the safe input for the arch, whereas the area over the curve indicates collapse input. In order to accomplish this goal, once the frequency was assigned, the amplitude

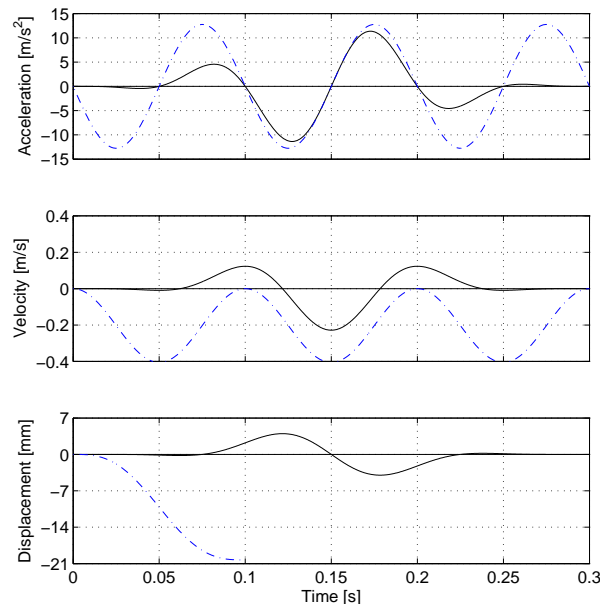


Figure 3-5. 1.3 g, 10 Hz pre-and post-windowed signal (dash-dot blue line and black solid line, respectively)

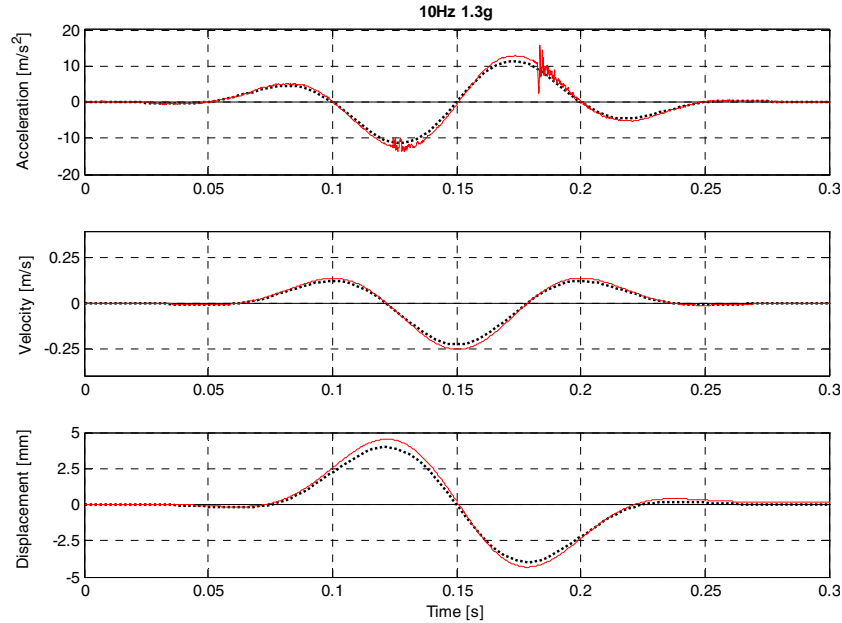


Figure 3-6. Comparison between input signal (drive) and recorded signal (dot black line and red solid line, respectively)

was scaled until at least two collapses were registered. In fact, given the possible assembling imperfections, each test was repeated three times (runs).

In general, the arch failed after the end of the input signal without experiencing any sliding between the blocks (due to the slenderness of the arch). Rocking motion occurred through apparent chaotic alternating four-hinge mechanisms. Conversely to the case of one-cycle sine impulse and already discussed in literature [De Lorenzis et al., 2007; DeJong et al., 2008], additional hinges occurred when a clear four-hinge mechanism was interrupted by further impulses out-of-phase with the rocking motion. Moreover, Clemente [1998] found that the arch can even (temporarily) experience larger and unsafe rotations if the subsequent impulse restores the displacements in a safety range. In general, these aspects have a stabilizing effect (larger amount of impacts leads to larger dissipated energy) and higher amplitude signals are usually necessary to bring the arch to collapse.

Focusing on the collapse trials (runs with failure), a certain trend in the behaviour of the arch was detected. Considering, for instance, the time history reported in Figure 3-5, the first and last cycle of sine (i.e. up to 0.1 s and after 0.2 s) were not able to modify the arch configuration. In fact, even in the cases the amplitude was larger than the minimum acceleration that induces the rocking motion (i.e. the value provided by tilting test, 0.29 g), the sudden change of direction did not allow any clear hinge activation.

In terms of the displacement diagram, the central part of the time history resembles a one-cycle sine. With reference to Figure 3-7, three clear main base movements (phases) can be detected:

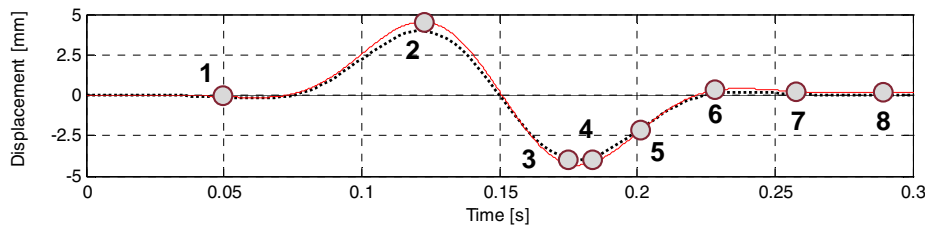


Figure 3-7. 1.3 g, 10 Hz signal: displacement time history

1-2, onward from rest position to the positive peak; 2-3, reverse movement, until the negative peak; 4-6, again onward; 4-8 until the rest position of the table. In order to provide a qualitative scheme of the hinge location and the overall displacements of the arch throughout the test, Figure 3-8 reports the frames at the instants denoted in Figure 3-7.

Looking at Figure 3-8, the displacement during the phase 1-2 produced a clear movement of the arch in the opposite direction, due to the inertial forces, but it is not easy to discuss whether hinges were open. During the subsequent phase 2-3, the previous displacement reversed developing a four-hinge mechanism, whose hinge location approximately matched those predicted by static analysis. The phase 4-8, completely out of phase, led to a more chaotic behaviour, with even a temporary occurrence of a fifth hinge. The ultimate configuration of the mechanism was reached at the instants 7-8.

According to the previous description, several features were persistent in most tests. With reference to Figure 3-9, hinges C and D kept opening until failure occurrence, without significant location changes. On the other hand, the location of hinges A and B showed a clear movement: after the initial location (phase 1-2), the hinges started to migrate according to the arrows depicted in Figure 3-9. Conversely to the case of one-cycle sine impulse, for which the most critical failure mode involves the post-impact behaviour [Zhang and Makris, 2001; DeJong and Ochsendorf, 2006] (see §3.2 and Figure 3-1), in the present case, failure seemed to occur without any flipping impact.

A total of 69 runs was performed and the results are collected in Figure 3-10. In order to highlight the trend of the experimental results, a linear regression analysis has been implemented (red dot line). By means of a logarithmic transformation of the data, an exponential curve constrained to asymptotically reach (for lower frequencies) the value provided by the tilting test was obtained. As it is possible to observe, the fitted line matches well the results, with a coefficient of determination equal to $R^2 = 0.98$. The result is reported in Equation (3-2), where f_p and a_p represent the frequency and impulse amplitude, respectively.

$$a_p = 0.0647e^{0.2801f_p} + 0.225 \quad (3-2)$$

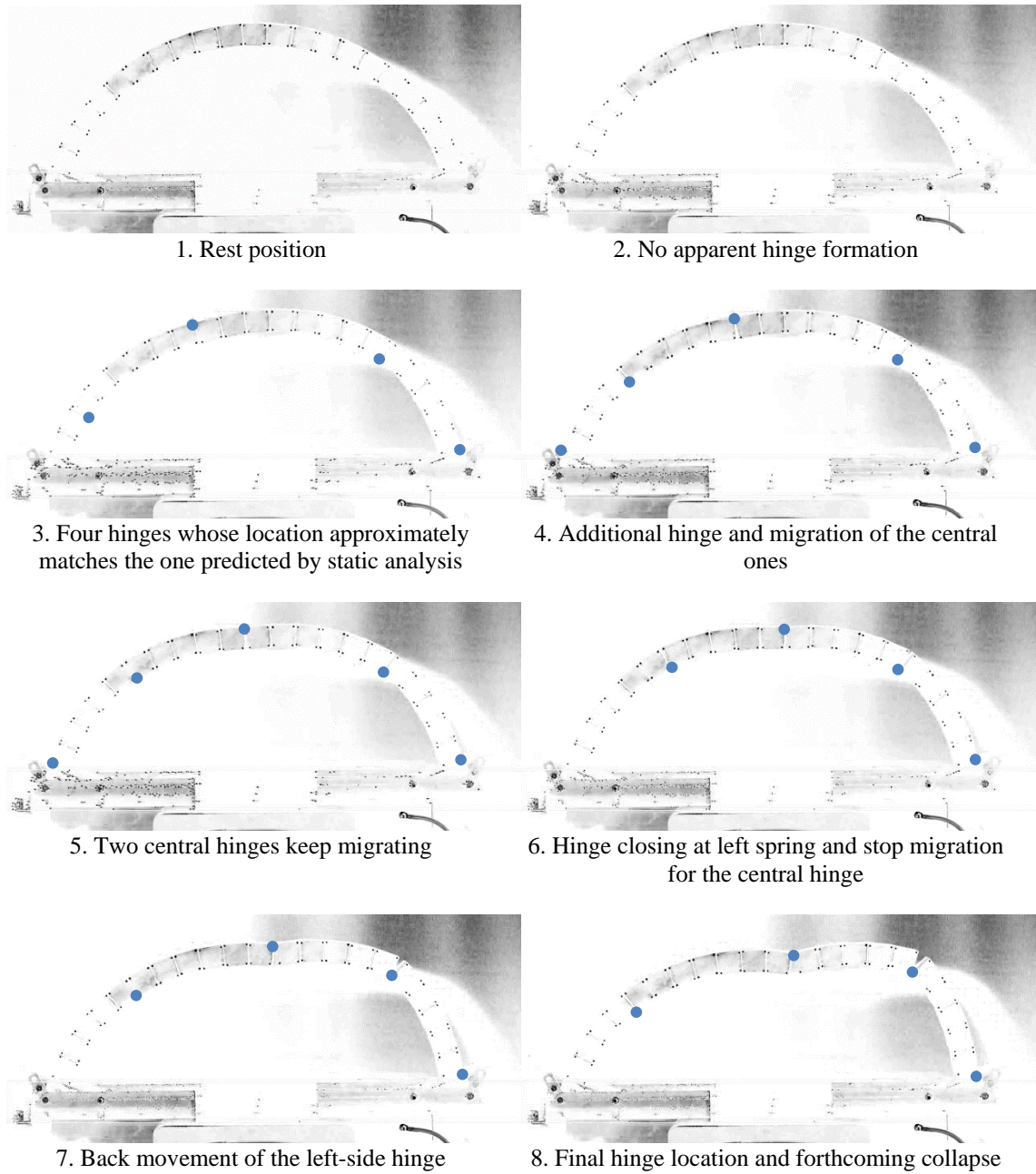


Figure 3-8. 7 Hz and 0.6 g impulse (first replicate): significant frames for hinge location

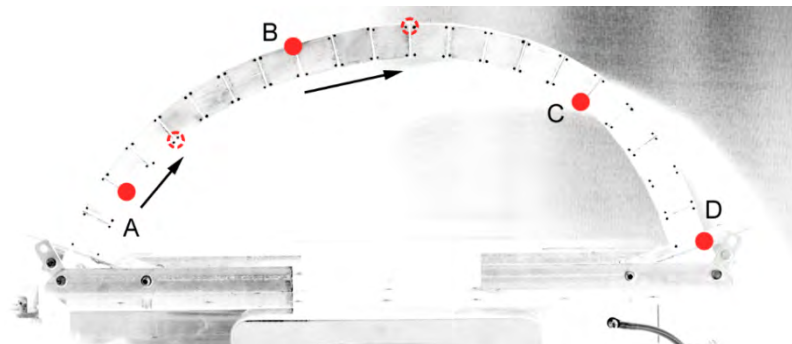


Figure 3-9. 7 Hz and 0.6 g impulse (first replicate): deformed shape at 0.17 s and hinge location

The results of the experimental campaign were compared with the curve computed according to DeJong et al. (2008, Table 3, with $\lambda = 0.30$, $C_1 = 0.02$, $C_2 = -0.81$, and $t_{min} = 0.11$). This curve represents the governing Mode 2 failure domain for a one-cycle sine impulse for the arch with 10% reduction thickness (as discussed in § 3.5.2). Given the different input adopted, the curve is considerably more conservative. As already stressed, the reason lies in the out-of-phase acceleration that allowed the arch to experience larger peaks of acceleration without failing.

The outcome of the tilting analysis (0.29 g) is also reported in Figure 3-10. Since the quasi-static nature of the test, this represents the expected asymptote (in the lower frequency range) of a dynamic test campaign. By extension, the horizontal load multiplier provided by the tilting test denotes the threshold of the region where impulses cause no hinge to form, i.e. the arch acts as a rigid body following the base motion. In general, the comparison between dynamic and tilting tests highlights how much a quasi-static analysis may underestimate the capacity of the arch.

Finally, it must be stressed that the elastic resonant frequency of the first mode was not evaluated. The results, in fact, are not affected by it (as for the case of elastic structures) because the natural frequency of rigid blocks changes with the displacement and the initial hinge formation immediately modifies the resonant frequency. At the most, resonance might force hinges to occur at a lower acceleration than expected [DeJong et al., 2008]. In the present study a non-random with constant frequency signals were adopted and the response for any constant frequency did not exhibit any resonant peak

3.5 Numerical analyses

3.5.1 Overall description

The numerical analyses has been carried out through a commercial FEM software, namely DIANA [TNO DIANA BV, 2014], considering rigid-infininitely resistant voussoirs and friction interface elements. In particular, a Coulomb friction interface has been adopted with cohesion, tensile strength and dilatancy set to zero. The friction angle was assumed 34° , as measures in experiments, whereas the mass density of the voussoirs was set equal to 450 kg/m^3 .

The normal and tangential stiffness assigned to the interfaces was of capital importance, playing the most important role. Since the peculiarity of the material adopted in the tests, which is ABS thermoplastic (with dry joints), there are no indications in literature for the stiffness parameters (see, among the others, Senthivel and Lourenço [2009]). In this regard a sensitivity analysis has been performed. In order to avoid large block interpenetration, values larger than $K_n = 0.1 \text{ N/mm}^3$ and $K_t = 0.04 \text{ N/mm}^3$ have been adopted.

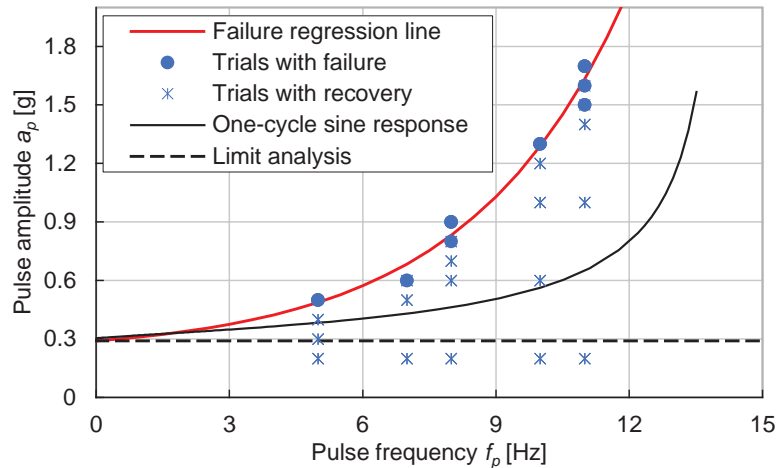


Figure 3-10. Results of the shaking table tests

Attention was paid also to the geometrical nonlinearities. The software [TNO DIANA BV, 2014] can use a Total Lagrange (TL) and an Updated Lagrange (UL) formulation, where the choice basically regards the reference configuration used to determine the stress and strain measures. In the TL formulation the initial configuration is used as reference, whereas in the UL formulations, the reference configuration corresponds to the one of the previous step.

Moreover, on the one hand, a TL description is useful if rotations and displacements are large and strains are small (e.g. large strain hyperelastic rubber-like material). On the other hand, an UL description can be used advantageously in case of large plastic deformations. Accordingly, since the deformation of the arch model is totally concentrated in the interface elements, exhibiting thus large displacements and strains, the UL has been selected. However, in order to evaluate possible inaccuracies, the analyses have been performed with and without nonlinear geometrical effects.

The mesh was generated considering plane triangle elements (T18IF) for the interfaces and tetrahedral elements (TE12L) for the voussoirs. The former (Figure 3-11a) is a triangular element between the two side planes of the voussoirs and, in order to better evaluate the nonlinear behaviour at the interface, three integration points were assigned to each element. The latter is a four-node, three-side isoparametric solid pyramid element. It is reported in Figure 3-11b together with the polynomials for the translations u_{xyz} (yielding a constant strain and stress distribution over the volume).

3.5.2 Static nonlinear analysis

Firstly, it must be noted that slight variations in block size, rounded corners and the imperfection of the manually assembled geometry, may lead to inaccurate match of the voussoir lateral surfaces or an imperfect semi-circular shape, ending up with an overall reduction of capacity. In order to

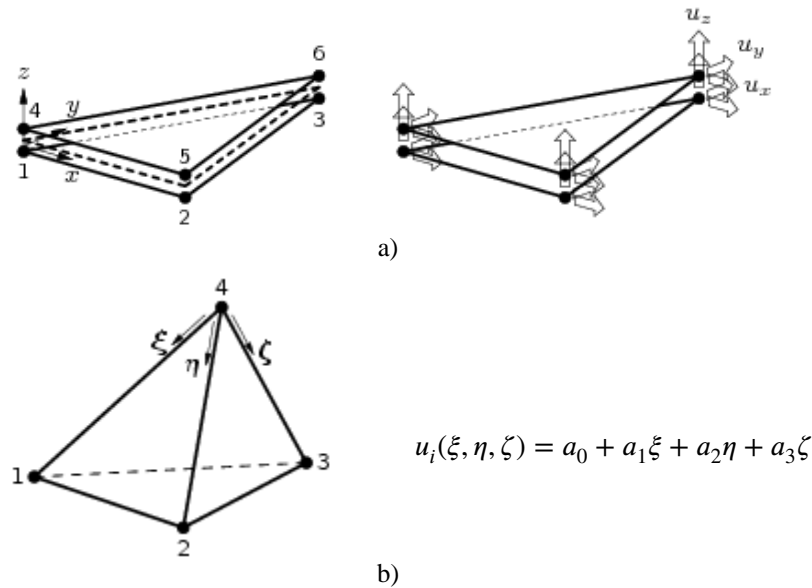


Figure 3-11. Elements adopted for the nonlinear DIANA FEM analysis: a) T18IF triangular interface element (topology and displacements); b) TE12L tetrahedral elements, geometry and shape function

account for these physical imperfections, DeJong et al. [2008] suggested to adopt a numerical model with reduced thickness of 20%, in comparison to actual tests. In the present study, considering the higher accuracy provided by the 3D printer, an overall reduction of the thickness of 10% was implemented (maintaining the same centreline radius).

Since the voussoirs are assumed rigid-infinitely resistant (whose behaviour is theoretically not affected by the FE discretization), in order to understand the effect of the mesh size in the description of the nonlinear behaviour of the interface elements, a mesh sensitivity analysis was performed. This is aimed at achieving an adequate balance between accuracy and computational effort, a crucial aspect for the following time history analysis and for the extension of the present model to the three-dimensional analysis of the groin vault, discussed in Chapter 4. The results of this study are reported in Table 3-2, where the comparison is limited to the multiplier of the horizontal load, as the mesh size does not significantly affect the failure mechanism.

As it is clearly noticed, the more refined is the mesh, the longer is the analysis, and the more accurate the results are. However, according to the goal of this study, the mesh with 32 elements, that is, at least eight elements along the thickness, was considered adequate for the subsequent analyses. This led only to 5% difference with respect to the most refined model with an impressive reduction of the running time.

Considering the horizontal displacement of the keystone as control point and a discretization of the interface by 32 elements, Figure 3-12 shows the capacity curve of the arch adopting three sets of interface stiffness, either with or without considering UL (dot and solid line, respectively). Neglecting UL, the curves approach asymptotically the result of the tilting test, showing, as

Interface elements	Load multiplier λ	λ percentage increment	Running time ¹
8	0.247	-	1 min
32	0.284	13.0%	>4 min
128	0.296	4.0%	>14 min
512	0.299	1.0%	>105 min

Table 3-2. Mesh sensitivity analysis ($\lambda = 0.29$ from tilting test)

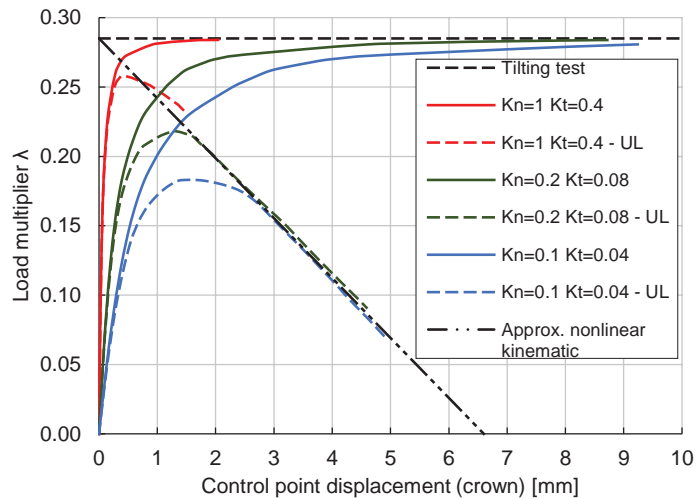


Figure 3-12. Arch capacity curves varying the interface stiffness

expected, a steeper initial branch for the stiffer interface. In case UL is accounted, instead, the results change dramatically. Although the early stage behaviour is the same in both cases (with or without UL), the main difference is that the capacity never reaches the one provided by the tilting analysis, unless for large values of stiffness.

This behaviour can be ascribed to the normal stiffness of the interface. A small value inevitably leads to interpenetration of the voussoirs and the position of the hinge (supposed either at the intrados or at the extrados) to move inward, “reducing” the effective thickness (Figure 3-13). This means the arch is basically thinner and with a lower capacity. In reverse, a hypothetical infinite value would cause the hinges to locate on the edge line of the arch. In this regard, higher values of stiffness provide more suitable results.

Moreover, the softening branch of the curves clearly tends to a unique displacement (estimated equal to 6.6 mm) which can be regarded as the ultimate displacement of the arch. The envelope of all the curves can be approximated with a straight line. This shape parallels the nonlinear kinematic capacity curve of a rigid block undergoing horizontal forces and rocking in the base.

¹ Processor: Intel Core i7-3820 (3.60 GHz)
RAM: 16 GB
Disk: SSD disk

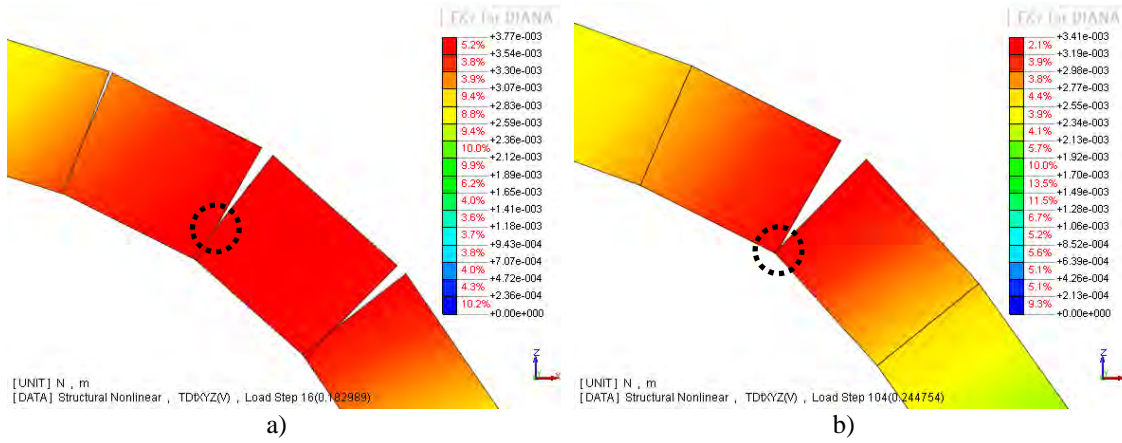


Figure 3-13. Hinge location for: a) $K_n = K_t = 0.1 \text{ N/mm}^3$, and b) $K_n = K_t = 10 \text{ N/mm}^3$

Table 3-3 reports a comparison of the results in terms of load multiplier and hinge location. In particular, the estimation provided by Clemente [1998] is also shown considering a thickness/centreline ratio equal to $36/385 = 0.094$. The location of the hinges is denoted according to the figure in the same table, whereas Figure 3-14 reports the frame of the collapsing arch during the tilting test and the analogous deformed shape of the static nonlinear analysis. As it is possible to notice, the analyses significantly approached the experimental results in terms of load multiplier and hinge locations. Small changes in the hinge locations will not affect the load multiplier in a significant extent.

	Load multiplier λ	Hinge location [°]			
		β_A	β_B	β_C	β_D
Tilting test	0.29	7	60	107	140
Clemente [1998]	0.30	0	52	106	140
DIANA	0.28	0	53	107	140

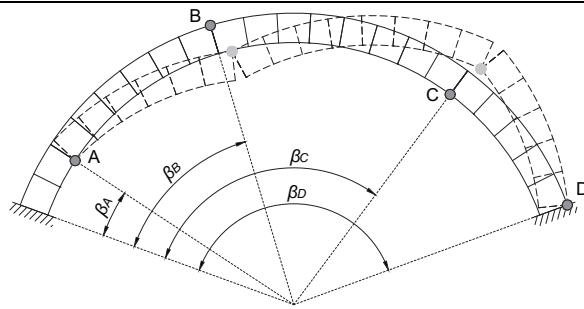


Table 3-3. Tilting test: comparison between experimental, literature [Clemente, 1998], and FE results

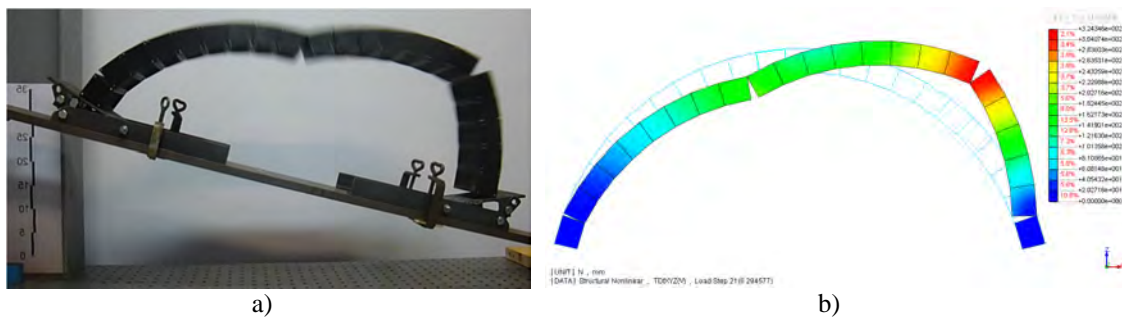


Figure 3-14. Tilting test failure mechanism: a) frame recorded during the experiment and b) deformed shape of the numerical analysis (the lowest voussoirs are additional and simulate the fixed supports)

3.5.3 Time history analysis

According to the FE model described in §3.5.1, after the quasi-static application of the self-weight, the accelerogram recorded on the slip table during the tests was used as input for the analysis. A minor filtering was necessary in order to correct the possible baseline drift and to remove the higher frequencies content (low-pass filter). Moreover, UL was used for non-linear geometrical effects and requested a very small time step for the analysis to converge. In the present case, the step size, i.e. time interval, was explicitly specified equal to 2×10^{-5} s. The equilibrium iteration method used for the steps was the Quasi-Newton (Secant) method based on BFGS algorithm. The energy norm convergence criteria for the equilibrium iteration process was adopted with a tolerance of 1×10^{-3} .

Regarding the time integration scheme, the Hilber-Hughes-Taylor method (HHT, also called α -method) was adopted. For $\alpha = 0$ the method reduces to the Newmark method. For $-1/3 \leq \alpha \leq 0$, the scheme is second order accurate and unconditionally stable in the linear range. Furthermore, with the HHT method it is possible to introduce numerical dissipation without degrading the order of accuracy. In particular, decreasing α means increasing the numerical damping, which mostly affects the high-frequency modes. For the present study α was set equal to -0.1 .

Regarding the damping ratio, although several authors have proposed more or less sophisticated approach, sometimes simply fitting the numerical results to the experimental outcomes [Liberatore et al., 1997; Peña et al., 2006], this aspect still requests more research.

One difficulty is posed by the mathematical approximation of damping. The most used approach is the viscous damping according to the Rayleigh formulation, but two main drawbacks must be highlighted. Firstly, although for structures regarded as a continuum the damping ratio is usually set equal to 5%, for rigid block dynamics there is no recommendation. In case, for instance, of DEM analysis, the value adopted in literature is at least one order of magnitude smaller [Peña et al., 2006; De Lorenzis et al., 2007]². Secondly, since rigid block structures hardly have natural frequencies (which depend on the displacement), it is not clear how to calculate the damping constants for the Rayleigh formulation.

² Dealing with dry-joint arch, De Lorenzis et al. [2007] set the minimum damping ratio equal to 0.001% at 0.05 Hz resulting thus in values less than 0.5% in the frequency range from $5 \cdot 10^{-5}$ to 50 Hz. On the other hand, regarding DEM analyses of rigid blocks, Peña et al. [2006] proposed a simplified formulation to take into account the nature of the impact as a source of energy dissipation. Basically, since viscous damping is proportional to mass and stiffness, in order to set null the damping ratio when there is no contact, the damping constant related to the mass was set zero. In this way, damping depends only on the stiffness, which is null as the interface has no tensile strength. However, also in this case, the adopted damping ratio was set around 10^{-3} at the frequency of 5 Hz.

Another possible schematization is represented by the structural damping, which is independent of the frequency and proportional to the displacement. It is usually suggested for models involving materials that exhibit frictional behaviour or where local frictional effects are present throughout the model, such as dry rubbing of joints in a multi-link structure [TNO DIANA BV, 2014]. Since the sliding occurrence was not evident in the tests and the present study is based on the stability of the arch (with large displacements), this form of damping can result in too conservative effects.

Moreover, assuming the impacts as the main source of energy dissipation, according to §3.4.3 and Figure 3-9, only the hinges A and B were involved in small impacts (defined as “migration”) and a clear flipping movement was never recorded. Considering also the very small values proposed in literature for DEM analysis of dry-joint arches, in the present study, a null value of damping ratio was implemented.

With the aim of validating the model against the experimental results, as for the case of the static nonlinear analysis, a sensitivity study regarding the interface stiffness was performed. This evaluation was essentially based on the comparison of the total displacement (in the plane of the arch) of two control points. In particular, the extrados corners of the sixth voussoir from both springs were selected (Figure 3-15). The position of Control point #2 is justified by the location of hinge C of Figure 3-9, whereas Control point #1 is simply the symmetric one with respect the central axis.

As far as the interface stiffness is concerned, K_n was assumed equal to 0.01, 0.1, 1, 10, 100 N/mm³, whereas K_t was assumed equal to 0.1, 0.4 and 1 times K_n , resulting thus in 15 different sets. Whereas on the one hand the ratio 0.4 is the same proposed by Senthivel and Lourenço [2009], on the other hand, the ratios 0.1 and 1 were considered as limit values. Normal stiffness out of the proposed range were also adopted, leading to severe problems of convergence. This aspect is stressed also in literature. As an example, although for DEM analysis the recommended values are much larger (order of magnitude of 10¹² N/mm³), De Lorenzis et al. [2007] stated that lower stiffness values led to contact overlap errors, whereas larger values led to excessively small time steps for the solution to remain stable.

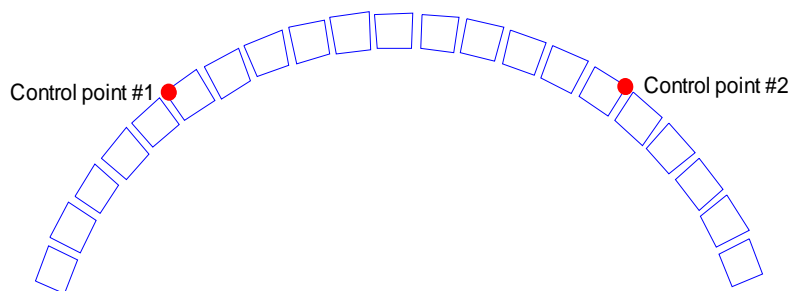


Figure 3-15. Sketch of the arch voussoirs by means of marker location and position of the control points

Regarding the sensitivity analysis, for a given normal stiffness, the influence of the tangential stiffness was slightly notable. However, in case $K_t / K_n = 0.1$, sliding between blocks was evident, although not expected from both literature perspective [De Lorenzis et al., 2007; D’Ayala and Tomasoni, 2011] and experimental evidences. Moreover, the best results were obtained considering $K_n = 0.1, 1\text{N/mm}^3$.

For the sake of brevity, only the results of the analyses regarding $K_n = K_t = 0.1, 1\text{ N/mm}^3$ and the signals 10 Hz - 1.3 g and 5 Hz - 0.6 g are reported in Figure 3-16 and Figure 3-17. Note that the time history of the displacements of the control points is shown up to the end of the signals (0.3 and 0.6 s, respectively).

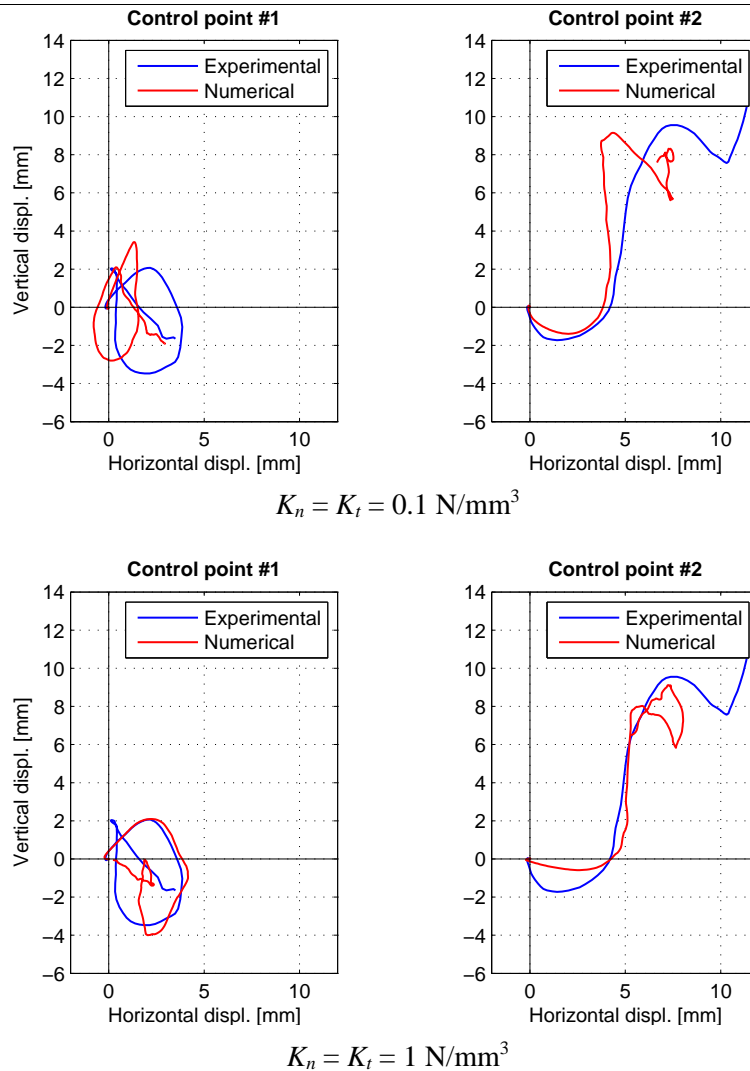


Figure 3-16. Displacement of the two control points: numerical and experimental results (10 Hz - 1.3 g signal)

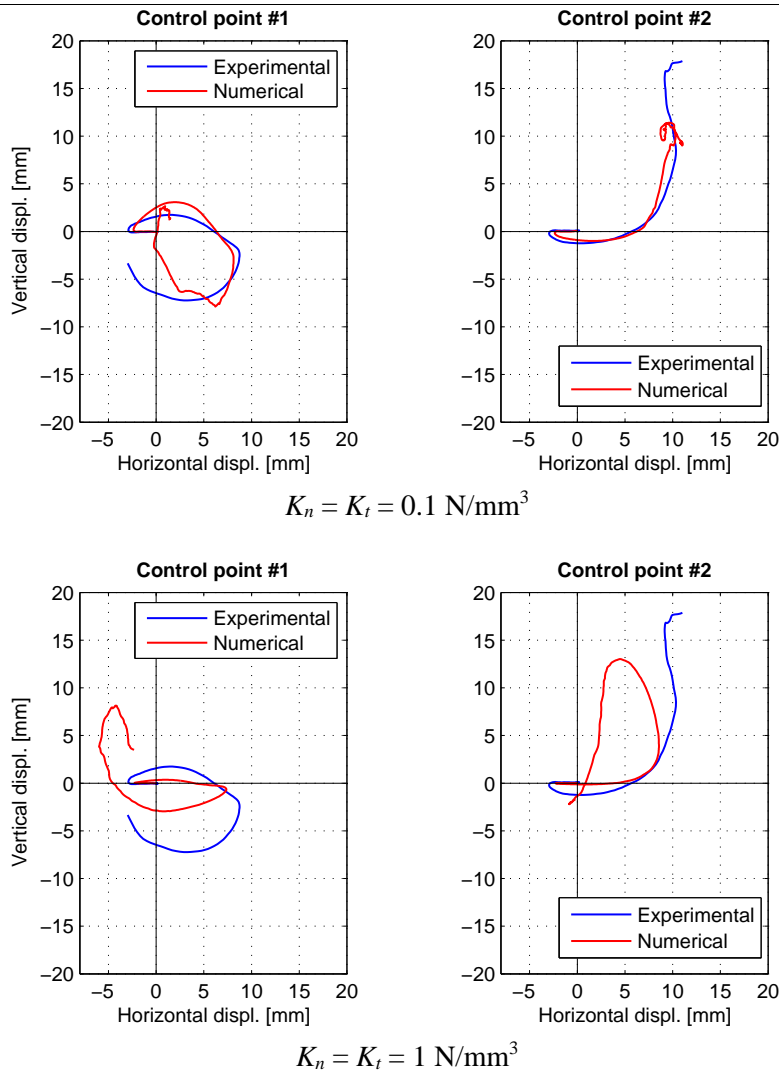


Figure 3-17. Displacement of the two control points: numerical and experimental results (5 Hz - 0.6 g signal)

Finally, the results of the numerical analyses, considering only the interface stiffness equal to $K_n = K_t = 0.1 \text{ N/mm}^3$ are reported in Figure 3-18 (which parallels Figure 3-10). The signals that brought the physical arch to collapse were scaled up to achieve a failure configuration in the numerical analyses. The results matched well the experimental outcomes in the low frequency range, overestimating the capacity for higher frequency values. The collapse mechanism were also well predicted by the numerical model. As an example, the deformed shape following the 1.3 g - 10 Hz signal is reported in Figure 3-19 (the lower voussoirs are fully constrained to account for the supports) together with the recorded frame of the tests.

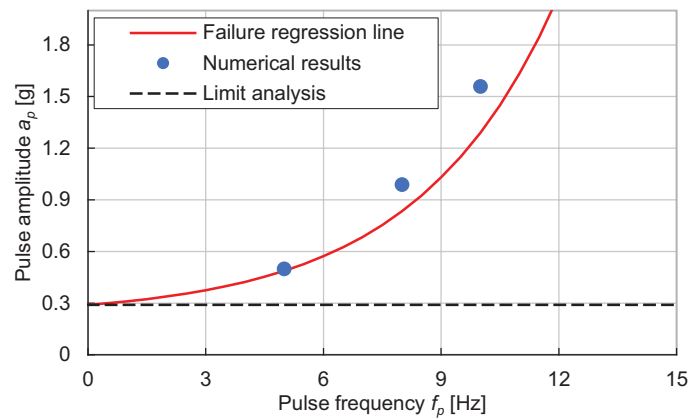


Figure 3-18. Results of the numerical analyses with $K_n = K_t = 0.1 \text{ N/mm}^3$

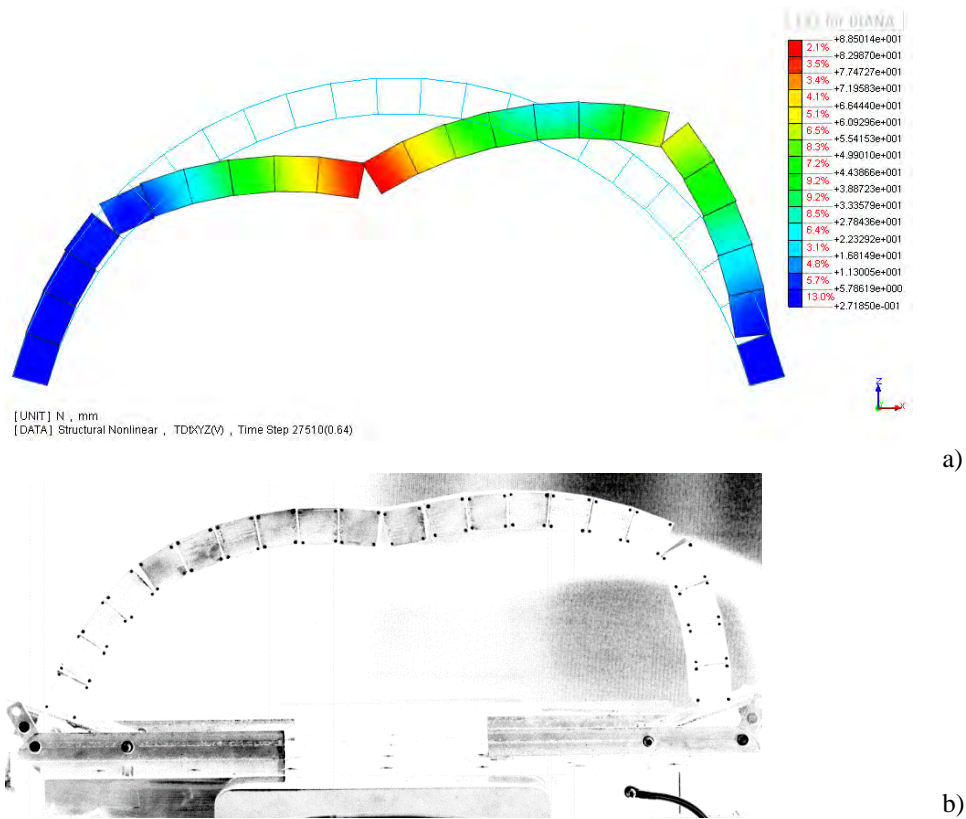


Figure 3-19. 1.3 g - 10 Hz signal ultimate displacement: comparison between a) FEM analysis (representation scale 1:1) and b) recorded frame of the test

3.6 Scale effect

Usually similitude laws are considered in order to account for scale effects between a real structure (model) and the specimen (usually referred to as mock-up), even if fracture mechanics issues are not included. Since the goal of the present study was not to describe the real behaviour

of a specific structure but to analyse the effects of a suite of given impulses on an arch shaped structure, the scale effect became a non-issue. However, for the sake of completeness, a few comments follow.

In case of linearly elastic behaviour (i.e. neglecting the nonlinear effects due to plasticity, cracking, etc.) a possible similitude law is described in Table 3-4. Basically, since in ordinary mechanics problems, length, time and mass represent the fundamental dimensions, the adopted similarity law should involve relations between these quantities. In particular, once the geometrical factor is defined as π , the impracticality of scaling the gravity acceleration requires a scale factor equal to $\pi^{0.5}$ for the time. On the other hand, the mass is scaled according to the material adopted in the experimental activities. For instance, adopting in the test the same material of the model leads to the same mass density ($\delta=1$) but a lower stress level (π). On the other hand, in order to get the same stresses of the model (that is, $\delta\pi=1$), the specimen must have a higher mass density ($\delta=\pi^{-1}$).

In case of rigid blocks, since the failure is a matter of stability, which does not concern the specific mass nor the strength of the material, the dimensional analysis can neglect the factor δ , focusing only on the time and length quantities [Liberatore and Spera, 2001; DeJong et al., 2008]. Regarding the arch analysed in the present study, the similitude law is thus limited only to the frequency. Basically, considering Figure 3-10, the performance of a similar arch (equal thickness/radius ratio and angle of embrace) is represented by the same curve scaled along the abscissa (frequency). As a matter of fact, discarding the possible damage due to higher energy impacts, larger arches make the curve move toward the origin, i.e. for an impulse of a given frequency and same shape arches, the capacity increases as the average radius increases [De Lorenzis et al., 2007; DeJong et al., 2008].

Quantity	Dimension	Factor
Length	L	π
Area	L^2	π^2
Volume	L^3	π^3
Specific mass	ML^{-3}	δ
Mass	M	$\delta\pi^3$
Displacement	L	π
Velocity	Lt^{-1}	$\pi^{0.5}$
Acceleration	Lt^{-2}	1
Weight/Force	MLt^{-2}	$\delta\pi^3$
Moment	ML^2t^{-2}	$\delta\pi^4$
Stress/strength	$ML^{-1}t^{-2}$	$\delta\pi$
Strain	-	1
Time	t	$\pi^{0.5}$
Frequency	t^{-1}	$\pi^{-0.5}$

Table 3-4. Scale factors for similitude law (linearly elastic behaviour), where L, t and M stand for length, time and mass, respectively

3.7 Summary

The present chapter had a twofold goal: giving insight on the seismic behaviour of a scaled arch and validating the in-plane FEM model, subsequently extended in the next chapter for the three-dimensional analysis of a groin vault.

For what concerns the first goal, the present study focused on the behaviour of a dry-joint scaled arch under constant horizontal acceleration and a windowed sine pulse, tilting and shaking table tests, respectively. The former provided results in good agreement with literature, whereas the latter gave valuable information to validate the FEM model. Great attention has been paid to the nonlinear properties of the friction interface elements, eventually proposing suitable values for both static nonlinear and time history analyses. However, given the critical role of the interface nonlinear properties, still more research is needed in case different scales, materials, or stress level are concerned.

Regarding the shaking table tests, the comparison with the results available in literature for one-cycle sine pulse [De Lorenzis et al., 2007; DeJong et al., 2008] highlighted two main outcomes. Firstly, considering the same amplitude and frequency, the windowed sine pulse (adopted in the present study) resulted more conservative than the one-cycle sine pulse. This is due to the out-of-phase contribution of the former, which led to a more chaotic response. By extension, this behaviour may be regarded as more representative of the real performance of an arch during an earthquake. More research is still requested on this topic, where the windowed signals can be implemented to consider main pulses with initial conditions different from the rest position.

Secondly, the curve that better fits the failure cases is again of exponential type. Further experimental or numerical activities may extend this result to arches of different geometry and validate this trend for other kinds of pulse. This may represent an efficient strategy for the seismic assessment of masonry arches, in case a primary base acceleration impulse can be extracted from an earthquake motion.

Moreover, the proposed simplified schematization about the hinge location could represent a valuable basis for an analytical approach. In this regard, the available literature deals only with simple shape pulses with a symmetric behaviour based on *a priori* defined mechanism. A more sophisticated model able to localize the hinges according to an energetic criterion is desirable.

Finally, the feature tracking technique adopted to monitor the shaking table tests, although developed for fluid mechanical experiments, provided excellent results also in the structural engineer field. A systematic analysis of the acquired data may constitute a valuable tool for micro-impact detection and temporary hinge formation.

References

- Clemente, P. (1998). Introduction to dynamics of stone arches. *Earthquake Engineering & Structural Dynamics*, 27(5), 513–522.
- D’Ayala, D., and Tomasoni, E. (2011). Three-dimensional analysis of masonry vaults using limit state analysis with finite friction. *International Journal of Architectural Heritage*, 5(2), 140–171.
- De Lorenzis, L., DeJong, M., and Ochsendorf, J. (2007). Failure of masonry arches under impulse base motion. *Earthquake Engineering & Structural Dynamics*, 36(14), 2119–2136.
- DeJong, M. (2009). *Seismic assessment strategies for masonry structures*. PhD dissertation, Massachusetts Institute of Technology.
- DeJong, M., De Lorenzis, L., Adams, S., and Ochsendorf, J. A. (2008). Rocking Stability of Masonry Arches in Seismic Regions. *Earthquake Spectra*, 24(4), 847–865.
- DeJong, M., and Dimitrakopoulos, E. G. (2014). Dynamically equivalent rocking structures. *Earthquake Engineering & Structural Dynamics*, 43(10), 1543–1563.
- DeJong, M., and Ochsendorf, J. (2006). Analysis of vaulted masonry structures subjected to horizontal ground motion. In P. B. Lourenco, P. Roca, C. Modena, & S. Agrawal (Eds.), *5th International Conference on Structural Analysis of Historical Constructions* (pp. 973–980). New Delhi, India.
- Dimitri, R., De Lorenzis, L., and Zavarise, G. (2011). Numerical study on the dynamic behavior of masonry columns and arches on buttresses with the discrete element method. *Engineering Structures*, 33(12), 3172–3188.
- DONGLING Technology. (2015). <http://www.donglingtest.com>. (last visit 09/15/2015).
- Housner, G. W. (1963). The behavior of inverted pendulum structures during earthquakes. *Bulletin of the Seismological Society of America*, 53(2), 403–417.
- Liberatore, D., Larotonda, A., and Dolce, M. (1997). Analisi dinamica di archi in conci lapidei soggetti ad azioni sismiche. In *2nd Seminario Nazionale “Il patrimonio culturale e la questione sismica”* (pp. 551–571). Rome.
- Liberatore, D., and Spera, G. (2001). Response of slender blocks subjected to seismic motion of the base: Experimental results and numerical analyses. In T. G. Hughes & G. N. Pande (Eds.), *5th Int. Symposium on Computer Methods in Structural Masonry* (pp. 117–124). Rome.
- MakerBot. (2015). <http://www.makerbot.com>. (last visit 09/15/2015).
- Moroni, M., and Cenedese, A. (2005). Comparison among feature tracking and more consolidated velocimetry image analysis techniques in a fully developed turbulent channel flow. *Measurement Science and Technology*, 16(11), 2307–2322.
- Moroni, M., and Cenedese, A. (2015). Laboratory Simulations of Local Winds in the Atmospheric Boundary Layer via Image Analysis. *Advances in Meteorology*, 2015, 1–34.
- Oppenheim, I. J. (1992). The masonry arch as a four-link mechanism under base motion. *Earthquake Engineering & Structural Dynamics*, 21(11), 1005–1017.
- Peña, F., Lourenço, P. B., and Lemos, J. V. (2006). Modeling the dynamic behaviour of masonry walls as rigid blocks. ECCOMAS.

- Senthivel, R., and Lourenço, P. B. (2009). Finite element modelling of deformation characteristics of historical stone masonry shear walls. *Engineering Structures*, 31(9), 1930–1943.
- Shindler, L., Moroni, M., and Cenedese, A. (2012). Using optical flow equation for particle detection and velocity prediction in particle tracking. *Applied Mathematics and Computation*, 218(17), 8684–8694.
- TNO DIANA BV. (2014). *DIANA finite element analysis; User's manual release 9.6*. Delft: TNO DIANA BV.
- Zhang, J., and Makris, N. (2001). Rocking response of free-standing blocks under cycloidal pulses. *Journal of Engineering Mechanics*, 127(5), 473–483.

Chapter 4.

Seismic analysis of masonry groin vaults

4.1 Abstract

Considering the outcomes of the previous chapter, the numerical model was extended to the analysis of a groin vault. The main goal was to validate the three-dimensional model for further developments and future works. In this regard, and in according with the available literature, the experimental tests performed by Rossi and Co-workers [2014, 2015; 2015] were considered. With the aim of achieving a simplified approach for the global analysis of historic masonry buildings, these authors carried out an intense experimental campaign on 1:5 scaled groin vault. The experimental setup, the specimen properties and the main outcomes are briefly reviewed in the first part of this chapter.

In the present study, attention has been initially given to the block arrangement, seeking an appreciable accommodation between the complexity of the real arrangement (as follows from ancient construction manuals) and the computational effort. Then, paralleling the previous chapter, the influence of interface normal and tangential stiffness is discussed. Comparisons between numerical and experimental results are presented in terms of ultimate strength capacity and failure mechanisms. Regarding the mechanism labelled as in-plane shear, the comparison concerned also the experimental capacity curve.

4.2 General aspects on block interlocking

According to the available literature (e.g. [Romano and Grande, 2008; Tomasoni, 2008]), the block arrangement plays an important role in the capacity of masonry vaulted structures, above

all in case of concentrated or horizontal loads. Although this aspect was not necessary for the in-plane analysis of the arch (described in Chapter 3), now some comments are needed.

In general, in micro- and simplified micro-modelling, interlocking between blocks is of fundamental importance in stress transmission through masonry units. In addition, masonry bond (or the arrangement of the units) yields to a macroscopic masonry tensile strength: thanks to the frictional behaviour of the interface, the compressive stress orthogonal to the joints and the dilatancy upon shearing produce tensile strength in the direction parallel to the joints, in case of a stepped failure mode. In reverse, the crack development is strongly influenced by the position of the joint, often representing the weakest part of the elements.

In case compound vaults are concerned (e.g. cross and cloister vaults), rather than for the webs, the influence of interlocking is crucial along the groins, representing the only connection between the two shells. In this regard, considering the structural behaviour of cloister vaults under gravitational loads, Tomasoni [2008] stated that the block arrangement parallel to the springings may facilitate the occurrence of the typical diagonal cracks due to the alignment of the mortar joints along the groins.

However, in order to effectively guarantee a good interlocking between bricks or stone blocks at the groins (Figure 4-1a), in the antiquity, accurate expertise was requested in the field of stereotomy [Becchi and Foce, 2002; Wendland, 2007; Trevisan, 2011]. On the contrary, in case of rib vault (Figure 4-1b), the bricks at the web intersections, being usually supported by the rib, could be placed close to each other without any interlocking.

Regarding the historical construction manuals, three arrangement were mainly suggested and are reported in Figure 4-2. According to the generatrix of the web, the arrangement can be orthogonal, parallel and oblique (herringbone bond). The last pattern supposes courses oriented perpendicularly with respect to the plane of the groins and connected in the middle of the webs [Levi, 1932; Protti, 1935]. Finally, in what concerns the vault thickness, and according to the load to be carried, the block could be laid according to their smaller or larger size (as “stretchers” or “facers”, respectively) or in more than one layer.

More recently, Giovannetti [2000] presented a detailed study on this topic, describing the brick disposition and the necessary cut for the elements shaping the groin. Two cases are examined, namely, arrangement along the generatrix of the webs and herringbone bond, reported in Figure 4-3 and Figure 4-4, respectively. As it possible to observe, the former, which can be regarded as the most traditional and frequent, necessarily implies a more experience workmanship for the springings and the groin treatment.

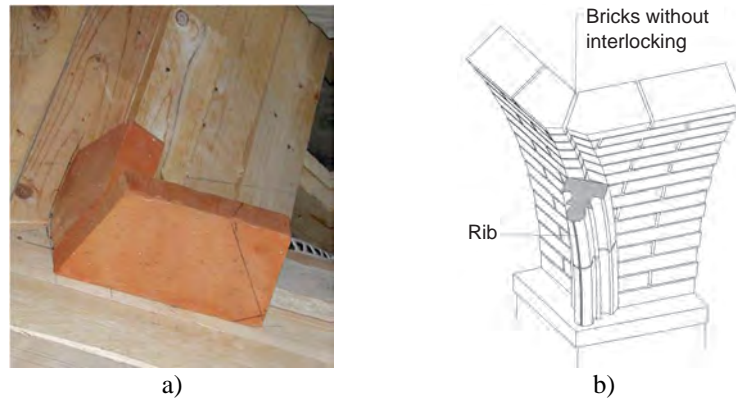


Figure 4-1. Brick arrangement: a) contemporary bricks placed at the intersection by means of timber scaffolding; b) usual intersection of webs in a rib vault [Cangi, 2012 after Rossi, 2015]

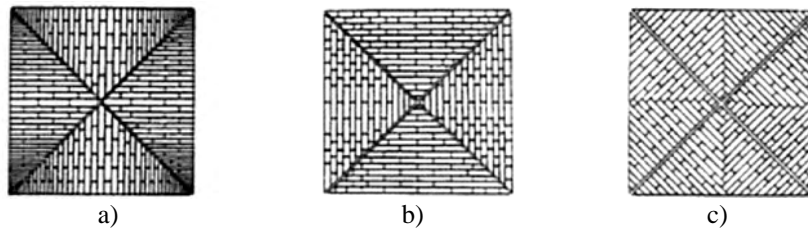


Figure 4-2. Different blocks disposition on a cross vault with respect the web generatrix: a) parallel; b) orthogonal; c) oblique (herringbone bond)

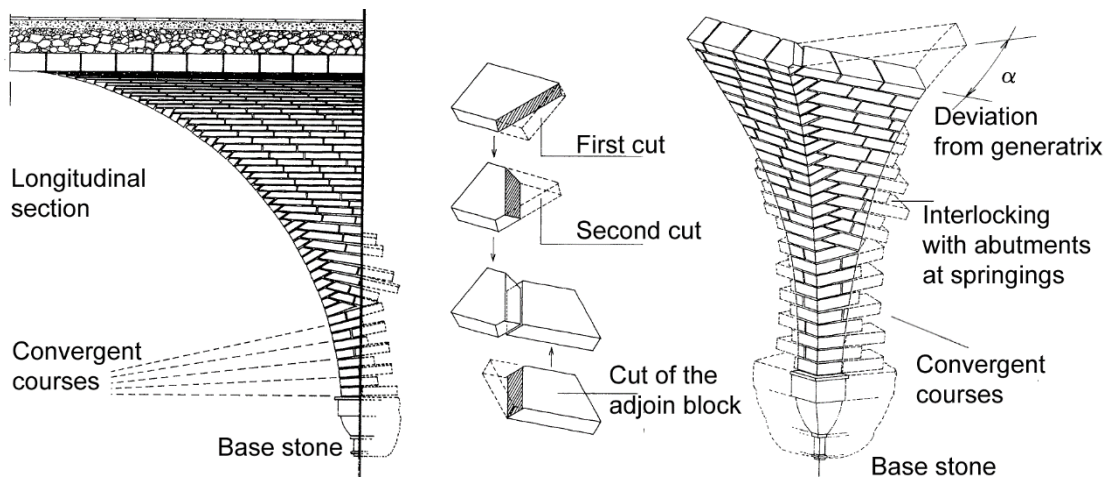


Figure 4-3. Groin vault: block arrangement parallel to the generatrix [Giovanetti (ed. by), 2000]

With respect to experimental tests, the strict respect of the traditional rules may request a significant effort and a simpler approach is usually employed. In the literature, as described in Chapter 2, only three experiments have been performed on groin vaults. For the sake of clearness,

the details of the blocks arrangements of the three models [Shapiro, 2012; Van Mele et al., 2012; Rossi et al., 2014] are reported in Figure 4-5. As it clearly visible, the two first research groups built the groin with unrealistic blocks (V-shaped), completely neglecting the real pattern and providing the model with higher stiffness and strength in the groins (not on the safe side). On the other hand, Rossi proposed a simplified and more accurate approach based on a 1:5 scaled modern brick ($6 \times 12 \times 24 \text{ cm}^3$). The geometrical construction is detailed next, since it is similar to the one adopted in the present study.

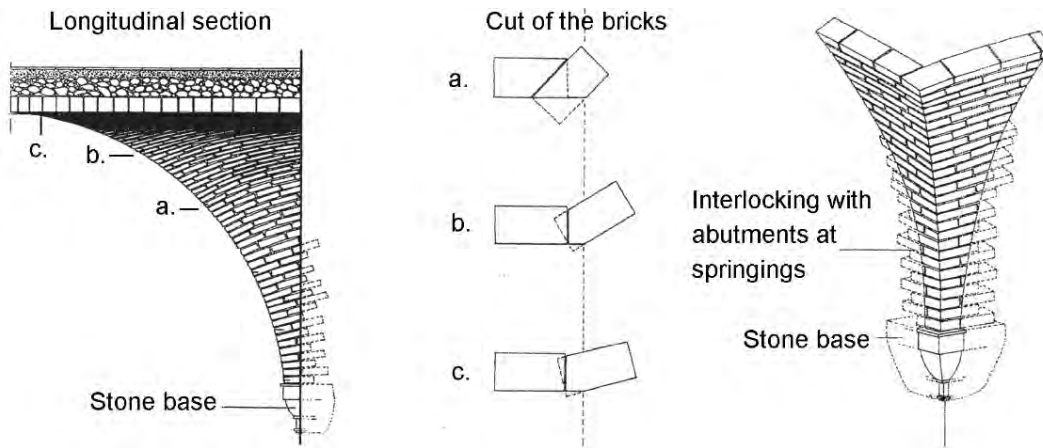


Figure 4-4. Groin vault: herringbone bond arrangement [Giovanetti (ed. by), 2000]

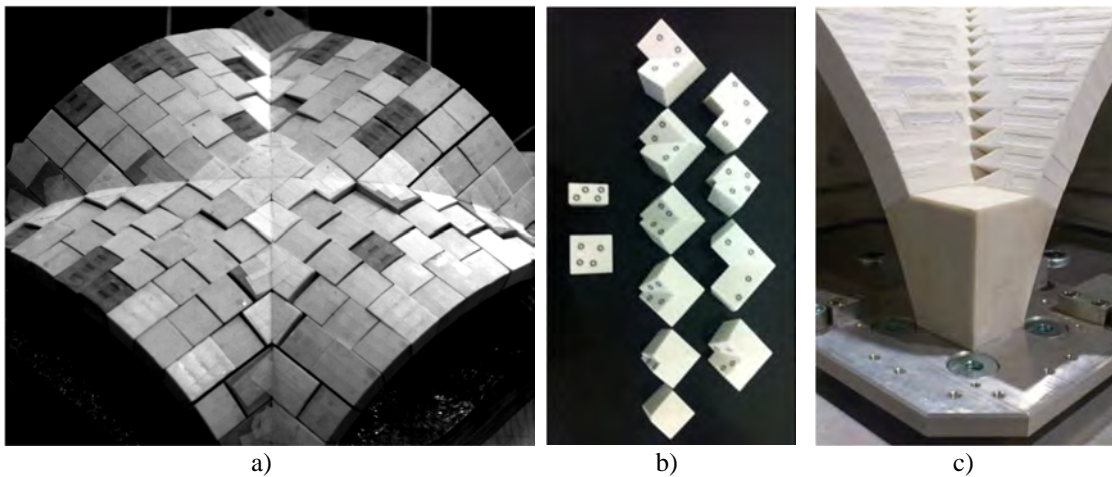


Figure 4-5. Experimental model for cross vault testing: a) [Shapiro, 2012]; b) [Van Mele et al., 2012]; c) [Rossi, 2015]

4.3 Brief description of experimental tests and results

4.3.1 Layout

The model adopted in the present study is the one experimentally tested by Rossi et al. [2014, 2015; 2015]. The experimental tests were performed on a 1:5 scaled groin vault made by dry-joint 3D printed plastic blocks. The geometry of the vault was generated on a square bay by the intersection of two semi-circular barrel vaults with an inner radius of 0.326m. All the geometrical quantities are reported in Figure 4-6. In particular, considering the four fully constrained supports on which the model rests (black in Figure 4-6a), the portion of the vault effectively involved in the tests had a net span and rise of 0.57 m and 0.167 m respectively. However, for the sake of clearness, in the present chapter, the quantities reported in the original papers are referred to.

The blocks were made by a 3D prototyping technique called SLS (Selective Laser Sintering). Based on plastic powder sintering, it represents an efficient method to generate small-scale models with high geometrical accuracy (0.1 mm starting from a 3D digital model). The mean friction coefficient $\mu = 0.56$ of the blocks was determined by testing 12 couples of blocks. The elastic modulus $E = 120$ MPa was measured by testing three assemblages of six blocks each under uniaxial compression. The density of the plastic material was $\rho = 550$ kg/m³. Since this quite low value would have compromised the model stability under accidental actions, the weight of the model was increased by inserting a steel plate within each block. This technical measure allowed achieving an equivalent density of about 2700 kg/m³. The mass of the whole structure was about 35.6 kg.

As far as the experimental layout is concerned, the authors tested the groin vault under two different conditions, namely: (a) two displacement settings, representing damage mechanisms recurrently observed during post-earthquake surveys, i.e. in-plane horizontal shear distortion (A) and longitudinal opening/closing of the abutments (B) of Figure 4-7; (b) horizontal inertial forces proportional to the mass of the structure (Figure 4-8).

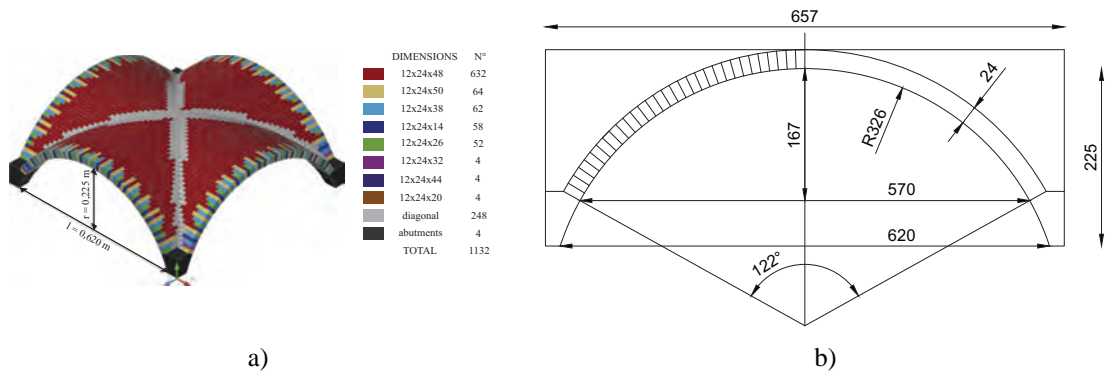


Figure 4-6. Overall dimension of the model: a) [Rossi et al., 2015]; b) front view (measures in mm)

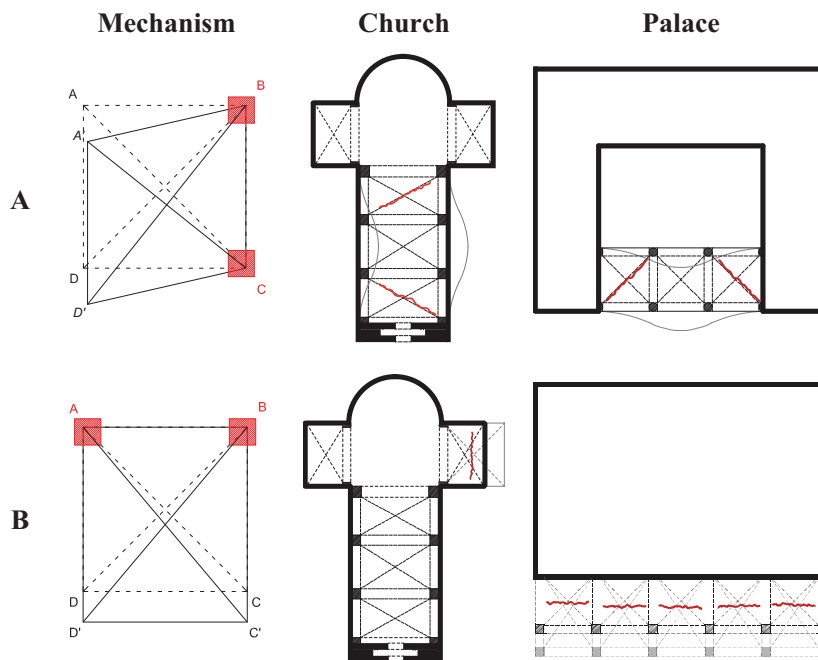


Figure 4-7. Displacement settings considered in the experimental campaign

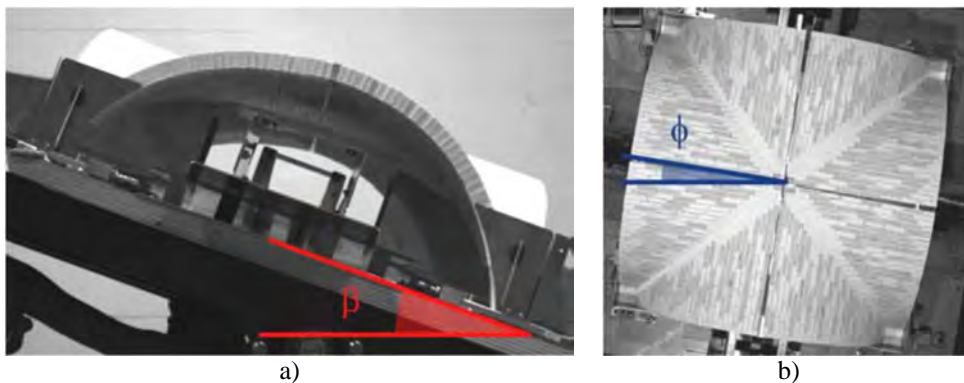


Figure 4-8. Tilting tests: a) tilting angle β and b) rotation ϕ around its orthogonal axis

Regarding the first group, mechanism A, is recurrent in churches characterized by a large difference in stiffness between the two sides of the vault, e.g. the internal colonnade and lateral wall, nave and façade (and/or transept), and in palaces with laterally constrained porches or loggias. Mechanism B may occur in churches and palaces with porticos on the façade; in this case, the difference in stiffness between the building and the external pillars or columns may induce an inward/outward rotation of the latter, causing a transversal opening/closing mechanism of the related vaults.

The second group, instead, was aimed at evaluating the ultimate load multiplier of the horizontal loads (proportional to the mass), through tilting tests. However, since the seismic actions can hit the structure from any direction, the vault response was investigated considering six different

seismic directions, from $\phi=0^\circ$ (orthogonal to the web profile) to $\phi=45^\circ$ (along the diagonal axis), as depicted in Figure 4-8.

In the following, only the mechanism A of the first group (labelled hereinafter as in-plane shear) and the tilting tests are described and addressed by the numerical analyses. In both cases, the experiments were performed in a static way through the device reported in Figure 4-9. The device consisted in a special frame made by four steel squared plates, linked between each other by means of couples of aluminium bars hinged at both ends with uni-ball joints. The abutments of the vault were rigidly fixed on top of the plates, which were able to move freely on a flat aluminium surface thanks to four spherical wheels. However, thanks to the couples of linking bars, the distance between them cannot vary and their rotations along the vertical axis were inhibited. In Figure 4-9 only the case of in-plane shear action is reported, whereas the tilting tests were performed thanks to an inclinable plane, fixing all the supports.

4.3.2 Main results

Four monotonic tests have been performed on the model to check the in-plane shear mechanism. Looking at the observed deformation at failure, the authors individuated a typical four hinge asymmetric arch mechanism, where the hinge location is inverted (extrados-intrados) for opposite webs (Figure 4-10a), together with the typical diagonal shear crack. The results in terms of force/displacement curves are reported in Figure 4-10b where the value of maximum force ($F_{s,A}$) varies approximately from 13 ÷ 17% of the total weight, while the shear distortion is in the range 3.8 ÷ 4.8% of the span. Moreover, it can be observed that the system has a rather ductile response. In particular, the maximum force was attained at about 3% of the displacement over span ratio, a little more than half of its collapse value. The vault underwent no evident damage until the achievement of maximum strength.

Regarding the tilting tests, Figure 4-11 shows the values of the ultimate angle of tilting according to the direction of the seismic action. The value of the collapse angle is in the range $18^\circ \div 19.2^\circ$ (i.e. horizontal load multiplier λ in the range 0.32 ÷ 0.35). In reality, the smallest value achieved was $\phi = 18^\circ$ ($\lambda = 0.30$) but, according to the authors, this was probably due to an improper assembling of the model, and should not be considered. In general, it can be seen that the results are almost constant.

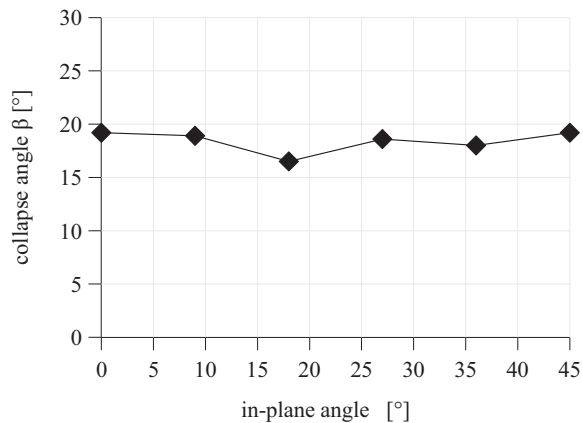


Figure 4-11. Tilting angle of the vault β on the basis of the seismic action direction ϕ

4.4 Numerical modelling

In order to replicate the results through numerical analyses based on rigid-infinitely resistant blocks and friction interface elements, great attention has been paid to the discretization of the vault. As already stressed, the physical model was accurate, providing: a) an appreciable block interlocking at the groin, b) no distortion of the block shape (only plane slicing from the original parallelepiped shape), and c) an overall block pattern simplification. However, from the computational point of view, meshing the real size block may represent a significant increment of DOFs, i.e. more effort and time of running.

In this regard, the numerical model was built considering a “macro-block” composed by two physical blocks, that is, to merging two blocks of $24 \times 12 \times 48 \text{ mm}^3$ each into a macro-block of $24 \times 24 \times 48 \text{ mm}^3$. Moreover, starting from stretcher bond (the simplest arrangement for masonry elements), the methodology adopted for the block pattern is sketched in Figure 4-12 and is synthesized into three main steps:

- slicing the bricks according to the plane of the orthogonal course of the adjoin web (Figure 4-12a);
- beginning one of the webs with an half brick for a geometrical shift of the courses (Figure 4-12a);
- finishing the intrados surface (Figure 4-12b).

As it is possible to notice, the main drawbacks of this approach are the gaps along the extrados of the groin, more pronounced close to the springings. However, comparing Figure 4-12b with Figure 4-5c, the gaps are better distributed, equal in size and shape, and with an overall half amount of blocks. Finally, it is worth noting that, in both experimental and numerical model, the

shape of the blocks was slightly trapezoidal to geometrically compensate for the lack of mortar joints.

Regarding the boundary conditions, the lowest elements were constrained and the rest of the vault simply leaned against them through friction interfaces. Furthermore, even though the authors did not describe this aspect in details, the vault corners were laterally constrained by steel plates (Figure 4-10a). In this regard, it was stated that the corners were not allowed to rotate around the vertical axis [Rossi et al., 2015], and minor sliding phenomena were visible near the confining plates [Rossi et al., 2014]. As a matter of fact, the plates constrained the springing part of the vault against outward displacement, with a consequent increase of stiffness and capacity. Although it is not clear how the plates worked (if they were in touch with the vault since the assembling, etc.) their effects are clearly visible in the pictures of the tests. For the sake of clearness, Figure 4-13 reports two main effects: a) the sliding of the upper unconstrained part of the vault, and b) crack interruption due to the confining plates. According to the numerical model described in the present thesis, the influence of the lateral constrains is discussed below in the text.

The FEM model was based on the assumptions discussed in Chapter 3, to which the reader is referred for further details. In particular each block was modelled by way of rigid-infinitely resistant elements with nonlinear friction interfaces. From the previous analyses, the stiffness values in the range $0.1 \div 1$ MPa were the most suitable for the analyses, together with the discretization of the thickness using 4 elements.

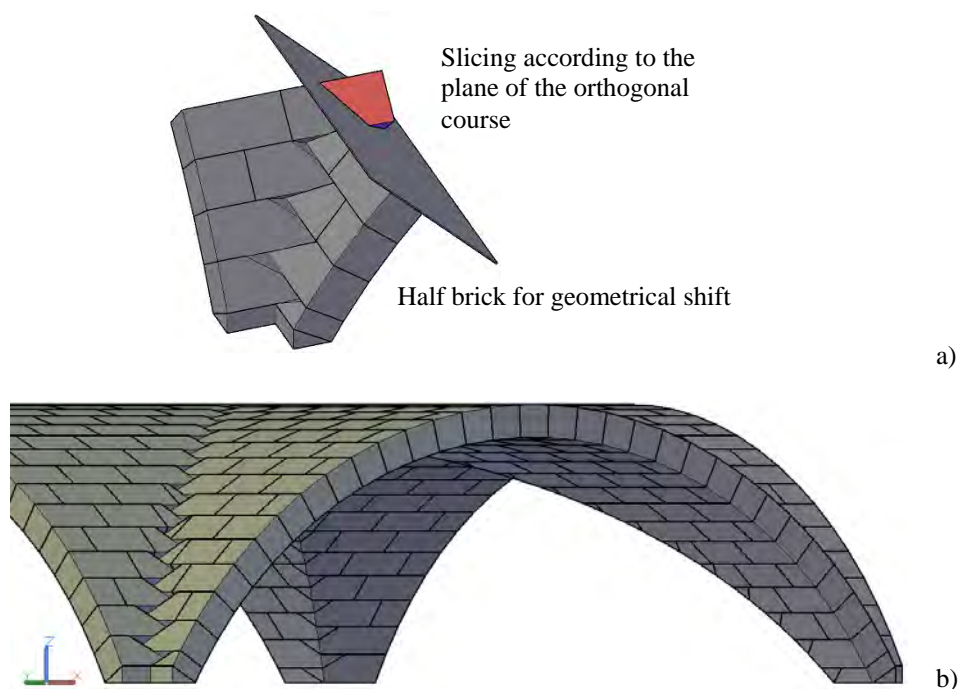


Figure 4-12. Block pattern adopted in the present study: a) methodology; b) extrados and intrados view

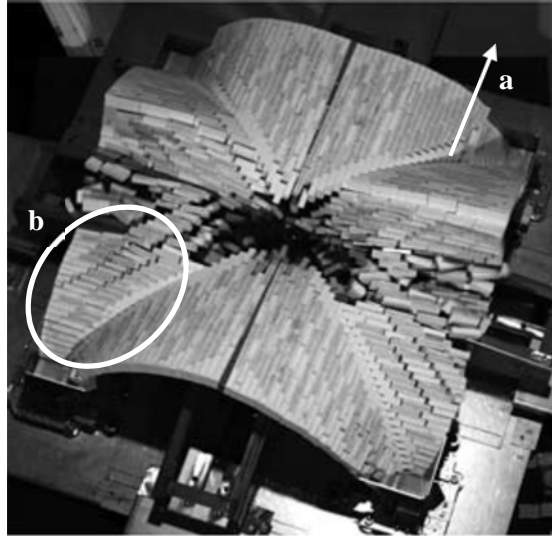


Figure 4-13. Zenith view of the vault during the tilting tests with $\phi = 9^\circ$: a) sliding of the upper part of the vault, b) crack interruption

4.5 In-plane shear mechanism

In the previous chapter the analyses focused on several features, namely the influence of: a) the normal and tangential stiffness, b) the consideration of geometrical nonlinearities. Moreover, as stressed before, even though no detailed information is available for the lateral steel plates at each corner of the vault (Figure 4-10a and Figure 4-13), their effect is also discussed here. In short, the analyses regarded the parameters reported in Table 4-1.

According to the experimental setup, the numerical model has been studied considering an imposed horizontal displacement applied to the lower side corners of Figure 4-14a, and the upper side corners were modelled as simply supported. Neglecting the lateral plates, the consequent deformed shape is reported in Figure 4-14 where a clear outward displacement of the elements near the abutments can be observed. This fact confirms the hypothesis that the steel plates (discussed in Figure 4-13) confine the most fragile part of the vault, providing a substantial increment of capacity. As seen in the last part of Chapter 2 (concerning the most frequent damages in a seismic event), the vault corners usually display a brittle failure (due to shear action and instability) which the lateral plates somehow prevented in the tests.

Confined corners	K_n	K_t	Geometrical nonlinearities
Yes - No	0.5 - 1 - 10 MPa/mm	0.1 - 0.4 - 1 $\times K_n$	Updated Lagrange formulation Yes - No

Table 4-1. In-plane shear mechanism: parameters adopted for the nonlinear static analyses

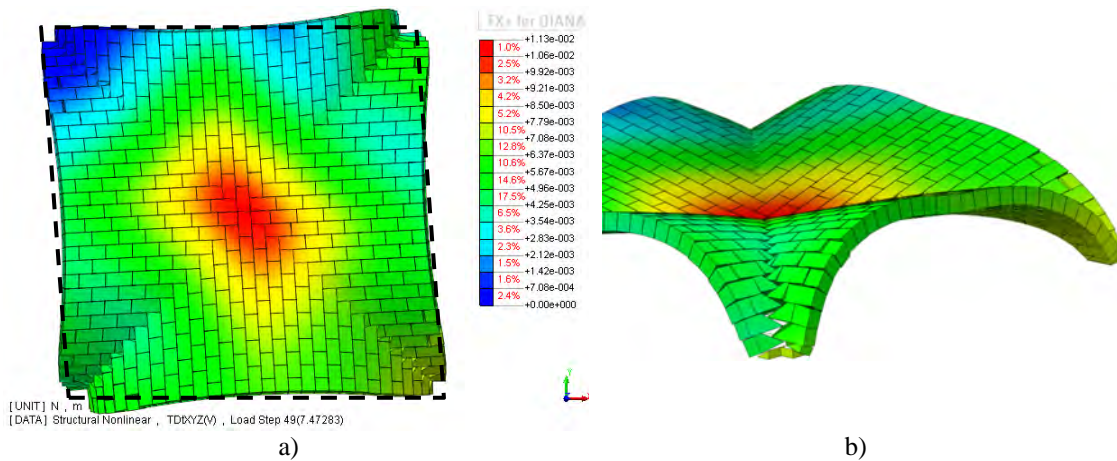


Figure 4-14. Typical deformed shape of the vault after in-plane shear action without lateral constraints (graphic scale 10:1): a) zenith view and b) detail of the corner

In order to better compare the numerical model with the experimental results, the elements covered by the steel plates (see Figure 4-10) were constrained in the fashion depicted in Figure 4-15. As no information is provided on this topic, the procedure represents a limit condition that approximates well the real behaviour of the tested vault. In particular, conversely to the real conditions, the numerical constraints are not unilateral (theoretically, they can work either in compression or in tension). However, due to the stereotomy adopted and the gravitational loads, the displacement of the blocks is supposed to be outward. This assumption is confirmed by Figure 4-14 and the issue becomes not relevant.

4.5.1 Interface stiffness

The first aim of the analysis was to investigate the influence of the interface stiffness. For an illustrative purpose, only the results with normal stiffness $K_n = 1$ MPa/mm and tangential stiffness $K_t = 0.1, 0.4, 1$ MPa/mm are reported below. Neglecting the geometrical nonlinearities, Figure 4-16 shows the comparison in terms of force-displacement diagram. According to Figure 4-10b, the quantities are dimensionless with respect to the weight of the vault W and the span l , respectively. In terms of capacity, no appreciable differences can be detected, being anyway slightly larger than the experimental results. More in detail, the curve with $K_t = 0.1, 0.4$ MPa/mm are almost coincident, while the curve with the lowest tangential stiffness provides much different initial stiffness (more similar to the experimental one).

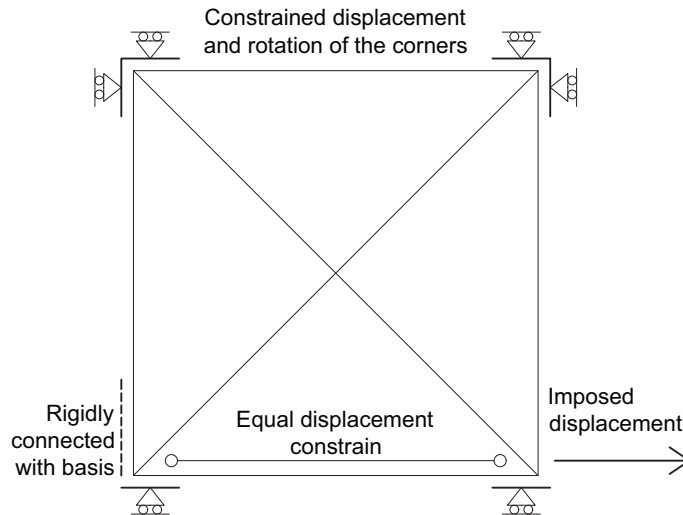


Figure 4-15. Layout of the numerical model for in-plane shear mechanism

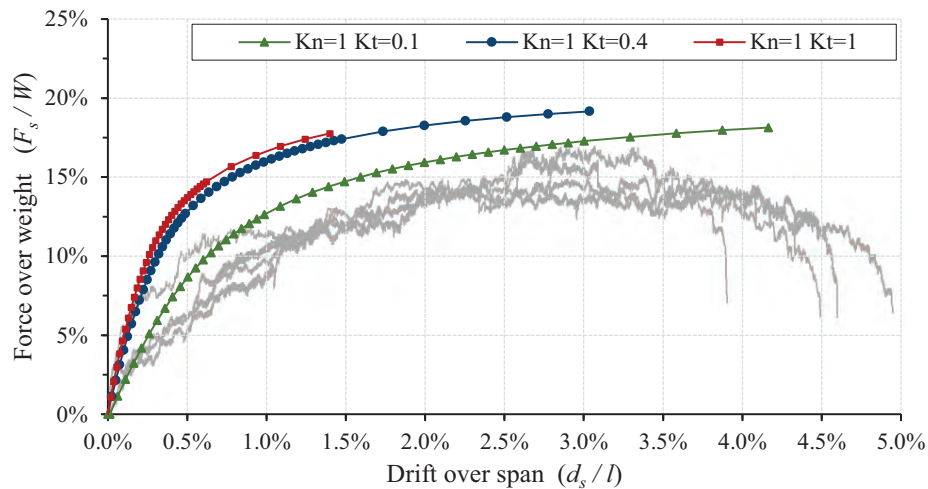
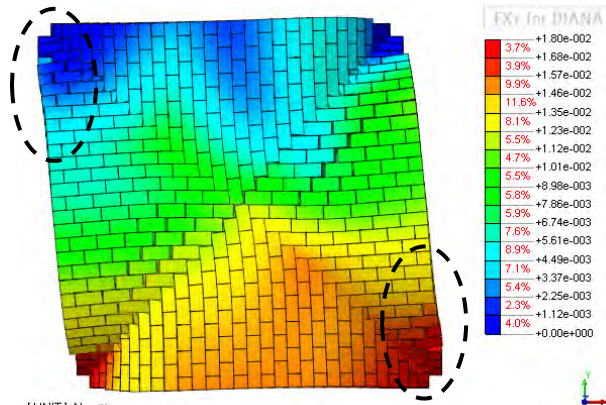
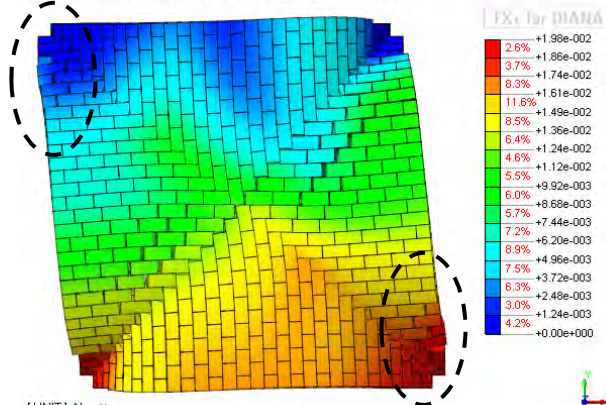


Figure 4-16. In-plane shear mechanism: comparison between the experimental (grey) and the numerical results with $K_n = 1$ and $K_t = 0.1, 0.4, 1$ MPa/mm (neglecting UL)

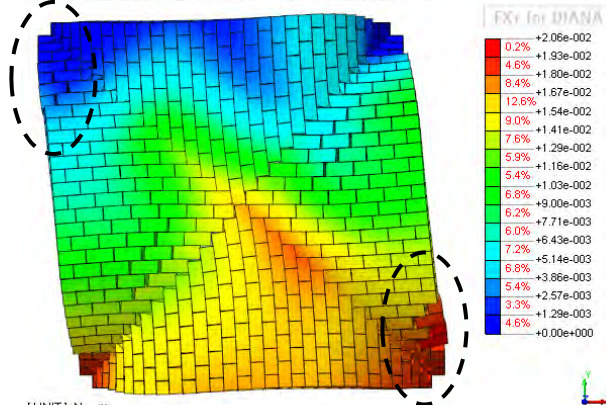
In terms of failure mechanism, again no significant differences were noted for $K_t = 0.1, 0.4$ MPa/mm (Figure 4-17). Moreover, considering the lowest value of tangential stiffness, a more pronounced vertical displacement was observed at the crown. Finally, the numerical results are compared with one picture of the test. The crack pattern correctly approaches the one provided by the experimental test along the diagonal. On the other hand, the local failure of perimetral blocks, due to tensile action at the interface and non-influential on the overall behaviour of the vault, are placed close to the abutments, as indicated by circles in Figure 4-17. However, it is worth noting that the detachment of one block means an overall null stress, which suggests the perimetral force flow do not pass through the perimetral arches (e.g. slicing technique).



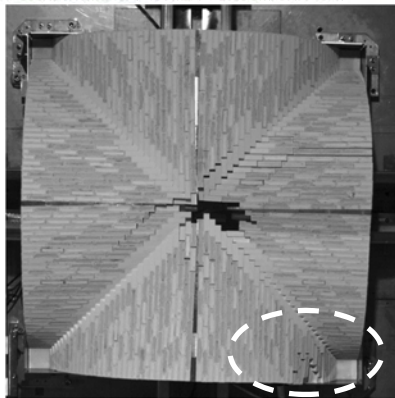
$K_n = 1, K_t = 1 \text{ MPa/mm}$



$K_n = 1, K_t = 0.4 \text{ MPa/mm}$



$K_n = 1, K_t = 0.1 \text{ MPa/mm}$



Picture of the test

Figure 4-17. In-plane shear mechanism: deformed shape with $K_n = 1, K_t = 0.1, 0.4, 1 \text{ MPa/mm}$ (neglecting UL) and d_s/l around 3% (graphic scale 4:1 with colours according to total x-y-z displacement). Picture of the test. Circles indicate local failure of perimetral blocks

In general, neglecting the geometrical nonlinearities, no matter the interface stiffness, all the calculated capacity curves displayed an increasing monotonic trend achieving a maximum capacity equal to around 20% of the weight. This behaviour is stressed in Figure 4-18, which reports the capacity curves for three values of K_n and $K_t = K_n$. Although the analyses are not able to estimate the ultimate displacement, the curve with $K_t = K_n = 0.5$ MPa/mm is the closest to the experimental results.

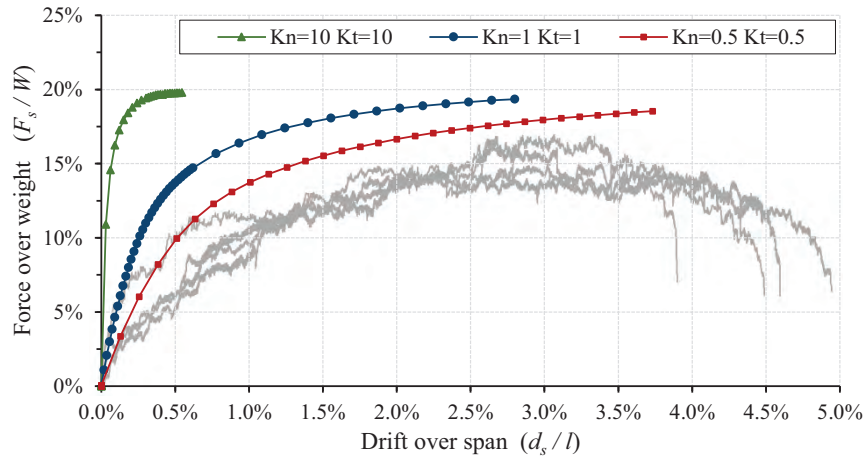


Figure 4-18. In-plane shear mechanism: numerical results considering $K_n = K_t = 0.5, 1, 10$ MPa/mm

Similarly to what was shown in Chapter 3, the effect of a 10% reduction of the overall thickness of the vault (to account for slight variations in block size, rounded corners and the imperfection of the manually assembled geometry) is assumed for Figure 4-19. In particular, assuming $K_t = K_n = 0.5$ MPa/mm, the curve provides a good agreement in terms of maximum strength (around 15% of the weight) and most of the capacity curve. In terms of failure mechanism, no significant difference were noted with respect to the ones already discussed, thus in line with the experimental one.

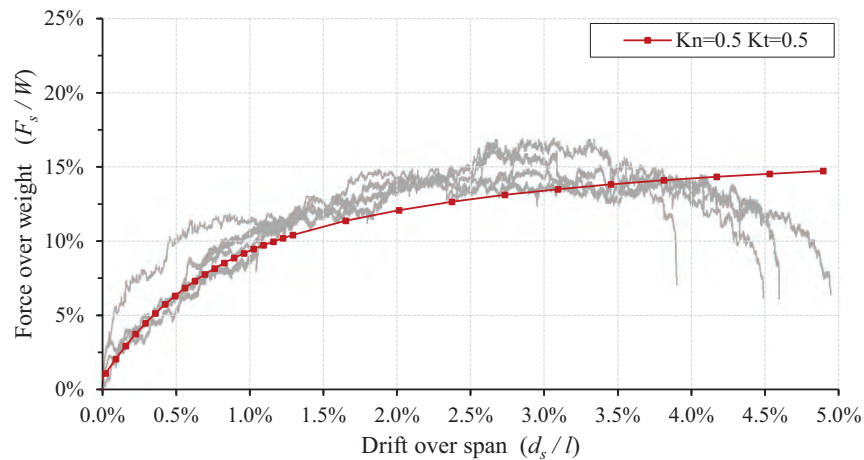


Figure 4-19. In-plane shear mechanism: capacity curve considering a 10% reduction of the thickness and $K_n = K_t = 0.5$ MPa/mm

4.5.2 Influence of geometrical nonlinearities

The analyses presented in the previous subsection are now discussed according to the Updated Lagrange formulation (UL). For an illustrative purpose, only the results following normal stiffness $K_n = 1$ MPa/mm and tangential stiffness $K_t = 0.1, 0.4, 1$ MPa/mm are reported in Figure 4-20. The numerical results significantly differ from the experimental ones in terms of strength and ultimate displacement. In particular, the capacity is almost 14.5% of the total weight for $K_t = 0.4$ and 1 MPa/mm (similar to the experimental results), and to 11.1% for $K_t = 0.1$ MPa/mm. On the other hand, as already stressed in §4.3.2, the experimental results reveal a significant ductility of the vault. In detail, the ultimate displacement recorded in the tests is larger than 4% of the span, whereas the one achieved with the numerical model is around 3%.

Regarding the failure mechanisms, the pictures are reported in Figure 4-21, displaying no substantial difference from what already observed. However, major local failure (close to the abutments) are notable.

Given the similarity of the results in case $K_t / K_n = 0.4$ (which approximates the ratio of the values suggested by [Senthivel and Lourenço, 2009]) and 1, and since the ratio equal to 0.1 can be regarded as too severe (with more pronounced sliding and local failures not detected in the experimental results), it seems interesting to limit the comparison only to the cases $K_n = K_t$. Moreover, for $K_n = 10$ MPa, the influence of K_t has been seen not relevant. The graph in Figure 4-22 shows the difference in case different values of normal stiffness are adopted. The curves are in disagreement with the experimental results, and some comments are given next.

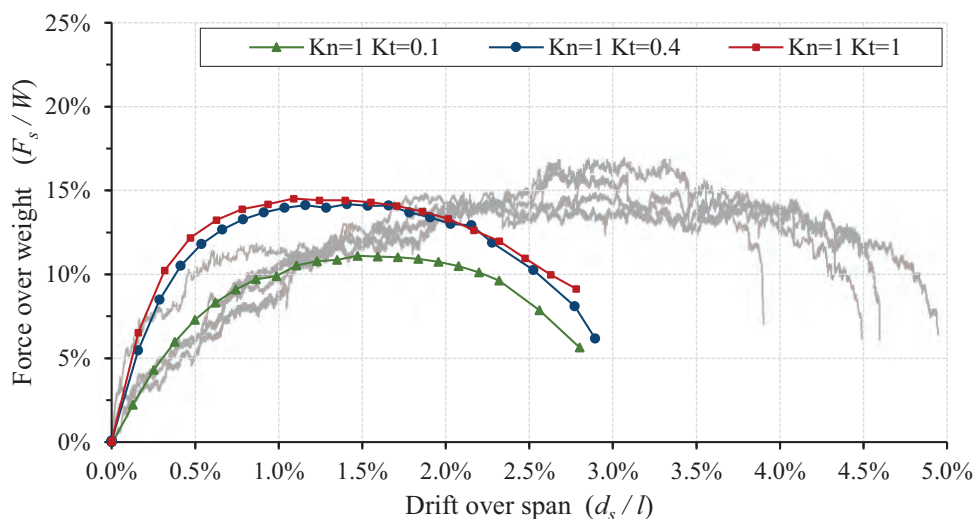


Figure 4-20. In-plane shear mechanism: comparison between the experimental (grey) and the numerical results with $K_n = 1$ and $K_t = 0.1, 0.4, 1$ MPa/mm (considering UL)

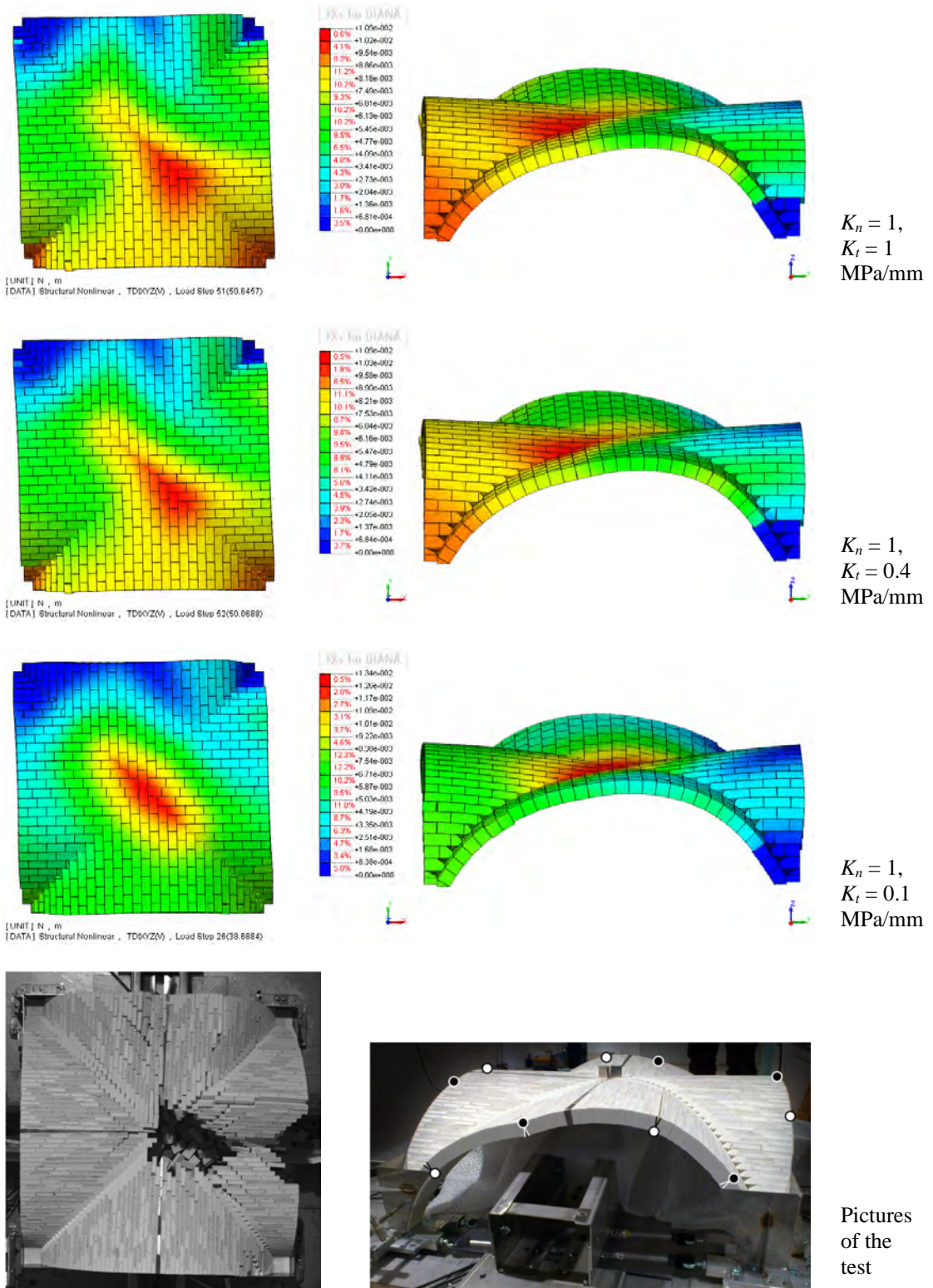


Figure 4-21. In-plane shear mechanism: deformed shape with $K_n = 1, K_t = 0.1, 0.4, 1$ MPa/mm (considering UL) - graphic scale 3:1 with colours according to total x-y-z displacement.

Pictures of the test

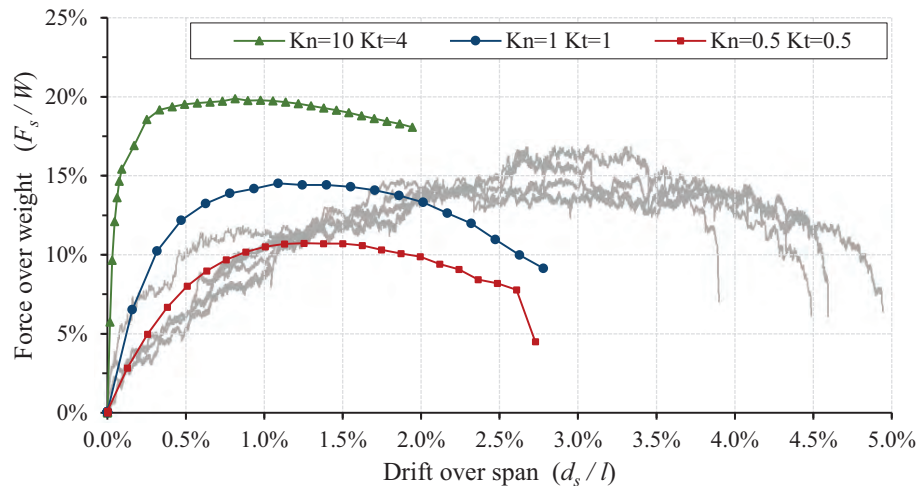


Figure 4-22. In-plane shear mechanism: numerical results considering $K_n = K_t = 0.5, 1, 10$ MPa/mm

The maximum value of K_n yields to a capacity close to the one calculated without accounting for UL, that is 20% of the weight (Figure 4-16). The reason lies in the normal stiffness and the consequent interpenetration. Neglecting UL means assuming the initial configuration as reference for the equilibrium conditions to be calculated. Therefore, since the failure is due to equilibrium loss (i.e. instability), neglecting the real position of the blocks provides the maximum capacity. On the other hand, performing the calculation according to UL, the same result can be achieved only with larger values of stiffness which prevent initial displacement and deformation in the early stage of the analysis.

From the physical point of view, this choice represents the limit condition of block surfaces perfectly smooth with the entire area involved in the contact between each other, that is, Heyman's hypothesis of masonry elements infinitely resistant in compression [1966]. In this regard, it seems interesting to analyse the nonlinear behaviour of a rigid block undergoing horizontal action, whose simple schematization is presented in Figure 4-23. For further description on this topic, among others, the reader is referred to [Doherty et al., 2002; Griffith et al., 2003, 2004; de Felice, 2011; Al Shawa et al., 2012].

Figure 4-23a shows the theoretical nonlinear behaviour of the block for the limit conditions of rigid-infinitely resistant elements (for both the block and the support). In order to activate the hinge and the right bottom toe, an initial larger horizontal force is requested. Once the mechanism is activated, the larger the displacement, the lower the horizontal force which complies with equilibrium conditions. In general this behaviour is approximated by a straight line, up to a displacement that corresponds to a null horizontal force, i.e. collapse. On the other hand, a more realistic behaviour is depicted in Figure 4-23b: the structure follows the previous curve only after a linear and plastic branch. It is easy to note that, in case the hinge does not coincide with the

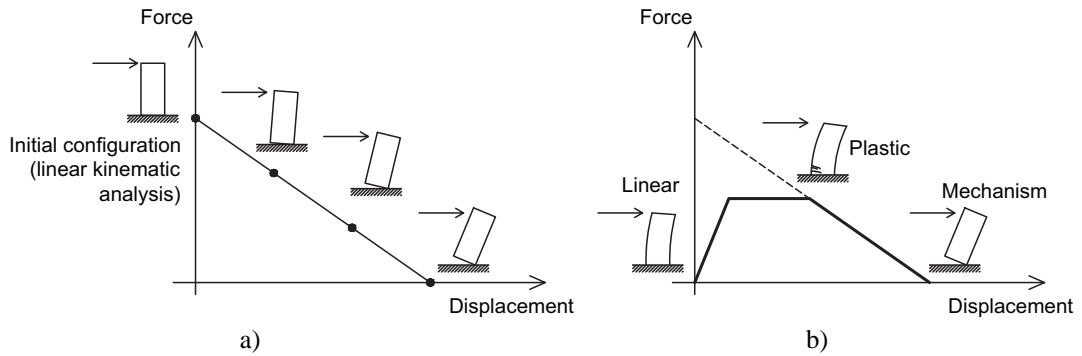


Figure 4-23. Schematization of the nonlinear behaviour of a rigid block undergoing horizontal action: a) limit condition and b) supposed real behaviour

corner (due to a finite resistance and stiffness of both the block and the support, i.e. interpenetration), the ultimate displacement may be reduced.

Moving back to Figure 4-22, the experimental curve and the one following the largest interface stiffness are in strong analogy with the single block behaviour described in Figure 4-23b. Unfortunately, the FEM model suffered problems of convergence because large peaks of strain and stress were faced (high values of stiffness lead to pinned hinges and neat cracks) and in case of isolated failure of perimetral blocks, without achieving the ultimate displacement.

4.6 Tilting test

According to the experimental setup, the numerical model has been studied considering an incremental horizontal load proportional to the mass (pushover analysis) imposing fully constrained supports. However, as far as the lateral plates are concerned, the limit schematizations adopted for the seismic direction equal to 0° and 45° are depicted in Figure 4-24. The layouts proposed follow from the analyses of the vault without considering confining action. For the sake of conciseness, only the results regarding the seismic direction at 0° and $K_n = K_t = 1 \text{ MPa/mm}$ are reported in Figure 4-25 and Figure 4-26 (lateral and azimuth view, respectively). In the pictures, apart from the consequent differences in terms of capacity, the confining effect is evident with strong influence on the failure mechanism.

4.6.1 Interface stiffness

The first aim of the analysis was to investigate the influence of the interface stiffness. For an illustrative purpose, only the results using normal stiffness $K_n = 1 \text{ MPa/mm}$ and tangential stiffness $K_t = 0.1, 0.4, 1 \text{ MPa/mm}$ are reported below. Neglecting the geometrical nonlinearities, Figure 4-27 shows the comparison in terms of horizontal load multiplier λ vs. horizontal displacement diagram. In terms of capacity, no appreciable differences can be detected, being anyway

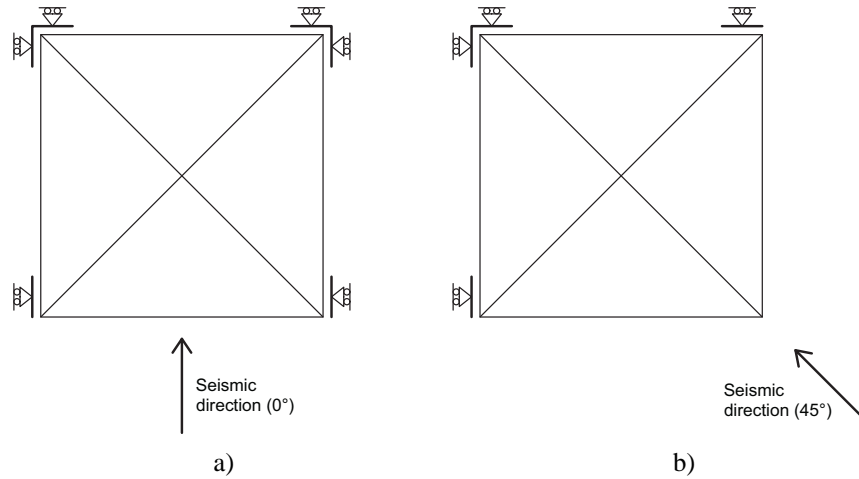


Figure 4-24. Layout of the numerical model for tilting test

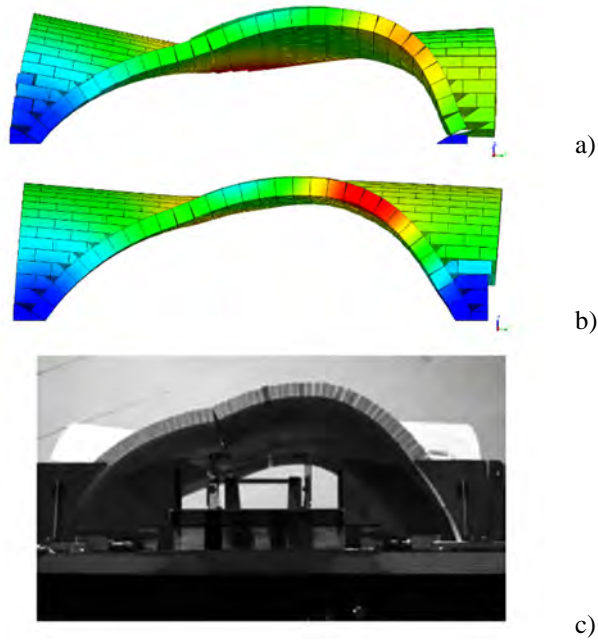


Figure 4-25. Lateral view of tilting test for increasing load: nonlinear analyses ($K_n = K_t = 1 \text{ MPa/mm}$), a) with and b) without considering lateral steel plates (graphic scale 1:1); c) experimental result

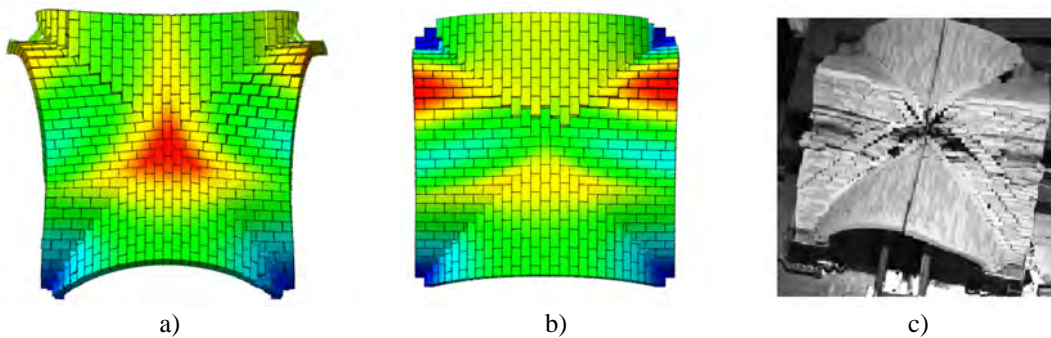


Figure 4-26. Azimuth view of tilting test: nonlinear analyses ($K_n = K_t = 1 \text{ MPa/mm}$), a) with and b) without considering lateral steel plates (graphic scale 2:1); c) experimental result

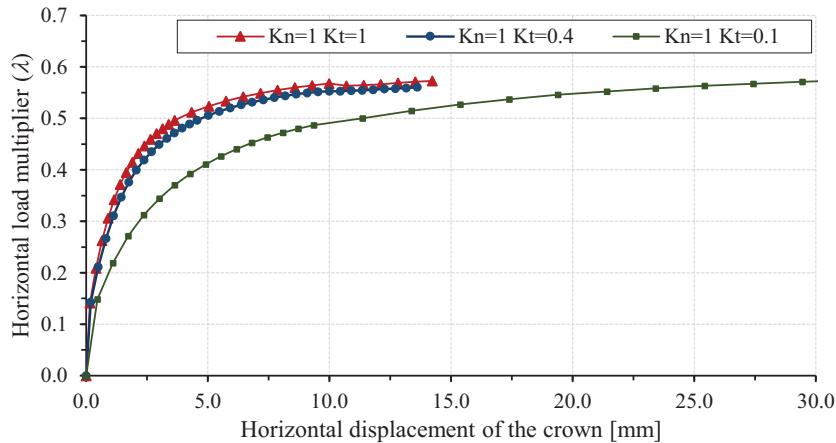


Figure 4-27. Tilting test: numerical results with $K_n = 1$ and $K_t = 0.1, 0.4, 1$ MPa/mm (neglecting UL)

much larger than the experimental results ($\lambda = 0.35$). More in detail, as already observed for the in-plane shear mechanism, the curve with $K_t = 0.1, 0.4$ MPa/mm are almost coincident.

As far as the failure mechanism is concerned, the results are shown in Figure 4-28. Again, no significant differences were found for $K_t = 1, 0.4$ MPa/mm. On the other hand, considering $K_t = 0.1$ MPa/mm, even though the same overall mechanism was detected, a more pronounced vertical displacement was observed at the crown. Finally, the numerical results are compared with one picture of the test. The crack pattern correctly approaches the one provided by the experimental test. On the other hand, local failure of a few blocks (non-influential on the overall behaviour of the vault) are evident close to the abutment $K_t = 0.1$ MPa/mm. Sliding is also notable close to the lateral plates (see also Figure 4-13)

Finally, as for the case of in-plane shear mechanism, when geometrical nonlinearities are not accounted for, no matter the interface stiffness (either normal or tangential), all the curves displayed a monotonic increasing trend achieving a horizontal load multiplier almost equal to $\lambda = 0.58$, considerably different from the experimental outcome ($\lambda = 0.35$).

4.6.2 Influence of geometrical nonlinearities

The analyses presented in the previous subsection are now discussed According to the Updated Lagrange formulation (UL). For an illustrative purpose, only the results following normal stiffness $K_n = 1$ MPa/mm and tangential stiffness $K_t = 0.1, 0.4, 1$ MPa/mm are reported in Figure 4-29. The first two values of tangential stiffness provide a good approximation of the real capacity of the vault ($\lambda = 0.35$), whereas the lowest value is too conservative. Conversely to the in-plane shear mechanism already discussed, no information is available for the nonlinear capacity curve and the ultimate displacement.

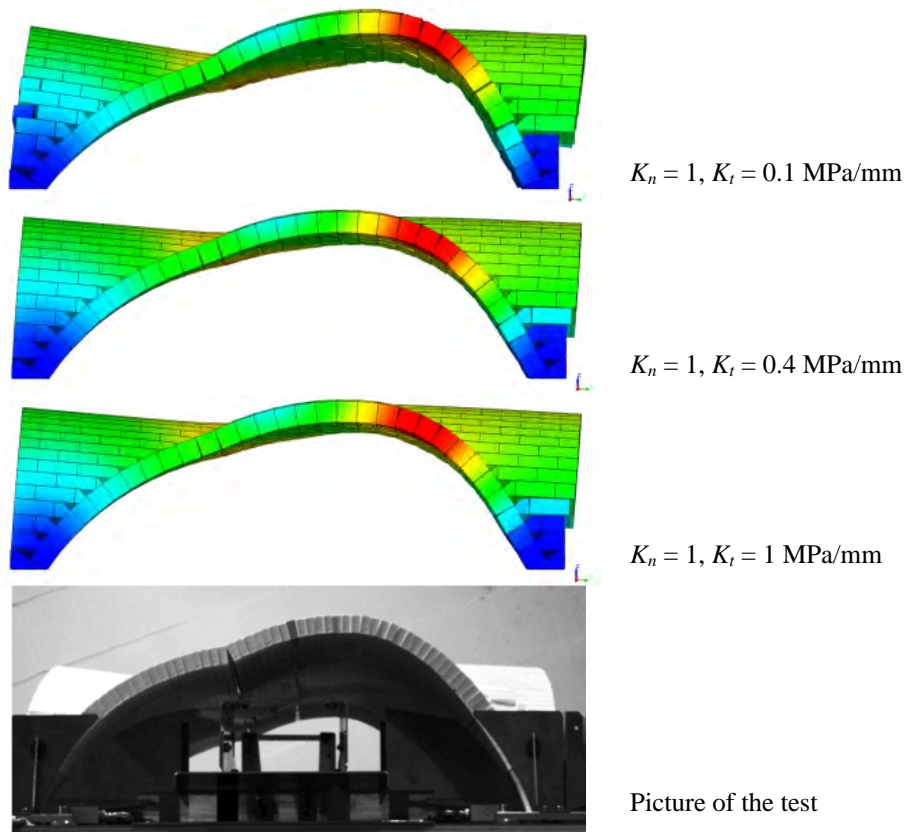


Figure 4-28. Tilting test: deformed shape with $K_n = 1$, $K_t = 0.1, 0.4, 1$ MPa/mm (neglecting UL), graphic scale 1:1 and colours according to total x-y-z displacement (see also Figure 4-25)

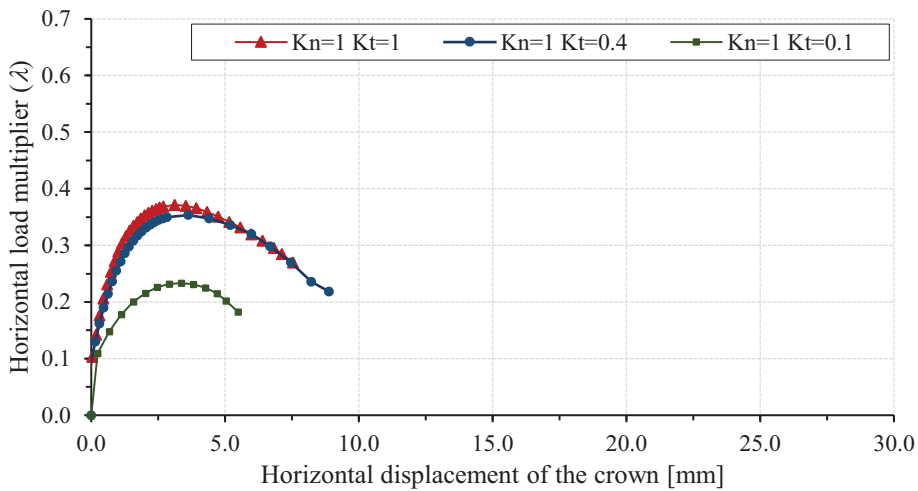
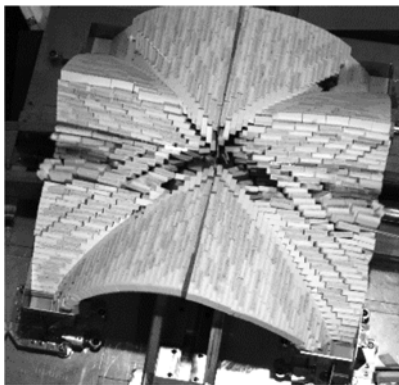
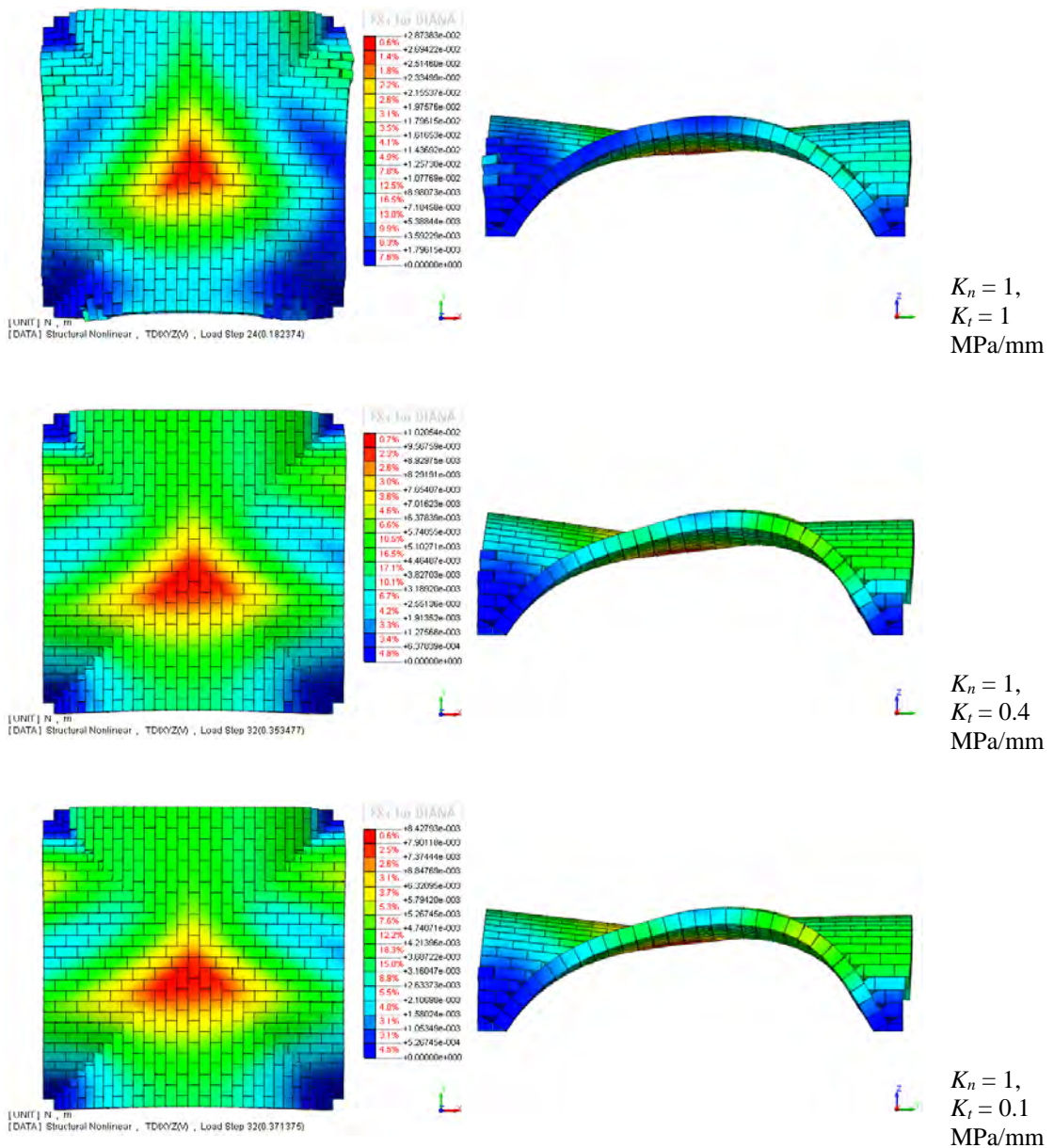


Figure 4-29. Tilting test: numerical results with $K_n = 1$ and $K_t = 0.1, 0.4, 1$ MPa/mm (considering UL)

The results in terms of failure mechanism are reported in Figure 4-30, displaying no substantial differences from what already shown.



Pictures of the tests

Figure 4-30. Tilting test: deformed shape (seismic direction = 0°) with $K_n = 1, K_t = 0.1, 0.4, 1$ MPa/mm (considering UL)

Again, given the similarity of the results in case $K_t / K_n = 0.4$ [Senthivel and Lourenço, 2009] and 1, and since the ratio equal to 0.1 can be regarded as too severe (with more pronounced sliding), it seems interesting to limit the comparison only to the cases $K_n = K_t$. Moreover, also in this case, with $K_n = 10$ MPa/mm, the influence of K_t has been seen not relevant. Figure 4-31 shows the difference in adopting several values of normal stiffness and, according to what already discussed in §4.5.2, the results are in line with the schematization of Figure 4-23.

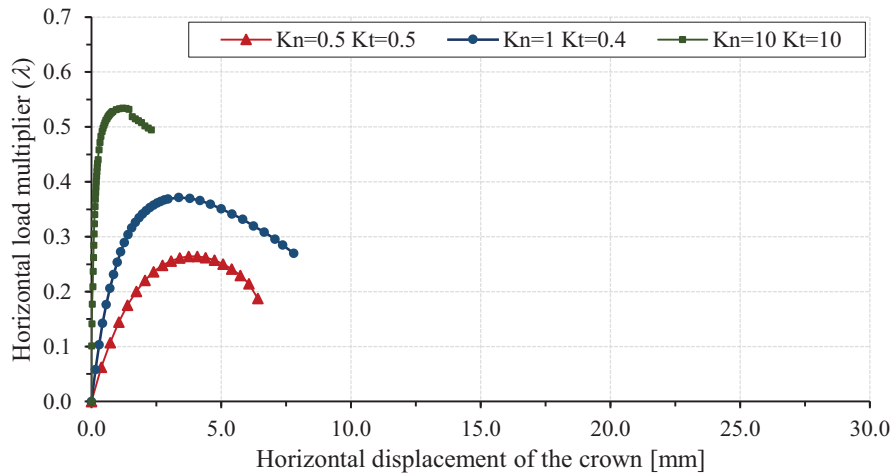


Figure 4-31. Tilting test: numerical results considering $K_n = K_t = 0.5, 1, 10$ MPa/mm

4.6.3 Seismic direction

Since the values of interface stiffness that best fitted the experimental results are $K_n = K_t = 1$ MPa/mm, only the relative results are shown next. According to the constrains adopted to model the lateral plates, the results in terms of maximum strength are reported in Figure 4-32. The capacity is overestimated by the numerical model (up to 20% in case $\phi = 45^\circ$) and, conversely to the experimental results, the capacity increases from 0° to 45° . The differences between the deformed shapes are shown in Figure 4-33

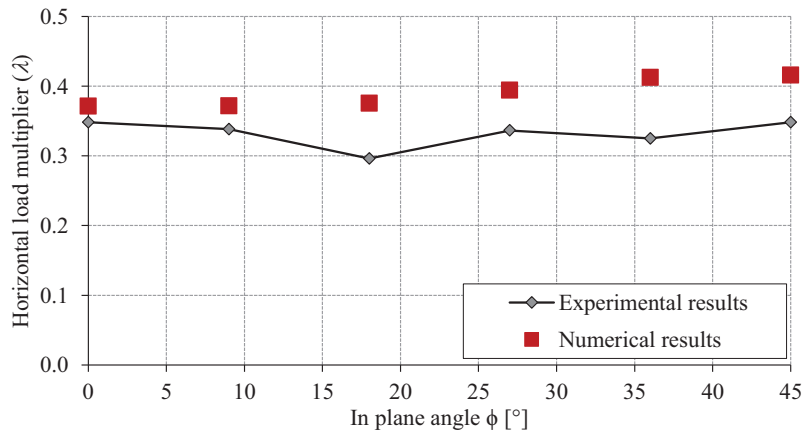


Figure 4-32. Horizontal load multiplier of the vault according to the seismic direction ϕ : experimental and numerical results ($K_n = K_t = 1$ MPa/mm)

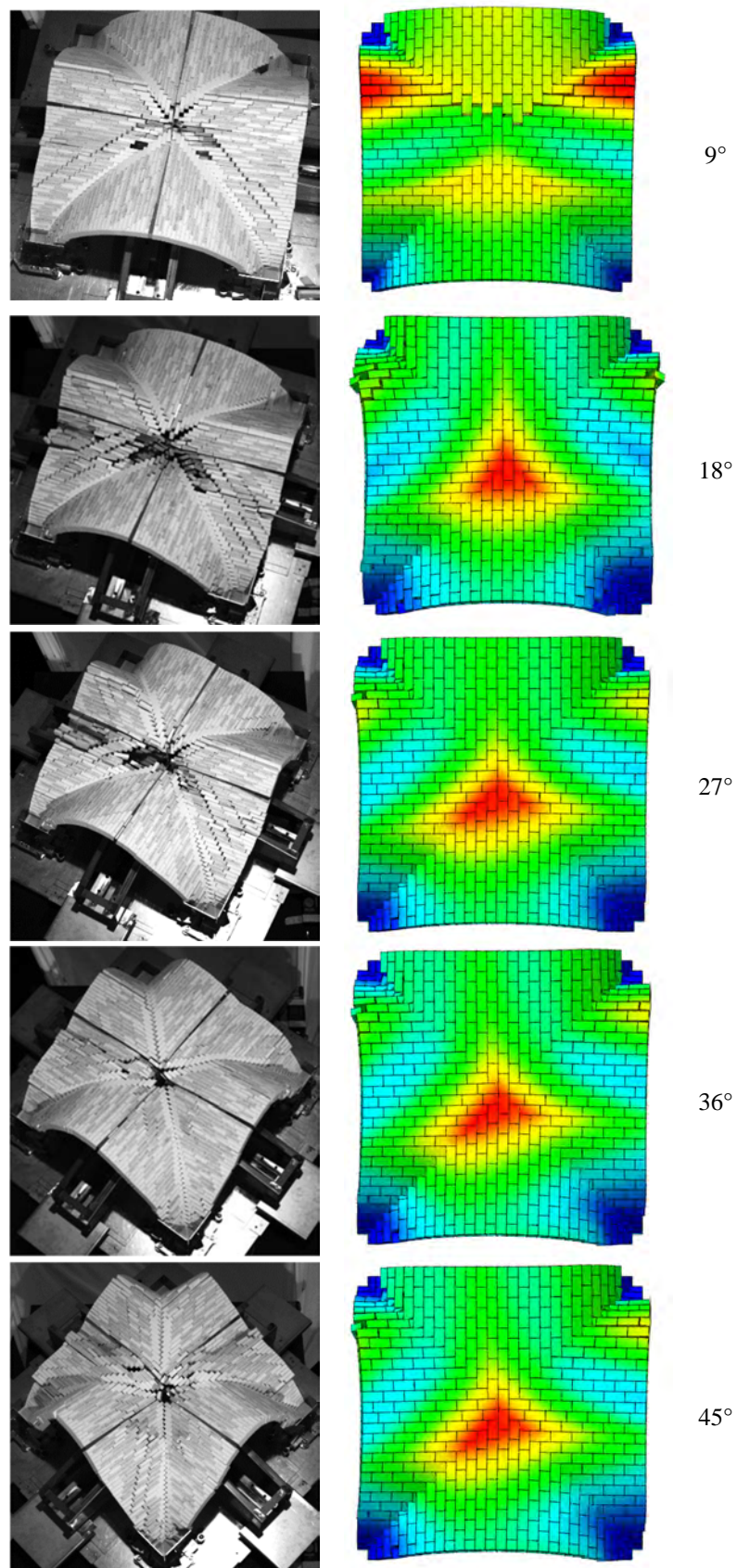


Figure 4-33. Comparison between the experimental and numerical failure mechanism according to different seismic directions (9° , 18° , 27° , 36° , 45°) with $K_n = K_t = 1$ MPa/mm (azimuth view)

4.7 Summary

This chapter presented the numerical analyses performed according to the experimental campaign carried out by Rossi et al. [2014, 2015; 2015] on a scaled groin vault. The FEM analyses were aimed at validating the 3D model (following the outcome of the previous chapter) by understanding the influence of the interface stiffness in two different experimental configurations: in-plane shear distortion and tilting test. The assumptions and the main results are briefly reviewed.

The model was implemented adopting a moderately different block pattern and dimensions of the blocks used in the experimental tests. The motivations of this choice were the sensible reduction of DOFs and of the amount of interface elements (the only source of physical nonlinearities), as well as the overall simplicity of the pattern adopted. In terms of catching the failure mechanism, no significant differences were notable between the experimental and numerical results, with an overall good matching of the crack pattern. On the other hand, the main drawback was detected in the local failure of perimetral blocks with only three adjoin elements. As already stressed, although this aspect is not influencing the overall behaviour of the vault, convergence problems arose for FEM analyses, which may be solved by extra constraints. Once validated, the presented discretization can be extended to the study of different kinds of masonry vault, even in case an algorithm for automatic mesh generation is adopted (e.g. Grasshopper[®], which is a graphical algorithm editor integrated with Rhinoceros).

Regarding the nonlinear behaviour of the vault, the numerical results were slightly discordant with the experimental ones. In particular, the ultimate displacement of the in-plane shear tests and the capacity of the vault for the tilting tests were not well represented by the numerical model. This is presumably due to the complexity of the experimental setup, e.g. boundary conditions. As far as the interface stiffness is concerned, it is worth noting that the third and the present chapter addressed the study of two scaled vaulted structures build with plastic blocks and with an overall low level of stress (if compared with real structures). Being these aspects crucial in the definition of the interface stiffness, an experimental campaign concerning different scale and mass density is rather desirable.

All the results of the numerical analyses described in the present chapter can be synthesized as follow. In particular, according to Figure 4-23, a possible strategy for evaluating the nonlinear behaviour of the vault is presented:

- assess the limit capacity of the vault through a FEM analyses without accounting for geometrical nonlinearities;

- estimate the limit curve of Figure 4-23a (assumed straight) as an envelope of nonlinear analyses adopting large values of interface stiffness (≥ 10 MPa/mm);
- calculate the elastic and plastic branch of Figure 4-23b through either a model with 10% reduction of the thickness (neglecting geometrical nonlinearities) or with fully nonlinear analyses with the real dimensions of the vault. In both cases, values of stiffness in the range $0.5 \div 1$ MPa/mm provided good results in terms of initial stiffness and maximum strength of the capacity curve. Moreover, considering the tangential over normal stiffness ratio equal to 0.4 and 1 provided almost coincident results, whereas a ratio equal to 0.1 may lead to unrealistic sliding between blocks. These results are in line with the outcomes of Chapter 3;
- finally, regarding the failure mechanism, no appreciable difference were noted varying the interface stiffness (being, obviously, more pronounced for low values).

References

- Al Shawa, O., de Felice, G., Mauro, A., and Sorrentino, L. (2012). Out-of-plane seismic behaviour of rocking masonry walls. *Earthquake Engineering & Structural Dynamics*, 41(5), 949–968.
- Becchi, A., and Foce, F. (2002). *Degli archi e delle volte: arte del costruire tra meccanica e stereotomia*. (Marsilio, Ed.). Venezia.
- Cangi, G. (2012). *Manuale del recupero strutturale e antisismico* (2nd ed.). Rome: DEI.
- de Felice, G. (2011). Out-of-plane seismic capacity of masonry depending on wall section morphology. *International Journal of Architectural Heritage*, 5(4-5), 466–482.
- Doherty, K., Griffith, M. C., Lam, N., and Wilson, J. (2002). Displacement-based seismic analysis for out-of-plane bending of unreinforced masonry walls. *Earthquake Engineering & Structural Dynamics*, 31(4), 833–850.
- Giovanetti (ed. by). (2000). *Manuale del recupero del Comune di Città di Castello*. Rome: DEI.
- Griffith, M. C., Lam, N. T. K., Wilson, J. L., and Doherty, K. (2004). Experimental investigation of unreinforced brick masonry walls in flexure. *Journal of Structural Engineering*, 130(3), 423–432.
- Griffith, M. C., Magenes, G., Melis, G., and Picchi, L. (2003). Evaluation of out-of-plane stability of unreinforced masonry walls subjected to seismic excitation. *Journal of Earthquake Engineering*, 7(sup001), 141–169.
- Heyman, J. (1966). The stone skeleton. *International Journal of Solids and Structures*, 2(2), 249–279.
- Levi, C. (1932). *Trattato teorico-pratico di costruzioni civili, rurali, stradali ed idrauliche*. (U. Hoepli, Ed.) (2 books.). Milano.
- Protti, E. (1935). *Archi volte scale nella moderna edilizia*. Edizioni tecniche-utilitarie.
- Romano, A., and Grande, E. (2008). Masonry barrel vaults: influence of the pattern. In *The 14th World Conference on Earthquake Engineering*. Beijing, China.
- Rossi, M. (2015). *Evaluation of the seismic response of masonry cross-vaults*. PhD dissertation, University of Genoa.
- Rossi, M., Calderini, C., and Lagomarsino, S. (2015). Experimental testing of the seismic in-plane displacement capacity of masonry cross vaults through a scale model. *Bulletin of Earthquake Engineering*.
- Rossi, M., Calderini, C., Lagomarsino, S., and Milani, G. (2014). Seismic response of masonry vaulted structures: experimental and numerical modelling. In P. B. Lourenço, B. A. Haseltine, & G. Vasconcelos (Eds.), *9th International Masonry Conference*. Guimarães: Universidade do Minho.
- Senthivel, R., and Lourenço, P. B. (2009). Finite element modelling of deformation characteristics of historical stone masonry shear walls. *Engineering Structures*, 31(9), 1930–1943.
- Shapiro, E. E. (2012). *Collapse mechanisms of small-scale unreinforced masonry vaults*. Master thesis, Massachusetts Institute of Technology.
- Tomasoni, E. (2008). *Le volte in muratura negli edifici storici: tecniche costruttive e comportamento strutturale*. PhD dissertation, Università degli Studi di Trento.

- Trevisan, C. (2011). *Per la storia della stereotomia. Geometrie, metodi e costruzioni*. Roma: Aracne.
- Van Mele, T., McInerney, J., DeJong, M., and Block, P. (2012). Physical and computational discrete modelling of masonry vault collapse. In Jerzy Jasieńko (Ed.), *Structural Analysis of Historical Constructions* (pp. 2552–2560). Wrocław.
- Wendland, D. (2007). Traditional Vault Construction Without Formwork: Masonry Pattern and Vault Shape in the Historical Technical Literature and in Experimental Studies. *International Journal of Architectural Heritage*, 1(4), 311–365.

Chapter 5.

Sensitivity analysis on groin vaults

5.1 Abstract

A sensitivity analysis on the seismic capacity of masonry groin vaults is described in this chapter. The main objectives of the study were: 1) assessing the effects and the influence of the main geometrical and mechanical properties, 2) proposing an analytical formulation for evaluating the seismic capacity of groin vaults (as a guidance to practitioners). In particular, the influence of the vault diameter, thickness, angle of embrace (or arc of embrasure, which is the angle created by the two lines extending from the centre point of the defining arc to the springing point of each side of the arch / vault), presence of the infill, and masonry tensile strength was investigated. The interaction with the rest of the structure was accounted by choosing two different boundary conditions. The analyses have been performed using a non-commercial software based on the upper bound approach of standard limit analysis. The code framework, labelled as UBLA, is briefly described in the first section of the chapter and the reader is referred to [Milani et al., 2009a, 2009b] for further details.

With the aim of identifying the most frequent failure mechanisms, the results of the analyses have been visually inspected and sorted according to the input parameters. This also gave the possibility to heuristically deduce the range of parameters associated to a particular mechanism. The resulting catalogue, together with multiple linear regression analyses, provided valuable tools for expedite seismic evaluation of groin vaults, which represent a first step for the lack of recommendations in the current Codes of Practice.

5.2 Adopted structural analysis code

The FE discretization of the groin vault was represented by means of rigid flat six-noded wedge elements. The utilization of wedges (i.e. 3D elements) instead of shell elements provides the further possibility of adopting the same model in case of surface reinforcement with FRP strips (either at the intrados or extrados). Moreover, assuming rigid infinitely resistant wedges (hypothesis widely adopted in literature) implicitly assures transverse sections to remain plane and the internal dissipation is allowed only at the interfaces between neighbouring elements.

More in detail, the kinematic variables for each wedge element E are represented by three centroid velocities (u_x^G, u_y^G, u_z^G) and three rotations around centroid G , ($\Phi_x^G, \Phi_y^G, \Phi_z^G$), as reported in Figure 5-1a. The edge surface Γ_{12}^E , which connects P_1, P_2, P_4 and P_5 nodes, is rectangular and the jump of velocities on it is linear. In particular, the velocity field of a generic point P with global coordinates (x_P, y_P, z_P) , on Γ_{12}^E is expressed in the global frame of reference as:

$$\mathbf{U}_{(P)} = \begin{bmatrix} u_x \\ u_y \\ u_z \end{bmatrix} = \begin{bmatrix} u_x^G \\ u_y^G \\ u_z^G \end{bmatrix} + \begin{bmatrix} 0 & -\Phi_y^G & \Phi_z^G \\ \Phi_y^G & 0 & -\Phi_x^G \\ -\Phi_z^G & \Phi_x^G & 0 \end{bmatrix} \begin{bmatrix} x_P - x_G \\ y_P - y_G \\ z_P - z_G \end{bmatrix} = \mathbf{U}_E^G + \mathbf{R}_E(\mathbf{P} - \mathbf{G}) \quad (5-1)$$

where $\mathbf{U}_{(P)}$ is the point P velocity, \mathbf{U}_E^G is the element E centroid velocity and \mathbf{R}_E is the element E rotation matrix. From Equation (5-1), the jump of velocities $[\mathbf{U}_{(P)}]$ at a point P on the interfaces I between two contiguous elements N and M can be evaluated as the difference between the velocities of P belonging, respectively, to N and M :

$$[\mathbf{U}_{(P)}] = \mathbf{U}_M^G - \mathbf{U}_N^G + \mathbf{R}_M(\mathbf{P} - \mathbf{G}_M) - \mathbf{R}_N(\mathbf{P} - \mathbf{G}_N) \quad (5-2)$$

Denoting \mathbf{R}^I as the rotation matrix with respect to the global coordinate system, the jump of velocities may be written in the local system (Figure 5-1b) as follows:

$$[\tilde{\mathbf{U}}_{(P)}] = \begin{bmatrix} \Delta r_1 \\ \Delta r_2 \\ \Delta s \end{bmatrix} = \mathbf{R}^I [\mathbf{U}_{(P)}] \quad (5-3)$$

where Δr_1 , Δr_2 and Δs are velocities jumps (two tangential and mutually orthogonal and one perpendicular to the interface). Hereinafter, for the sake of clearness, the superscript I will be suppressed. Once the jump of velocities in the local frame of reference is known, it is possible to evaluate the power dissipated on a generic interface I of area Ω_{12} as follows:

$$\pi_{int} = \int_{\Omega_{12}} [\tilde{\mathbf{U}}_{(P)}]^T \boldsymbol{\sigma}_{(P)} d\Omega = \int_{\Omega_{12}} (\Delta r_1 \tau_1 + \Delta r_2 \tau_2 + \Delta s \sigma_s) d\Omega \quad (5-4)$$

where $\boldsymbol{\sigma}_{(P)}^T = [\tau_1, \tau_2, \sigma_s]$ represents the stress vector acting at P on element M , in local stress coordinates (Figure 5-1b).

Regarding the masonry failure surface, as experimental evidences show, the basic failure modes for masonry walls with weak mortar are sliding along the joints, direct tensile splitting of the joints, and compressive crushing at the interface. These modes may be gathered adopting a Mohr-Coulomb failure criterion combined with a tension cut-off and a cap in compression [Lourenço and Rots, 1997].

Aiming at treating the problem within the framework of linear programming, a piecewise linear approximation of the failure surface is adopted. A homogenized strength domain $\phi = \phi(\boldsymbol{\sigma})$ in the local coordinate system $(\tau_1, \tau_2, \sigma_s)$ and constituted by m planes is supposed. Such a linearization for each interface (and, in principle, for each point of the interface) can be obtained applying the procedure recommended by Krabbenhoft et al. [2005], and the reader is referred there for further details.

In particular, a generic linearization plane q has equation $\phi^q: \mathbf{A}^{qT} \boldsymbol{\sigma} = A_{r1}^q \tau_1 + A_{r2}^q \tau_2 + A_s^q \sigma_s = C^q$, where $1 \leq q \leq m$ is assumed. Adopting the normality rule and introducing plastic multiplier rates

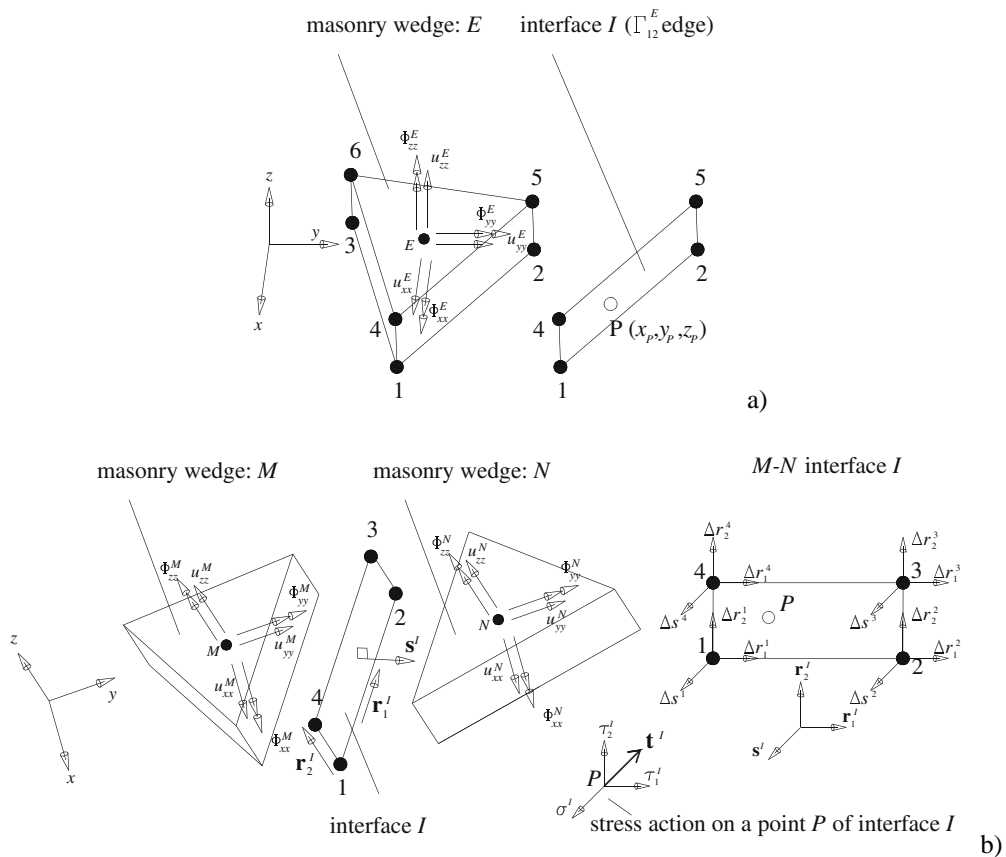


Figure 5-1. Masonry six-noded wedge: a) single element and four-noded interface; b) contiguous masonry elements (global and local frame of reference) [Milani et al., 2009b]

$\dot{\lambda}_{(P)}^q$ (one for each linearization plane), the jump of velocity $[\tilde{\mathbf{U}}_{(P)}]$ field is given by:

$$[\tilde{\mathbf{U}}_{(P)}] = \sum_{q=1}^m \dot{\lambda}_{(P)}^q \frac{\partial \phi^q}{\partial \boldsymbol{\sigma}} \quad (5-5)$$

In order to solve Equation (5-4), since the jump in velocity on interfaces is assumed to vary linearly, e.g. Equation (5-3), it is necessary to evaluate Equation (5-5) only in correspondence of three different positions $P_k = (x_k, y_k, z_k)$ on I . Therefore, from Equations (5-4) and (5-5), the internal power dissipated on the generic interface I is expressed by:

$$\pi_{int} = \int_{\Omega_{12}} [\tilde{\mathbf{U}}_{(P)}]^T \boldsymbol{\sigma}_{(P)} d\Omega = \int_{\Omega_{12}} \sum_{q=1}^m \dot{\lambda}_{(P)}^q \left[\frac{\partial \phi^q}{\partial \boldsymbol{\sigma}} \right]^T \boldsymbol{\sigma}_{(P)} d\Omega = \frac{\Omega_{12}}{3} \sum_{q=1}^m C^q \sum_{k=1}^3 \dot{\lambda}_{(P_k)}^q \quad (5-6)$$

where all the symbols have already been introduced. It is interesting to notice from Equation (5-6) that the internal power estimation depends on the plastic multiplier rates of points P_k only.

Moving to the global scale, the external power dissipation can be written as:

$$\pi_{ext} = (\mathbf{P}_0^T + \lambda \mathbf{P}_1^T) \mathbf{w} \quad (5-7)$$

where \mathbf{P}_0 is the vector of permanent loads, λ is the load multiplier for the structure examined, \mathbf{P}_1 is the vector of variable loads (dependent on load multiplier) and \mathbf{w} collects elements centroid velocities. As the amplitude of the failure mechanism is arbitrary, a further normalization condition $\mathbf{P}_1^T \mathbf{w} = 1$ is usually introduced. Hence, the external power becomes linear in \mathbf{w} and λ and can be written as $\pi_{ext} = \mathbf{P}_0^T \mathbf{w} - \lambda$.

After some elementary assemblage operations, where the objective function is the total internal power dissipated minus the power dissipated by external loads, not dependent on the load multiplier, a linear programming problem is obtained, as:

$$\left\{ \begin{array}{l} \lambda = \min_{\hat{\mathbf{x}}} \left\{ \sum_{I=1}^n \pi_{int} - \mathbf{P}_0^T \mathbf{w} \right\} \\ \mathbf{P}_1^T \mathbf{w} = 1 \\ [\tilde{\mathbf{U}}_{(P_k)}] = \sum_{q=1}^m \dot{\lambda}_{(P_k)}^q \frac{\partial \phi^q}{\partial \boldsymbol{\sigma}} \\ \mathbf{U}_{(P_k)} = \bar{\mathbf{U}} \end{array} \right. \quad (5-8)$$

where n is the total number of interfaces and $\hat{\mathbf{x}}$ is the vector of total optimization unknowns (i.e. elements centroid velocities (\mathbf{w}) and rotations (Φ), and interface plastic multiplier rates). The

constraints represent, respectively, normalization conditions, constraints for plastic flow in velocity discontinuities, and velocity boundary conditions (assigned velocity $\bar{\mathbf{U}}$).

Several linear programming tools suited for solving Equation (5-8) are available in literature. However, according to the characteristics of the present problem, which is large and sparse, the barrier method of the CPLEX was chosen as the best tool. This method is available in TOMLAB[®], which is a modelling platform for solving applied optimization problems in Matlab. Moreover, since only some of the unknown variables are required to be integers, the problem was addressed as a mixed integer linear programming (MILP) problem. For more details, the reader is referred to specific literature, e.g. [Chvatal, 1983; Wolsey, 1998].

5.3 Analysis overview

The goal of this study, as stated before, was to evaluate the influence of the main geometrical parameters (diameter, thickness, angle of embrace), tensile strength, infill and boundary conditions on the seismic capacity of the vault. All the parameters are grouped as follows and detailed in the subsequent sub-sections.

1. **boundary conditions**
2. geometry, namely **diameter, thickness, angle of embrace**
3. **infill** (as assigned load)
4. **tensile strength**

5.3.1 Boundary conditions

Two boundary conditions were considered, namely “simply supported”, “in-plane shear” (Figure 5-2). Although rather approximate, they are representative of two different scenarios within the buildings. The former regards the vaults with supports of the same stiffness, e.g. central nave columns. The latter deals with vaults in which the different stiffness of the supports allows a differential displacement, e.g. lateral nave with the colonnade more flexible than the lateral wall (see Figure 2-33 in Chapter 2). It must be stressed that both conditions account only for the local behaviour of the vault, neglecting any mutual interactions with the rest of the structure, even in case of in-plane shear where the pure sliding of one side does not consider the real stiffness of the supports.

Moreover, in order to properly simulate the equal horizontal displacement of the two sliding corners (e.g. two consecutive columns of a colonnade), an internal infinitely rigid constrain (strut/tie) has been implemented between the two rollers (upper side of Figure 5-2b). The aim of the fictitious constrain is to avoid the unreal corner spread out due to the gravitational load thrust.

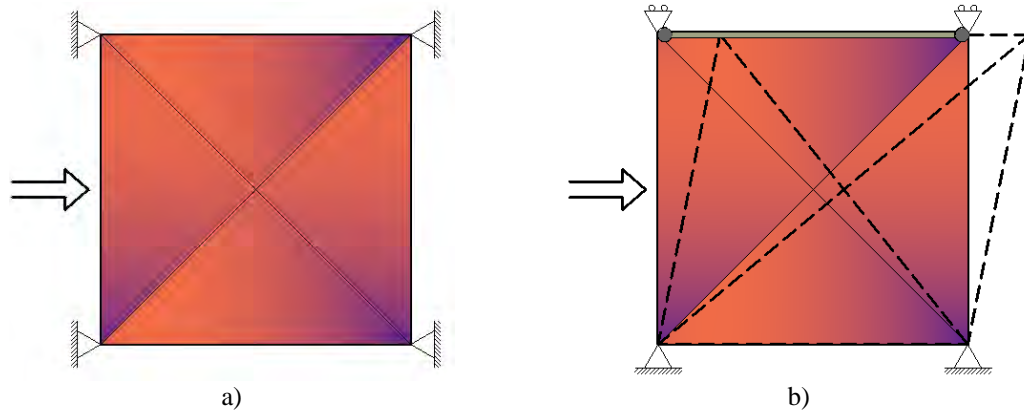


Figure 5-2. Plan view and boundary conditions for groin vaults: a) simply supported; b) in-plane shear (strut/tie between rollers)

5.3.2 Geometry: diameter, thickness, angle of embrace

Given the great importance that geometry plays in the capacity of masonry structures, all the descriptive parameters have been considered, namely angle of embrace, diameter and thickness. The adopted values are reported in Table 5-1, where the thickness is accounted as a ratio over the diameter. Regarding the angle of embrace, in order to provide consistent interface properties at the supports, the voussoirs underneath the last element of the vault were considered fully constrained (Figure 5-3a). Finally, in order to deal with *in situ* measurements, in the following, diameter and angle of embrace will be substituted by span and rise (Figure 5-3b).

Adopted values			
Diameter [m]	3.6	4.5	5.4
Thickness [diameter]	1/20	1/33	1/50
Angle of embrace	120°	130°	140°

Table 5-1. Geometrical parameters considered in the sensitivity analysis

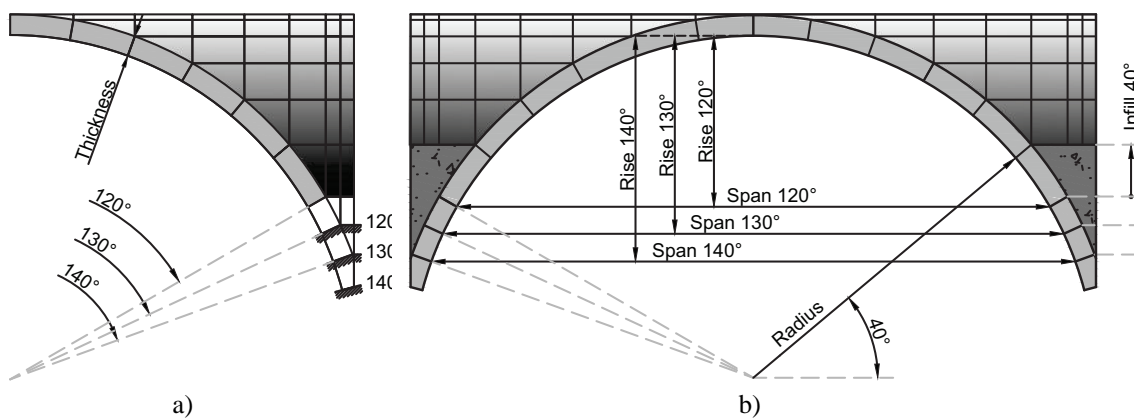


Figure 5-3. Groin vault description for three different angles of embrace (120°, 130° and 140°), which control other geometrical parameters: a) constraint location; b) span, rise and infill calculation

5.3.3 Infill as assigned load and mass

Regarding the presence of the infill, several studies demonstrated its crucial role in assessing the capacity of masonry vaulted structures [Gilbert, 2001; Cavicchi and Gambarotta, 2005, 2006; Milani and Lourenço, 2012]. Croci [2000], for instance, demonstrated how the collapse of the cross vault in the Basilica of Assisi during the earthquake of Umbria and Marche in 1997 was due to the continuous accumulation of loose infill which, during past earthquakes, increased permanent deformations, until the subsequent collapse.

For the sake of simplicity, the infill has been modelled as a distributed load and mass on the extrados of the vault, thus neglecting the proper distribution of vertical and horizontal pressure, the influence of the possible tensile strength (resulting as a loose material), and the nonlinear behaviour of the infill during motion (changes between active and passive pressure).

Although this approach is still poorly understood in the available literature, the recommendations by Clemente [1997] will be adopted next. Assuming the seismic action towards the right hand side, it is possible to consider (Figure 5-4): *I1*) only the contribution of the horizontal stripes of the left hand part of the infill; *I2*) as *I1* but on both sides; *I3*) the contribution of vertical stripes of the infill on both sides; *I4*) an overall distributed horizontal load whose resultant is equal to the entire mass of the infill. A comparison between the four strategies will be presented in the following.

Figure 5-5 shows the four levels of infill adopted in the analysis, indicated by a central angle equal to 0° , 40° , 60° , 90° , where 0° conventionally stands for no infill, while 90° represents the case in which the vault is completely covered. Also in this case, with the aim of considering only *in situ* measurements, next, the infill will be addressed according to the vertical height at the corner which depends on the angle of embrace (Figure 5-3b).

5.3.4 Description of the model

As far as the mechanical parameters are concerned, they were mostly chosen on the basis of the average values recommended by the Italian code for good stone masonry and brick masonry with lime mortar [CM, 2009], and reported in Table 5-2. Great attention has been paid to the tensile strength since it is considered the most influent features [Lourenço, 2002]. In particular, three values were adopted, namely $F_t = 0.05, 0.10, 0.20$ MPa, of which the minimum value may be accounted for the usual assumption of null strength.

The vault was discretized according to the directrix and generatrix of the webs. However, given the importance of the interface as a possible fracture line, the mesh was refined to accommodate more general fracture mechanisms. As it is clearly comprehensible, the resulting mesh depicted in Figure 5-6 is not representative of any real pattern and the block interlocking is neglected. Moreover, in order to accommodate dry-joint elements, their sides are concentric.

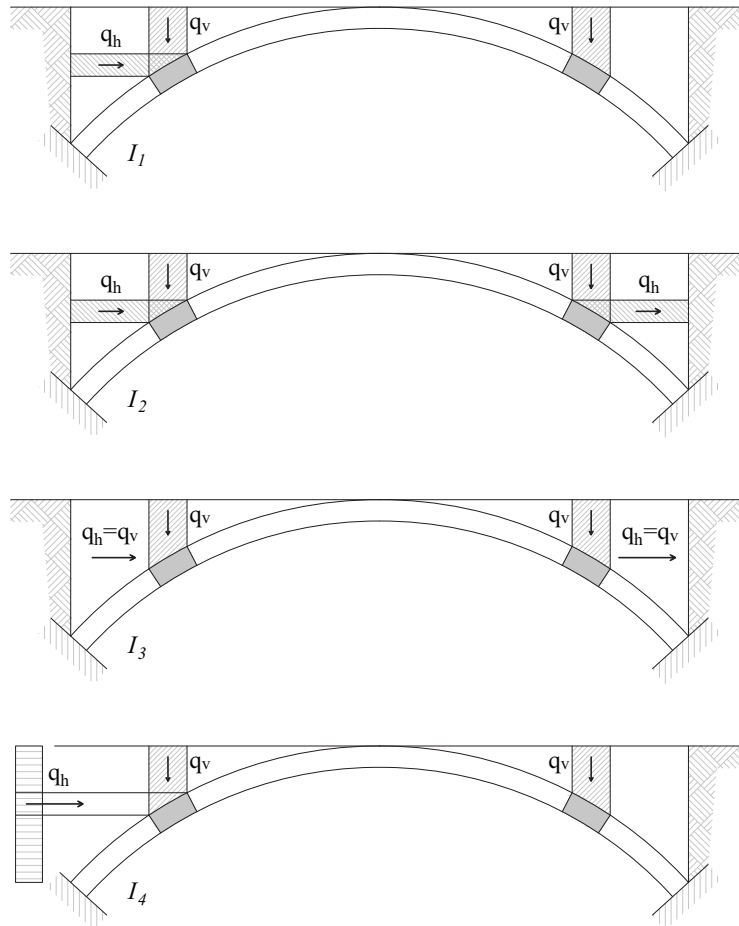


Figure 5-4. Schematization of the infill load/mass according to Clemente [1997]

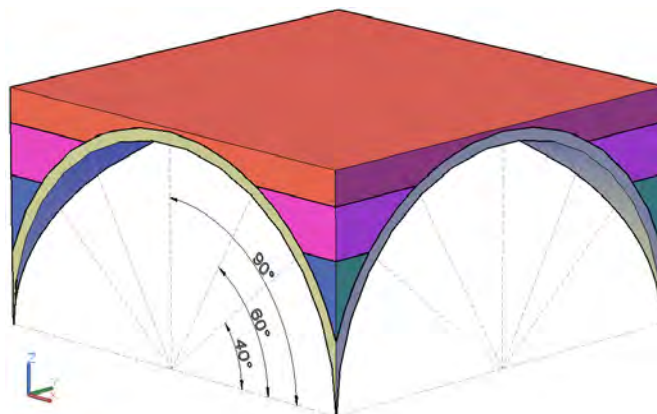


Figure 5-5. Infill schematization according to the central angle

A total of 2106 analyses were performed. As two different boundary conditions are involved, namely simply supported and in-plane shear (1053+1053 analyses), the results are split and are presented in the following two sections. Moreover, for the sake of clarity, according to Figure 5-3, the parameters are defined as:

- S span. In order to catch any possible scale effect, it is the single geometrical parameter considered as a dimensional quantity [m].
- R rise over span ratio
- Th thickness over span ratio
- I height of the infill over span ratio
- Ft tensile strength [MPa]

Regarding the infill, the categories 0, 40, 60, 90° (Figure 5-5) will be preferred if a more concise description is requested.

Mass density sound masonry	ρ_s	1.8ton/m ³
Mass density loose masonry (infill)	ρ_l	1.2ton/m ³
Compression strength	F_c	3.2MPa
Tensile strength	F_t	0.05, 0.10, 0.20MPa
Cohesion	c	1.5 F_t
Friction angle	Φ	30°
Compression linearized cap angle	Φ_2	60°

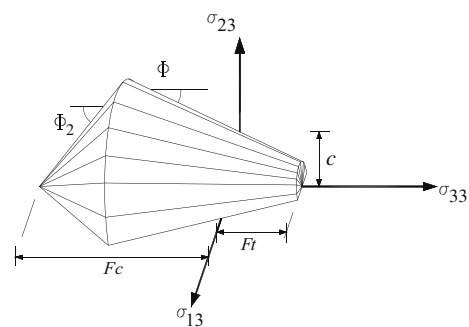


Table 5-2. Mechanical parameters adopted and piecewise linear approximation of the failure criterion [Lourenço and Rots, 1997]

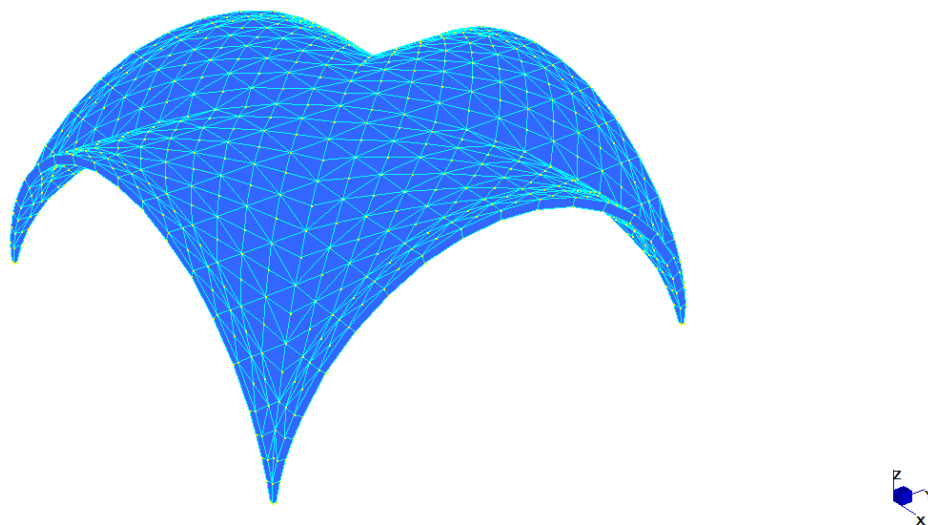


Figure 5-6. Mesh pattern adopted (e.g. $Th = 1/50$)

5.4 Simply supported vault

Considering the four different approaches proposed to model the infill, the first study was aimed at evaluating which approach provided the lowest load multipliers in the largest number of cases. Therefore, neglecting the cases with null infill and null capacity (for which a comparison cannot be made), the study involved 230 analyses (4 infill schematizations each, thus 920 cases). Accordingly, *I2* from Figure 5-4 resulted the most conservative schematization, leading also to the largest number of null capacity cases. As a consequence, in the subsequent discussion, only the results following the schematization *I2* will be considered.

5.4.1 Failure mechanisms

Considering only *I2*, 324 analyses (243 with and 81 without infill) were selected and the study was aimed at identifying the most frequent failure mechanisms. According to the wide range of input parameters adopted in the sensitivity analysis, these mechanisms can be regarded as the most plausible and representative ones for simply supported groin vaults. However, since the proposed simple schematization is based on the visual inspection by the author, it is not expected to be complete or rigorous (sometimes different cases showed a common feature). Moreover, as in the case of macro-elements (procedure widely adopted in case of masonry buildings, see Chapter 2), the mechanisms were well-defined only with a good quality masonry, which means, in the present study, larger values of Ft .

The results are collected in Table 5-3 together with the occurrence frequency. Discarding the three mechanisms with the lowest frequency (less than 1%), the main mechanisms are depicted in Figure 5-7. Since the symmetry of the problem, the mechanisms are basically in-plane, thus with strong similarity with the seismic behaviour of masonry arches. However, in case of groin vaults, the presence of the webs forces the inner hinges to locate in the central part of the vault (where the vault is more flat, thus less stiff), largely within $\pm 20^\circ$ from the crown line.

Mechanisms	Abbr.	Frequency
Four hinges	4H	49%
Two hinges and roller	2H&R	20%
Roller and two hinges	R&2H	17%
Two rollers	2R	6%
Null capacity	Null	5%
Three hinges and clamp	-	<1%
Clamp and three hinges	-	<1%
Roller, hinge and clamp	-	<1%

Table 5-3. Mechanism occurrence frequency for simply supported groin vault

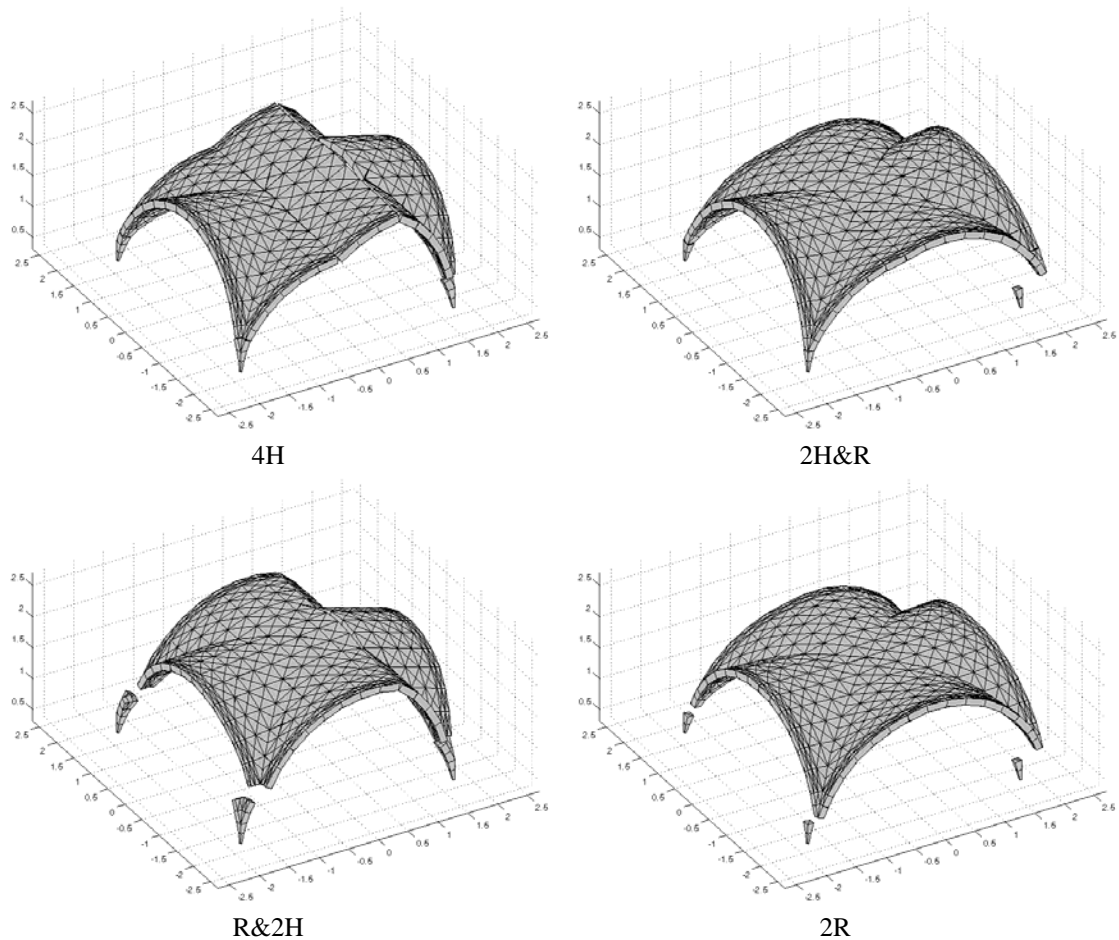


Figure 5-7. Most frequent mechanisms for simply supported groin vaults

5.4.2 Range of input parameters

Looking at the combination of the five parameters involved in the analysis, with the aim of defining a possible range of values in which a single mechanism develops, all the data have been arranged in the form of box-plots reported in Figure 5-8. According to each parameter and each mechanism, the figure shows the first, second (median) and third quartile, together with maximum, minimum values, and possible outliers (circles). In reverse, for any given set of values that describes an existing vault, it might be possible to evaluate the most plausible mechanism (or more than one in case of interval overlapping).

As can be seen, the results for infill equal to 0° and 40° are almost the same, which means that even small amount of debris at the vault corners do not affect the type of collapse failure. Further findings are collected in Table 5-4.

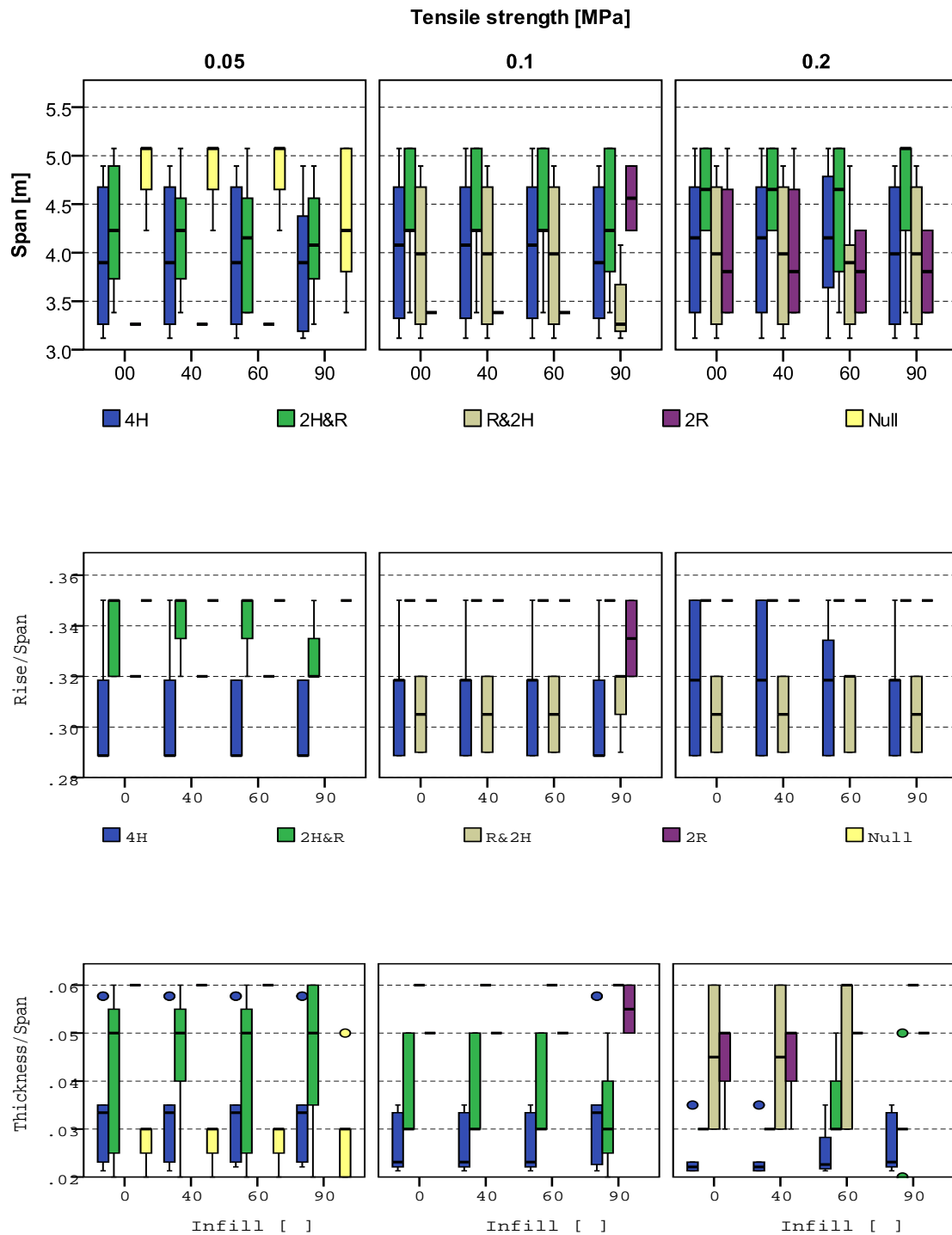


Figure 5-8. Ranges of the input parameters according to the most frequent mechanisms

	$S = [3.12, 5.07] \text{ m}$	$R = [0.29, 0.35]$ (from flat to high vaults)	$Th = [0.020, 0.060]$ (from thin to thick vaults)
4H	[3.12, 5.07] with a very slight reduction if infill is 90°	[0.29, 0.35] Larger F_t , larger R Larger infill, lower R	[0.021, 0.035] except for isolated cases (corresponding to min R)
2H&R	[3.38, 5.07]	[0.32, 0.35] if $F_t=0.05$ MPa. $R=0.35$ with larger F_t	[0.020, 0.060] if $F_t=0.05$ MPa, lower values for larger F_t
R&2H	[3.12, 4.89] with no substantial trends	[0.29, 0.32] with no substantial trends	Generally $Th = 0.060$. If $F_t = 0.20$ MPa and infill up to 60°, $Th = [0.030, 0.060]$
2R	[3.26, 3.38] if $F_t=0.05$ and 0.10MPa, except one isolated case. [3.38, 5.07] if $F_t=0.20$ MPa, lower values for larger infill	$R=0.32$ if $F_t=0.05$ MPa $R=0.35$ if $F_t=0.10$ and 0.20MPa (except one isolated case)	$Th=0.060$ if $F_t=0.05$ MPa $Th=0.050$ if $F_t=0.10$ and 0.20MPa (except few isolated cases)
Null	[4.23, 5.07] except two isolated cases with infill 90° where $S=3.38$	$R=0.35$	$Th < 0.030$, except one isolated case with infill 90° where $Th =0.050$

Table 5-4. Variation of the input parameters according to the most frequent mechanisms

In order to have a more qualitative idea regarding the occurrence of the mechanisms, Figure 5-9 reports the number of times they developed according to the input parameters. From the first two charts it is clearly visible that the span S and height of infill I do not produce significant changes in terms of number of occurrences, unless for the null capacity, which is more frequent with larger span. Moreover, as stressed above, the results with infill 0° and 40° are practically the same.

Considering the rise R , only 4H and R&2H are associated to a value of 0.29 (flatter vault). On the other hand, if $R=0.35$ (the highest vaults of the database), R&2H never occurred. $R=0.35$ is also the single value which leads to vaults with null capacity. Generally, increasing R (that is, from flat to high-rise vaults), the occurrence of 4H decreases, unlike 2H&R and 2R which increases.

Regarding the thickness, moving from thin to thick vaults, the occurrence of 4H decreases whereas 2H&R and R&2H's increases. Moreover, the value $Th=0.02$ leads to only two mechanisms (and vaults with null capacity), namely 4H and 2H&R, with a strong prevalence of the former. Furthermore, with the highest values of Th , almost all the vaults have a capacity larger than zero and a significant occurrence of 2R is now notable.

Finally, regarding the tensile strength, the lowest value (0.05 MPa) does not lead to R&2H but, as expected, it is the only one which leads to null capacity vaults. Increasing the strength, two trends can be observed, namely 2H&R (decreasing), and 2R and R&2H (increasing). The mechanism 4H does not present any significant variation.

Finally, the comparison in terms of load multiplier (λ) is reported in Figure 5-10. In general, the

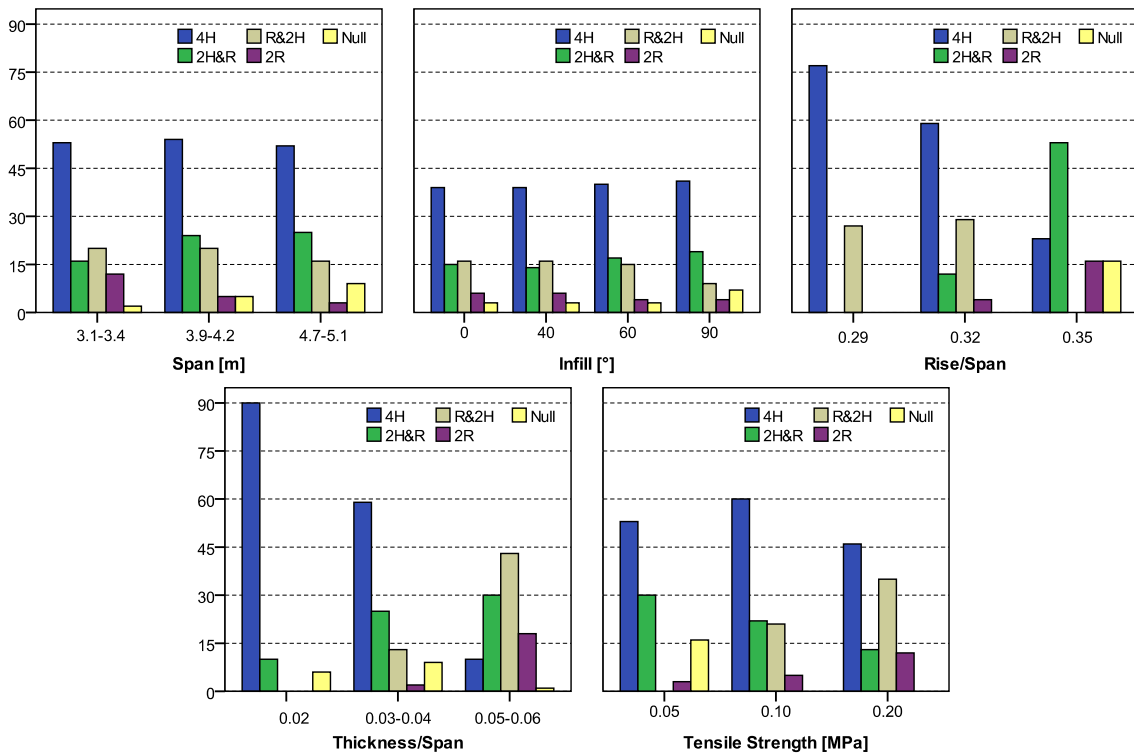


Figure 5-9. Frequency of the most frequent mechanisms according to the input parameters

capacity of the vault decreases as the span, the infill and the rise increase. On the other hand, it is possible to catch an inverse relationship with the tensile strength. Regarding the thickness, there is a positive relation in case of 4H and 2H&R, whereas it is negative in case R&2H and 2R are considered. Regarding the horizontal load multiplier λ associated to each mechanism, 2H&R provided the lowest range (up to 0.87) whereas 4H and 2R set upon medium ones (a wider interval for the former). R&2H, instead, got values of λ notably larger within [0.90, 2.64].

In general, since the clear trend associated to rise and tensile strength, according to the database considered, they can be addressed as the most crucial parameters in determining the capacity of simply supported groin vaults.

5.4.3 Multiple linear regression analysis (MLR)

MLR is a very well-known technique which allows finding (linear) relations between dependent and independent variables (predictors), that is, between the load multiplier λ and the input parameters. In order to apply MLR, a linear relation between the predictors and λ is assumed. Although the relation between the variables is non-linear, this approach is still valid when a first order relation is sought. The general prediction formula is reported in Equation (5-9). In the following, the estimated values will be indicated with an overline. For instance, the value from the limit analysis is labelled as λ whereas the one from the regression model as $\bar{\lambda}$:

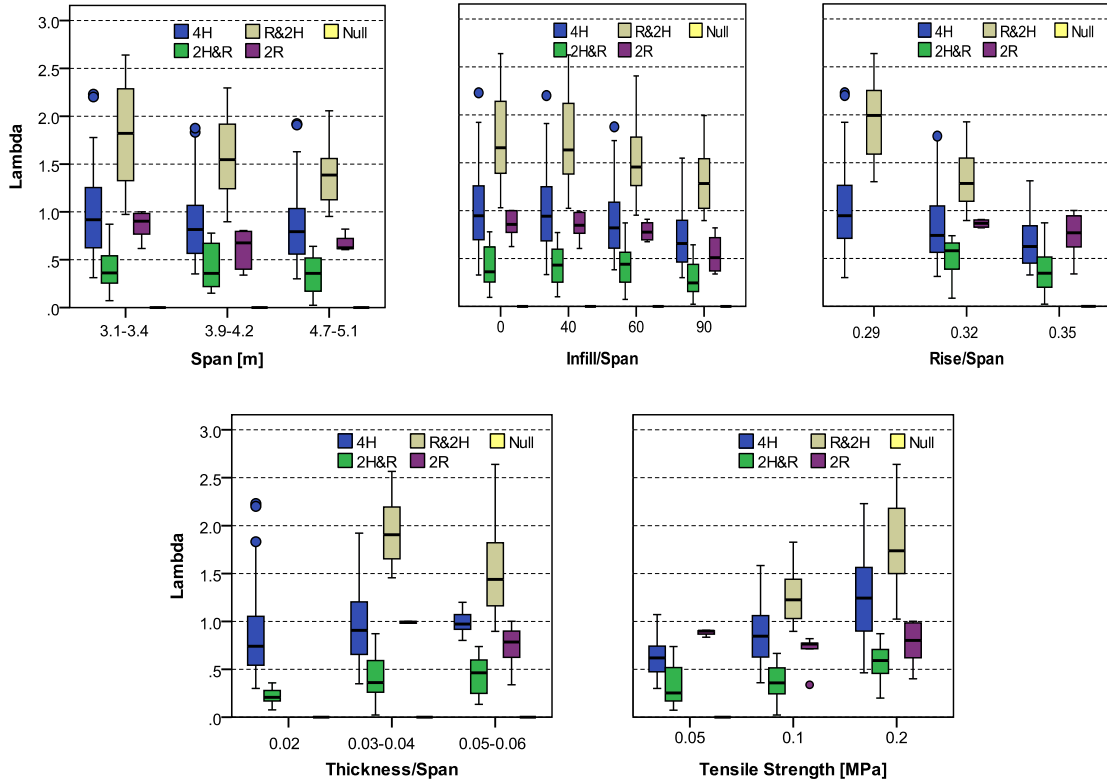


Figure 5-10. Variation of the load multiplier according to the failure mechanisms and the input parameters

$$\begin{aligned} \bar{\lambda}_k &= \bar{\beta}_0 + \sum_{i=1}^p \bar{\beta}_i x_{ki} & k = 1 \dots n \\ \bar{\lambda} &= \mathbf{X} \bar{\beta} \\ \bar{\lambda} &= \begin{bmatrix} \bar{\lambda}_1 \\ \bar{\lambda}_2 \\ \vdots \\ \bar{\lambda}_n \end{bmatrix} & \bar{\beta} = \begin{bmatrix} \bar{\beta}_0 \\ \bar{\beta}_1 \\ \vdots \\ \bar{\beta}_p \end{bmatrix} & \mathbf{X} = \begin{bmatrix} 1 & x_{11} & x_{12} & \dots & x_{1p} \\ 1 & x_{21} & x_{22} & \dots & x_{2p} \\ \vdots & \vdots & \vdots & \dots & \vdots \\ 1 & x_{n1} & x_{n2} & \dots & x_{np} \end{bmatrix} \end{aligned} \quad (5-9)$$

where $\bar{\lambda}$ is the vector of the k observations, $\bar{\beta}$ the vector of the regression coefficients ($\bar{\beta}_0$ is the intercept at the origin), \mathbf{X} is the design matrix with p predictors, namely S , R , Th , I and Ft . It must be stressed that there is no need to discuss about multicollinearity because each parameter has its own physical meaning. This approach, although lacking of a deep physical support, is still considered appropriate for having valuable information (even only mathematical) to predict the horizontal load multiplier and to assess the influence of each parameter. Finally, in order to get rid of less significant parameters, a procedure named Stepwise Regression is adopted. This procedure allows to identify the smallest possible set of predictors with a significance close to the maximum. According to this method, given a set of independent variables, each of them is

evaluated under both forward selection and backward deletion. Shortly, predictors are entered in Equation (5-9) one at a time only if they meet a statistical criteria (F-test with 5% significance), but they may also be deleted at any step where they no longer contribute significantly to the regression model (F-test with 10% significance).

In order to determine the unknown regression coefficients of $\bar{\beta}$ in Equation (5-9), the Ordinary Least Square method is applied, which is based on the minimization of the sum of squared residuals (defined as the differences between the observed values and the estimated values). The values of the regression coefficients are collected in the following equations, where S and Ft are in [m] and [MPa], respectively, and all the other parameters are dimensionless.

$$\bar{\lambda}_{4H} = 2.58 - 0.17S - 5.91R + 14.24Th - 1.34I + 5.86Ft \quad (5-10)$$

$$\bar{\lambda}_{2H\&R} = 3.70 - 0.13S - 9.38R + 6.77Th - 0.51I + 3.34Ft \quad (5-11)$$

$$\bar{\lambda}_{R\&2H} = 7.08 - 0.24S - 17.07R - 1.21I + 5.41Ft \quad (5-12)$$

$$\bar{\lambda}_{2R} = 1.42 - 0.14S - 0.61I \quad (5-13)$$

According to the previous considerations, the results of MLR are shown in form of scatter diagrams in Figure 5-11, where the limit analysis outcomes are reported in abscissa and the predicted values in ordinate, i.e. underestimated values below the bisector. As it is possible to see, the simple relations proposed for determining $\bar{\lambda}$ are in good agreement with the limit analysis results. In the diagrams, the coefficient of determination R^2 is also reported for each model, being considerably high, except for the 2R model for which the poor database did not allow a more accurate prediction.

However, given the large difference of the regression coefficients (and the predictors) in terms of orders of magnitude, with the aim of giving a qualitative indication on how much they are significant to describe the variation of $\bar{\lambda}$, the standardized regression coefficients are considered. They are obtained standardizing all the variables in the MLR, that is, setting the mean to zero and the standard deviation (SD) to one, conveying thus information in SD units: the regression coefficients represent the change in response (in terms of SD) for a change of one SD of a predictor. Although very appealing, this information is strictly connected to the input database and the relative distribution of each of the independent and dependent variable, that is, the methodology puts in relation the true SD of the variables in the database.

Nevertheless, as the predictors become now dimensionless and of the same scale, it is possible to compare the magnitude of the standardized regression coefficients to see which predictor is more effective in each model, and how their effectiveness changes between the models. All the results are collected in Table 5-5.

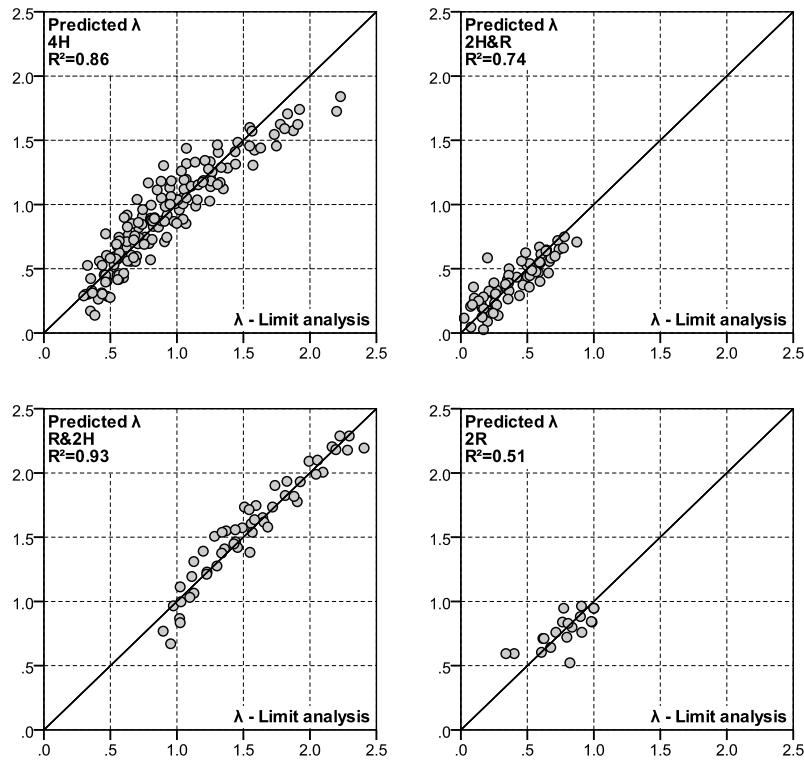


Figure 5-11. Scatter plots of the prediction models according to MLR

	Span	Rise/span	Thickness/span	H infill/span	Tensile strength
4H	-0.275	-0.317	0.327	-0.411	0.860
2H&R	-0.399	-0.542	0.408	-0.337	0.883
R&2H	-0.335	-0.541	-	-0.320	0.558
2R	-0.476	-	-	-0.478	-

Table 5-5. Standardized regression coefficients

In general, the tensile strength is the most important parameter except for 2R in which its effectiveness is zero. On the other hand, considering R&2H, the rise has the same effectiveness of the tensile strength whereas the span and infill plays a similar role (the thickness does not contribute). Finally, regarding 2R, only span and infill are involved with an equal importance.

Looking at the overall trend between the models, all the coefficients are positive for tensile strength and thickness, thus the larger they are, the larger the capacity is. On the other hand, all the others coefficients are negative with the inverse meaning. Moreover, as expected, since the stresses are considered, the scale effect is an important issue highlighted by the coefficients of the span, which is the only dimensional parameter, being crucial in pure sliding mechanism (2R).

5.4.4 Characteristic value and uncertainties

As shown in the previous subsection, for a given set of predictors, the fitted models of the MLR provide single values that can be considered as the average taken over a range of likely values. If higher precision is required, confidence intervals are usually recommended, i.e. the interval where the average value may fall within a given confidence level. Following the indications of the current Codes of Practice, the confidence level is often equal to 90% and the lower value is referred as 5% fractile, i.e. the value that have the 95% of possibility of being exceeded. It is possible to compute confidence intervals for either the mean of likely values or for the single likely value. However, for the purpose of the present study, only the approach for the individual prediction is presented.

Without entering into the merits of statistical details, for which the reader is referred to standard literature, e.g. [Bulmer, 1979; Draper and Smith, 1998], the simple relation for calculating the confidence interval reads:

$$\frac{\bar{\lambda}_{k,0.95}}{\bar{\lambda}_{k,0.05}} = \bar{\lambda}_k \pm t_{0.05,(n-p-1)} SD_k \quad (5-14)$$

where $\bar{\lambda}_k$ is the predicted value, $t_{0.05,(n-p-1)}$ is the critical t-value which is exceeded with probability 0.05 in a t-distribution with $n-p-1$ degrees of freedom (DOF), n is the number of samples and p is the number of predictors involved in the model (the unit stands for the intercept). The standard deviation of the single prediction can be calculated according to the following relations:

$$SD_k = SD_{\bar{\lambda}} \sqrt{(1 + \mathbf{x}'_k (\mathbf{X}'\mathbf{X})^{-1} \mathbf{x}_k)} \quad (5-15)$$

$$\mathbf{x}'_k = [1, x_1, \dots, x_p] \quad (5-16)$$

$$SD_{\bar{\lambda}} \cong \sqrt{\frac{\sum (\lambda_i - \bar{\lambda}_i)^2}{n - p - 1}} \quad (5-17)$$

where \mathbf{x}_k represents the vector of the set of parameters for which the prediction is requested, \mathbf{X} is the design matrix described in Equation (5-9), and $SD_{\bar{\lambda}}$ is the standard deviation of the regression model, which is constant for each model. Since the radicand in Equation (5-15) is typically slightly larger than 1, it is possible to assume $SD_k \approx SD_{\bar{\lambda}}$ and get a quick estimation of the 5% fractile (although not on the safe side). According to the database of the sensitivity analysis and Equation (5-14), Table 5-6 reports all the calculated quantities, where $\Delta\lambda \cong t_{0.05,(n-p-1)} SD_k$ stands for the average quantity may be subtracted from the predicted value $\bar{\lambda}_k$ in order to get the 5% fractile $\bar{\lambda}_{k,0.05}$.

Model	DOF = n-p-1	$t_{0.05,DOF}$	$SD_k \approx SD_{\bar{\lambda}}$	$\Delta\lambda$
4H	153	1.65	0.16	0.26
2H&R	59	1.67	0.11	0.19
R+2H	51	1.68	0.13	0.21
2R	17	1.74	0.14	0.24

Table 5-6. Calculation for the 5% fractile of the predicted values

In order to conclude this section, it must be stressed that the present study did not take into account the measurement uncertainties. This is a crucial aspect especially for the tensile strength, which is difficult to be evaluated and, at the same time, addressed as one of the most important and decisive parameters. With the aim of taking into account this aspect, the propagation of the variance associated with the measurements should be calculated. Considering predictors not correlated, given a general expression that links the $\bar{\lambda}$ to p variables in Equation (5-18), the variance of $\bar{\lambda}$ (equal to the square root of the standard deviation SD) can be computed as the summation of the square partial derivative times the variance of the predictors, see Equation (5-19).

$$\bar{\lambda} = f(x_1, x_2, \dots, x_p) \quad (5-18)$$

$$SD_{\bar{\lambda}}^2 = \left(\frac{\delta\bar{\lambda}}{\delta x_1}\right)^2 SD_{x_1}^2 + \left(\frac{\delta\bar{\lambda}}{\delta x_2}\right)^2 SD_{x_2}^2 + \dots + \left(\frac{\delta\bar{\lambda}}{\delta x_p}\right)^2 SD_{x_p}^2 \quad (5-19)$$

However, considering the outcome of MLR, since the regression coefficients of the polynomial expression are affected by uncertainties too, the formula becomes rather complicated, going beyond the scope of the present work.. On the other hand, in case the regression coefficients are considered with no uncertainties, the partial derivatives coincide with the regression coefficients, a simpler relation reads:

$$SD_{\bar{\lambda}} = \sqrt{\bar{\beta}_1^2 SD_{x_1}^2 + \bar{\beta}_2^2 SD_{x_2}^2 + \dots + \bar{\beta}_p^2 SD_{x_p}^2} \quad (5-20)$$

5.5 In-plane shear

This section is similar to the previous one and the reader is referred to it for further explanations. In particular, the infill schematization *I2* resulted again the most conservative one, leading also to the largest number of null capacity cases. Consequently, in the discussion below, only the results following the schematization *I2* will be considered.

5.5.1 Failure mechanisms

Considering only *I2*, 324 analyses (243 with and 81 without infill) were selected. Within the context of the kinematic approach of the limit analysis, the study was aimed at identifying the most frequent failure mechanisms, which can be regarded as the most plausible and representative ones for the groin vault subjected to in-plane shear.

The results are collected in Table 5-7 together with the occurrence frequency. Given the three-dimensional behaviour of the vault, a larger amount of mechanisms was detected and only the ones that covered 90% of all the cases will be considered in the following. Three bending (B) and three sliding (S) mechanisms were detected, together with the one labelled as “diagonal” (D). All of them are depicted in Figure 5-12.

Mechanisms	Abbreviation	Frequency
Bending 1	B1	30%
Sliding 1	S1	12%
Sliding 2	S2	10%
Diagonal	D	10%
Bending 2	B2	9%
Bending 3	B3	8%
Null	Null	7%
Sliding 3	S3	3%
Others	-	<10%

Table 5-7. Mechanism occurrence frequency for groin vaults subjected to in-plane shear

5.5.2 Range of input parameters for each mechanism

Given the difficulties posed by the combination of the five parameters in achieving a straightforward range of values in which a single mechanism develops, all the data have been arranged in the form of box-plots reported in Figure 5-13. In reverse, for any given set of parameters that describe a real vault, it is possible to evaluate the most plausible mechanism (or more than one in case of interval overlapping). Also in this case, the range of parameters for infill equal to 0° and 40° are almost the same, which means that even a small amount of debris at the vault corners does not affect the type of collapse failure (at least for static loading).

In general, since the notable difficulty arising from three-dimensional mechanisms, only the main findings are reported in Table 5-8, neglecting the trends based on only a few cases.

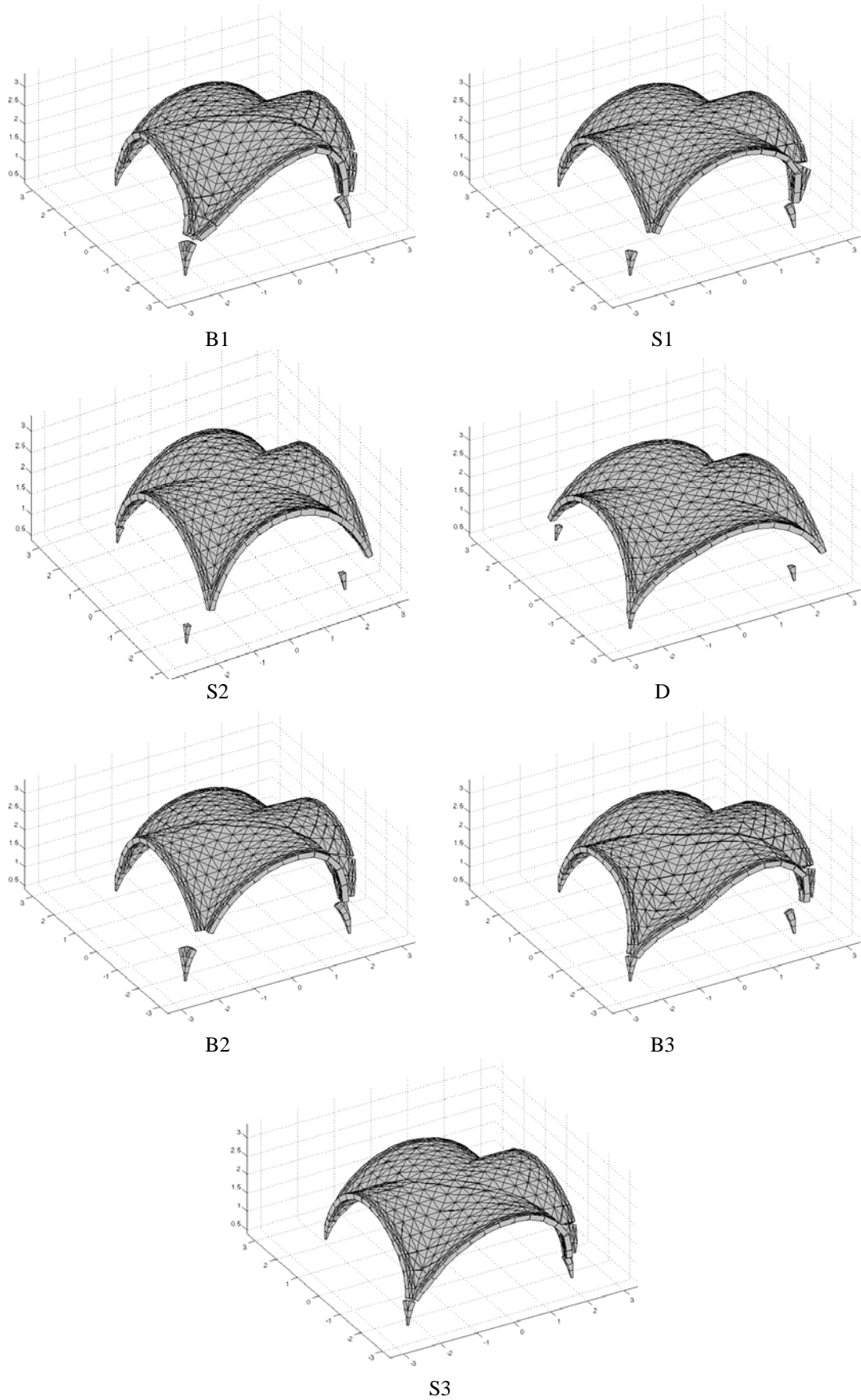


Figure 5-12. Most frequent mechanisms for groin vaults subjected to in-plane shear

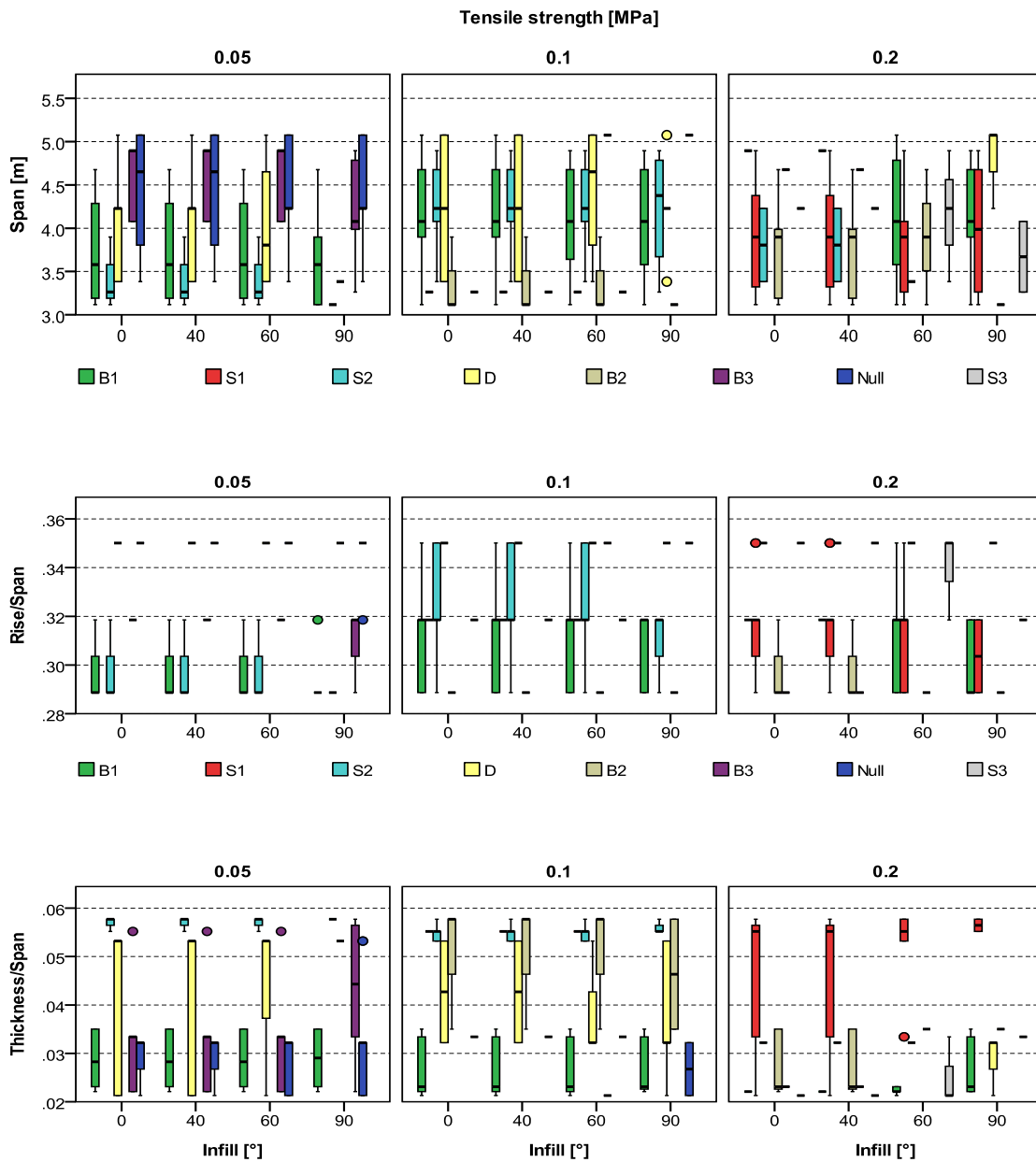


Figure 5-13. Ranges of the input parameters for each failure mechanism (in-plane shear)

In order to have a more qualitative idea regarding the occurrence of the mechanisms, Figure 5-14 reports the number of times that the mechanisms developed according to the input parameters. The increment of the span does not produce significant changes, unless for B2 occurrence, which decreases, and B3 and Null's which increase. Regarding the presence of the infill, the results with infill 0° and 40° are practically the same. Moreover, incrementing the level of the infill (from bare to completely covered vault), S1, S2 and B2 occurrence decreases, whereas the occurrence of null capacity vaults increases.

	$S = [3.12, 5.07] \text{ m}$	$R = [0.29, 0.35]$ (from flat to high vaults)	$Th = [0.020, 0.060]$ (from thin to thick vaults)
B1	[3.12, 5.07] Lower values if $F_t=0.05\text{MPa}$	Generally within [0.29, 0.32]	[0.021, 0.035]
S1	[3.12, 4.89] Only if $F_t=0.20\text{MPa}$	[0.29, 0.35] generally low values	[0.020, 0.060], larger values for higher infill
S2	[3.12, 3.90] if $F_t=0.05\text{MPa}$ [3.26, 4.89] if $F_t=0.10\text{MPa}$ [3.38, 4.23] if $F_t=0.20\text{MPa}$	[0.29, 0.35] the larger F_t , the higher rise	[0.053, 0.058] $Th=0.032$ if $F_t=0.20\text{MPa}$
D	[3.38, 5.07] If $F_t=0.20$, only with infill 90	$R=0.35$	[0.021, 0.053] lower values for larger F_t .
B2	[3.12, 3.90] if $F_t=0.10\text{MPa}$ [3.12, 4.68] if $F_t=0.20\text{MPa}$	$R=0.29$ if $F_t=0.10\text{MPa}$ [0.29, 0.32] if $F_t=0.20\text{MPa}$	[0.035, 0.058] if $F_t=0.10\text{MPa}$ [0.022, 0.035] if $F_t=0.20\text{MPa}$
B3	[3.26, 4.89] lower values if $F_t=0.05\text{MPa}$, and infill 90°	[0.29, 0.32] lower values if $F_t=0.05\text{MPa}$, and infill 90°	[0.020, 0.060] generally higher values if infill is 90°
Null	[3.38, 5.07] if $F_t=0.05\text{MPa}$	$R=0.32$	[0.021, 0.032]
S3	[3.26, 4.89] only if $F_t=0.20\text{MPa}$ and infill 60°, 90°	[0.32, 0.35]	[0.021, 0.033]

Table 5-8. Variation of the input parameters according to the most frequent mechanisms of groin vaults subjected to in-plane shear

Considering the rise, from flat to high-rise vault, only B1 and B2 show a decreasing trend. S1 and B3 have a maximum in frequency in the mid-size vault, whereas D and Null are present only in the highest vault. Regarding the thickness, moving from a thin to thick vault, two clear trends are identifiable: B1 decreases whereas S1 and S2 increases. Null and S3 are basically present only in medium-small thickness vaults, and D and B3 have a minor variation, increasing and decreasing respectively. Finally, looking at the material properties, Null and B3 are present only in case of low F_t , whereas S1, B2 and S3 are present only with higher values, with the occurrence increasing as the F_t increases. D is the only mechanism that decreases as F_t increases, whereas B1 and S2 have a maximum in frequency with the medium value of the tensile strength.

Finally, the comparison in terms of load multiplier (λ) is reported in Figure 5-15. In general, the capacity of the vault decreases as the infill and the rise increase. On the other hand, it is possible to catch an inverse relationship with the tensile strength. Regarding the other parameters, there are no appreciable trends. However, in general, according to the obtained database and this boundary condition, the groin vaults with $R=0.35$ and $F_t=0.05\text{MPa}$ lead to a horizontal load multiplier lower than 0.8, whereas the largest values can be reached only with S1 and B2 mechanisms.

SEISMIC PERFORMANCE OF MASONRY CROSS VAULTS

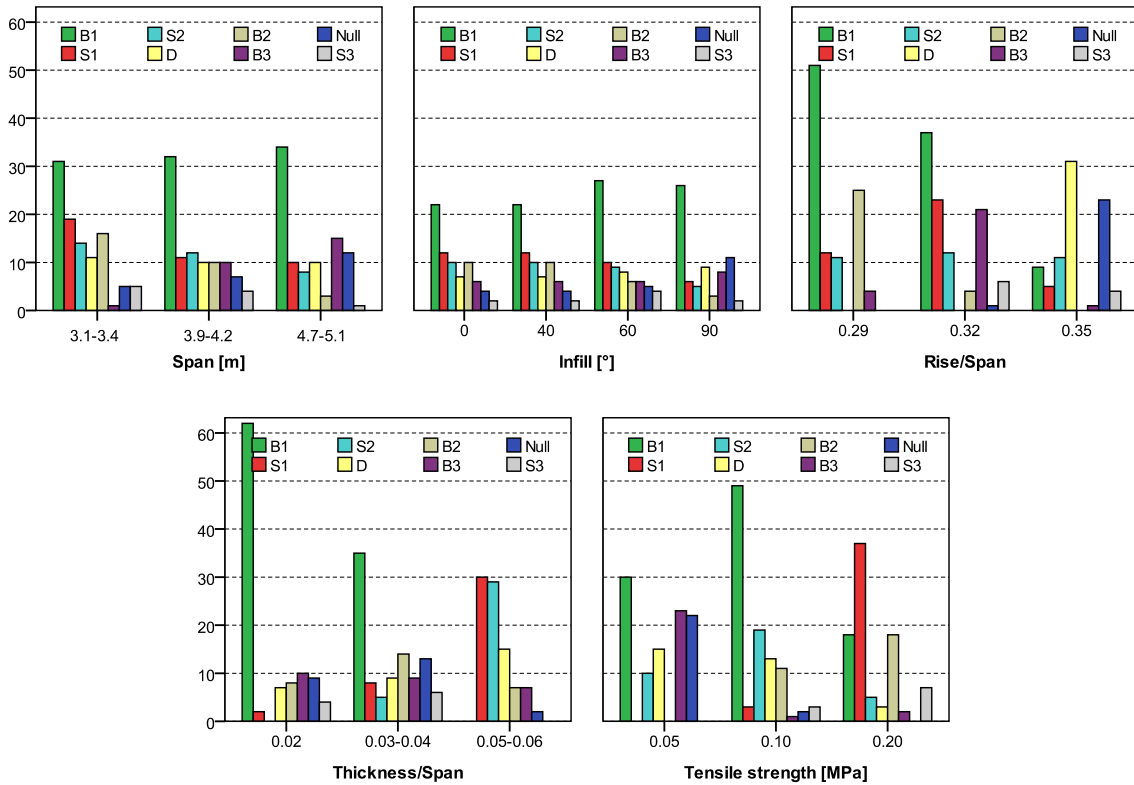


Figure 5-14. Frequency of the most frequent mechanisms according to the input parameters for groin vaults subjected to in-plane shear

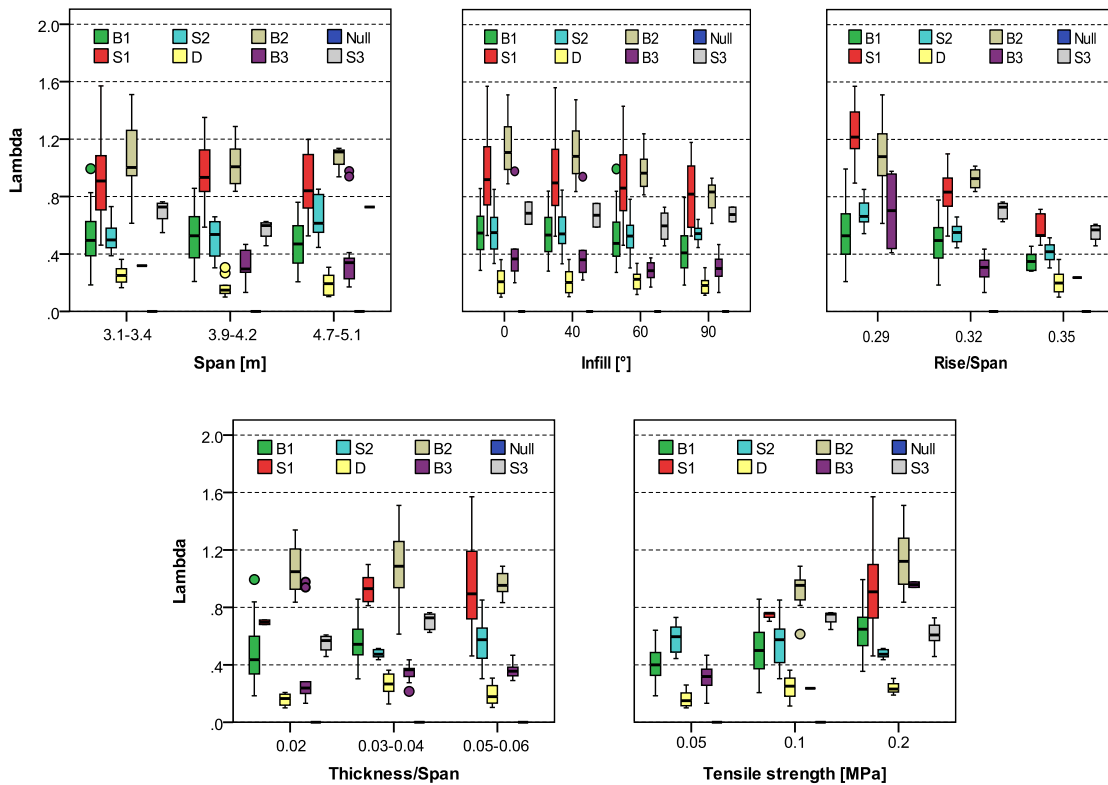


Figure 5-15. Variation of the load multiplier according to the most frequent mechanisms and the input parameters for groin vaults subjected to in-plane shear

5.5.3 Multiple linear regression analysis

According to what described in §5.4.3, the results of MLR are reported in form of scatter diagrams in Figure 5-16, whereas the values of the regression coefficients are collected in the following equations, where S and Ft are measured in [m] and [MPa], respectively, and all the other parameters are dimensionless.

$$\bar{\lambda}_{B1} = 1.06 - 0.92S - 2.23R + 12.72Th - 0.82I + 2.93Ft \quad (5-21)$$

$$\bar{\lambda}_{S1} = 5.83 - 1.79S - 13.95R - 3.68Th - 0.70I + 2.34Ft \quad (5-22)$$

$$\bar{\lambda}_{S2} = 1.54 - 0.73S - 6.27R + 17.24Th - 0.32I + 4.42Ft \quad (5-23)$$

$$\bar{\lambda}_D = 0.36 - 0.81S - 0.23I + 2.40Th + 1.63Ft \quad (5-24)$$

$$\bar{\lambda}_{B2} = 3.23 - 1.80S - 8.30R + 7.96Th - 1.03I + 4.46Ft \quad (5-25)$$

$$\bar{\lambda}_{B3} = 1.31 - 0.69S - 3.07R + 4.28Th - 0.36I + 3.86Ft \quad (5-26)$$

$$\bar{\lambda}_{S3} = 0.32 + 13.80Th - 0.32I \quad (5-27)$$

As it is possible to see in Figure 5-16, the simple relationships proposed for determining $\bar{\lambda}$ are in good agreement with the limit analysis results. In the diagrams the coefficient of determination R^2 is reported for each model, being rather high except for the D mechanism (with values lower than 0.4).

Considering the standardized regression coefficients, all the results are collected in Table 5-9.

	Span	Rise/span	Thickness/span	H infill/span	Tensile strength
B1	-0.357	-0.262	0.434	-0.585	0.886
S1	-0.413	-0.963	-0.148	-0.312	0.222
S2	-0.325	-1.131	1.069	-0.294	1.518
D	-0.711	-	0.410	-0.412	0.919
B2	-0.476	-0.428	0.509	-0.551	1.085
B3	-0.167	-0.205	0.301	-0.247	0.815
S3	-	-	0.871	-0.417	-

Table 5-9. Standardized coefficients for groin vaults subjected to in-plane shear

In general, the tensile strength is always the most important parameter except for S1 and S3, in which the rise and the thickness are the most important parameters, respectively. On the other hand, the rise plays a significant role in S1 and S2. The span and the infill have no decisive roles. Finally, S3, although based on few cases, is governed exclusively by thickness and infill, almost two third and one third respectively.

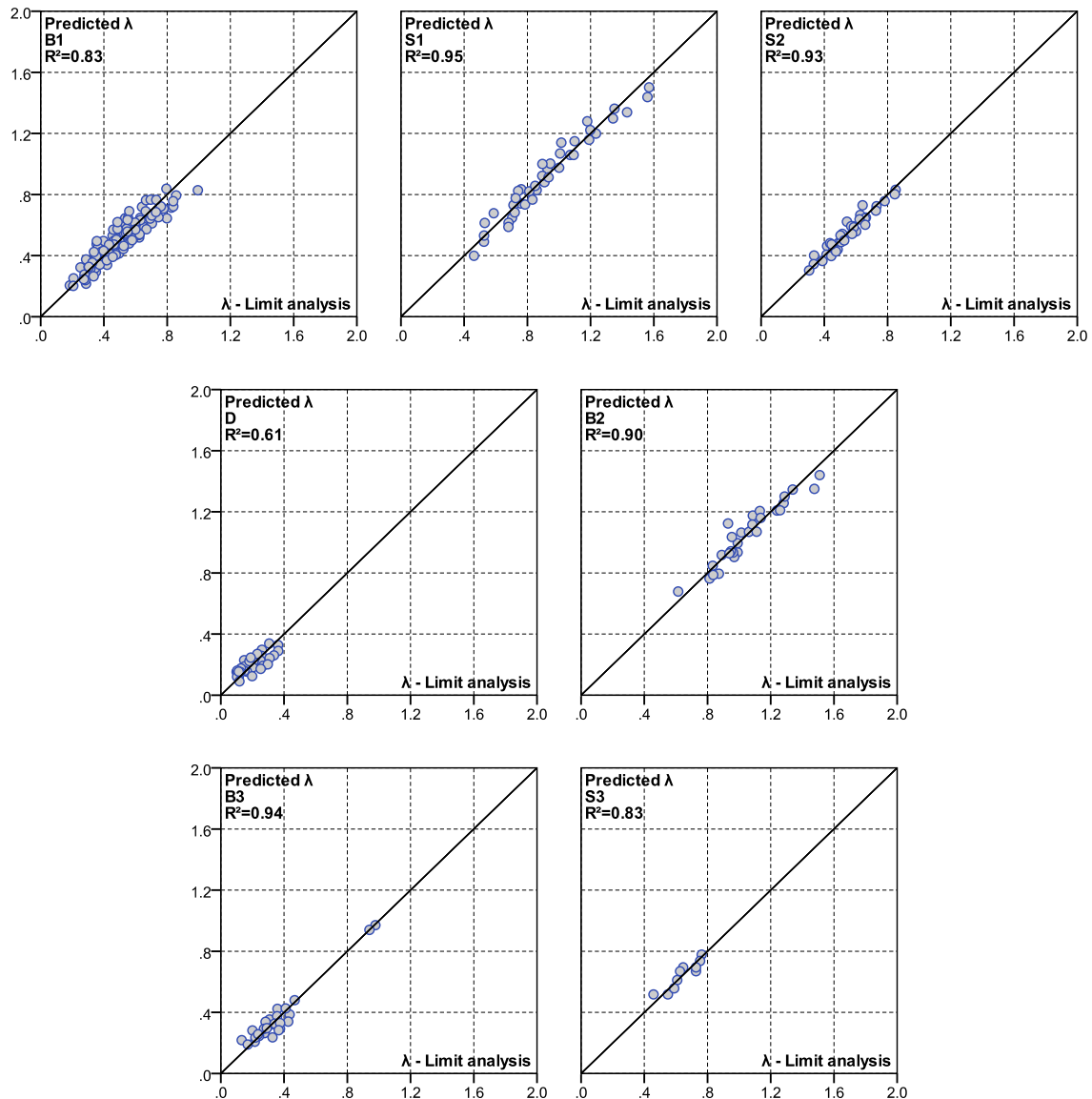


Figure 5-16. Scatter plots of the prediction models according to MLR (in-plane shear)

Looking at the overall trend between the models, all the coefficients are positive for tensile strength and thickness (except for S1), thus the larger they are, the larger the capacity. On the other hand, all the other coefficients are negative with the inverse meaning. Moreover, as expected, when the stresses are considered, the scale effect is an important issue highlighted by the coefficients of the span, which is the only dimensional parameter.

5.5.4 Characteristic value and uncertainties

According to §5.4.4, Table 5-10 reports all the calculated quantities to get the 5% fractile $\bar{\lambda}_{k,0.05}$. For further comments on the measurement uncertainties and the propagation of the variance associated with the measurements, the reader is referred to §5.4.4.

Model	DOF = n-p-1	$t_{0.05,DOF}$	$SD_k \approx SD_{\lambda}$	$\Delta\lambda$
B1	91	1.66	0.07	0.12
S1	34	1.69	0.07	0.12
S2	28	1.70	0.04	0.07
D	26	1.71	0.05	0.09
B2	23	1.71	0.07	0.12
B3	20	1.72	0.05	0.09
S3	7	1.89	0.05	0.09

Table 5-10. Calculation for the 5% fractile of the predicted values

5.6 Summary

This chapter has presented the results of a sensitivity analysis on the seismic capacity of masonry groin vaults. The objective was to investigate the influence of the geometrical parameters, as well as the tensile strength, the boundary conditions, and the presence of the infill. The main outcomes of this study can be summarized as follows.

Although approximated, among the four infill schematizations examined, considering the contribution of horizontal stripes on both sides of the vault provided the lowest load multipliers in the largest number of cases. Regarding the boundary conditions, the simply supported vault showed, as expected, a behaviour similar to the masonry arch one. However, the presence of perpendicular webs forced the internal hinges to locate close to crown where the stiffness is lower. On the other hand, the vault subjected to in-plane shear showed a more complicated behaviour and more effort is still requested on this configuration.

In general, the visual inspection of the deformed shapes allowed detecting four and seven elementary mechanisms for fully supported vault and in-plane shear, respectively. Although this approach need to be validated by experimental evidences and more sophisticated analyses, the failure mechanisms individuated may shed light on the structural behaviour of the vault. Moreover, a possible schematization by means of arch of variable thickness and equivalent arch assemblage (respectively), may represent a valuable support for further studies and in the professional field.

Finally, the Multiple Linear Regression analysis (based on the inspection of the failure mechanisms) provided valuable results that can support the analyst in assessing the seismic capacity of groin vaults. Future steps may interest their validation with experimental tests and more sophisticated analyses. In addition, in order to evaluate the effect of measurements uncertainties on the capacity of the vault, Monte Carlo simulations may be advisable.

References

- Bulmer, M. G. (1979). *Principles of Statistics*. Courier Corporation.
- Cavicchi, A., and Gambarotta, L. (2005). Collapse analysis of masonry bridges taking into account arch–fill interaction. *Engineering Structures*, 27(4), 605–615.
- Cavicchi, A., and Gambarotta, L. (2006). Two-dimensional finite element upper bound limit analysis of masonry bridges. *Computers & Structures*, 84(31-32), 2316–2328.
- Chvatal, V. (1983). *Linear Programming*. New York: W.H. Freeman and Company.
- Clemente, P. (1997). *La verifica degli archi a conci lapidei*. ENEA, Unità comunicazione e informazione.
- CM. (2009). Instruction for the application of the Building Standard for Constructions. G.U. n. 47 del 26-2-2009. Suppl. Ordinario n.27 – Circolare 2 febbraio 2009, n. 617; 2009 [in Italian].
- Croci, G. (2000). General methodology for the structural restoration of historic buildings: the cases of the Tower of Pisa and the Basilica of Assisi. *Journal of Cultural Heritage*, 1(1), 7–18.
- Draper, N. R., and Smith, H. (1998). *Applied regression analysis, Volume 1* (3rd ed.). Wiley.
- Gilbert, M. (2001). RING: A 2D rigid block analysis program for masonry arch bridges. In *3rd International Arch Bridges Conference* (pp. 109–118). Paris.
- Krabbenhoft, K., Lyamin, A. V., Hjjaj, M., and Sloan, S. W. (2005). A new discontinuous upper bound limit analysis formulation. *International Journal for Numerical Methods in Engineering*, 63(7), 1069–1088.
- Lourenço, P. B. (2002). Computations on historic masonry structures. *Progress in Structural Engineering and Materials*, 4(3), 301–319.
- Lourenço, P. B., and Rots, J. G. (1997). Multisurface interface model for analysis of masonry structures. *Journal of Engineering Mechanics*, 123(7), 660–668.
- Milani, G., and Lourenço, P. B. (2012). 3D non-linear behavior of masonry arch bridges. *Computers & Structures*, 110-111, 133–150.
- Milani, G., Milani, E., and Tralli, A. (2009a). Upper Bound limit analysis model for FRP-reinforced masonry curved structures. Part I: Unreinforced masonry failure surfaces. *Computers & Structures*, 87(23-24), 1516–1533.
- Milani, G., Milani, E., and Tralli, A. (2009b). Upper bound limit analysis model for FRP-reinforced masonry curved structures. Part II: Structural analyses. *Computers & Structures*, 87(23-24), 1534–1558.
- Wolsey, L. A. (1998). *Integer programming*. New York: John Wiley and Sons.

Chapter 6.

Conclusions

6.1 Summary of results

The present dissertation have dealt with the seismic behaviour of masonry groin vaults by means of experimental tests and numerical analyses. The motivation and the objectives of this work have been discussed in the introduction and throughout the thesis. In brief, and in the words of several scholars of the past (although referring to the design of new constructions), a proper knowledge of the structural element may avoid unpleasant and drastic interventions that could compromise the charm and originality of cultural heritage buildings [Jacopo Barozzi da Vignola, 1562; Scamozzi, 1616; Wren, 1750; Branca, 1783; Cavalieri San-Bertolo, 1826].

In conjunction with the comments reported at the end of each chapter, here a more heuristic insight is adopted. For the sake of clearness, it is worth remarking the research strategy adopted:

- **Knowledge of the structural topology.** Regarded as one of the most important features in the study of heritage constructions, the first step addressed the historical evolution of cross vaults from architectural, constructive and stability points of view. The recurrent damages following both gravitational and seismic loads were also analysed.
- **Experimental activity.** The difficulties posed by the dynamic analysis of a complex element such as a masonry cross vault required a preliminary study on a simple vaulted structure. Given the wide literature on the topic, a scaled dry-joint arch was chosen, providing good insight for its seismic behaviour and the validation of the in-plane numerical model.
- **Numerical analysis.** Based on the outcomes of the previous step, the results of a recent and extensive experimental campaign on a scaled groin vault were discussed and compared with the numerical analyses of a three-dimensional model.

- **Sensitivity study.** Conversely to the detailed analysis of the previous steps, according to the main geometrical and mechanical parameters, more general aspects have been addressed here (by means of a standard limit analysis code), namely seismic capacity and most frequent failure mechanisms.

In order to properly define the object of the thesis, an historical approach was chosen, with particular reference to ancient manuals, treatises and dedicated literature. This study provided valuable information for the structural analysis of this element, from geometrical aspects (e.g. double curvature resistant-by-shape webs) to the rules of thumb adopted to size cross vaults in the past. The result of this research is a comprehensive and concise chapter which may represent a valid support for researchers and engineers involved in the analysis of masonry cross vaults.

Regarding the experimental activity on the dry-joint scaled arch, the main goal was to define a proper strategy for the dynamic tests of masonry vaulted structures (e.g. cross vaults). The proposed methodology is economical and the consequent voussoirs are hard enough to limit the damage and to allow the repeatability of the tests. However, two main drawbacks must be stressed.

The first drawback regards the friction on the lateral surfaces, which in the present study was modified by coating the voussoirs with a mixture of resin and fine sand, changing inevitably (and randomly) the geometry. Although this aspect can be negligible for unidimensional elements (the arch) where the contact between the blocks is mostly guaranteed, it is possibly decisive in bidimensional elements, e.g. shells and vault webs. The imperfect geometry, in fact, may compromise the correct block interlocking, thus the stability of the vault, even under gravitational loads. A different material or printing technique could represent a valuable alternatives to solve this issue.

The second drawback regards the mass density. Conversely to the current trend of ultralight-ultrastiff 3D printed materials, dealing with scaled model of masonry elements, a certain amount of mass density is required for assuring an overall stability of the model under accidental actions. Moreover, dealing with friction, which is a complex physical phenomenon, a relatively high value of mass density can provide a suitable level of normal stress. However, since the mass density is a non-issue in the similitude laws for rigid block dynamics, there is no recommendation on this side. In this regard, considering the general low density of 3D printed material, heavier inserts may represent a practical and economical solution, but also problematic for complex block shapes.

Using 3D printed elements as formworks could avoid the discussed disadvantages. In particular, adopting lightweight concrete materials, all the mechanical parameters would be already suitable with high geometrical accuracy. In addition, fibre reinforcing may prevent shrinkage and minor

damages thanks to an overall larger robustness. Moreover, given the equal geometry of the majority of the blocks, this strategy can be quick and effective.

The experimental tests on the arch were essential to develop a valuable expertise for further studies on masonry vaults. In particular, as already stressed, the main goal of this study was to validate the FEM model for static and dynamic nonlinear analyses. The objective was entirely accomplished, but some considerations must be added. The major concern of this research was the implementation of FEM analyses for simulating a physical phenomenon which is discrete (due to dry joints). However, the model with friction interface elements (where all the nonlinearities are condensed) caught well the behaviour of the arch, even in case of large (finite) displacements. The comparison between the numerical results and the displacements recorded with a feature tracking technique showed an appreciable match.

The dry-joint arch was tested under a novel signal built by a windowed three-cycle sine. Compared with the available literature, the specimen was subjected to the main pulse when it was not at rest, facing out-of-phase acceleration. Thanks to a high speed camera, the recordings were inspected and no flipping impacts or sliding effects were detected. On the other hand, a simplified schematization of the complex behaviour of the specimen was proposed, which can be helpful for an analytical formulation of the problem. A representation in the frequency-amplitude domain was adopted. Compared with one-cycle sine impulse [DeJong et al., 2008], the signal adopted here resulted less conservative because the out-of-phase content allowed the arch to, temporarily, experience unsafe displacements (coming back to a safe configuration soon after). However, in agreement with literature, the best regression line fitting the failure inputs was exponential.

As far as the numerical model is concerned, since the external coating inevitably affect the geometry of the voussoirs, in order to account for slight variation of the geometry, the analyses regarded the arch with an overall reduction of 10% of the thickness, as also proposed by other authors. Great attention has been paid to the stiffness of the interface elements. A sensitivity study was presented for both statical nonlinear and time history analysis. Regarding the former, in case the geometrical nonlinearities were not accounted for, no matter the stiffness, all the capacity curves asymptotically assessed the capacity of the arch. On the contrary, the ultimate displacement is incorrectly reproduced. On the other hand, adopting an Updated Lagrange formulation, the envelope of the capacity curves with different stiffness represented well the nonlinear behaviour of the arch.

With respect to the time history analyses, a large number of results were achieved for normal and tangential stiffness in the range 0.1 - 1.0 MPa/mm and zero damping (lower values of stiffness led to convergence problems). In both nonlinear static and time history analyses, notable

differences were found varying the ratio between tangential and normal stiffness (0.1, 0.4, 1). Compared with literature [De Lorenzis et al., 2007; D'Ayala and Tomasoni, 2011] and experimental evidences, the cases with ratio equal to 0.1 led to unreal sliding occurrence. On the other hand, the ratio equal to 0.4 (value adopted in literature, see [Senthivel and Lourenço, 2009]) and 1 provided almost coincident results.

Once validated, the model was extended to nonlinear static analysis of a masonry groin vault. The consequent three-dimensional analysis highlighted the limitations of FEM for this kind of study. Conversely to the in-plane analysis of the arch, where the hinges involve only two adjoin voussoirs and they (the hinges) keep opening as soon as activated with no sliding occurrence (at least for common values of friction angle and the given thickness to span ratio), here the problem is more complicated. First of all, the amount of interface elements is larger, covering four lateral faces with a single block usually surrounded by six other blocks. Given the bidimensional behaviour of the shells, sliding between blocks is unavoidable for the interfaces with low levels of normal stress. Furthermore, in case of peaks of stresses and strains (as a result of high values of interface stiffness), convergence problems may arise. The same issue was faced when the failure of the structure involved only a few and isolated blocks, a phenomenon which is badly handled by FEM analysis.

The three-dimensional model was built upon the experimental campaign recently performed on a scaled groin vault by Rossi and co-workers [2014, 2015; 2015]. Given the similarities of this specimen with the arch studied in the previous step (e.g. 3D printed blocks, dry joints, and overall dimensions) the same numerical model was used to replicate the experimental results.

Firstly, a simplified schematization of the block pattern was proposed providing a significant block interlocking at the groins of the vault. Secondly, similarly to the previous chapter, the influence of interface stiffness and geometrical nonlinearities was discussed, highlighting no significant differences in terms of failure mechanisms and capacity. The values of interface stiffness that better fitted the experimental results are in the range $0.5 \div 1$ MPa/mm, in line with the results of the previous chapter. Few discrepancies were also notable, e.g. ultimate displacement in the in-plane shear test, presumably due to the complexity of the experimental setup and boundary conditions.

A strong analogy with the nonlinear behaviour of a free-standing rigid block undergoing incremental horizontal force was stressed. In this regard, according to the comparison between experimental and numerical results, a possible strategy for assessing the capacity curve in terms of horizontal load multiplier vs displacement was proposed. Further studies are still requested on this topic.

On the other hand, with the aim of addressing general aspects on the seismic behaviour of groin vaults, conversely to the detailed models described in the previous steps, a sensitive study based on standard limit analysis was performed. The adopted code is originally from Milani et al. [2009a, 2009b], with minor changes. Although approximated, the quick analyses regarded two boundary conditions and a wide range of parameters, providing valuable results on the seismic capacity and the most frequent failure mechanisms of groin vaults. In particular, span, rise, angle of embrace, infill and masonry tensile strength were discussed. The outcome of this study was analysed using multiple linear regression analysis resulting in a helpful tool for expedite seismic evaluation of groin vaults.

More in detail, four strategies for modelling the infill as lumped load/mass in the centroid of each wedge (by which the vault is discretized) were implemented. On a safe side perspective, applying on both sides of the vault the equivalent load of horizontal stripes of infill resulted in the most conservative schematization. According to two boundary conditions, the most influencing parameters were shown, usually represented by tensile strength, and thickness and rise over span ratios. Possible scale effects were also observed.

6.2 Future works

Each step presented in the previous section may represent a starting point for future works.

The study of ancient treatises and construction manuals of the past represents an important source and guide for achieving a proper knowledge of cultural heritage buildings. Only recently this approach have been identified as essential in the analysis of historical constructions, and more research is still required in this field. On the other hand, an extensive database of case studies, which is currently missing, seems to be needed to support the relevance of this historic information.

Regarding the experimental tests on the dry-joint arch, a systematic analysis of the data collected by the feature tracking system is expected for a better understanding of the arch behaviour and for detecting micro-impacts and temporary hinges. On the other hand, once validated by further experiments, the evolution of the proposed mechanisms (i.e. hinge location throughout the test) may represent a valuable support for enhance the analytical formulation of arch dynamics. In particular, given the features of the adopted signal, this step may account for hinge location not assumed *a priori* or with initial conditions not at rest, in an overall more realistic perspective.

On the other hand, with the due precautions discussed above, the experimentation of a scaled (or true scale) model of a groin vault represents the direct extension of the present thesis. Starting

from the outcomes of the dynamic tests and the analyses of the dry-joint arch, an experimental campaign may represent a valuable source of data for better assessing the seismic behaviour of cross vaults.

Regarding the three-dimensional analysis of groin vaults, the simple procedure adopted for the block patterns can represent a useful tool to be implemented for other types of vaults or in algorithms for automatic mesh generation. On the other hand, the interface stiffness still represents a delicate issue. It must be noted, indeed, that the values of stiffness discussed in the present thesis were estimated according to scaled vaulted structures built with dry-joint plastic blocks, without reaching the stress level of real scale masonry elements. This crucial aspect still requests more efforts and the behaviour of vaulted elements with different scale and materials should be investigated.

Considering the last step of the thesis, according to the main outcomes of the sensitivity analysis, which are the analytical formulation for the seismic capacity evaluation and the most recurrent failure mechanisms, few aspects can be still developed. Since the methodology adopted was based on standard limit analysis, in order to highlight possible discrepancies, a comparison with more sophisticated approaches is required (either nonstandard limit analysis, FEM or DEM). Conversely, the proposed mechanisms can be analysed by means of equivalent arches: whereas on the one hand this study would provide a valuable insight into the mechanics of the vault, on the other hand, it would offer a schematic approximation of its behaviour to be easily implemented in the current Codes of Practice. As an example, considering the in-plane shear mechanism, a schematization of the vault by means of the six main arches (four perimetral and two diagonal) can be pursued.

As a future work, the sensitivity analysis should address the influence of the uncertainties on the input parameters. In this regard, a Monte Carlo simulation may represent a helpful tool for defining the confidence factors to be adopted in the analysis. Moreover, the study may be extended to the influence of the friction, different block patterns, and a more detailed description of the boundary conditions.

Finally, the same strategy adopted in the present thesis can be extended to other types of masonry vaulted structures, e.g. different shapes of cross vaults, as well as dome and cloister vaults.

References

- Branca, G. (1783). *Manuale d'architettura*. (V. Monaldini, Ed.) (4th ed.). Roma: Con licenza dei Superiori.
- Cavalieri San-Bertolo, N. (1826). *Istituzioni di architettura statica e idraulica*. Bologna: Tipografia Cardinali e Frulli.
- D'Ayala, D., and Tomasoni, E. (2011). Three-dimensional analysis of masonry vaults using limit state analysis with finite friction. *International Journal of Architectural Heritage*, 5(2), 140–171.
- De Lorenzis, L., DeJong, M., and Ochsendorf, J. (2007). Failure of masonry arches under impulse base motion. *Earthquake Engineering & Structural Dynamics*, 36(14), 2119–2136.
- DeJong, M., De Lorenzis, L., Adams, S., and Ochsendorf, J. A. (2008). Rocking Stability of Masonry Arches in Seismic Regions. *Earthquake Spectra*, 24(4), 847–865.
- Jacopo Barozzi da Vignola. (1562). *Regola delli cinque ordini d'architettura*. Rome: Con licenza dei Superiori (edition 1732).
- Milani, G., Milani, E., and Tralli, A. (2009a). Upper Bound limit analysis model for FRP-reinforced masonry curved structures. Part I: Unreinforced masonry failure surfaces. *Computers & Structures*, 87(23-24), 1516–1533.
- Milani, G., Milani, E., and Tralli, A. (2009b). Upper bound limit analysis model for FRP-reinforced masonry curved structures. Part II: Structural analyses. *Computers & Structures*, 87(23-24), 1534–1558.
- Rossi, M. (2015). *Evaluation of the seismic response of masonry cross-vaults*. PhD dissertation, University of Genoa.
- Rossi, M., Calderini, C., and Lagomarsino, S. (2015). Experimental testing of the seismic in-plane displacement capacity of masonry cross vaults through a scale model. *Bulletin of Earthquake Engineering*.
- Rossi, M., Calderini, C., Lagomarsino, S., and Milani, G. (2014). Seismic response of masonry vaulted structures: experimental and numerical modelling. In P. B. Lourenço, B. A. Haseltine, & G. Vasconcelos (Eds.), *9th International Masonry Conference*. Guimarães: Universidade do Minho.
- Scamozzi, V. (1616). *L'idea di architettura universale*. (T. Stefano, Ed.). Milano: Coi tipi di Borroni e Scotti (edition of 1838).
- Senthivel, R., and Lourenço, P. B. (2009). Finite element modelling of deformation characteristics of historical stone masonry shear walls. *Engineering Structures*, 31(9), 1930–1943.
- Wren, C. (son). (1750). *Parentalia: or, Memoirs of the Family of the Wrens*. London: Published by Stephen Wren.